Bistable Interlocking Mechanism in SHCC-to-SHCC Interfaces
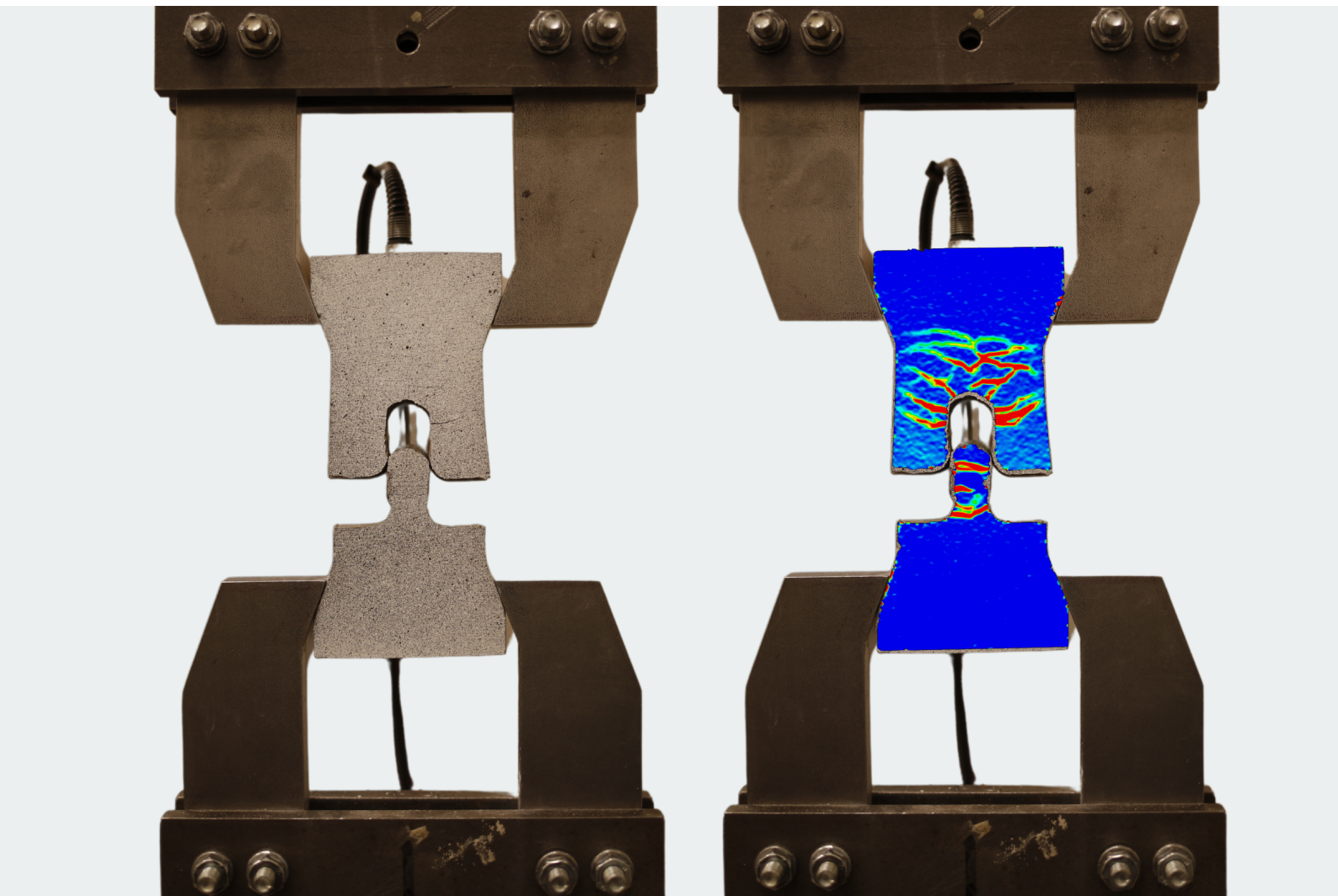
Sofia Papoulidou

TUDelft

Bistable Interlocking Mechanism in SHCC-to-SHCC Interfaces

An Experimental Study

by

Sofia Papoulidou

to obtain the degree of Master of Science,
at the Delft University of Technology,
to be defended publicly on Friday, February 23, 2024, at 1.00 PM.

Student Number:	5382734	
Faculty:	Civil Engineering & Geosciences, TU Delft	
Thesis committee:	Dr. ir. M. Luković (chair)	TU Delft, Concrete Structures
	ir. S. He (daily supervisor)	TU Delft, Materials & Environment
	Dr. ir. B. Šavija	TU Delft, Materials & Environment

An electronic version of this thesis is available at http://repository.tudelft.nl/.

TUDelft

Acknowledgments

Completing this thesis marks the end of my journey as a master's student at TU Delft. It has been a challenging yet incredibly rewarding experience that has transformed me both personally and professionally. I feel grateful for the vibrant academic community here and the inclusivity of the university; I felt it was a place for personal and professional growth.

First and foremost, I extend my heartfelt gratitude to my supervisors. Mladena, your unwavering belief in me and the opportunity to collaborate on this innovative and demanding project have been truly inspiring. Your enthusiasm and dedication to this topic motivated me to push my boundaries and challenge myself. Starting with my research project and then my thesis, you were always involved and helpful. I also want to express my appreciation for allowing me to work with you as a student assistant in a course I thoroughly enjoyed; it was a fantastic learning experience and a lot of fun!

Branko, thank you for consistently offering a unique material-related perspective to my thesis, and provoking deeper thinking and research. Your insights were always on point and guided me through this academic journey. Collaborating with you and Mladena, experts in materials and concrete has been a valuable experience for me.

My daily supervisor, Shan He, deserves special recognition. Shan, your extensive knowledge of SHCC and experimental design significantly eased my thesis journey. Thank you for always being available and making me feel confident in asking more questions, even if sometimes were a bit too many! Your invaluable assistance in the experimental phases, from casting to testing and result analysis, was instrumental. You've been an exceptional mentor.

I'd like to express my gratitude to all the lab technicians I had the privilege of working with, as well as all those who contributed to this journey. Maiko, thank you for your unwavering assistance, even when it meant sacrificing your lunchtime to answer my questions. Thank you for including me in the Microlab activities, it was fun to socialize with the Microlabers! Kies, your help in fixing and calibrating the test setups was indispensable; without you, my experiments would have faced many issues. You dedicated a great deal of effort to assist me with the Instron and even showed me how to calibrate it! Learning from you was truly enjoyable. Albert, thank you for your support and advice and for lending me the necessary equipment for my tests. And Giorgos, your eagerness to assist with my DIC was remarkable. You were always taking the time to help me and show me all the DIC secrets. I felt more confident in my results because of that.

I extend my thanks to all the Ph.D. students—Jinbao, Yading, Mohammed, Angeliki, and Hagar—for their support and valuable advice throughout this process. Special thanks to Prof. Florentia Kavoura for trusting me to be her student assistant and consistently motivating me. Florentia, I cannot adequately express the confidence you instilled in me, and I deeply appreciate it.

To all my wonderful international and Dutch friends, I am immensely grateful. All the stimulating conversation during our coffee breaks, lunch, and parties, and all your support means the world to me! A heartfelt thank you to U-Base for organizing numerous enjoyable activities and connecting structural and building engineers from around the world. Being part of the Value of Design committee was a truly special experience.

A special mention goes to my dearest friends from Greece. Despite sometimes not speaking for days, I always felt your support from afar.

Lastly, I want to express my gratitude to my family—my incredible mom, dad, and brother—and my beloved fiancé, Antonis. Your patience in listening to the details of my engineering endeavors and your unwavering support at every step of this journey is beyond words. Σας ευχαριστώ!

Sofia Papoulidou
Delft, February 2024

Abstract

The current structural demands include complex designs, efficient utilization of material resources, and maintenance of existing structures and infrastructure. In all these cases, the connections between structural components are the main focus of design since they are widely considered the weakest link in a structural system. The demand for strong and durable connections with cementitious materials is higher than ever. Creating reliable connections is largely connected to material reuse, waste reduction, ease of disassembly, and the ability to extend the life cycle of structures. These principles contribute to a more sustainable approach to construction.

Recent research shows that by implementing intricate interlocking geometries, toughness can be added to inherently brittle materials like ceramics or polymers. With the concept of "toughness by segmentation," new metamaterials emerge with enhanced properties compared to the monolithic material they are made of. In this study, the focus is on bistable interlock, a new type of connection. Inspired by nature, the connection is based on double-radii morphologies that geometrically lock into two equilibrium positions under tensile load, exhibiting two distinctive peaks in their force-displacement diagram. When the bistable interlock mechanism was applied to Acrylonitrile Butadiene Styrene (ABS), a relatively brittle yet strong polymer, the sutured material was up to 10 times tougher than monolithic ABS. The focus of this research is to manufacture the bistable interlock mechanism with cement-based materials and specifically, Strain Hardening Cementitious Composite (SHCC). SHCC belongs to the category of fiber-reinforced concrete and is distinguished by its tensile hardening behavior and pseudo-ductility stemming from its fiber-bridging property. Combined with the geometrical hardening of bistable interlock, the ultimate goal is to create resilient connections that balance toughness and strength.

The performed literature study was focused on three areas: the bistable interlock mechanism, interfacial load transfer mechanisms in concrete-to-concrete interfaces such as friction, chemical bond, and mechanical interlock, and the material and mechanical properties of Strain-Hardening Cementitious Composites (SHCC).

Two main areas of interest were the objects of the experimental study. The first was to understand the tensile behavior of bistable interlocks, and the second was to optimize it by appropriately tailoring the interface and geometry. The design of the experiments featured three parameters: the key shape (straight & curved keys), the interface treatment (untreated & lubricated interface between the two parts), and the geometry (based on width-to-height ratios for straight keys & radii ratios for curved keys).

From the experimental results, it was found that the shape of the keys changed the tensile response of the specimens greatly. The influence was different for untreated and lubricated interface specimens. For the untreated specimens, the complex shape of the bistable interlocked geometry combined with interface adhesion led to 78% of the untreated specimens rupturing at the interface. Only 44% of the straight keys showed failure under the same conditions. In this application of bistable interlock, no benefits of geometrical hardening could be exploited due to the strong adhesive bond causing premature failure of the keys at the interface. For the lubricated specimens, shifting from straight to curved geometry brought simultaneous increases in force and energy (i.e. defined as the area under the force-displacement diagram) for all the specimens, fully exploiting the benefits of the frictional contact of the bistable interlock mechanism. The increase in force documented ranged from 41-62% and in energy from 9–96%.

The aforementioned difference in tensile response highlights that the interface treatment is a governing parameter. Only 56 and 22% of untreated straight and curved specimens fully delaminated (e.g. instead of breaking) in comparison to 89% of their lubricated equivalents. The rest of the specimens exhibited (localized) SHCC failure due to the strong interface bond. Untreated specimens showed a higher resistance force (approximately 20% for straight and 10% for curved keys) but a more brittle response, resembling a monolithic connection, while lubricated specimens showed less resistance to tension, resembling a sliding connection. This trend is consistent with broader findings in the literature: inherently brittle monolithic materials compared to their architectured counterparts exhibit greater strength but lower toughness. For the straight keys, lubrication made the failure mode more uniform

but decreased the strength and energy. The strong bond of untreated specimens, accompanied by a hardening response due to fiber activation against torsion and/or bending, was responsible for this result. Specimen imperfections caused this state of combined loading. Curved lubricated keys showed an enhancement in energy absorption (i.e. area under the force-displacement diagram) due to the exploitation of the bistable interlocks. Special curved keys made of assembled parts were investigated, simulating a precast-to-precast connection. The assembled keys did not outperform the lubricated and untreated curved keys in terms of strength and energy absorbed. Their benefits lie in two areas: they were easier to manufacture, and they attained a larger second peak than the first in the force-displacement diagram. This characteristic is beneficial for the mechanical stability of the system.

To optimize the response, the specific geometry of the specimens was analyzed (w/h and R_1/R_2). The influence of the geometry on the tensile response was not as prominent as the interface treatment. However, improvements were noticed when increasing geometry parameters. For untreated and lubricated straight keys, increasing the length led to a proportional increase in absorbed energy but not in strength. For the curved untreated specimens, the increase in geometry yielded no major differences since the interface treatment governed the response. Conversely, for the lubricated specimens, with a geometry increase, the response was enhanced in both strength and energy and eventually, a design threshold at $R_1/R_2 = 1.10$ was noticed. A clear trend of an increase in the first peak, and a decrease in the second peak as the geometry increased, existed. Extensive cracking and loss of stiffness after the second equilibrium position due to the geometrical interference of larger keys were responsible for that.

Overall, the architectured SHCC material, straight or curved, attained 1/3 of the strength of the monolithic SHCC. This was even lower for lubricated keys. When it came to energy absorption, the lubricated curved keys with bistable interlocks performed better, reaching up to 75% of the SHCC's energy. This is contrary to the literature findings, where bistable interlocked materials made of ABS were tougher than monolithic ABS. In the case of SHCC, the material properties were different. Due to the extensive cracking of the key, reduced frictional contact occurred, and reduced energy was absorbed. However, a beneficial characteristic of the architectured SHCC keys was their sustained resistance to tension at higher strain levels. That makes them beneficial for many engineering applications where energy absorption and resistance to impact loads and thermal and/or hygral effects are prioritized. Another benefit exists in the customization of their tensile response by fine-tuning geometrical parameters. For a radii ratio of 1.10 in bistable interlocked keys, a satisfactory balance of strength and toughness was achieved, showing that with appropriate design, the connections have promising results.

Symbols & Abbreviations

Symbols

ξ	Peak force ratio F_2/F_1
R_a	Average Roughness
A_r	True area of contact
δ_0	Peak crack opening
E_m	Matrix Young's Modulus
H	Hardness of the softer contacting material
N	Normal force
μ	Friction coefficient
μ_a	Coefficient of adhesive friction
μ_k	Coefficient of sliding friction
η	Viscosity of the lubricant
σ_0	Fiber bridging capacity (peak stress)
σ_{ss}	Steady-state matrix cracking stress
τ_j	Average shear strength of junctions
$\theta_{0,1,2}$	Interlocking angles 0, 1, 2
ν	Velocity of the surface
J'_b	Complementary energy
J_{tip}	Crack tip energy
K_m	Matrix fracture toughness
R_1/R_2	Radii ratio
Ra	Average roughness
w/h	width to height ratio

Abbreviations

ABS	Acrylonitrile Butadiene Styrene
BFS	Blast Furnace Slag
B-and-M	Brick and Mortar
CCG1, 2, 3	Curved Key, Untreated Interface, Geometry 1, 2, 3
CLG1, 2, 3	Curved Key, Lubricated Interface, Geometry 1, 2, 3
CO_2	Carbon Dioxide
CP	Curved Key, Prefabricated Interface
DIC	Digital Image Correlation
DLP	Digital Light Processing
FA	Fly Ash
FRC	Fiber-Reinforced Concrete
HMPE	High Modulus Polyethylene
LVDT	Linear Variable Differential Transformer
PVA	Polyvinyl Alcohol
PE	Polyethylene
PP	Polypropylene
RH	Relative Humidity
SCG1, 2, 3	Straight Key, Untreated Interface, Geometry 1, 2, 3
SEM	Scanning Electron Microscope
SHCC	Strain Hardening Cementitious Composite
SLG1, 2, 3	Straight Key, Lubricated Interface, Geometry 1, 2, 3

Contents

List of Figures

List of Tables

<div style="text-align: right; font-size: 3em;">1</div>

Introduction

1.1. Background & Problem Definition

In light of the ongoing demand for more durable and sustainable concrete structures, special attention is drawn to the connections between structural members and materials.

Civil engineering projects often involve the construction of various components connected at different construction stages. Current structural demands and complex designs in infrastructure and the built environment involve the connection of a variety of different materials. Many countries, such as the Netherlands, are experiencing a growing demand for preserving existing structures. To shift to a more sustainable future, the extended service life of engineering projects involving repairs, refurbishments, or maintenance is desired. All these examples involve different components connecting, thus creating an interface between them. The existence of interfaces between structural components in civil engineering is inevitable, and the requirement of those to ensure compatibility and structural integrity is of utmost importance. The reason that the interface role is crucial is that it is widely considered to be the weakest link regarding the structural reliability of a composite structure or system.

When it comes to concrete elements (partially or entirely prefabricated), dominant in engineering practice, the most common types of these connections are *precast-to-precast* concrete connections and *precast-to-in situ* connections.

Interface failures, such as debonding, crack formation, delamination, and fiber pullout when fibers are involved, can compromise the structure's load transfer capacity & eventually structural integrity. When it comes to real-life examples, in bridge engineering, debonding or crack formation at the concrete-to-concrete interface can lead to a decrease in serviceability standards and even a compromise in the structure's overall load-bearing capacity. Similarly, in tunnel lining applications, interface issues in the connection between segments or layers of the lining can compromise the tunnel's structural integrity. Creating strong and durable interfaces can ensure the safe and reliable operation of structures and infrastructure, but it can also prevent costly repairs or replacements due to premature interface failures [1]. This aligns with the requirements to create more sustainable concrete structures.

Establishing that the interface should be the focus of the design, the local properties are essential in achieving a good concrete-to-concrete connection. In principle, a reliable structural interface is based on the interfacial load transfer mechanisms of *friction, adhesive bonding,* and *mechanical interlock* [2]. Surface roughness can increase friction and enhance the bond between two layers of concrete by creating interlocking features between them or by increasing the surface area available for bonding. Factors influencing chemical bonding between concrete layers include moisture exchange, curing and stress conditions at the interface, compatibility of the materials, the presence of any bonding agents or adhesives, and more. In the same line of thought, a mechanical interlock between two layers improves the bond between them. It is a common practice to create grooved or chiseled interfaces to avoid delamination failure of interfaces [3]. Also, other mechanical interlocking features, like shear keys, can increase the shear transfer capacity of a connection.

High chemical and mechanical strength and a rough surface are beneficial for a stronger interface. However, a stronger interface can often result in localized cracks and brittle failure. A smoother interface

<div style="text-align: center;">1</div>

and lower interfacial strength can, in many cases, promote the formation of more cracks and partial relief of stresses. In such a way, higher energy dissipation and better use of the materials' ductility can be achieved [1], [4]. The attainment of both strength and toughness is a vital requirement for structural materials; however, these properties in practice are mutually exclusive [5]. The goal for durable connections is to create a balance between strength and toughness and enable the uniform behavior of a multi-layer system as a monolithic one.

This goal, along with inspiration from nature, has driven material research toward the design and implementation of engineered materials. Creating hybrid materials that combine the best qualities of their constituent parts is the key challenge. Materials such as nacre, bone, enamel, and shells are acting as inspiration to move toward engineered "ultimate" materials. A common characteristic of those is that they implicate geometrical interlocking in their structure to dissipate energy and generate toughness [6]. To do that, their structure usually involves hard phases with complex geometries and compliant, flexible phases linked together.

This research is focused on a special type of engineered material involving sutured jigsaw-like morphologies (tabs), designed to geometrically lock into two different stable states (Figure 1.1). Due to this characteristic, this mechanism was named *Bistable Interlock* by Mirkhalaf et al. [7].

Some of the characteristics of bistable interlocked geometries are that without obvious damage accumulation, the system is capable of interchanging between two equilibrium positions [7]. With their special geometry, a type of *geometric hardening* mechanism takes place, making the material able to postpone the localization of strains and spread nonlinear deformations. This mechanism can increase the toughness of brittle materials and also dissipate energy coming from external loads into larger volumes of material [6]. The geometry of the tabs of this connection can be fine-tuned to change the mechanical response of these materials through design [7]. This means that toughness can be added to the system without major losses in strength. This is a favorable characteristic for achieving the aforementioned balance in strength and toughness of a connection.

The primary focus of this study is to manufacture the bistable interlock mechanism with cement-based materials. Specifically, Strain Hardening Cementitious Composite (SHCC) was chosen. SHCCs are materials that belong to the family of fiber-reinforced concrete and are distinguished by their tensile hardening behavior [8], stemming from their fiber-bridging property. With the use of the *strain hardening* property along with the *geometric hardening* of bistable interlocks, the advantages could be even greater when it comes to ductile and damage-tolerant connections.
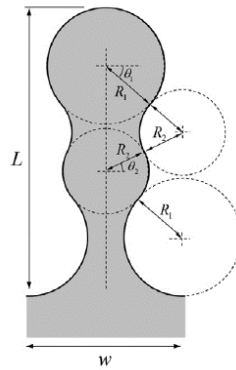
Figure 1.1: A typical geometry designed with bistable interlock [7]

While the bistable interlock mechanism has not yet been put into practice, many research possibilities have arisen for its employment. With the implementation of multiple layers of bistable interlocked material (Figure 1.2), the deformations can be spread to large volumes, acting as a damping mechanism for impact loads. In applications such as protective structures, retaining walls, and earthquake-resistant structures, this mechanism could be useful.

Since the bistable interlocked materials tested in [7] showed no visible damage accumulation, an interesting possibility would be the demountability and re-manufacturability of connections using these types of interlocks to simplify the construction process.

With the ability of bistable interlocks to sustain resistance to tension at larger deformations, possible

benefits for connections susceptible to imposed deformations are possible. This characteristic would be valuable in situations where imposed deformations are expected, such as thermal expansion and contraction or settlements.
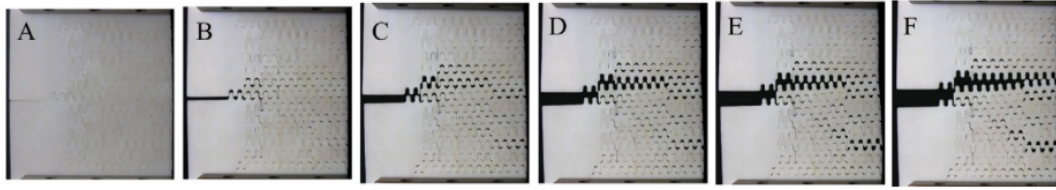
Figure 1.2: In-situ images of the formation of a triangular process-zone in the bistable interlocked material, followed by progressive fracture [7]

1.2. Objective & Research questions

This research aims to investigate the tensile performance of bistable interlocks in sutured geometries made of Strain-Hardening Cementitious Composites. Additionally, straight keys made of SHCC are going to be investigated and act as a benchmark. The ultimate goal is to design reliable connections of cementitious materials with higher damage tolerance by exploiting the shape of bistable interlock and fine-tuning geometrical properties to get a "desired performance" based on toughness and strength.

The main research questions and sub-questions of this study are:

RQ1: To what extent can the implementation of the bistable interlock mechanism enhance the toughness and strength of interlocking keys made of SHCC under tensile loading?

- What is the tensile response of *straight* interlocking SHCC keys, in terms of toughness and strength?
- What is the difference in the tensile response of *curved* interlocking SHCC keys compared to straight SHCC keys?

RQ2: How can the tensile response of different interlocking SHCC keys be optimized in terms of toughness and strength?

- What is the influence of an *untreated interface* & *interface lubrication* on the tensile response of both straight and curved keys? What is the influence of an *out-of-plane assembled interface* on the tensile response of curved keys?
- How do *straight keys* with different width-to-height ratios & *curved keys* with different radii ratios behave under the aforementioned interface treatments regarding strength and toughness? What types of failure are observed as the geometry changes?

1.3. Research Methodology

To realize the goal of the research, a parametric study of various straight and bistable interlock specimens was designed. The specimens were experimentally tested to explore the effect of geometry and interface properties on the tensile performance of straight and bistable interlocked keys. Through *design exploration* and change of their *interface properties*, SHCC specimens containing straight and curved geometries were cast and tested under uniaxial monotonic tension. The results were documented via Digital Image Correlation (DIC) and Linear Variable Differential Transformers (LVDTs).

The parametric study includes specimens containing interlocking keys of:

- Two different shapes,

  - straight keys,
  - curved keys.

- Three different interfacial conditions,

  - left as-cast interface,
  - lubricated interface,
  - "assembled" interface created by the sliding of the two parts in the out-of-plane direction.

- Three geometry variations per shape.

  - different width-to-height ratios (w/h) for straight keys,
  - different radii ratios (R_1/R_2) for the curved keys.

The methodology followed in this research is shown below:
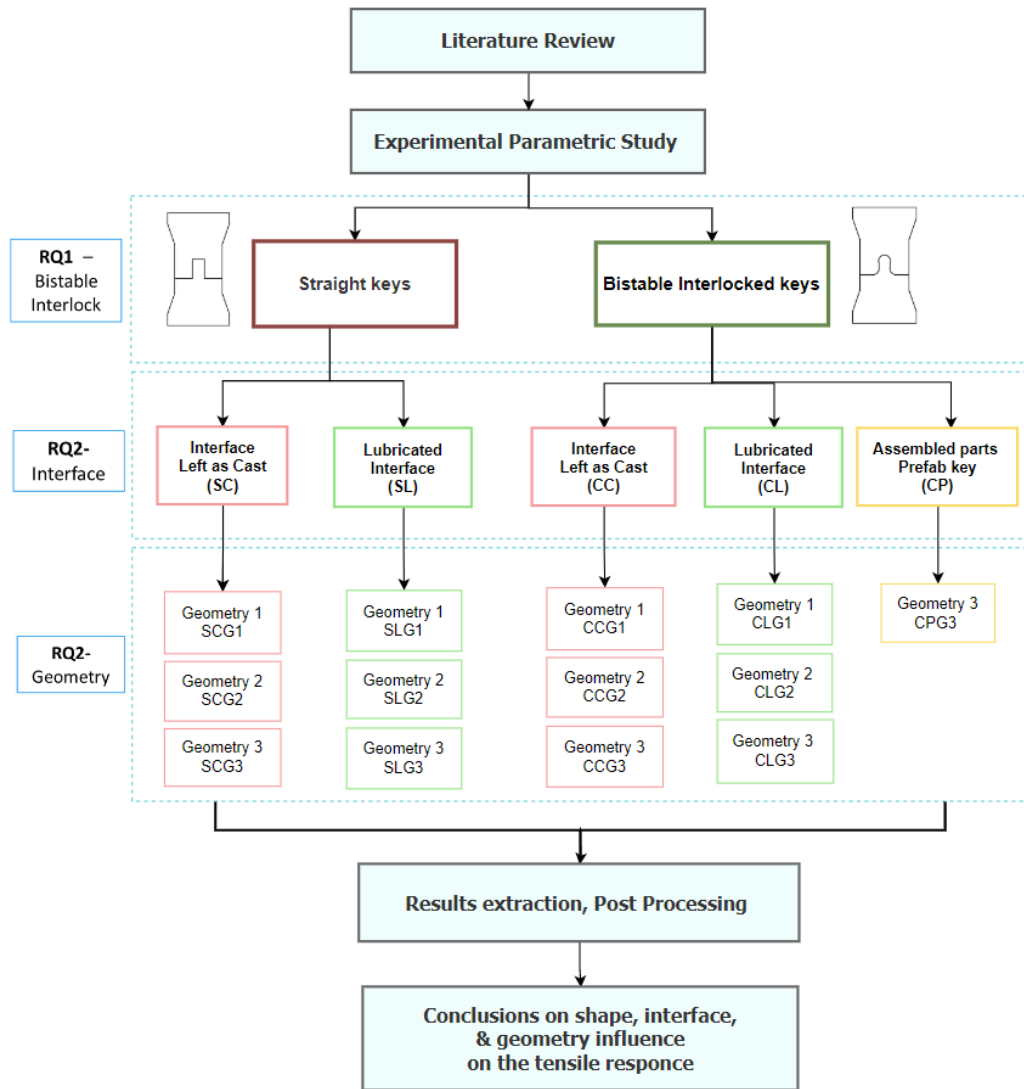
Figure 1.3: Thesis Methodology

1.4. Outline of the thesis

The general outline of the report's structure is presented below.

- **Chapter 1:** An introduction to the project background. The problem definition, the research objective and research questions, and the methodology and outline of the research were included.
- **Chapter 2:** A literature review was performed focusing on the bistable interlock mechanism, the interfacial load transfer mechanisms (friction, bond, and mechanical interlock) in concrete-to-concrete interfaces, and the material and mechanical properties of SHCC.
- **Chapter 3:** The experimental study was presented, focusing on the design of specimens, the production of the SHCC mix, mould and specimen preparation, and structural testing, along with the data measurement methods.
- **Chapter 4:** The experimental results of DIC on one specimen from each category will be presented and analyzed.
- **Chapter 5:** Discussion of the results and comparison of specimens with different shapes, interface treatment, and geometry.
- **Chapter 6:** Conclusions and recommendations for future research.

2

Literature Review

The literature review chapter focuses on the development of architectured materials in materials science, drawing inspiration from nature. The focal point is to produce materials utilizing complex geometries with interlocking features to improve ductility and energy absorption. The study explores the main load transfer mechanisms at interfaces, such as friction, chemical adhesion (bond), and mechanical interlock. Additionally, it discusses Strain-Hardening Cementitious Composites (SHCCs), known for their pseudo-ductility and post-crack resistance, outlining essential design conditions and material properties for SHCCs. The strain-hardening property, combined with geometric hardening from bistable interlocks, offers the potential for materials with enhanced ductility and damage tolerance.

2.1. Bistable interlock

2.1.1. Inspiration from Natural materials

The constantly increasing requirements for enhanced structural performance of materials drive research to the investigation and development of stronger, tougher, and lighter materials. Drawing inspiration from nature, an increasing trend in adopting biomimetic approaches to create innovative materials with enhanced mechanical properties is observed. These bio-inspired materials and their intricate architectures often pose manufacturing challenges due to their complex, non-monolithic structures [9]. In recent years the introduction of advanced fabrication methods such as *3D printing* has demonstrated potential in addressing these challenges [10]. The new hybrid materials (e.g. materials containing interlocks) show promise in combining the best properties of their components.

Natural materials such as nacre, bone, enamel, diatoms, and shells (Figure 2.1) are the inspiration of many researchers to develop the enhanced engineered materials [7], [11], [12], [10]. A common feature amongst them is the use of **geometric interlocking** in their complex micro-structures to dissipate energy and increase the toughness of otherwise brittle materials. In material science, this principle is referred to as **"Toughness by segmentation"**. The concept of toughness by segmentation is that through precise material architectures and complex yet well-defined interfaces, a new architectured material emerges with enhanced properties compared to the monolithic material [12].
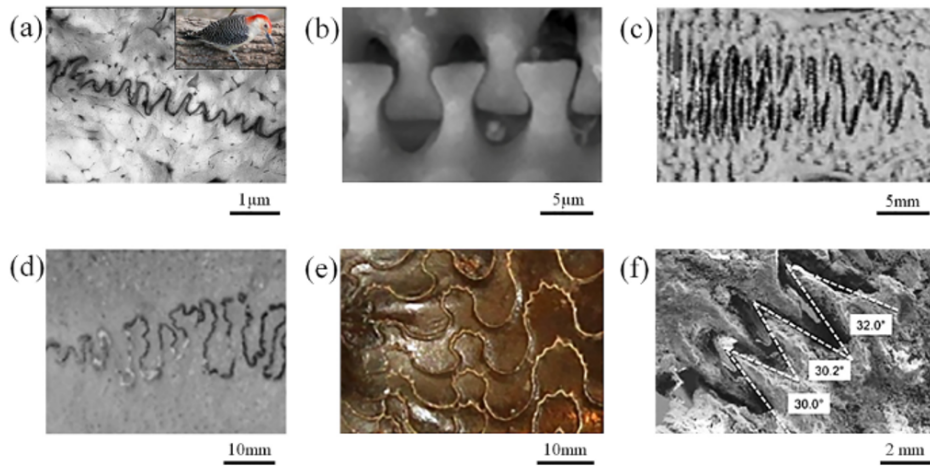
Figure 2.1: Different cases of interlocking mechanisms in nature (a) Red-bellied woodpecker beak (b) Linking girdles of diatoms (c) Marine threespine stickleback (d) Pan troglodytes cranial sutures (e) Ammonite shell (f) Osteoderms of sea turtle shell [6]

Another important concept inspired by nature is the **"Brick and Mortar mechanism"** *(B-and-M)*. In biomineralized tissues like nacre, bone, and tooth, the structure of "staggered hard crystals embedded in a soft matrix" is frequently observed [11]. These materials typically have numerous interfaces at various length scales between **stiff** and **compliant** constituents (Figure 2.2). This is metaphorically referred to as a *"brick and mortar"* structure [11], [13]. By implementing the B-and-M mechanism in bio-composite materials, a *balance* between strength and toughness can be achieved. For instance, the stiff phases' geometry and spatial arrangement compensate for the compliant phase's lack of strength. On the other hand, toughening processes like plastic yielding of the compliant phase, microcracking, crack bridging, and pulling-out of the stiff phase from the compliant phase would result in more energy dissipated and consequently higher toughness of the material [13].

A stiff interface is not always beneficial for the mechanical performance of B-and-M composites. Interfaces with overly high strength (e.g. perfect bonding) would prohibit the occurrence of these toughening mechanisms [13]. This stems from the general principle that combining a satisfactory level of strength and toughness is challenging and to a certain degree mutually exclusive [5].
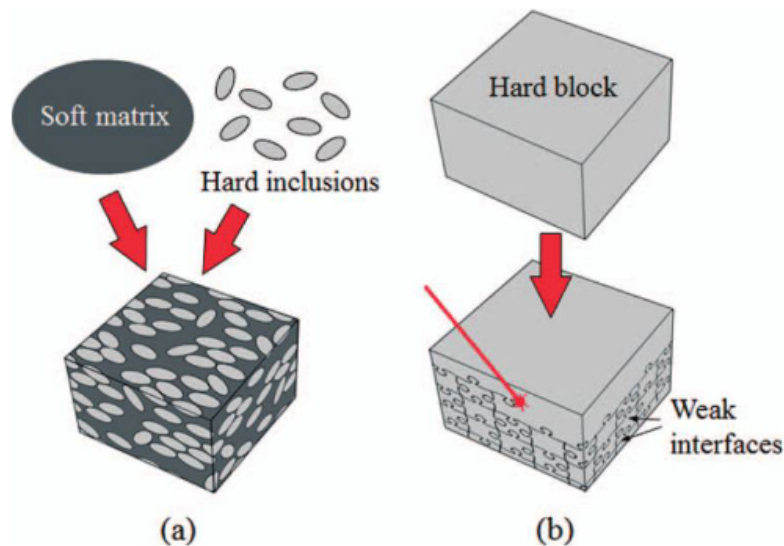
Figure 2.2: Brick-Mortar mechanisms, (a) bottom-up approach, ingredients are assembled into architectures and (b) top-down approach, material is removed from a hard block to generate architectures [11]

2.1.2. Interlock Implementation in material engineering

Ceramics are a prime example of a strong but brittle material. In the quest to add ductility and damage tolerance to a ceramic plate, Mirkhalaf et al. [12], demonstrated that segmenting a monolithic ceramic plate into interlocking blocks can alter its mechanisms of deformation and fracture resulting in larger energy absorption, and impact resistance. A summary of the mechanical performance of monolithic and architectured ceramic plates under a quasi-static push-out loading is displayed in Figure 2.3a.

The architectured panels' strength ranges from 1/4 to 1/2 than that of the monolithic. This is a common characteristic of architectured systems, as mentioned before. The frictional interfaces tend to make systems less rigid and strong but more flexible and damage tolerant [5]. In Figure 2.3, the clear advantage of those panels is shown. The architectured panel can absorb 5 to 20 times more energy before fracture than the monolithic ones (Figure 2.3 b) and has a very localized failure mode; the rest of the panel remains intact. In comparison, the monolithic panel sustained a much larger force ($\approx$ 200 N) but resulted in brittle failure dominated by flexural cracks (Figure 2.3c). In applications where kinetic energy from impact loads must be absorbed, this is a remarkable improvement. Additionally, the fabrication approach is adaptable, & scalable [12].
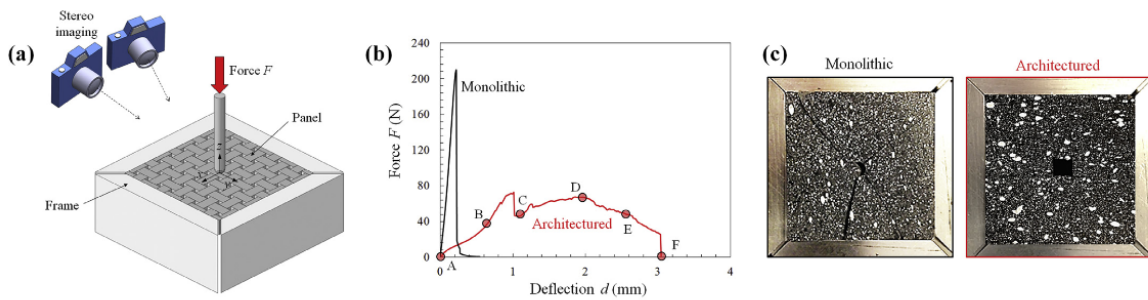
Figure 2.3: (a) Testing of ceramic panels in quasi-static loading (b) Comparison between the force-deflection curves of the monolithic and the architectured ceramic panels (c) Failure patterns of monolithic and architectured material [12]

Another application of the *"Toughness by Segmentation"* principle was the research subject of Dyskin et al. [14]. *Topological interlocking* based on matching non-planar surfaces of contacting elements was used to create a special block shape and assemble them in a masonry-like arrangement (Figure 2.4). Concerning the bone-like shape of these blocks, their assembly is referred to as *osteomorphic* [14]. Essentially, solely by implementing geometrical (kinetic constraints), the osteomorphic assembly can localize the failure to specific blocks, not allowing it to spread into the rest of the structure. Topological interlocking was achieved by appropriately choosing matching curved surfaces of the elements in contact, specifically, the convex parts of the surface of one block, matched with the concave parts of the adjacent blocks (see Figure 2.4a). When the blocks are brought in contact, no relative movements in the xy-plane are possible due to a frame acting as a constraint at the periphery of the assembly in the z-direction (Figure 2.4b).

(a) Assembling and layering of osteomorphic blocks

(b) Geometry of one block
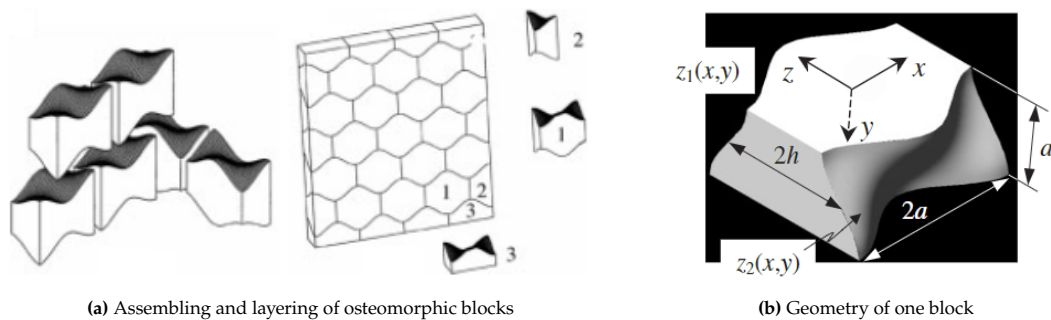
Figure 2.4: Geometry and assembly of osteomorphic blocks in a plate [14]

The assembly and the reference solid plate were made of polyester casting resin Polylite 61-209

[14]. They were held in a specially designed frame with a controlled lateral load and tested under a concentrated load (push-out) and a constant displacement rate (2mm/min). The results indicated that compared to the reference plate, the osteomorphic assembly has a much lower bending stiffness (Figure 2.5). The reference plate (monolithic) fails at a higher load indicating that the assembly has a significantly lower bearing capacity. However, the assembly can withstand sizable deformations that are comparable to its thickness. Figure 2.6 depicts the drastically different failure patterns in the solid plate and the assembly. While cracks started in the middle of the plate for the monolithic plate and spread throughout its entirety, only a small number of elements failed in the second case, with the assembly as a whole maintaining its structural integrity even with some blocks missing. Figure 2.5 shows that the response of the structure improves as the lateral constraint (applied as pressure) increases.
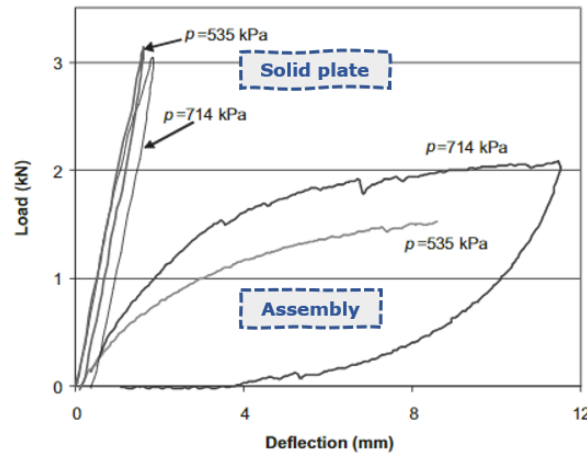
Figure 2.5: Loading vs. deflection curves for the assembly and the solid plate for two values of lateral pressure, p = 535 kPa and p = 714 kPa [14]
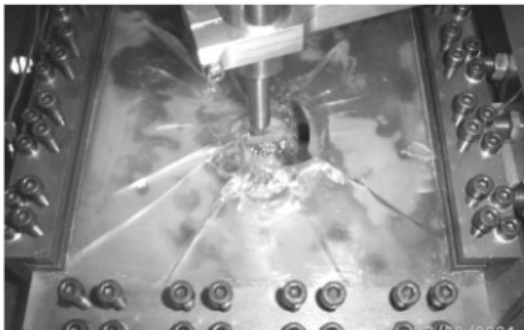
(a) Failure pattern for monolithic plate
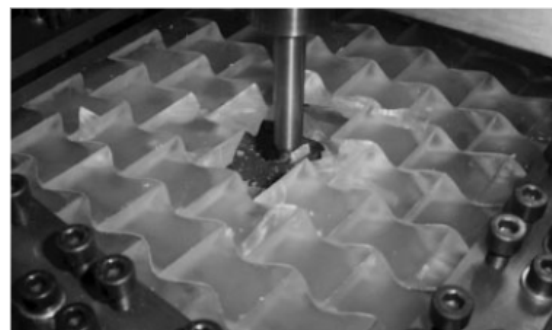
(b) Failure pattern for the assembly of osteomorphic blocks

Figure 2.6: Comparison of failure patterns in a monolithic and block-assembled plate [14]

Taking a step further, Molotnikov et al. [15] demonstrated that the constraining lateral pressure required to hold the blocks together and provided by an external frame as seen in [14], can be considered a design parameter. In essence, the maximum load the assembly can sustain and its stiffness increased linearly with the magnitude of the aforementioned applied lateral load.

The overall behavior of the osteomorphic assembly made of polyurethane in [15] is similar to the test performed by Dyskin et al. [16]. During the push-out test, the monolithic plate demonstrated a typical brittle behavior (Figure 2.7b). For the segmented plate, the push-out test created an initial deformation at low strains in which the assembled structure bent and the central block was pushed halfway. The test concluded when the central block lost contact with the adjacent blocks and was pushed out by the indenter (Figure 2.7c). The segmented plate remained intact around the block that was pushed out, and it even recovered its original stiffness [15].
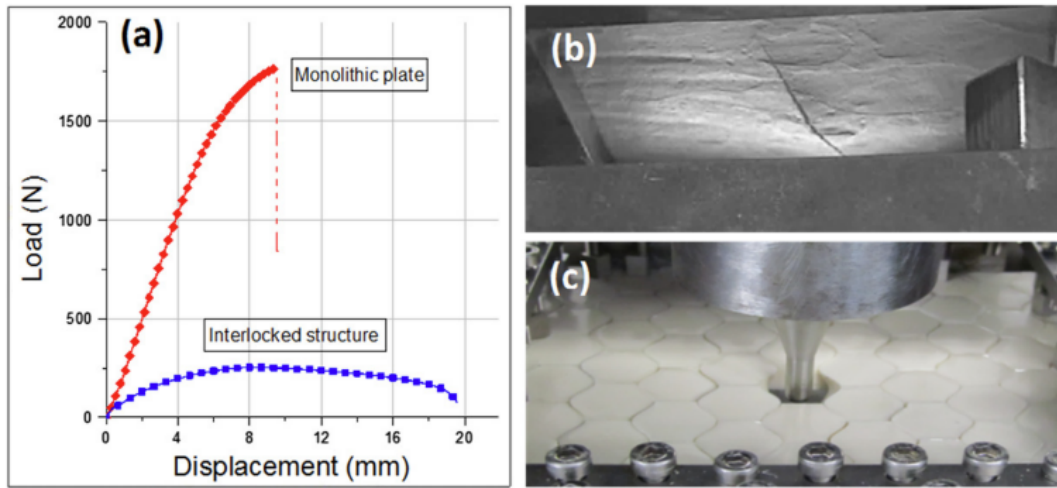
Figure 2.7: (a) Load-displacement graph for normal loading of a segmented plate assembled from osteomorphic polyurethane elements and a monolithic plate, & comparison of (b) a fractured monolithic plate and (c) a segmented plate after maximum deflection [15]

As mentioned before, with a higher constraint load (measured as torque in the constraining screws of the frame) the bearing capacity increases. For example, an increase in the constraining torque from 1 to 10 Nm resulted in an increase of the maximum push-out load from 250 N to approximately 500 N (Figure 2.8). The ability of the assembly to sustain bending deformation during this increase remained intact [15].
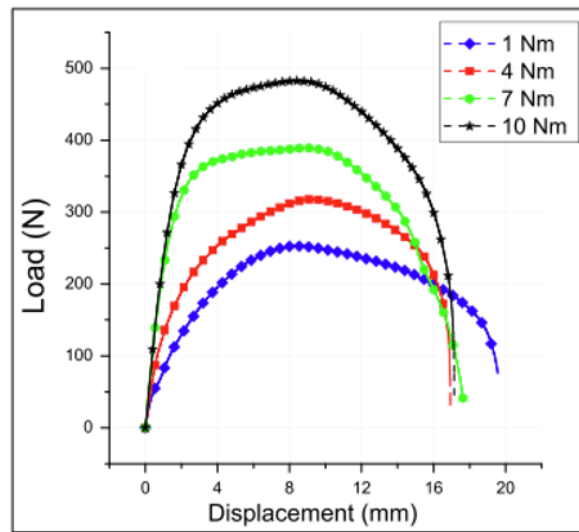
Figure 2.8: Load–displacement plots for normal loading of polyurethane osteomorphic assemblies as a function of the magnitude of the lateral constraint (as torque on the constraining screws) [15]

Malik et al. [6], examined the design and optimization of sutured geometries with jigsaw puzzle-like arrangements (tabs) (Figure 2.9). In this research analytical models were presented that were later verified with finite element (FE) simulations and mechanical testing of 3D printed Acrylonitrile Butadiene Styrene (ABS) samples. The focus was on the non-linear traction behavior generated by the frictional pullout of the tabs without other types of bonding (adhesion). The models showed that the pullout strength and energy absorption increase with higher interlocking angles (θ_0) and for higher coefficients of friction (f), but after a threshold the high stresses in the solid can result in tab fracture. The sutured interface was deemed remarkable for its toughness; it was measured as 45 times tougher than plain ABS.
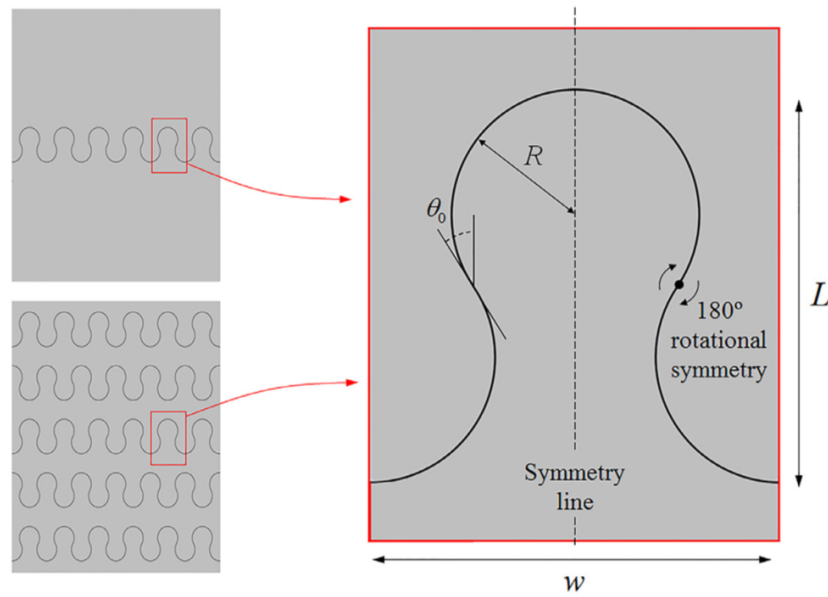
Figure 2.9: A series of sutured geometries and a closer look of the geometrical characteristics of an individual suture [6]

2.1.3. Mechanism of bistable Interlock

Concept

Based on inspiration from natural materials & by applying the principles of toughness by segmentation, a new type of material was built. The sutured geometry (tab) is similar to the one Malik et al. investigated [6] (Figure 2.9), but in this case, it is built of geometries containing 2 circular parts (Figure 2.10) instead of one. The suture's shape is made of jigsaw-like pieces, created by tangentially blending a sequence of arcs of circles with radii R_1 and R_2 at positions indicated by angles θ_1 and θ_2 as seen in Figure 2.10.
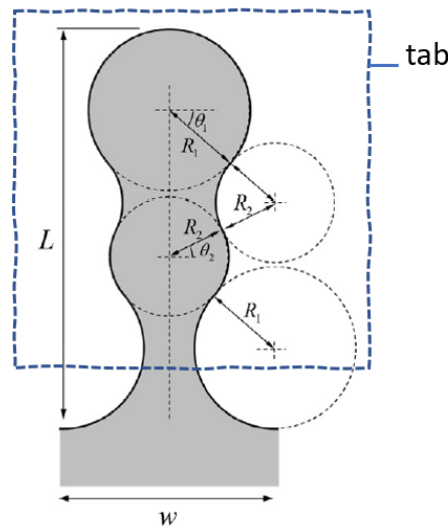
Figure 2.10: Overview of the suture's geometry and tab [7]

Mirkhalaf et al. noticed that the tensile behavior of these tabs under monotonic tension resulted in a curve with two equilibrium positions (I & II) (Figure 2.11). The name *bistable interlock* was adopted to highlight this ability of the tabs. The second equilibrium position (II) results in a second peak in the force-displacement graph and also at a larger area under the graph. Since the area under the graph indicates the systems' energy absorption, the interlocked materials tested were up to 10 times tougher than the polymer they were made of [7]. In [7] the polymer used was Acrylonitrile Butadiene Styrene

(ABS). A more detailed description of how the bistable interlock mechanism works will be provided in subsection 2.2.3.
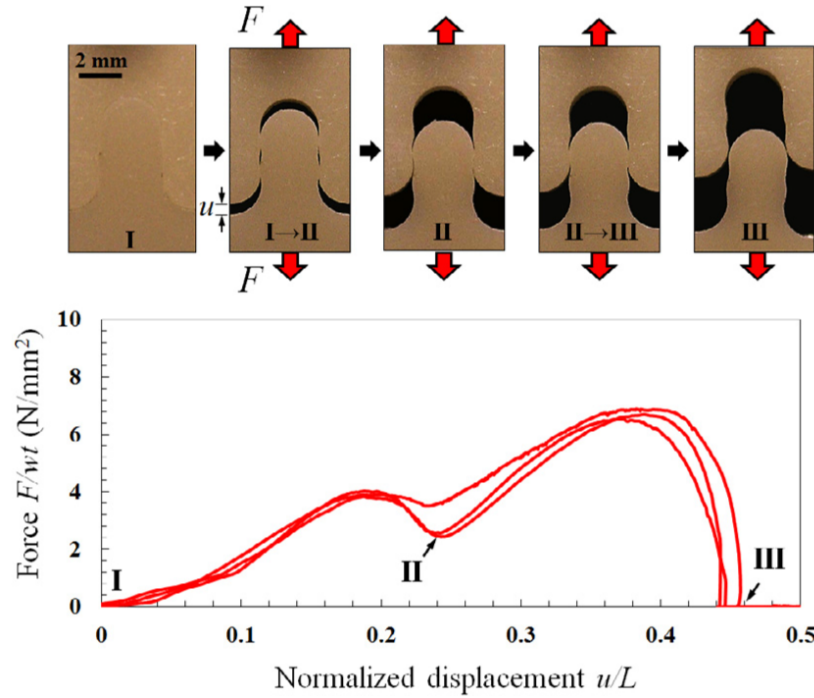
Figure 2.11: Bistable interlock response under pull out of the sutured geometries [7]

Design

By changing the geometric parameters (R_1, R_2, θ_1, θ_2) shown in (Figure 2.10), the system's mechanical response can be programmed and tuned. For instance, higher locking angles (θ_1, θ_2) result in larger geometric interference and require greater pullout force to separate the tabs. In [7], to investigate this feature, the radius R_1 was made larger than R_2 in order to increase the force needed for a full pullout of the tab. Since there was no specific length scale associated with the mechanisms (they all rely on friction and elasticity of the bulk material), the non-dimensional R_1/R_2 was chosen as a basic design parameter.

Further examination of the geometry reveals that the four *main* parameters (R_1, R_2, θ_1, θ_2) are not independent of one another. Other parameters of interest that depend on them are:

- the angle θ_2,
- the length L,
- the width w.

The formulas below show the connection to the main parameters [7]:

$$\theta_2 = cos^-1 * [1/2 * (R_1/R_2 + 1) * cos(\theta_1)] \tag{2.1}$$

$$L = 2 * [R_1 * (1 + sin(\theta_1) + R_2 * (sin(\theta_1) + sin(\theta_2))] \tag{2.2}$$

$$w = 2 * (R_1 + R_2) * cos(\theta_1) \tag{2.3}$$

To design the sutures with a bistable interlocking effect, the parameters chosen must be mechanically and functionally significant.

Some design limitations are mentioned below:

- Only the cases with $R_1/R_2 \geq 1$ are acceptable,
- Cases where $R_1/R_2 < 1$ can result in a loose and unstable connection,

- Cases with very high θ_1 and/or the ratio R_1/R_2 can result in excessive contact stresses and tab fracture; an undesirable failure mode for the suture (brittle failure).

After extensive design and experimental research performed by Mirkhalaf et al. in [7], the admissible domain for the main parameters R_1/R_2 and θ_1 was defined (Figure 2.12):
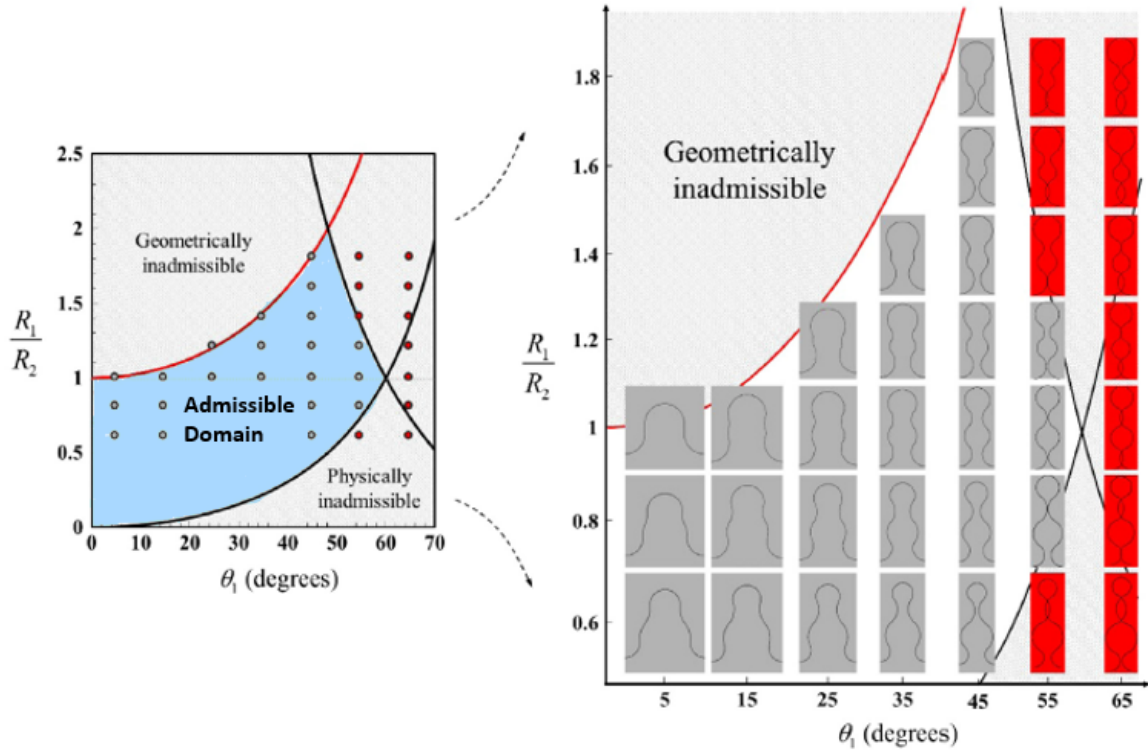
Figure 2.12: Admissible domain of design parameters of the tabs [7]

Figure 2.13 depicts the relationship between the geometry of the tabs and the stresses generated in them. A higher ratio R_1/R_2 and θ_1 can result in stronger tabs as the interlocking effect is more pronounced, but it may cause brittle tab failure.
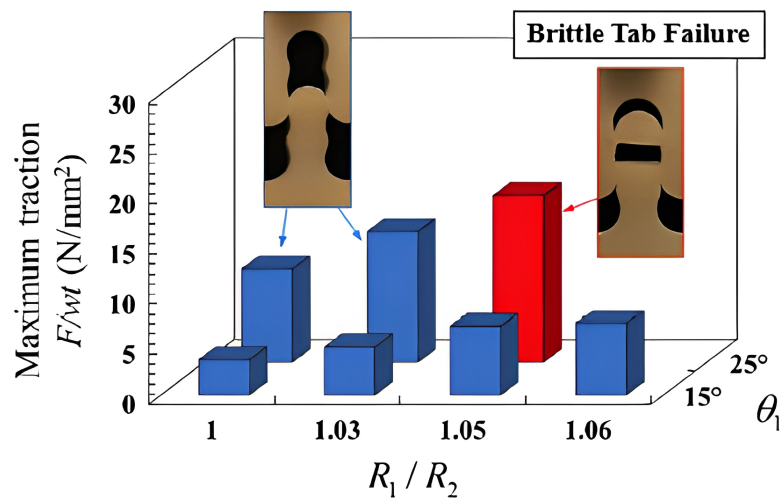
Figure 2.13: Effect of R_1/R_2 and θ_1 combination on the maximum pullout traction [7]

Fabrication with 3D printing

To experimentally investigate the pullout response of the samples with bistable interlocks, Mirkhalaf et al. [7], 3D printed samples with individual bistable interlocked tabs. Different combinations of interlocking angles ($\theta_1 = 5\,°$, $15\,°$, $25\,°$, $35\,°$) and different radii ratio ($R_1/R_2 = 1$, 1.03, 1.05, 1.06) were examined [7]. All the samples had an out-of-plane thickness of t = 2 mm and they were comprised of a single tab.

Some important fabrication aspects of [7] are summarized below:

- The material used was Acrylonitrile Butadiene Styrene (ABS). ABS is a relatively stiff and strong polymer with elastic modulus $E = 1.7 \pm 0.2$ GPa, flexural strength = 118 ± 12 MPa, (measured experimentally with flexural tests), and relatively brittle, with a flexural strain at failure of 0.112 ± 0.18.

- The 3D printer used was a high-resolution (80 μ m) EnvisionTech's Micro HiRes Machine that uses **Digital Light Processing** (DLP) technology. This method allows for the printing of pore-free, homogeneous, and mechanically isotropic components. The morphological fidelity provides a consistent friction coefficient and minimization of stress concentrations.

- The two solid parts of the tabs were 3D printed separately and were combined in a sliding, out-of-plane motion. The assembly was performed smoothly and required very little force in the out-of-plane direction.

- The gap at the interface after assembly was roughly 8 μ m. This distance was broad enough to ensure that the tabs were unloaded before testing, and small enough to assume that were initially in contact.

- To minimize in-plane bending and deformation modes not representative of a long suture line, the total width of the sample was approximately six times the width of the individual tabs.

2.2. Interfacial Load Transfer Mechanisms

The focus of this research is the bistable interlock mechanism in the SHCC-to-SHCC interface. As mentioned before, the mechanism is highly reliant on the interface contact mechanisms; hence, analysis of *load transfer mechanisms* at the interface is necessary.

When it comes to the SHCC-to-SHCC interface, while scientific findings exist, it is not yet commonly used in practice. However, the vastly applied concrete-to-concrete interface can offer a good starting point for understanding the interface mechanisms regarding load transfer between cementitious materials.

According to FIB Model Code [2], forces are carried across concrete-to-concrete interfaces through three main mechanisms:

- Friction,
- Adhesive bonding & mechanical interlocking,
- Dowel action of reinforcement/ connectors crossing the interface.

These mechanisms are widely accepted for reinforced concrete structures, but in the case of this research, only the *first two* are relevant (friction, adhesive bonding, and mechanical interlocking). The dowel action of the reinforcement and the aggregate interlock (since only fine particles are included in the mixes used in this research) are not contributing mechanisms and are not going to be further discussed.

2.2.1. Friction

Nature and Laws of Friction

The study of friction has long been a subject of interest in engineering. The foundational principles of friction, commonly found in textbooks, can be traced back to the work of the fifteenth-century scientist Leonardo da Vinci. Nowadays these principles are frequently associated with the seventeenth and eighteenth-century researchers Guillaume Amontons and Charles-Augustin de Coulomb due to their published contributions [17]. In 1950's David Tabor and Sir David Bowden introduced the idea of "asperities," leading to the development of the concept of "adhesive" and "abrasive" friction [18].

To explain the phenomenon of friction on the microscale, *surface roughness* is an important concept to introduce. All mechanical surfaces are, in reality, rough. Surface roughness is the existence of tiny ridges, pits, and scratches at the surfaces called *asperities* (Figure 2.14). These discrete spots are connected and interlock when two nominally flat surfaces come into contact [19], [20]. The existence of asperities is the reason that the *true area of contact* between two surfaces is much smaller than the *apparent area* (Figure 2.15) [19].
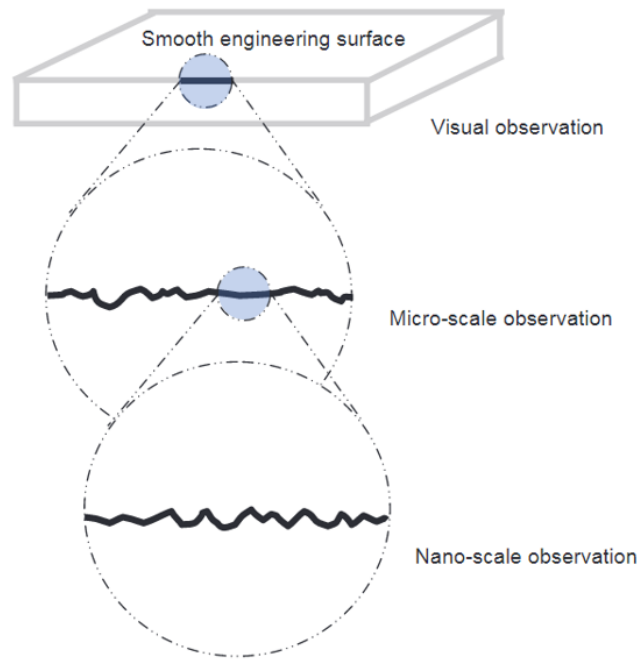
Figure 2.14: Surface roughness in microscale and nanoscale [21]

When two solid bodies come in contact and are subjected to forces that tend to produce relative sliding motion, stresses develop on the interfaces that tend to oppose that motion. This phenomenon is called **friction**. Friction is often discussed in terms of the resultant of the stresses, i.e. friction force [17].
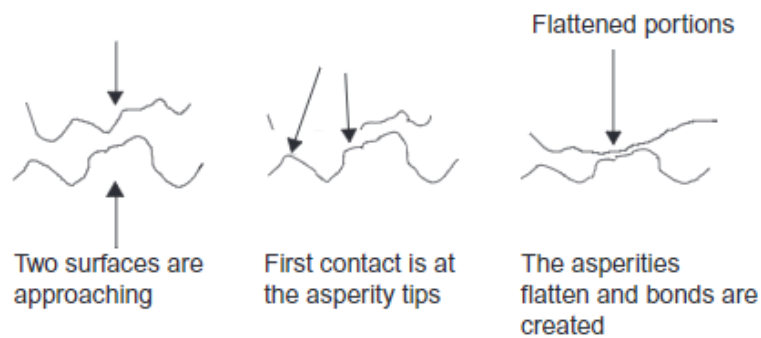
Figure 2.15: Asperities before and during contact of surfaces [20]

Amonton's *first law* of friction states that the friction force (F) (at the onset of sliding and during sliding) is proportional to the normal load (N) [22]:

$$F = \mu * N \tag{2.4}$$

Where:

- N, the compressive normal force,
- F, the friction force,
- μ, the friction coefficient.

The coefficient of proportionality μ, is known as the coefficient of friction. Often, two values of μ are quoted: the coefficient of static friction, μ_s, which applies to the onset of sliding, and the coefficient of kinetic friction, μ_k, which applies during sliding motion. From empirical principles and experimental

observations, the static coefficient is greater than the kinetic coefficient [19]. This means that once the sliding stops, the force needed to initiate sliding is greater than the force needed to sustain sliding [22].

Amontons' *second law* of friction states that the friction force is independent of the apparent area of contact. Both laws, apply to non-lubricated contacts between metallic bodies and are generally observed to hold for gross motions of effectively rigid bodies [17].

Bowden and Tabor's theory assumes that interfacial friction is mainly happening due to two causes: the shearing of metallic joints between the surface asperities (adhesion) and the plastic deformation of the softer surface by harder asperities (abrasion) [19], [17].

Bowden and Tabor also provided a mathematical explanation of Amontons' laws of friction [19]. They stated that when two clean metal bodies are put in contact, plastic flow at the tips of the asperities, and local welding between opposing asperities will always occur. This comes from the assumption that the stresses at the extremely small areas of the asperity tips will always be high enough to create permanent deformation. The true area of contact is then proportional to the normal load (N) [19]. So, it holds:

$$A_r = N/H \tag{2.5}$$

Here A_r is the true area of contact, N is the normal load, and H is the hardness of the softer of the contacting materials.

Neglecting the contribution of plowing, the friction force is then equal to the force F_a required to shear the junctions formed during the plastic deformation of the asperities tips. If τ_j is the average shear strength of the junctions, then it holds:

$$F_a = A_r * \tau_j = (N/H) * \tau_j \tag{2.6}$$

When dividing by the normal force N, the *adhesive coefficient of friction* can be derived:

$$\mu_a = \tau_j/H \tag{2.7}$$

Due to plastic yielding and work-hardening, the interface between welded asperities is as strong or probably stronger than the undeformed bulk material. Hence, the average shear strength of the junctions (τ_j) can be assumed to be equal to the shear strength of the softer of the contacting materials (τ). Consequently:

$$\mu_a = \tau/H \tag{2.8}$$

This verifies Amontons' laws of friction stating that the friction force is proportional to the normal load and independent of the apparent area of contact.

The coefficient of friction as seen in Equation 2.8, is not dependent on the normal load or sliding velocity but on the surface properties of the sliding materials and the experimental conditions. With the exception of hydrodynamic lubrication, the nominal range for the coefficient of friction for sliding is situated between 0.01 and 2 [22]. For most materials, τ is of the order of 0.2H, hence $\mu_a \approx 0.2$ [19].

According to the FIB Model Code [2] representative mean values for the friction coefficient μ for concrete grades $\leq$ C50/60 are given below:

Table 2.1: Representative mean values of the friction coefficient μ for concrete grades $\leq$ C50/60 [2]

Category	Range of friction coefficient
Smooth interface	$0.5 - 0.7$
Rough interface	$0.7 - 1.0$
Very rough interface	$1.0 - 1.4$

Lubricated Contact

As it was previously established, friction is always present between contacting surfaces, since no surface is smooth in reality. Frictional effects (stick-slip behavior, adhesion, plowing, frictional damping) are frequently ignored if the frictional forces on the contacting boundaries are small enough. Hence in engineering, there are two types of contact problems: *frictional* and *frictionless*, with the latter being much easier to solve.

Practically contact with less friction can be achieved through the application of lubricants to decrease the friction coefficient. **Lubrication** is an important aspect of tribology. It is vastly used to reduce friction and wear on mechanical surfaces, acting as a shield. The lubricant film covers and fills the asperities of the sliding surfaces and forms a boundary between them so that any direct contact between the surfaces is limited, resulting in limited friction. As a general rule, the lubricant chosen should have small enough viscosity, (internal molecule friction) to reduce the internal resistance between the particles of the lubricant and at the same time, it should remain in place to efficiently separate the surfaces [23]. Apart from the dependence on the lubricant viscocity in lubricated contact, friction is known to display velocity dependence. It is established that lubrication modes fall into three categories. These are *hydrodynamic lubrication*, *mixed lubrication* and *boundary lubrication*, as expressed by the Stribeck curve (Figure 2.16) [24], [17]. The distinction can be made with the calculation of the Hersey number (see Equation 2.9).

$$\text{Hersey number} = \eta * v/p \tag{2.9}$$

Where:

- η is the viscosity of the lubricant,
- v is the velocity of the surface,
- p is the pressure.

This practically means that a pair of tribo-surfaces is separated by the pressure buildup of a sufficiently thick liquid film. When the Hersey number is small, the lubrication regime is a *boundary regime*. For instance, at low velocities, the hydrodynamic pressure buildup in the contact is negligible and the contact load is assumed to be transmitted mostly by mechanical contact between the asperities [17]. As a result, high friction and wear are observed. A *mixed lubrication regime* is an intermediate regime between hydrodynamic lubrication and boundary lubrication and the friction then is partly caused by asperity interactions and due to the shear stresses in the lubricant [24]. In the *full-film regime*, the surfaces are completely separated by the pressure buildup in the lubricant and the friction corresponds to the shear stresses in the lubricant [24].
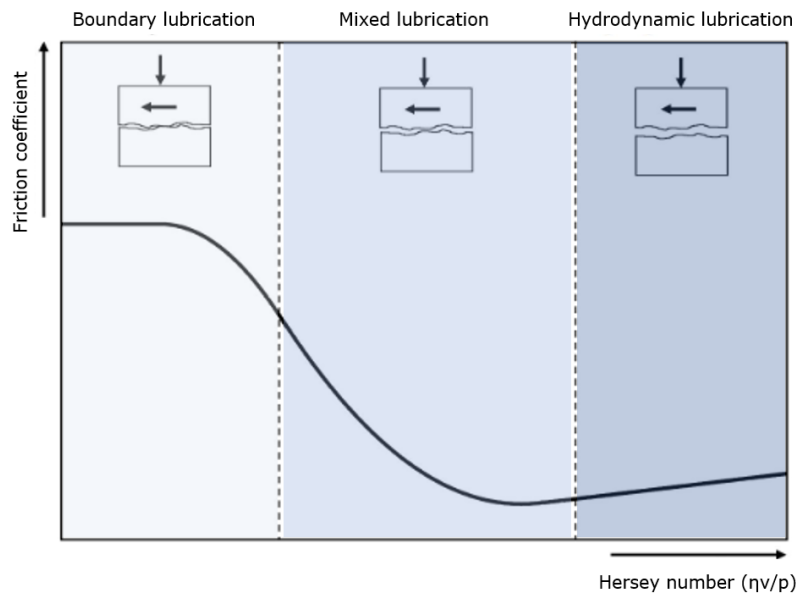
Figure 2.16: Stribeck curve [24]

Friction & interlock
Friction and mechanical interlock are mechanisms used to create bonds between two mechanical surfaces. Malik et al. [6] studied the combination of these mechanisms in simple jigsaw structures with radius **R** and interlocking angle θ_0 (Figure 2.17).

The solid parts of the suture were considered isotropic and linear elastic with no adhesion at the interface, to solely focus on the frictional contact. Under a pullout force and enforcing the boundary conditions shown in Figure 2.17, an analytical model was created.
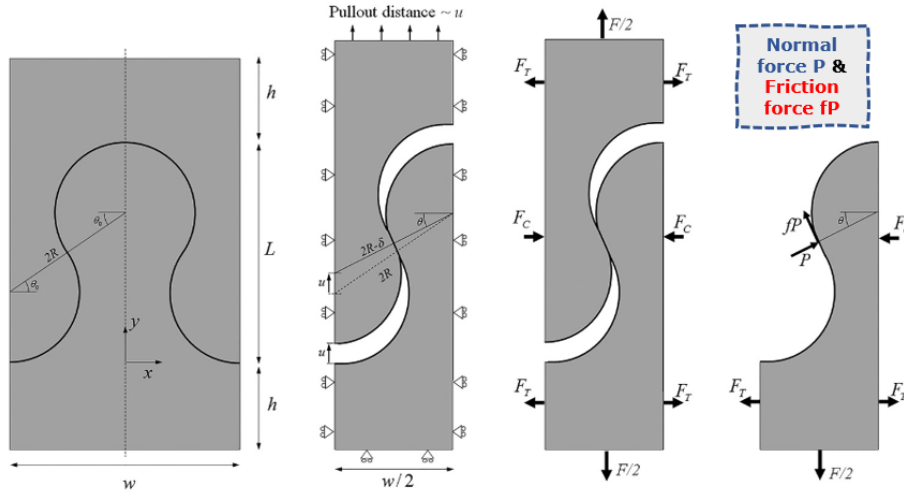
Figure 2.17: Sutured geometry and enforced boundary conditions [6]

The results of the analytical pull-out model using three different friction coefficients are shown in (Figure 2.18). The case with no friction *(f=0)* can generate stiffness through solely geometric interlocking, but it does not absorb energy. When friction is increased *(f>0)* the sliding of the tab generates frictional forces and the shear traction acting on the contact area that increase the energy absorption of the system (area under the graph) [6]. Consequently, for this case of application and extending to bistable interlock, frictional stresses are imperative for increasing the system's ductility.
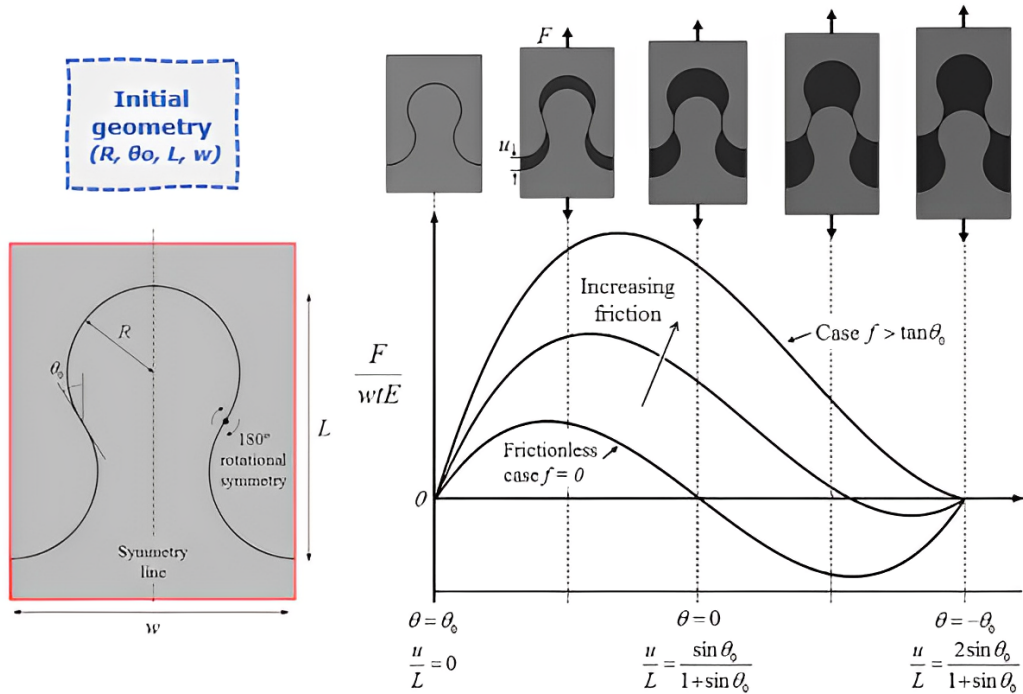
Figure 2.18: Traction separation curves obtained from the analytical pullout model (with three different friction coefficients) [6]

However, parametric studies performed by Malik et al. [6] showed a counter-intuitive guideline. A

higher coefficient of friction can promote strength, stiffness, and energy absorption. However, the high frictional stresses at the interface also generated large tensile stresses in the contact areas, leading to tab fracture. In contrast, low friction coefficients minimized the tensile stresses in the contact regions, allowing the use of higher interlocking angles without fracturing the tabs, which in turn generated high stiffness and strength. In Figure 2.19 this is highlighted. With reduced friction (lubricated sample interface), the interlocking angle could be increased to $\theta_0 = 35°$ without breaking the tabs. For the non-lubricated sample (higher friction coefficient) fracture of the tabs was observed for $\theta_0 = 20°$ [6].

After design optimization regarding the energy absorption performed in [6] it was concluded that for relatively weak and stiff materials (simulated by $\sigma_s/E = 1/1000$) a small friction coefficient of 0.018 provided the optimal results while for strong and compliant materials ($\sigma_s/E = 1/100$) a friction coefficient of 0.08 gave the optimal results.

(a) Pull-out behavior of non-lubricated tabs

(b) Pull-out behavior of lubricated tabs
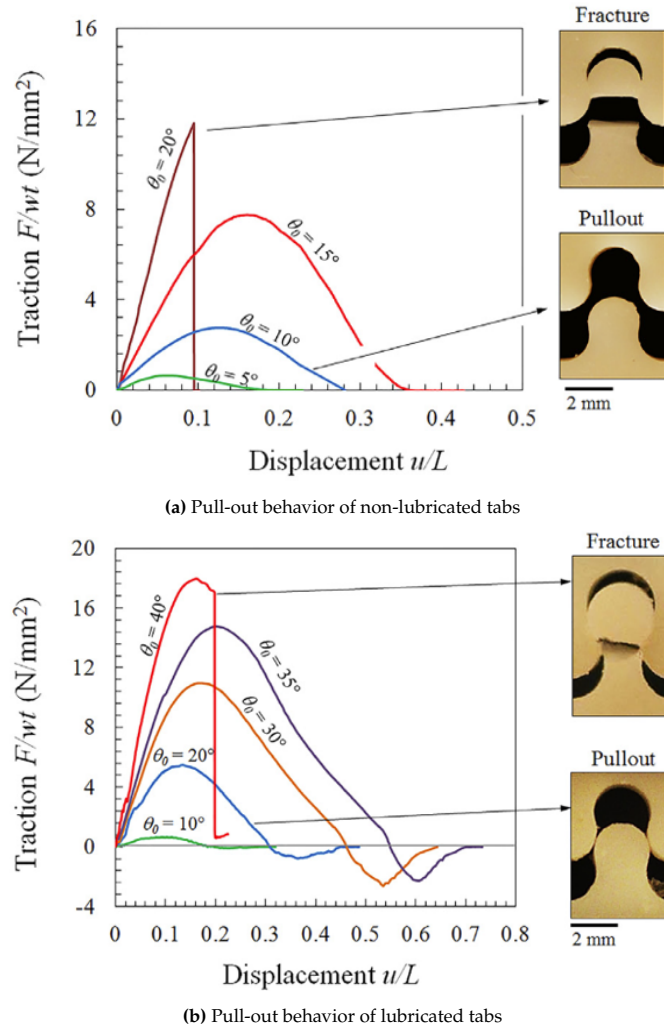
Figure 2.19: Non-lubricated and lubricated representative pull-out behavior of single tabs, with different interlocking angles θ_0 showing two different failure mechanisms: *tab pull-out* and *fracture* [6]

2.2.2. Chemical bond

Bond properties

To achieve a reliable connection between two concrete or SHCC layers cast at different times, a good bond is a key factor. Bonding mechanisms can be divided basically into mechanical interaction, thermodynamic mechanisms, and chemical bonding [25]. The term bond between two layers of material usually refers to the **chemical adhesion** of the applied product (overlay) to the substrate [1]. Chemical adhesion occurs when the atoms of two materials form chemical bonds (ionic, covalent, hydrogen) across the joint surface [20]. Chemical bonds are usually stronger than the inherently weak friction bonds, which are related to Van der Waals intermolecular forces (stemming from temporary alignments of electrons in the outermost shell of atoms) [20].

Bonded cement-based material overlays and their substrates constitute a hybrid composite structural system. On the microscale, chemical reactions take place between the surfaces of the fresh and cured concrete. Further chemical bonding between the two layers is happening due to the continued hydration of non-reacted cement particles in the cured layer, resulting in the formation of additional C-S-H gel. Moisture exchange also happens between the two layers. Water infiltrates the capillary pores in the cured layer and facilitates further hydration reactions, contributing to the interpenetration of cement hydration products between the two layers [1], [26].

Bond strength refers to the required force for the complete separation of two adhered parts along the interface. In this research, the focus is on tensile bond strength, which is usually defined as the tensile strength perpendicular to the plane of the interface [27]. Bond strength in shear has an inherent role and intrinsic relationship with tensile behavior [28], but the tensile bond strength is much easier to measure.

In practice, the bond strength is determined by coring and pull-off tests (Figure 2.20) [27]. The failure stress can be calculated by dividing the maximum force by the area of the cross-section. It is important to note that the bond strength only equals the failure stress if the failure occurs completely at the interface (Figure 2.20 case b). When the failure is completely or partly in substrate or overlay (see Figure 2.20 cases a & c), the failure stress is only a lower bound of the bond strength [27]. The last case in Figure 2.20 (case d) is invalid and the test needs to be repeated.
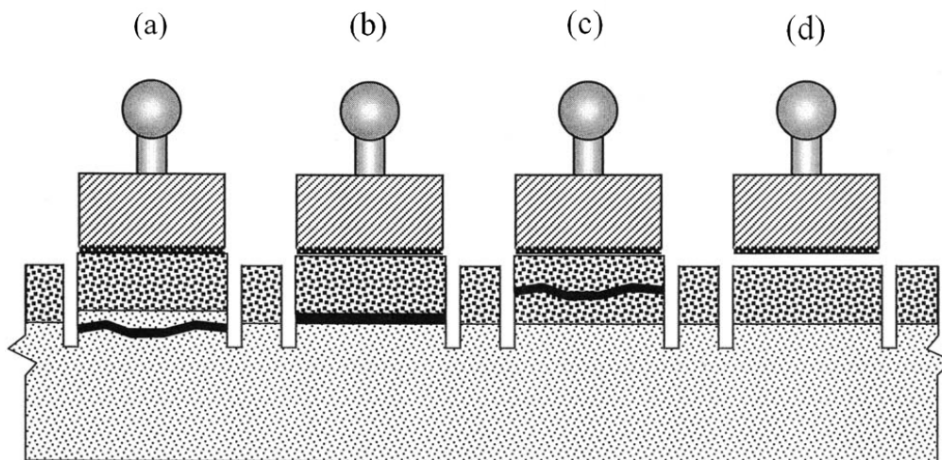
Figure 2.20: Direct tension (pull-off) test with 4 failure modes (a) Failure in the substrate, (b) bond failure at the interface, (c) failure in the overlay or repair material & (d) bond failure at the overlay interface (invalid) [29]

The interaction and bond strength of the system are dependent on many parameters [27], [30], [1], the most important of which are mentioned below:

- the moisture exchange between the two layers, & the moisture level of the substrate,
- the surface roughness of the substrate,
- the curing conditions of both concrete layers and possible differential shrinkage,
- the fluidity and workability of the overlay,
- the stress state at the interface,
- any presence of cracking at the substrate,

- the compatibility of properties (deformational, physical, chemical, electrochemical) between the two layers,
- the potential application of bonding agents,
- the presence of mechanical connectors (e.g. steel reinforcement).

Surface roughness is a critical factor affecting bond strength in repair systems. To achieve the desired roughness of the concrete substrate, various surface treatments are employed, including hammering, sandblasting, hydrojetting, scarifying, acid-etching, and shot-blasting (Figure 2.21) [1], [31].
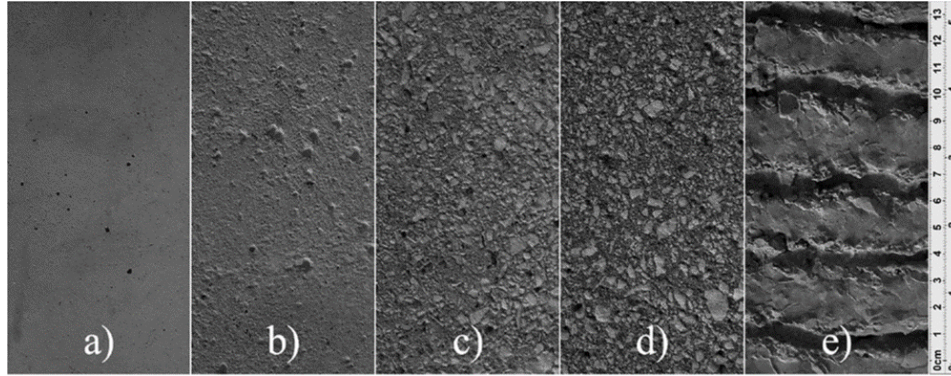
Figure 2.21: Common concrete surface preparation methods: (a) left as-cast, (b) wire-brushing, (c) sand-blasting, (d) shot-blasting, & (e) hand-scrubbed. (The pictures are at scale) [31]

Guidelines for the surface roughness and its influence on interface strength between concretes cast at different ages can be found in the codes for reinforced concrete structures [2], [32]. Depending on the average roughness (Ra) (referring to the average deviation of the profile from a mean line) and the applied surface preparation method, the following categories are introduced:

Table 2.2: Classification of surface roughness depending on the average roughness R_a as presented in FIB Model Code [2]

Category	R_a [mm]
Very smooth (e.g. cast against steel formwork)	not measureable
Smooth (e.g. untreated, cast against	< 1.5 mm
Rough (e.g. sand blasted, high pressure water blasted etc.)	≥ 1.5 mm
Very rough (e.g. high pressure water jetting, indented)	≥3 mm

Regardless of the importance given to the surface preparation, bond test results [27] showed that the surface roughness has a rather small influence on the adhesion. The bond strength of rough and smooth surfaces, prepared with water jetting and sandblasting, was found to be almost equal. However, the debonding failures were more frequent at the smooth surfaces [1]. Regarding that, it was concluded that roughness does not always enhance adhesion but reduces the risk of debonding in repaired structures. On the other hand, higher adhesion is not sufficient without adequate surface roughness to prevent debonding [1]. In [27] was stated that possibly a threshold value for roughness exists, above which further improvement does not enhance the adhesion between the two materials [1].

Moisture exchange is another critical parameter affecting adhesion between concrete substrate and overlay. This process is driven by the difference in relative humidity (RH) between two layers of concrete cast at different times (overlay and substrate) and the environment. Water moves from areas with higher RH to areas with lower RH. If there is no drying of the overlay, moisture exchange will be driven only by capillary absorption by the concrete substrate and the hydration of the repair material [1].

The effect of surface moisture on the bond between existing and fresh concrete has been the subject of extensive research. Dry surfaces have the tendency to absorb water from the newly applied concrete overlay, potentially resulting in the formation of a non-uniform, porous region in proximity to the interface (i.e. wall effect) [27], [1]. Conversely, when the surface is excessively wet, a zone characterized by a high water-cement ratio can develop near the interface, thereby causing a localized reduction in the strength of the overlay. Moreover, the presence of free water on the surface can lead to a complete deterioration of the bond. According to Bissonnette et al. [27], the "saturated substrate with dry surface" was judged as one of the best surface preparation methods.

While numerous factors can influence adhesion, it's important to note that achieving the highest bond strength may not always result in the optimal performance of a concrete-to-concrete connection. High bond strength can lead to increased constraint levels at the interface, increasing the possibility of cracking. While a paradox, the presence of defects or local debonding can sometimes have a positive impact by providing a mechanism for stress relief and reducing constraint levels at the interface [33], [1]. Rather than solely pursuing greater adhesion between the repair material and the concrete substrate, the ultimate objective should be to attain monolithic behavior and a uniform distribution of stresses between the two layers.

Common types of bonding failures are adhesive/interface failure, cohesive failure, and substrate/adhesive failure [34]. Adhesive failure occurs when there is a clean separation between the interface of adhesive and adherent. Cohesive failure mode arises when there is breakage along the adhesive layer. Usually, a layer of adhesive material on both the faces of the adherend is observed (Figure 2.22). Substrate failure takes place when the mechanical strength of the substrate is lower than the adhesive bond strength.
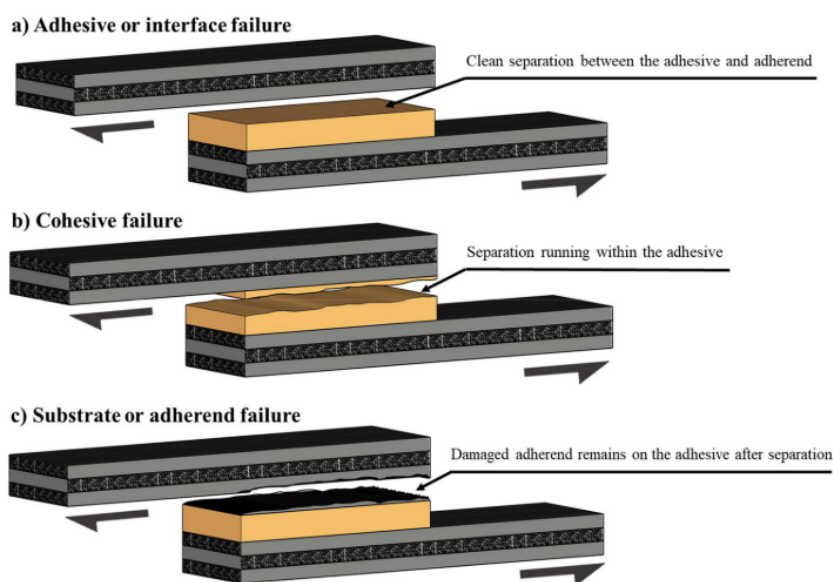
Figure 2.22: Different types of bonding failure mechanisms [34]

Bond & Interlock

Chemical bonding can be combined with mechanical interlock to provide even stronger connections with many applications involving anchoring systems, concrete repairs, and joints.

An example of the combination of mechanical interlock and chemical adhesion was presented in Hamilton et al. [35]. By using microstructured interlocking features, the goal was to increase the strength of single-lap joints. Ultimately, the adhesive joints can enhance strength, toughness, and repeatability. A common practical approach to improving adhesion is to roughen the adherent surfaces via laser ablation or microstructuring. In [35], the structured joints that presented micro-structured adherent surfaces via injection moulding (a process of injection of molten material in a mould) were tested under tension until failure.
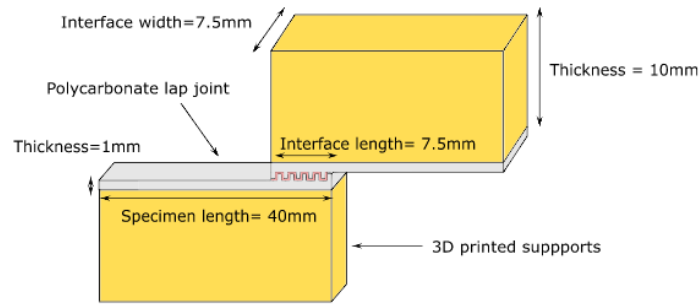
Figure 2.23: Structured interlocking joint [35]

Planar untreated (un-abraded) and roughened (abraded) joints were tested to provide a benchmark. Their results were compared to the micro-structured adherent joints (Figure 2.23). As expected, all structured cases resulted in significantly higher mean strength as compared to the planar untreated and planar roughened interfaces. Compared to the planar roughened joints, results for the micro-structured joints revealed an increase of up to 95.9% for strength and up to 162% for work to failure. This increase was attributed to the mechanical interlocking of the interlocking features that were resisting the loading via progressive bending. When their bending progressed at higher levels until the interlocked surface could not sustain additional load, cohesive failure took place. In the latter stages of joint deformation work to failure increased by the tortuous crack path required for cohesive failure in the structured interfaces. In summary, structured interlocking in single-lap joints applied [35] could partially facilitate a more even distribution of loading over the joint and showed promise in increasing the overall strength and toughness [35].

Another case of mechanical interlocking and chemical adhesion for improvement of strength on larger specimens has been applied by Amiri & Farahani in [36]. Amiri & Farahani focused on increasing the strength of adhesive single-lap joints in composite panels by embedding a button-shaped geometry (see Figure 2.24). Geometrical parameters (height and radius of the button) and physical factors (type of adhesive) influenced the response of the joint [36].
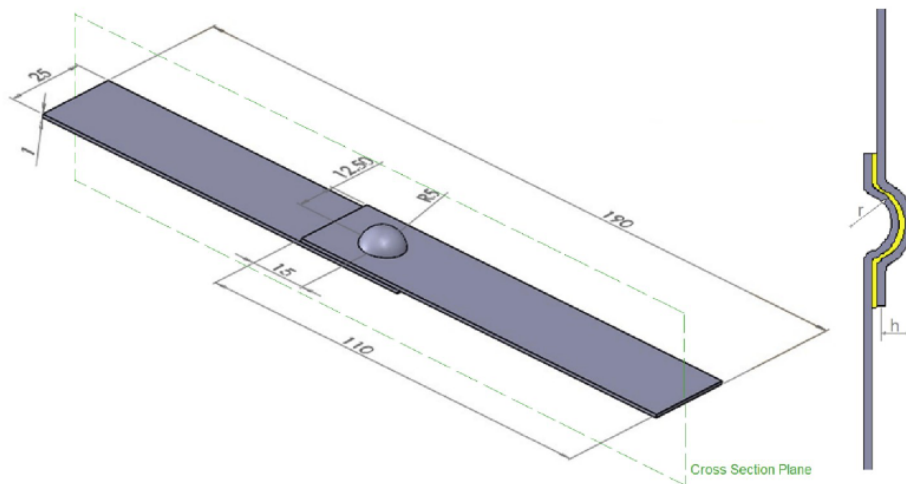
Figure 2.24: Button shape connection implementing geometrical interference and adhesion [36]

As expected, the tensile load-bearing capacity was significantly increased with the embedded button geometry compared to the single-lap joints due to the mechanical interlocking. By increasing the button radius, the response was enhanced until it reached the optimal radius value of 6t (where t was the thickness of the adhesive). For higher radii, the effectiveness of the button-shaped connection decreased. Radii equal to 4t, 5t, 6t, and 7t increased the bond strength by 258%, 280%, 300%, and 260%, respectively. When the button height was raised, the load-bearing capacity was increased. The use of r/3, 2r/3, & r

heights increased the bond strength by 128%, 183% & 275%, respectively. The optimal combination (height and radius equal to 6t) resulted in a 300% increase in the load-bearing capacity.

When the button height and radius increased, the *cohesive* failure was dominant, increasing the joint's ductility. For the radii higher than 6t, stress concentration was dramatically increased in the button shape zone and edges of the connection, decreasing the connection strength. With lower radius and height, the *adhesive* failure was dominant, and the joint was acting more like a single lap joint and failing in a more brittle manner (Figure 2.25).
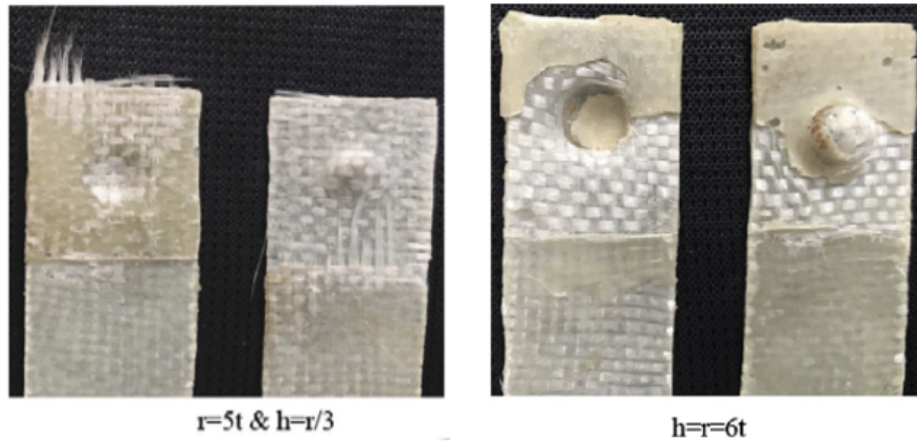
Figure 2.25: Button shape connection with r=5t and r=6t failure modes: Adhesive failure mode (on the left) and thin layer cohesive failure mode (on the right) [36]

Lin et al. [9] investigated the difference in unbonded and bonded tip regions in sutured interfaces with different types of interlocks in regard to the shear strength of the interface. The geometries that were tested, were inspired by nature and had 4 different shapes *(anti-trapezoidal, trapezoidal, rectangular, triangular)* as seen in Figure 2.26a. Several important geometric parameters were examined: the bonded or unbonded tip region, the tip angle, and the geometry (Figure 2.26b); by changing those the performance could be tuned. Analytical models and experiments on 3D-printed polymer physical prototypes were performed. The stiff parts (teeth) were made of an acrylic-based polymer and a rubber-like compliant material was used for the interface layer.

(a) Natural interlocked surfaces acting as inspiration
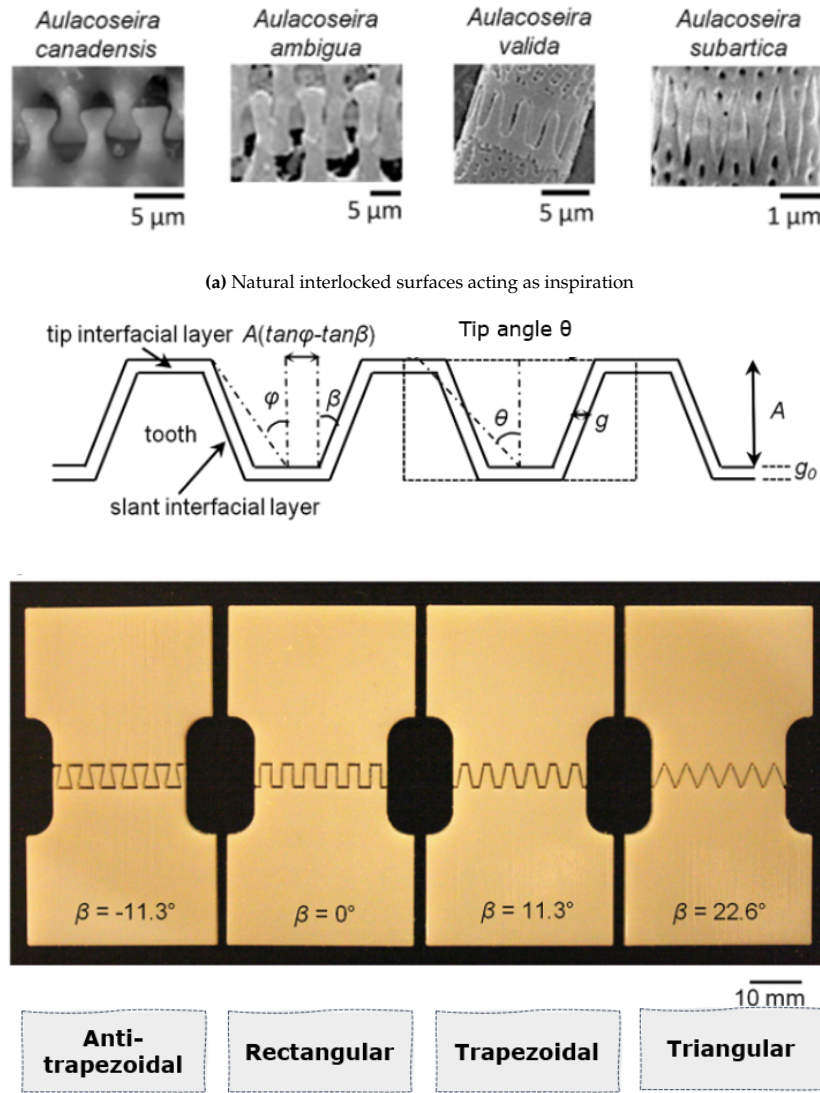
(b) Interface prototypes inspired by natural interlocked surfaces

Figure 2.26: Suture interface types [9]

For the sutured interface with a bonded tip region under tension, two peaks in the stress–strain curve are expected (Figure 2.27). The first peak is linked to the *failure of the bond* of the tip interface, while the second peak corresponds to the failure of the slanted interfacial material and/or possibly the tooth material. The second peak could be considered the *strength* of a suture interface without a bonded tip area under tension [9]. Geometries with a bonded tip region showed a higher initial stiffness due to the double peak in the stress–strain curve.

The tip angle and geometry (Figure 2.26) govern the stress distributions in the teeth and in the interfacial layers and determine the failure mechanism of the suture. Rectangular sutured interfaces simply fail by shearing of the interfaces. Trapezoidal and triangular interfaces fail by a combination of shear and tensile normal stresses in the interface, leading to plastic deformation, and stretching of interfacial ligaments. Anti-trapezoidal suture interfaces with small tip angles fail catastrophically due to tooth failure caused by high-stress concentrations at the teeth, whereas larger tip angles exhibit a more ductile shear failure of the interfaces. To improve stiffness, a bonded tip and decreased tip angle can result in additional strain energy and increased load transfer to teeth. To improve strength, a decreased tip angle can result in simultaneous tooth and interface failure. To improve the toughness, larger tip angles can result in ductile failure of the interface [9].
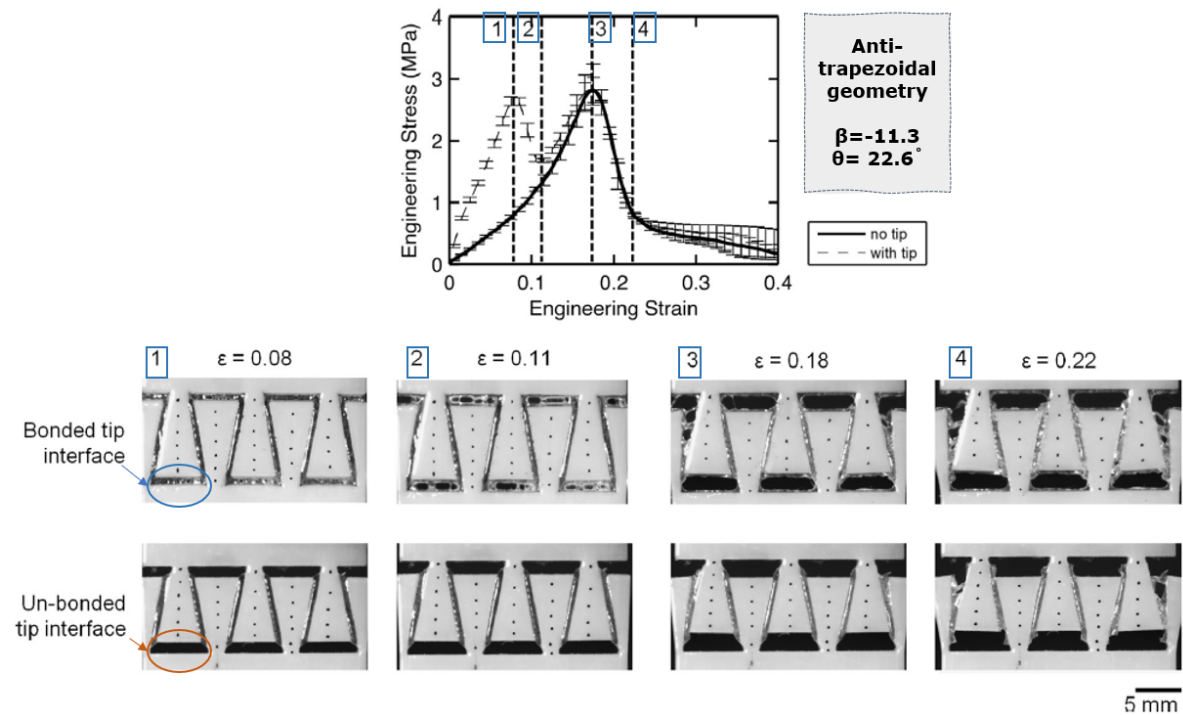
Figure 2.27: Deformation of bonded and unbonded tip sutures of anti-trapezoidal geometry for 4 strain values [9]

2.2.3. Mechanical Interlock

This type of bond occurs due to mechanical interlocking between two dissimilar phases. Usually in concrete structures, it is used to describe the bond between steel rebars with the concrete or the aggregate interlock in the concrete-to-concrete interface. In this research, the effect of reinforcement and aggregate interlock is not relevant. However, mechanical interlock occurs due to *geometrical interference* caused by the curvatures of the sutured geometries at the interface. Due to the two interlocking positions, this mechanical interlock case is referred to as a **bistable interlock**. The details on how the specimens incorporating bistable interlocks were designed are explained in subsection 2.1.3. The focus of this section is on the way this mechanism works under tensile load to boost the ductility in the tensile response of the sutured geometries.

Mirkhalaf et al. [7] manufactured sutured geometries from ABS incorporating interlocking parts shown in Figure 2.28. The bistable interlock mechanism of the tabs in quasi-static tensile loading (displacement rate = 5 μ m/s) worked as follows (Figure 2.28):

- As the initial configuration is at equilibrium, it provides the system with the first stable position (**stage I**).
- As the tabs are pulled out of their starting position due to tensile stresses applied across the suture line (**stage I→ stage II**), the pull-out is resisted by geometric interference, contact stresses, and friction acting at *two pairs* of contact points [6].
- With more pull-out stresses applied, the tabs' ends move to the second cavity-like position, locking the system in the second stable state (**stage II**).
- At this point, if compression is applied to the tabs, the system returns to the first stable position (**stage II→ stage I**). With the cycling of the system between 2 stable positions, reversible deformations can be achieved and the system can stay in the elastic regime [7] for many cycles. This case will not be examined in this research.
- Alternatively, if more tension is applied to the tabs (**stage II→ stage III**) it will be pulled out completely (**stage III**). This case is relevant to this research.
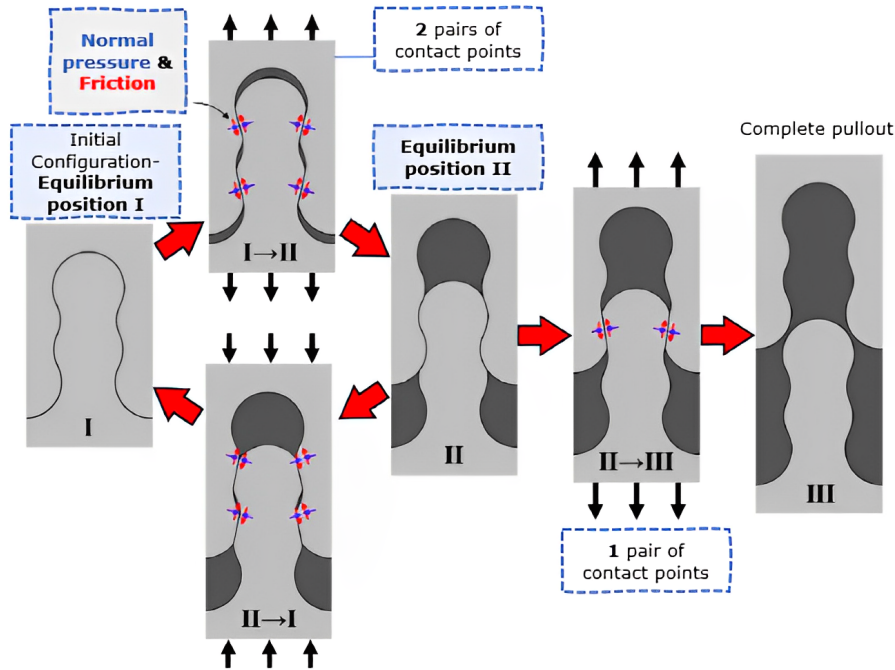
Figure 2.28: Equilibrium positions while tensile stresses are applied to the specimen [7]

Different arrangements of the main geometrical parameters applied (interlocking angle θ_1 and R_1/R_2) were tested in [7]. For each arrangement, three samples of each were manufactured and the

figure 2.29 displays a collection of typical tensile responses. Two basic geometry cases were investigated as seen in Figure 2.29:

- $R_1/R_2 = 1.00$
- $R_1/R_2 = 1.05$
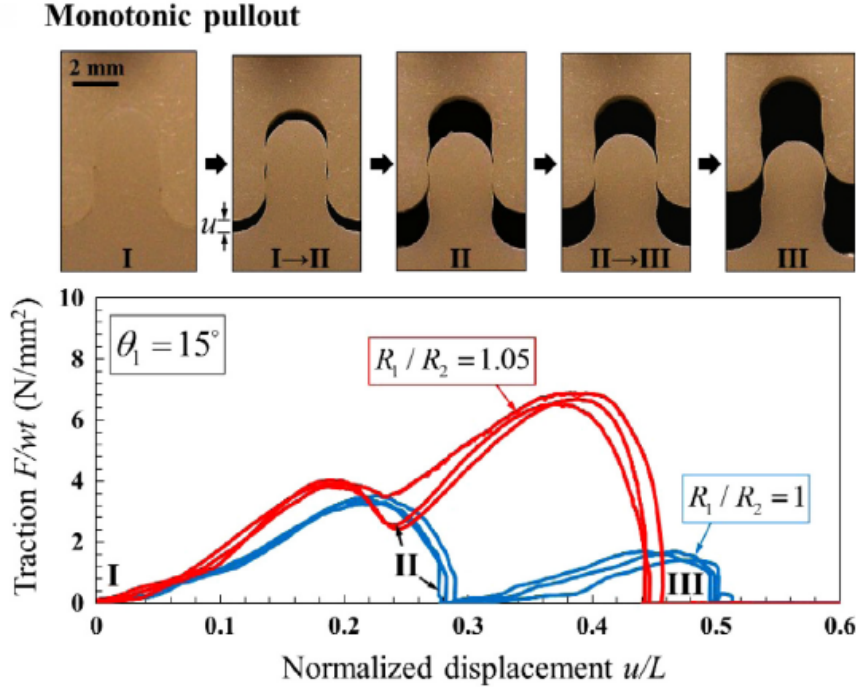
Figure 2.29: Force-traction relation for two different R_1/R_2 ratio of samples (F/wt is used for traction and u/L is used for pullout displacement) [7]

Initially, in the traction-displacement graph (Figure 2.29) the pullout traction grew, with normal and frictional forces at two pairs of contact points resisting the tab's removal. Between **stage II** and **stage III**, the traction reached the first maximum. When the tab approached its second equilibrium position, it dropped to a local minimum, **(stage II)**. When the tab was pulled out even more (between **stage II** and **stage III**) the same contact mechanisms took place but in that stage, there was a single pair of contact points (Figure 2.28) resisting the pullout. **Stage III** represents the completion of the pull-out of the top part.

To investigate further the effect of geometry and curvature a closer look at the difference in the response of $R_1/R_2 = 1.00$ & $R_1/R_2 = 1.05$ is needed (Figure 2.29):

- In the case of R_1/R_2 **=1.00** the traction begins to increase until it reaches a local maximum due to the contact stresses generated from the tensile forces applied to the suture. The traction at the equilibrium position II was **zero** because the interlocking parts fitted without any stresses. The second peak was *lower than the first* as it can be seen in figure 2.29. Specifically, the second peak was only half of the traction at the first peak. This makes the system *vulnerable to tension* once the second equilibrium position is reached and jeopardizes the general stability.
- In the case of R_1/R_2 **=1.05** the traction increased until it reached a local maximum due to the contact stresses generated from the tensile forces applied to the suture (between **stage I** and **stage II**). Then as the equilibrium position II was reached, the traction was higher than in the previous case (where it was zero) since there were some contact stresses between the tabs as the R_1 should fit in a smaller cavity. Since the second tab had a larger radius than the first, the second peak was higher than the first as can be seen in the figure 2.29.

It is obvious from the figure that a slight change in the geometry of the tabs (from $R_1/R_2 = 1.00$ to $R_1/R_2 = 1.05$) can increase the first peak and greatly increase the second peak. This means that a higher force was required to displace the tab from equilibrium position II to complete the pullout. This property can be particularly important for improving the stability of materials made up of multiple suture lines.

2.3. Strain Hardening Cementitious Composite (SHCC)

2.3.1. General Properties

Over the past 50 years, there has been a continuous rise in the use of fiber-reinforced concrete (FRC) as a means of overcoming plain concrete's brittleness and low tensile strength. To satisfy that need, **Strain-hardening Cementitious Composites (SHCC)** were developed. As their name suggests, these materials have the ability to resist increasing tensile forces even after crack formation, over a large tensile strain range; up to and beyond 5% (Figure 2.30). The increased resistance is possible due to the effective crack bridging provided by the fibers SHCC contains [37]. This gives SHCC a pseudo strain-hardening ability [37], [38]. SHCCs' increased ductility is of primal importance when it comes to serviceability criteria linked to durability and tight crack widths [39].
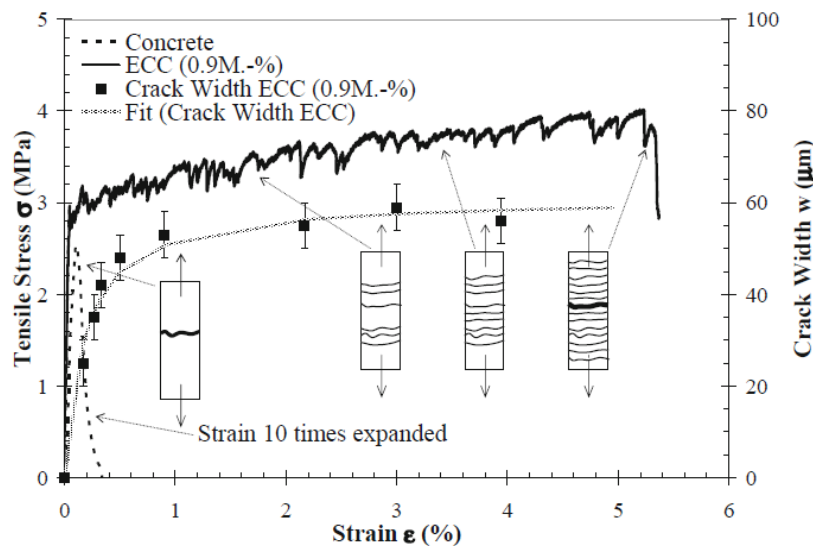
Figure 2.30: Direct tensile response of SHCC with crack widths less than $65\mu m$ [40]

SHCC is typically made of a binder, fine aggregates, water, and approximately 2% of fiber content (by volume). To facilitate controlled crack width and enhance ductility, it is desirable to employ a fine-grained matrix [37]. Predominantly, these composites have moderate tensile strength in the range of 3 to 8 MPa [37], [41]. While substantial increases in strength are limited, ductility has been greatly improved with the addition of fibers. By bridging cracks and enhancing the post-cracking ductility, their primary advantage lies in the ability to control the crack width and elevate the material performance once the matrix cracks [42].

As seen in Figure 2.30, while in concrete a brittle response is expected, SHCC is different. After the elastic regime, SHCC showcases a pseudo strain-hardening regime, where the crack-bridging phenomenon takes place. Post peak, the response declines due to crack localization [42].

When SHCC is loaded in tension, the matrix starts to crack in the weakest cross-section. The fibers crossing this crack resist the tensile load. As the fibers slip out of the matrix, the crack progressively opens. However, due to the slip-hardening behavior of fibers, the fibers resist further slip allowing new cracks to form at other locations. In this way, SHCC can carry an increasing load [43]. This process is repeated and SHCC exhibits multiple-cracking behavior (Figure 2.30).

The conditions for a material to exhibit multiple microcracking behavior can be better explained using fracture mechanics and **Griffith's theory of Fracture**. Griffith's theory of Fracture was proposed

in the 1920s by the British engineer Alan Arnold Griffith [44]. Griffith's theory suggests that a crack propagates if the energy released at crack propagation (*strain energy*- energy stored due to deformation in the material) is equal to or larger than the energy required to create a new crack surface (*surface energy* - energy needed to make new surfaces in the material) [44].

Essentially, Griffith's theory explains how brittle materials fracture when the energy required to create new crack surfaces is less than the energy released due to the crack opening. In the case of SHCC, there is a different scenario. The phenomenon of crack bridging takes place. This is explained by the **steady-state crack propagation** [45], [46]. Steady-state crack propagation means that a crack increases in length while having a constant crack opening δ_{ss} (with the exception of a small region near the crack tip) at an ambient tensile stress σ_{ss}. These are known as *flat cracks* (see Figure 2.31) [47].
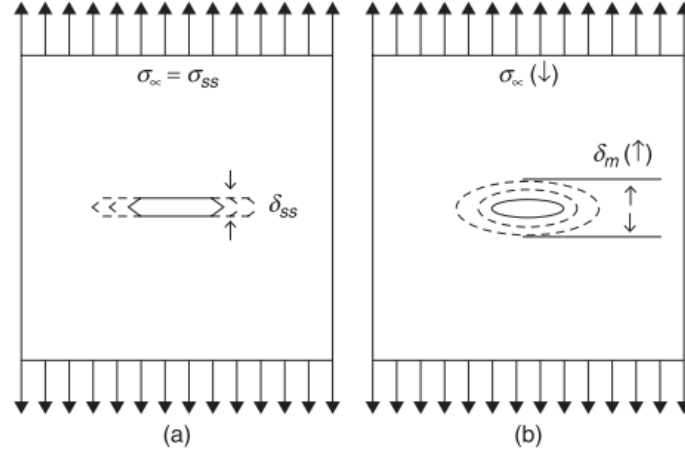
Figure 2.31: (a) Steady-state cracking with a constant crack opening δ_{ss} accompanied by a constant ambient load σ_{ss}; (b) Griffith cracking with a widening crack opening accompanied by a descending ambient load [48]

According to Li et al. [45], [47] this phenomenon prevails when two criteria are satisfied.

The **strength criterion** requires the steady-state matrix cracking stress (σ_{ss}) to be smaller than the fiber bridging capacity [σ_0], ensuring that the stress is bridged safely across all the cracked sections of the matrix [45], [47].

$$\sigma_{ss} \leq \sigma_0 \tag{2.10}$$

The **energy criterion** suggests that the crack driving energy (complementary energy J_b') of the bridging stress-crack opening should be greater than the resistance to crack propagation (fracture energy) at the tip of the crack [45], [47].

The crack tip energy approaches the matrix toughness in small fiber content; a realistic assumption for SHCC that contains fiber content usually below 3%. So it holds:

$$J_{tip} \approx K_m^2/E_m \tag{2.11}$$

- K_m is the matrix fracture toughness,
- E_m is the matrix Young's Modulus.

$$J_{tip} \approx K_m^2/E_m \leq \sigma_0 * \delta_0 - \int_0^{\delta_0} \sigma(\delta)\,d\delta \equiv J_b' \tag{2.12}$$

- δ_0 is the peak crack opening,
- σ_0 is the fiber bridging capacity (peak stress),
- $\int_0^{\delta_{ss}} \sigma(\delta)\,d\delta$ expresses the energy dissipated by inelastic spring deformations for a crack opens from 0 to δ_0.
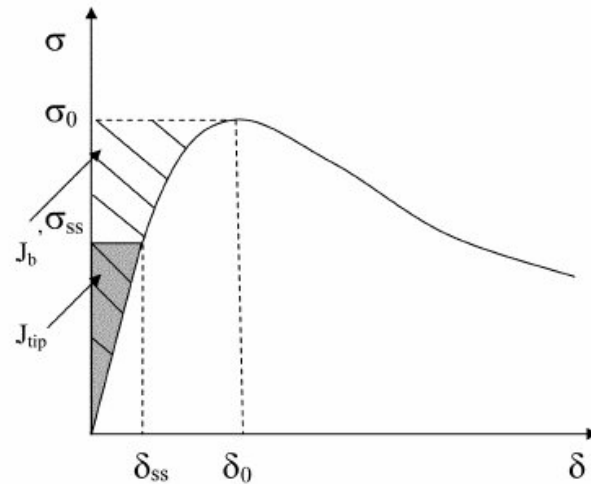
Figure 2.32: Stress-displacement curve with the stored crack tip and complementary energy [45]

The fiber and interface properties control the shape of the $(\sigma - \delta)$ curve and are therefore the dominant factors governing $J_{b'}$.

2.3.2. Matrix

SHCC matrix incorporates cement as its binder. However, in pursuit of sustainable and cost-effective alternatives for matrix production, various options have been explored. Among these, are materials such as Blast Furnace Slag (BFS), Fly Ash (FA), and Limestone Powder [43].

These materials exhibit several advantages, including lower energy requirements and reduced carbon dioxide (CO_2) emissions during their production processes. Notably, BFS & FA, are byproducts of industrial processes, ensuring their widespread availability and cost-effectiveness compared to cement. According to Zhou et al. [43], the incorporation of these materials in the SHCC binder presents additional benefits. These include enhanced workability, reduced permeability, and consequently, improved the durability of SHCC [37], [49].

The most commonly used SHCC matrix compositions consist of cement, fly ash, and fine silica sand. **Fly ash** is a "conventional" pozzolanic material, used to improve the matrix rheological properties, lower matrix fracture toughness, and reduce the cement content needed [47]. The overall improvements in durability with the addition of fly ash were relatively modest. Also, the repeatability of the properties of different mixtures is deemed difficult due to the variation in fly ash properties [47]. Thus, special attention has been given recently to the use of more reactive supplementary cementing materials, as blast furnace slag, silica fume, and metakaolin [42].

This research follows the original mix design by Zhou et al. [43], incorporating BFS and limestone powder into the SHCC matrix.

BFS is a by-product in the manufacture of pig iron, and it is the main cement replacement material in the Netherlands. Due to its microstructure consisting of mono-silicates, BFS shows the potential for pozzolanic reaction. The pozzolanic reaction contributes to the formation of additional cementitious compounds and can potentially reduce the demand for cement. When mixed with Portland cement, BFS accelerates the hydration of Portland cement by reacting with calcium hydroxide ($CA(OH)_2$), one of the hydration products of Portland cement [43].

The experimental study of Zhou et al. [43] showed that even with a cement content as low as 15%, a strain capacity of 3.3%, a compressive strength of 38 MPa and a tight crack width of 57 μm can be achieved. It was concluded that the mixing procedure can be also simplified by using two materials (CEMIIIB 42.5N and limestone powder) instead of three (cement, BFS, limestone powder) since the properties of the mixes were very similar. Although the addition of BFS results in a lower strength at an early age, the replacement of Portland cement by BFS, up to 70%, does not have any negative effect on the compressive strength of concrete after 28 days. The addition of BFS can enhance the sulfate attack resistance and limit chloride ion penetration. Additionally, it can result in a more homogeneous fiber distribution in the matrix since BFS particles provide a driving force for fiber dispersion [43]. It is worth

mentioning that with a fine-grained matrix that did not include any large aggregates but only finer particles and with the addition of BFS the possibility of an increase of autogenous shrinkage can become higher [1].

Limestone is a naturally occurring rock primarily composed of calcium carbonate (CaCO3) and other minerals. Since only a small amount of limestone powder reacts with cement clinker or hydration products, it is usually considered an inert *filler* material. The incorporation of limestone powder with Portland cement has advantages on early compressive strength and durability [43]. The physical effects of limestone powder on the hydration process of a cementitious system include filler effect, nucleation, and dilution. It can replace other materials used in SHCC (such as silica sand) and lead to higher tensile strain and flexural deflection due to enhancement of particle packing of the composite [47]. However, according to Zhou et al. [43] who investigated different contents of limestone powder (ranging from 0.8 to 3 % of weight) there is a threshold to that increase (found to be at 2% of weight); after which the tensile strain and flexural deflection capacity of the mix decreases.

2.3.3. Fibers

In SHCC, the fiber characteristics (type, volume, shape, orientation) affect the mechanical properties of the material. In general, there are many types of fibers (synthetic fibers, steel fibers, glass fibers, and organic fibers) used in SHCC. To increase the strength of the composites, the fibers must have a modulus of elasticity equal to or greater than that of the matrix [42]. For cementitious materials, the modulus of elasticity ranges from about 15 to 40 GPa; hence, this condition is difficult to satisfy. Therefore, synthetic fibers (polyvinyl alcohol (PVA), polypropylene (PP), and polyethylene (PE)) with high modulus were created [50]. However, theoretical and applied research has shown that even in cases of low-modulus synthetic fibers, improvements in strain capacity, toughness, and crack control took place [42]. In most applications, the enhancement of these properties is of much greater significance than a mild increase in the tensile or flexural strength of the mix.
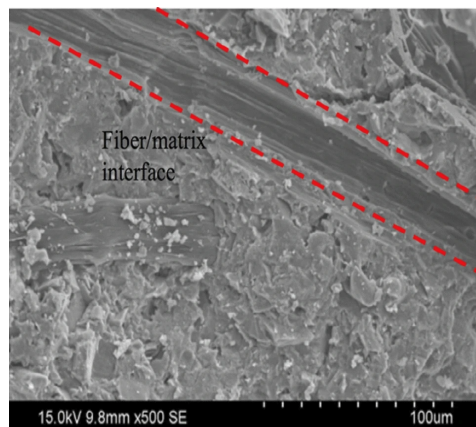
Figure 2.33: Scanning Electron Microscope (SEM) image of PE fiber/matrix interface [51]

The effectiveness of fibers in regard to enhancing the performance of the brittle matrix is dependent on the fiber–matrix stress transfer mechanisms [42]. Understanding those, provides the basis for the prediction of the stress–strain curve of the composite and its mode of fracture (ductile vs. brittle) [42]. Similarly to rebars and matrix stress transfer mechanisms, three types are particularly important:

- friction,
- physical and chemical adhesion,
- mechanical anchorage.

The adhesional and frictional bonding mechanisms between a fiber and cementitious matrix are relatively weak. They however have practical significance in the case of composites with high surface area fibers. Mechanical anchorage is induced by the deformations on the fiber surface or by the shape and overall complex geometry (e.g. crimps, hooks, deformed fibers) (see Figure 2.34). Utilizing different shapes in fibers is a practical solution to compensate for the short anchorage/embedment length and

low bond strength [52]. An additional element that should be considered is the orientation angle of the fiber, relative to the load direction [42].
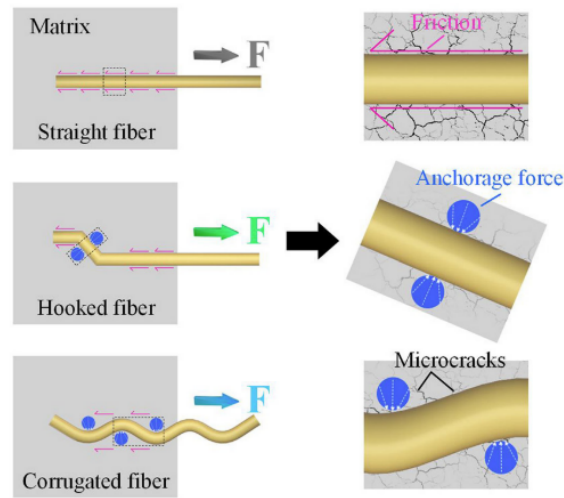
Figure 2.34: Bonding mechanisms of straight, hooked and corrugated steel fibers [52]

In brittle matrix composites, the stress-transfer effects between fibers and matrix should be considered for both the pre-cracking stage and the post-cracking stage, since the processes can be quite different. Before any cracking occurs, *elastic stress transfer* is the dominant mechanism and the longitudinal displacements of the fiber and matrix at the interface are geometrically compatible [42]. The stress developed at the interface is a shear stress which is required to distribute the external load between the fibers and matrix (since they differ in their elastic moduli) so that the strains of these two components at the interface remain the same (fibers and matrix act in a monolithic way). This elastic shear transfer mechanism is the basis for determining the limit of proportionality and the first cracking stress of SHCC [42].

At more advanced stages of loading, debonding across the interface takes place, and the process of stress transfer becomes *frictional slip*. In this case, relative displacements between the fiber and the matrix occur (fibers and matrix do not act in a monolithic way). The frictional shear stress is of greatest importance in the post-cracking zone, in which the fibers bridge the cracks. Properties such as the ultimate strength and strain of the composite are controlled by this mode of stress transfer [42].
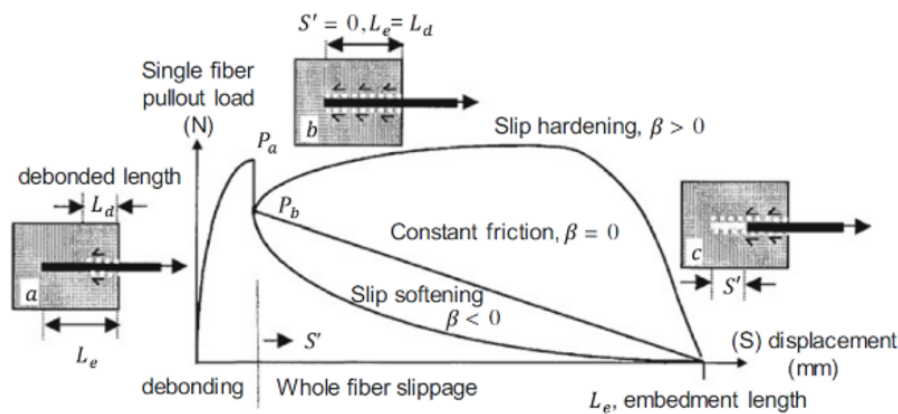
Figure 2.35: Typical pullout load (P) versus displacement (S) relationships in single fiber pullout tests [53]

Using the aforementioned principles to characterize the interface bonding properties of the fiber, the *single-fiber pullout test* has been widely used [53]. The stages of this test usually are three (Figure 2.35):

- **Stage I:** Initially, a stable fiber debonding process occurs along the fiber/matrix interface (elastic regime). The load increases up to Pa and then the debonded length equals the fiber-embedded length, Le. The fiber is then debonded over its entire length (Ld=Le), but the fiber tip is not yet moving. At this point, the displacement only consists of the elastic stretch of the debonded fiber segment and the free length of the fiber.
- **Stage II:** The load then decreases from Pa to Pb. In essence, this drop indicates the rupture of the chemical bond between the fiber and matrix. The strength of the chemical bonding can be estimated by the magnitude of the load drop.
- **Stage III:** The fiber starts to slide in the slippage phase from and after load Pb. Beyond this point, the pullout of the fiber is resisted by frictional forces. In some cases, the friction force increases linearly with increasing pullout distance. This increasing pullout resistance is referred to as the *slip-hardening* effect and is characterized by the slip-hardening coefficient β, ($\beta > 0$). Slip-hardening is a result of increasing fiber surface damage with increasing slippage distance, causing artificial confinement of the fiber matrix by the damaged fibrils or peeled-off fragments. Such a pullout behavior results in fiber rupture at larger displacements (wider crack openings) [54]. Depending on the nature of the interaction and the damage developed across the interface during the slip process, the friction can be assumed to be *constant* over the entire pull-out range, implying the ideal interfacial shear stress–displacement curve shown in Figure 2.35 (*beta* =0) or reduced at advanced stages of loading (*slip softening $\beta < 0$*).

The **fiber type** and **bond** that it creates with the matrix are very important for the overall performance.

The most commonly used fibers in a SHCC mix are high-strength Polyvinyl Alcohol (PVA) fibers. PVA fibers are hydrophilic. This means that due to their strong chemical bond with cement-based materials and their filament microstructure, they tend to break under tension instead of getting pulled out of the matrix [40], [55]. When fibers rupture, stress redistribution causes gradual fiber breakage in a section, which results in the abrupt brittle failure of the section as a whole under tension. As a result, various common treatments have been applied to lower the strength of the fiber/matrix interface, including oil coating the fibers and the supplement of an air-entraining agent.

In this study, the focus is on **High Modulus Polyethylene** (HMPE) synthetic fibers. HMPE fibers' hydrophobic nature has this type of behavior. They create weaker chemical bonds with the matrix and have better tensile strength and elastic modulus compared to the PVA fiber. During cracks initiation and propagation, HMPE fibers tend to be pulled out rather than rupture [56]. This characteristic (along with a higher modulus and tensile strength) is highly beneficial to flaw-size (crack) tolerance and complementary energy $J_{b'}$ [56].

This characteristic is preferable for the fiber behavior to follow a Coulomb-friction behavior, with lower adhesion and a weaker chemical bond between the fibers and matrix [55]. When the bond is broken, not all load-bearing capacity is lost, allowing the fiber to slip out of the matrix while continuing to transfer stresses to return to a state of equilibrium [55], [42].

In Chen et al. [57], a comparison between polyvinyl alcohol (PVA) fiber, polyethylene (PE) fiber, and steel fiber (SF), on the compressive strength, flexural strength, bending toughness, and tensile ductility of lightweight cement-based composites showed that the most significant enhancement in ductility was achieved by PE fibers with a tensile ductility reaching 2.56%.
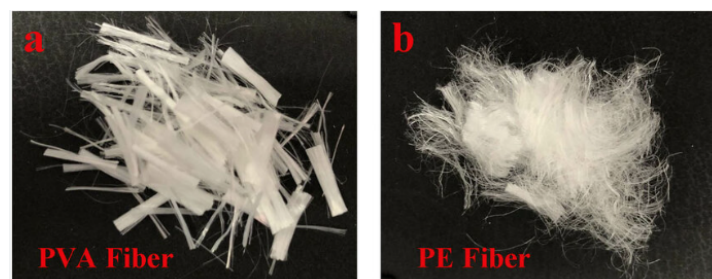
Figure 2.36: Morphology of common PVA & PE fibers [57]

According to [56], the mild slip-hardening capacity of PE fiber is one of the key factors that ensures strain-hardening in tension and is shown in (Figure 2.37).
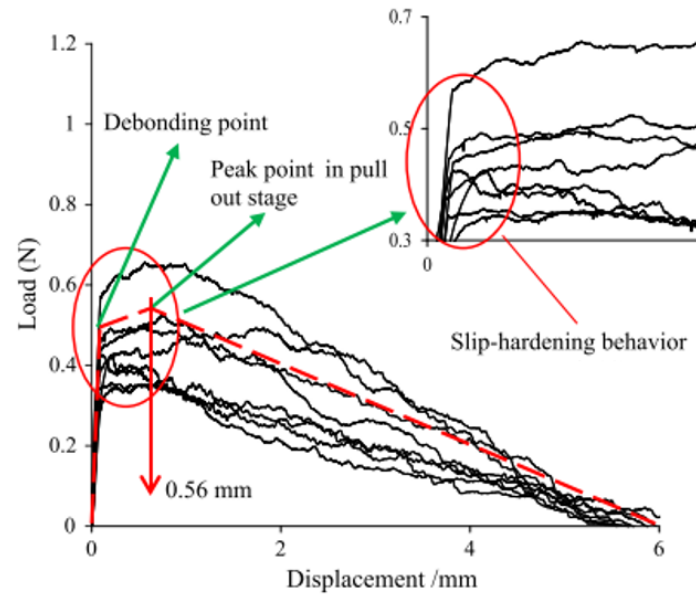
Figure 2.37: Single fiber pull out load-displacement curves for HMPE fibers [56]

2.4. Summary

Based on the literature review, a summary of the most important points is given below:

- With inspiration from natural materials, in the field of material engineering, novel hybrid materials with exceptional properties have emerged from modern fabrication techniques like 3D printing. These materials are made of intricate structural designs and interlocking characteristics, which enable them to effectively withstand impact forces and enhance energy absorption before failure. The incorporation of these interlocking elements has demonstrated an improvement in the material properties of the architectured materials when compared to the intrinsic characteristics of the constituent.

- An architectured material involving sutured curved geometries was tested by Mirkhalaf et al. [7] and due to its ability to lock in two stable positions before failure, it was called a Bistable Interlocked material. Sutures with bistable interlocks showed promising damage tolerance in cyclic and tensile loading.

- Bistable interlocked materials' geometrical properties can be tuned via design exploration (change of their main geometrical parameters) to further enhance their ductility and energy absorption.

- To explore the mechanisms responsible for the transfer of interface loads between two layers of SHCC featuring bistable interlocks, an examination of the fundamental load transfer mechanisms is imperative. These mechanisms encompass friction, bond (involving chemical adhesion), and mechanical interlock.

  – Friction is a complex phenomenon and under conditions of sufficient surface roughness, can be considered as a mechanism to increase the shear capacity on the interface. An increase in the frictional forces can enhance the shear capacity but also can cause large stress concentrations at the interface. Lubrication can mitigate that. Malik et al. [6] concluded that in specimens involving interlocking features under pull-out load, a smaller friction coefficient is more beneficial to create damage-tolerant connections.

  – Chemical bond, is usually connected to chemical adhesion at the interface. The formation and strength of chemical bonds between dissimilar phases are influenced by numerous parameters. In cementitious materials like concrete and SHCC, some of them are the moisture exchange between the layers, substrate moisture content, substrate surface roughness, curing conditions, interface stress conditions, compatibility of the connected phases, and more. Chemical adhesion is frequently complemented with interlocking features to achieve robust

connections. Numerous instances demonstrate the advantages of combining these bonding approaches, ranging from smaller-scale connections (by utilizing methods like laser ablation or injection molding [35]) to larger-scale applications (involving embedded button shear keys in single lap joints [36]). Structured interfaces incorporating bonded features exhibit promising characteristics, including enhanced energy absorption before failure, often characterized by a double-curve stress-strain relationship [9].

– Mechanical interlock in terms of shear transfer usually refers to the mechanical connectors (rebars) embedded in the concrete matrix or aggregate interlock. In this research due to the special curved geometries at the interface, it refers to the *bistable interlock mechanism*. Bistable interlocked geometries showcase a double-curved force-displacement graph enabling the structure to absorb more energy before failure by delaying the fracture localization and enhancing the systems' stability due to two equilibrium positions.

- Strain-hardening cementitious composites or SHCCs are cementitious materials that have the ability to resist increasing tensile forces even after crack formation, over a large tensile strain range. The high levels of strain are possible due to the crack-bridging property of the fibers the SHCCS contain.

- The main material design conditions for SHCC can be summarized as follows:

  – The crack bridging capacity of fibers (stress transfer across a crack) must be higher than the matrix cracking strength (stress level at initial cracking). This criterion can be ensured by sufficient fiber content, high fiber tensile strength, and adequate fiber-matrix bond strength.

  – The fiber-matrix bond strength should be limited to an extent that allows a progressive interfacial debonding of fibers bridging a crack, thus, ensuring sufficient free length for fiber deformation with crack opening and preventing premature fiber failure.

  – The fracture toughness of the matrix should be sufficiently low, and the matrix should contain numerous, well-distributed crack initiators (flaws) to promote the formation of multiple steady-state cracks.

- The matrix of cementitious composites can contain alternative materials such as fly ash, blast furnace slag, and filler materials such as limestone, to reduce the cement usage and ensure a "greener" SHCC mix.

- The bonding mechanisms of the fibers are similar to the concrete reinforcement bond (physical and chemical adhesion, friction, mechanical anchorage).

<div style="text-align: right; font-size: 3em;">3</div>

Experimental study

In this chapter, a detailed analysis of the experimental study is presented. A step-by-step procedure is presented, starting from the conceptual design of the specimens and the shape, interface, geometry variations, to the design and fabrication of molds, to casting and testing of specimens. The data measuring methods (DIC, LVDT) are analyzed.

3.1. Specimen Design

3.1.1. Bistable (curved) key specimens

Since the focus of this thesis is the bistable interlock mechanism, the design of the specimens was performed with this mechanism as a starting point.

According to the design of Mirkhalaf et al. [7], the radii ratio of the tab is the governing parameter of the design. Wang et al. [58] performed a parametric study quantifying the sensitivity of several parameters on bistable interlocks (R_1/R_2, friction coefficient, θ_1, material coefficient), and R_1 was judged to be the most sensitive parameter. Therefore, R_1/R_2 was the guiding parameter for the design of specimens.

In their research, Mirkhalaf et al. [7] explored different radii ratios, concluding that $R_1/R_2 \geq 1$ creates an interlocking phenomenon acting similar to strain hardening. In the force-displacement diagram, the second peak greatly increases with a larger R_1, adding mechanical stability to the system. When the R_1/R_2 ratio increased above a certain limit, it resulted in tab fracture [7]. Geometry with $R_1/R_2 = 1.05$ was judged to have a satisfactory combination of strength and ductility.

The initial geometry of $R_1/R_2 = 1.05$ **(geometry 1)** will be increased to *1.10* **(geometry 2)** and *1.20* **(geometry 3)** in an attempt to further improve the result of the geometrical interlock.

To define the magnitude of the radii and, by extension, the specimen size, two design boundaries needed to be taken into account. The first was the **"neck"** of the tab/key (Figure 3.1). The neck needed to be large enough to accommodate the dispersion of the fibers in the key as evenly as possible. The second one was the dimensions of the **test setup** used for monotonic tensile testing. To satisfy the first design boundary, a neck of $\approx 10mm$ was estimated to be sufficient for the dispersion of fibers of 6mm length. For the second design boundary, a specimen width of 43 mm was chosen. This width ensured that there would be enough bulk material enclosing the key to minimize in-plane bending. Some general design boundaries taken into account were the width of the specimen and the slope of the dogbone, to create a desirable gauge length without stress concentrations caused by the edges of the clamps while testing.
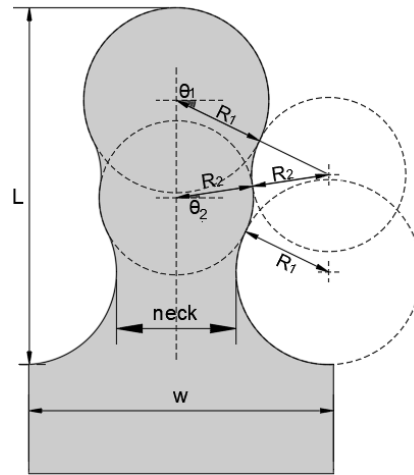
Figure 3.1: Guiding design parameters of bistable interlocked (curved) keys in accordance to [7]

Another important parameter chosen was the interlocking angle θ_1 (Figure 3.1). Along with the radii ratio, they define the *geometrically admissible range* of bistable interlocked keys (see Figure 2.12). By defining the main parameters θ_1 and R_1/R_2, the rest of the design parameters (θ_2, key length L, key width w) were calculated based on Equation 2.1, Equation 2.2, Equation 2.3 provided in [7].

After all those considerations, an overview of the chosen parameters for the 3 variations of bistable interlocked keys is shown in table 3.1.

Table 3.1: Design parameters of bistable interlocked (curved) keys

Parameters	R1/R2=1.05 (G1)	R1/R2=1.10 (G2)	R1/R2=1.20 (G3)
Radius R_1 (mm)	5.40	6.21	7.35
Radius R_2 (mm)	5.14	5.65	6.12
Interlocking angle θ_1 (°)	15.00	18.00	26.00
Interlocking angle θ_2 (°)	7.96	3.45	8.46
Key length L (mm)	17.75	20.84	28.34
Key width w (mm)	20.36	22.56	24.21

(a) Geometry 1   **(b)** Geometry 2   **(c)** Geometry 3
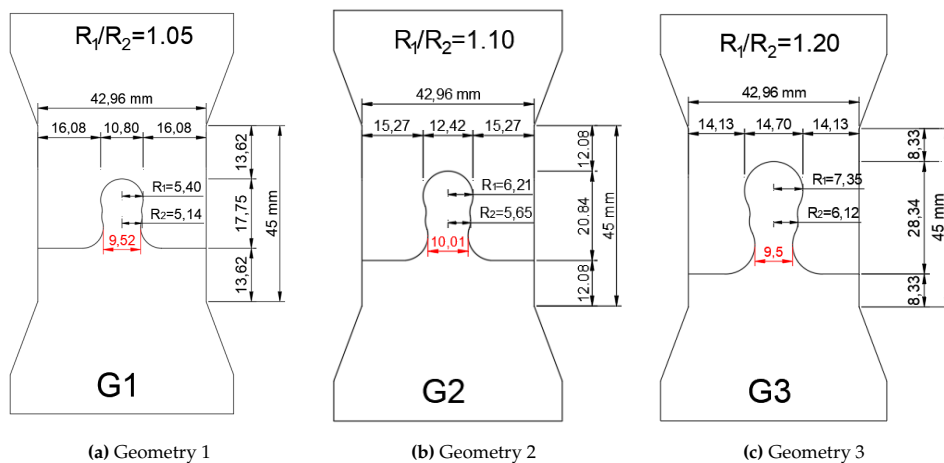
Figure 3.2: Designs of bistable interlocked keys - Geometries 1, 2, 3

A special interface case of curved keys was designed. It involved the separate fabrication of the top and bottom parts and the assembly of those in the out-of-plane direction. This key will also be

referred to as a "prefabricated" key from now on (Figure 3.3a). For this special key, the top part had to be designed with a tolerance to fit without any stresses when assembled (Figure 3.3b). On the other hand, the gap between the top and bottom needed to be small enough to ensure contact. The tolerance chosen in that case was 0.5mm (Figure 3.3a) to make sure that the assembly process would go smoothly. This practically meant that the top part was offset from the interface by 0.5mm resulting in a small R_1/R_2 decrease (1.18 from 1.20). Due to this decrease, it was judged necessary to choose geometry 3 with the largest radii ratio for this type of specimen.
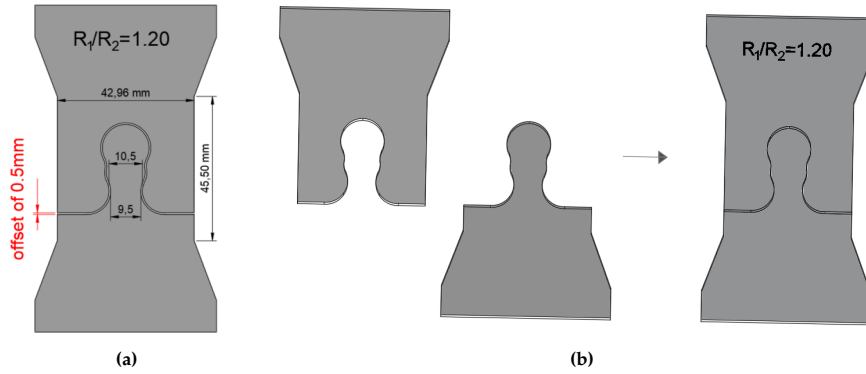
Figure 3.3: Prefabricated keys (a) design parameters & (b) assembly process

3.1.2. Straight key specimens

The design rules for the straight keys were simpler. The keys were designed in similarity to the bistable interlocked keys to provide a more controlled pull-out and to compare the pull-out mechanisms in terms of strength and ductility.

The governing design parameter for the straight key was the width/height ratio. The width was kept the same for all specimens at 10.80 mm. This value was chosen to accommodate the dispersion of fibers ($\approx$ 10mm was judged satisfactory) and to align with the widths of the bistable interlocked specimens. The values were kept as similar as possible to accommodate a reliable comparison between straight and curved keys (Figure 3.4). The width-to-height ratios chosen were *1.50, 1.00 and 0.50*. The parameters for each geometry are presented in Table 3.2.
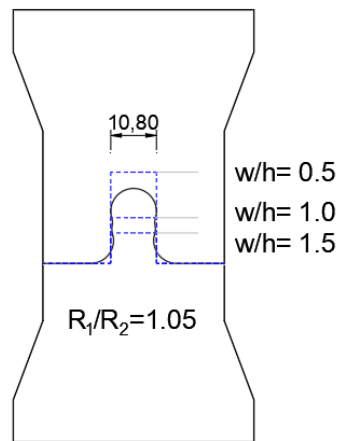
Figure 3.4: Different lengths of straight keys in comparison to bistable geometry

Table 3.2: Design parameters of straight keys

Design Parameters	w/h=1.50 (G1)	w/h=1.00 (G2)	w/h=0.50 (G3)
key width w (mm)	10.80	10.80	10.80
key height h (mm)	7.21	10.80	21.62

(a) Geometry 1 (b) Geometry 2 (c) Geometry 3
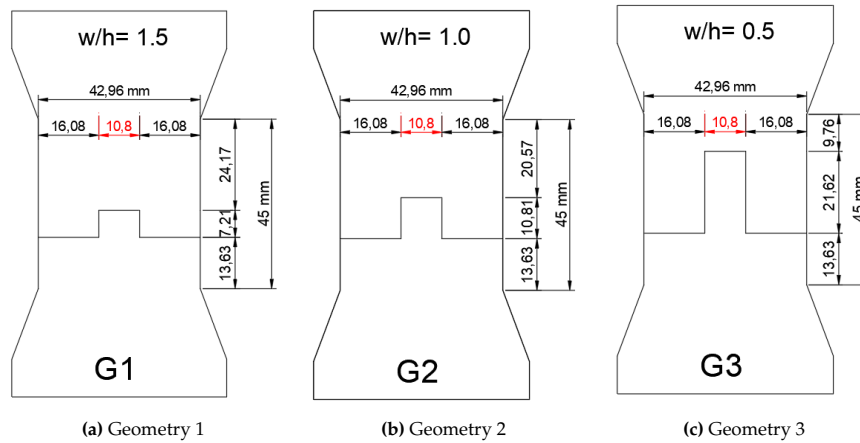
Figure 3.5: Designs of straight keys - Geometries 1, 2, 3

3.1.3. Total number of specimens

The total number of SHCC specimens produced was 39 (Figure 3.6). The three geometries of straight keys and curved keys were investigated in specimens with the two parts cast on top of each other with an untreated interface and an interface treated with lubricant. Three specimens of each geometry (for repeatability and quality control) were cast; this totals 18 straight keys and 21 total curved keys (including the special case of the "prefabricated" key).
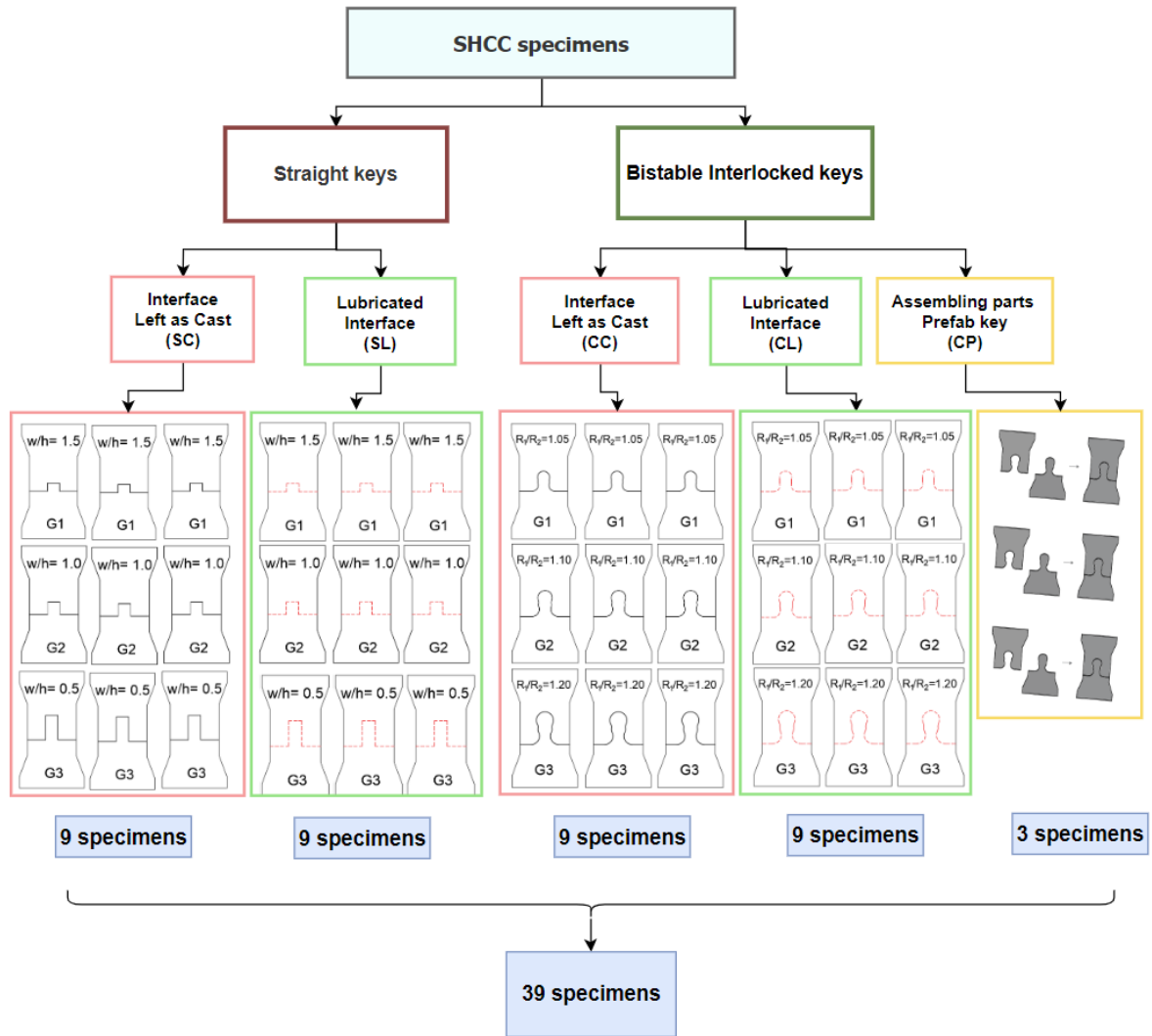
Figure 3.6: SHCC specimen overview

Mortar specimens with the same geometry as some SHCC specimens were tested to provide a reference between the two materials. The number of mortar specimens was 9 (Figure 3.7). Three straight key specimens (geometry 2 - w/h=1.00), three curved specimens (geometry 2 - R_1/R_2=1.10), and three prefabricated keys (geometry 3 - R_1/R_2=1.20).
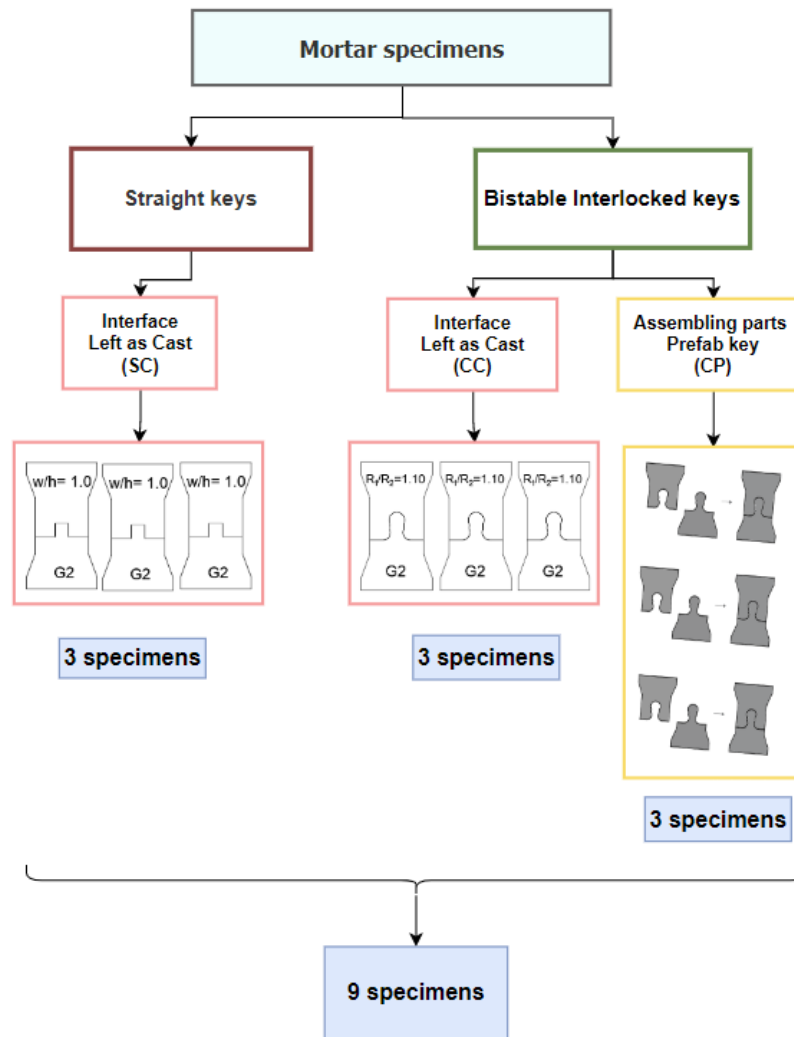
Figure 3.7: Mortar specimen overview

3.2. Materials

3.2.1. Strain Hardening Cementitious Composite (SHCC) mixture

The composition of the SHCC mixture used for casting consisted of cement, limestone powder, HMPE fibers, water, and superplasticizer. Further details of the mix composition of SHCC can be found in Table 3.3. This SHCC mix is an alteration of the originally designed mix in [43], [59].

The binder, CEM III/B 42.5 N, is delivered from ENCI (the Netherlands), and it consists of 66–80% blast furnace slag (BFS) and 20–34% clinker, according to [60], [52], [61]. The filler is finely ground limestone powder. The particle size distribution is similar to that of cement to further reduce matrix fracture toughness and accommodate uniform fiber dispersion. It is produced by Calcitec® from Carmeuse (Belgium). A polycarboxylate-based superplasticizer (MasterGlenium 51 with 35.0% solid content by mass) produced in BASF (Germany) was used to acquire the desired mixture workability. The properties of HMPE fibers can be found in Table 3.3. Since no documentation of bistable interlocks made of SHCC was available in the literature, a relatively high fiber volume was chosen for the initial mix to ensure sufficient ductility of the connection. The fiber volume was 2.6%. A high fiber volume was chosen to ensure sufficient ductility of the material for this connection. The water-to-binder ratio used was 0.40, the water-to-powder ratio was 0.20, and the filler-to-binder ratio was 1.00.

Table 3.3: (a) SHCC mix design and (b) properties of PE fibers used

Component	Dry weight (kg/m3)
CEM IIIB 42.5N	873
Limestone Powder	873
Water	349
Superplasticizer	7
PE fibers	26

(a)

Property	Ultra-high molecular weight polyethylene fibers (UHMWPE)
Tensile strenght (GPa)	3.0
Young's Modulus (GPa)	110
Density (g/cm^3)	0.97-0.98
Diameter (μm)	19-43
Length (mm)	6.0
Elongation (%)	2-3%

(b)

3.2.2. Mortar mixture

The mortar mix designed here aimed to produce reference specimens identical to the SHCC ones. Tested in the same conditions, these specimens would provide a benchmark for the material behavior. Therefore, the mix design was kept identical to the SHCC without the fibers and without the addition of any extra amount of superplasticizer in the mix (since there was no rheological loss caused by fibers). The mix design is shown in Table 3.4.

Table 3.4: Mortar mix design

Component	Dry weight (kg/m3)
CEM IIIB 42.5N	899
Limestone Powder	899
Water	360
Superplasticizer	4

3.3. Specimen preparation

3.3.1. Mould design & fabrication

3D printing

The SHCC specimens were required to fit in the test set-up of a servo-hydraulic testing machine (Instron® 8872) in which the tests would be performed. Additionally, they ought to have the necessary width and height to accommodate the bistable interlock mechanism (see Figure 3.2 & Figure 3.5). These requirements (mentioned in section 3.1) acted as guidelines for the fabrication of the moulds.

The first step was the design of the moulds in AutoCAD. 3D printing was chosen to create initial "trial" moulds (Figure 3.8a). The 3D printer used was a commercial Ultimaker 2 (Figure 3.8b); a filament-based 3D printer working with spools of thermoplastic filaments, in this case, ABS [62], [63].
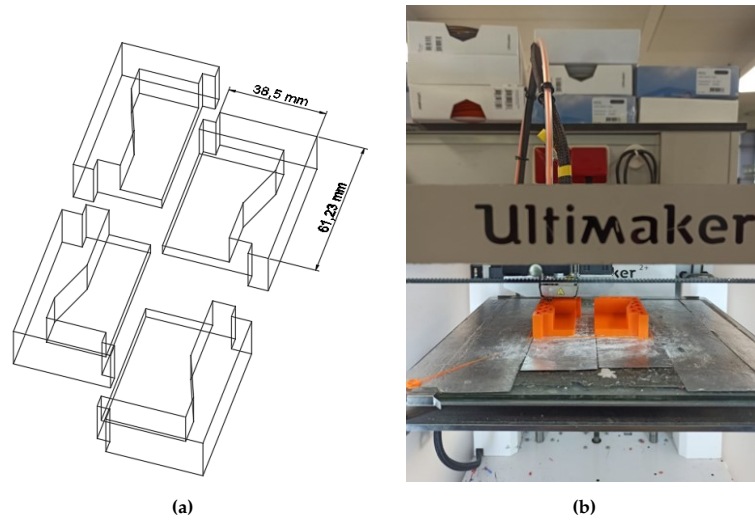
Figure 3.8: Moulds: (a) design in Autocad & (b) 3D printing in Ultimaker

Due to the limited size of the printing plate, the moulds were 3D printed in four parts, as shown in Figure 3.9a. The four parts (designed to interlock) were glued together, and the first SHCC specimens were cast in them (Figure 3.9b). These specimens were not used for testing but rather to ensure that the specimen geometry fitted properly the Instron setup (Figure 3.9c).
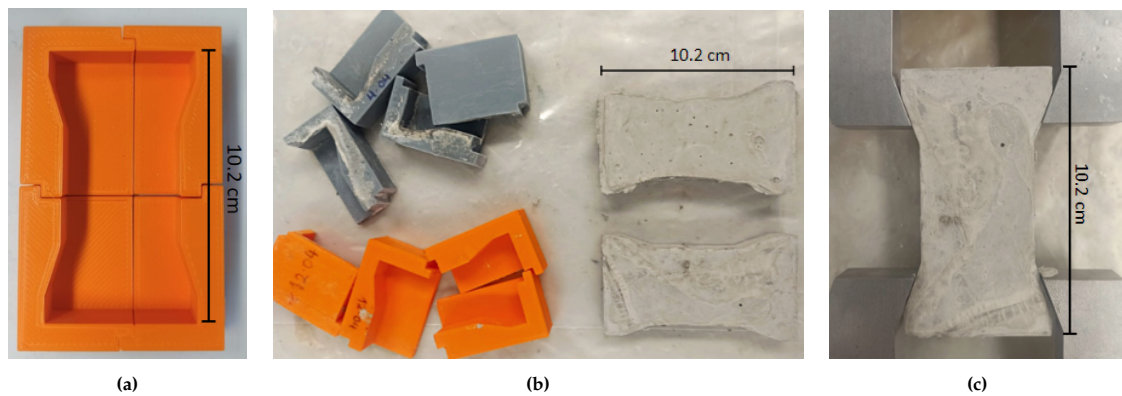
Figure 3.9: Fabrication of initial dogbones: (a) 3D printed mould (b) demoulding & (c) fitting in Instron setup

To create the geometrically sensitive interface of bistable interlocks and the straight key interface, auxiliary interface parts were 3D printed (Figure 3.10a). In Figure 3.10b, the top part depicted was printed with the aforementioned offset of 0.5mm, to create the designated moulds for the "prefabricated" keys. With the help of these parts, silicon rubber prototypes were created at a later stage for each interface variation.
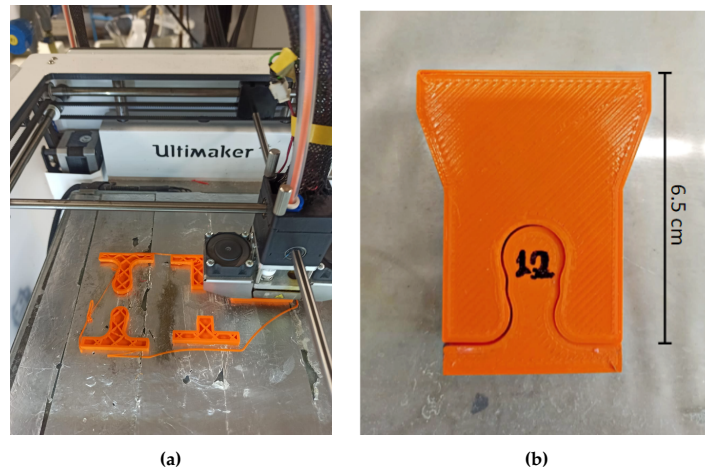
Figure 3.10: 3D printing of (a) interface elements & (b) top parts used for "prefabricated" keys

Silicon rubber casting

To create the 48 dogbone specimens (Figure 3.6, Figure 3.7), additional moulds were necessary to speed up the casting process and use fewer batches of SHCC. Therefore, silicone rubber moulds were made with the use of the previous SHCC dogbones (Figure 3.11). As a first step, 3 silicon rubber moulds identical to Figure 3.11b were created, and together with the three 3D printed moulds, 9 specimens were cast per batch.
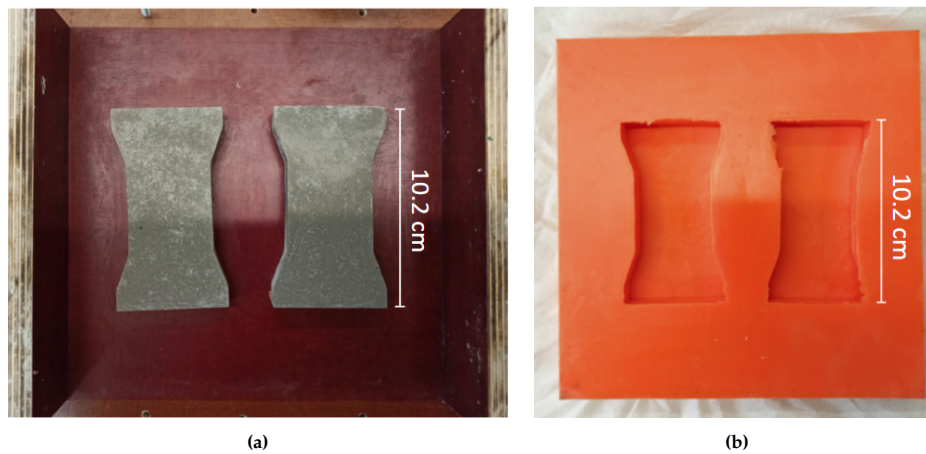
Figure 3.11: Silicon moulds for dogbone specimens: (a) preparation & (b) hardened silicon mould

The second step was to create the interfacial mould so the first part of the sutured specimen could be cast, and then the next part, on top of that. In Figure 3.12a, the 3D printed auxiliary parts mentioned before were used to create a "boundary" in which silicon rubber was cast. In this way, the top part of the silicon rubber and the desired interfaces (for straight and bistable interlocked keys) were created (Figure 3.12b). These were placed inside the silicon moulds (Figure 3.12c).
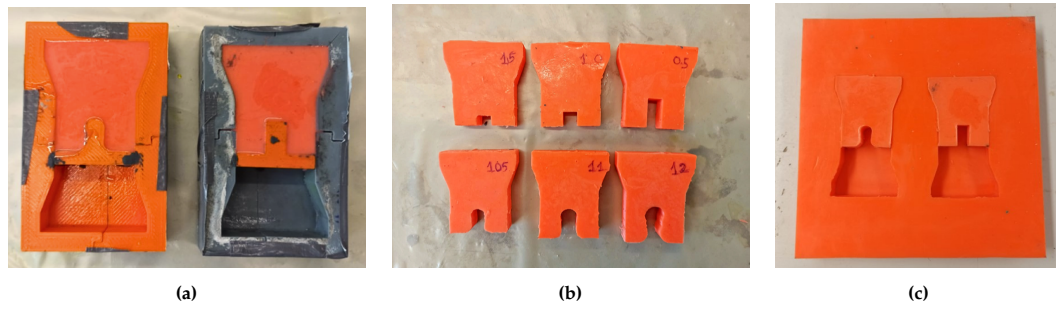
Figure 3.12: Silicon parts for interface elements: (a) silicon rubber casting (b) hardened silicon interface top parts & (c) mould preparation for SHCC casting

For the "prefabricated" keys, the top and bottom parts needed to be cast separately. A different silicone mould was created for the enlarged top parts (Figure 3.13a). The bottom parts were the same as the rest of the specimens, so there was no need for a different mould (Figure 3.13b).
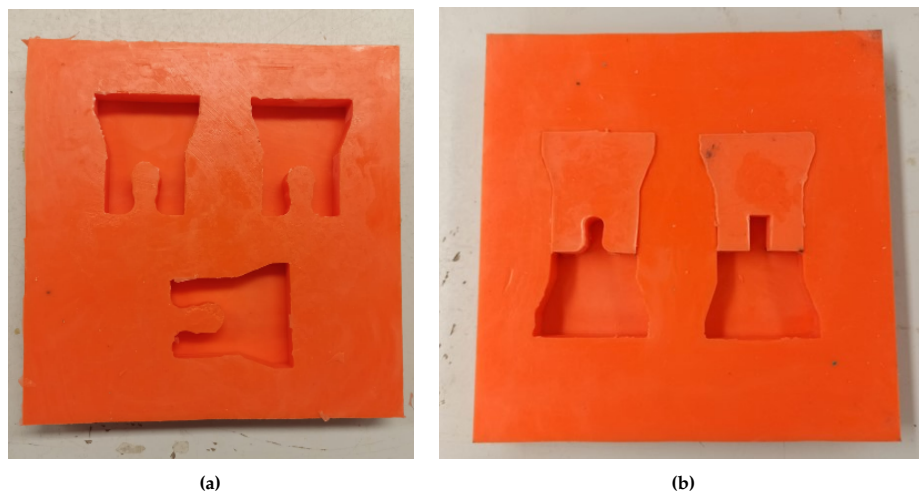
Figure 3.13: Silicon moulds for prefabricated keys: (a) top parts & (b) bottom parts

3.3.2. Casting & Curing

To prepare the SHCC specimens, BFS cement (CEM IIIB) and limestone powder were measured in a 1:1 binder-to-filler ratio. Then, they were dry mixed in a Hobart® mixer at a low speed for 5 minutes (Figure 3.14). Superplasticizer was diluted in water (only 62.5% of the total amount of superplasticizer was used at this stage), and then the liquid parts were slowly added to the mixture and mixed until the fresh paste was homogeneous. The addition of fibers to the mix followed within 5 minutes. At that time, the remaining 37.5% of superplasticizer was added to the mixture to improve the mixture's workability by compensating for the rheological loss stemming from the addition of fibers (Figure 3.15) [59].

(a)   (b)
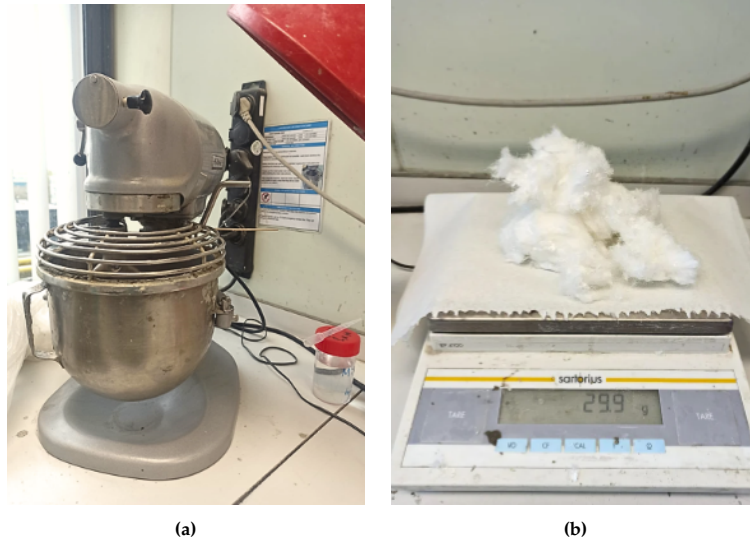
Figure 3.14: SHCC mixing: (a) Hobart mixer & (b) PE fibers used

(a)   (b)
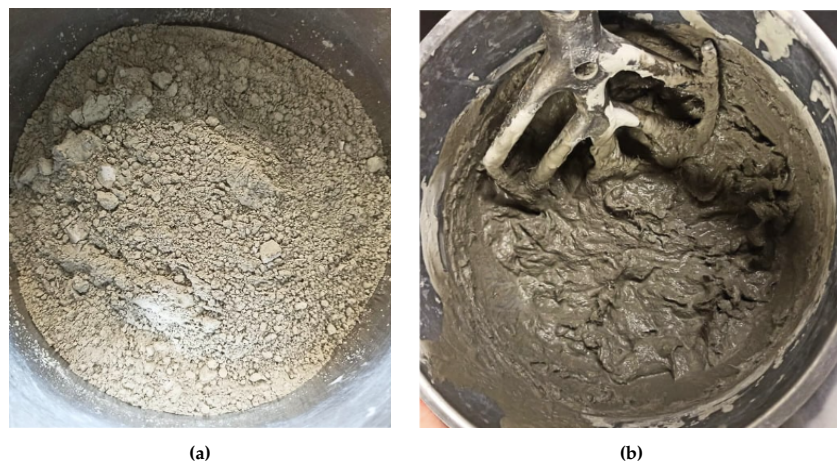
Figure 3.15: SHCC mixing: (a) dry ingredients & (b) fresh SHCC paste

The casting was performed in two stages. At first, the moulds were prepared with the designated interface elements (Figure 3.16a) to cast the bottom part. In some cases, tape was used to limit the warping of the top silicon parts inside the moulds.

After the casting, mild vibration of the specimens followed to remove entrapped air, and then they were wrapped with plastic film. The bottom part was left to harden at room temperature for one day (Figure 3.16b). After that, the silicon interface element was removed, and dirt and excessive material that overflowed sideways were removed from the interface. (Figure 3.16c). This was the case for the specimens with untreated interfaces. Then a second stage took place, which involved the casting of the top part. The mixing procedure and proportions used were identical to the previous step. After the casting, the specimens were vibrated, wrapped in plastic film, and left at room temperature to harden for one day. The next day, the specimens were demolded and left in a curing chamber (20 ° C and ≥ 98% RH) for at least 27 more days.
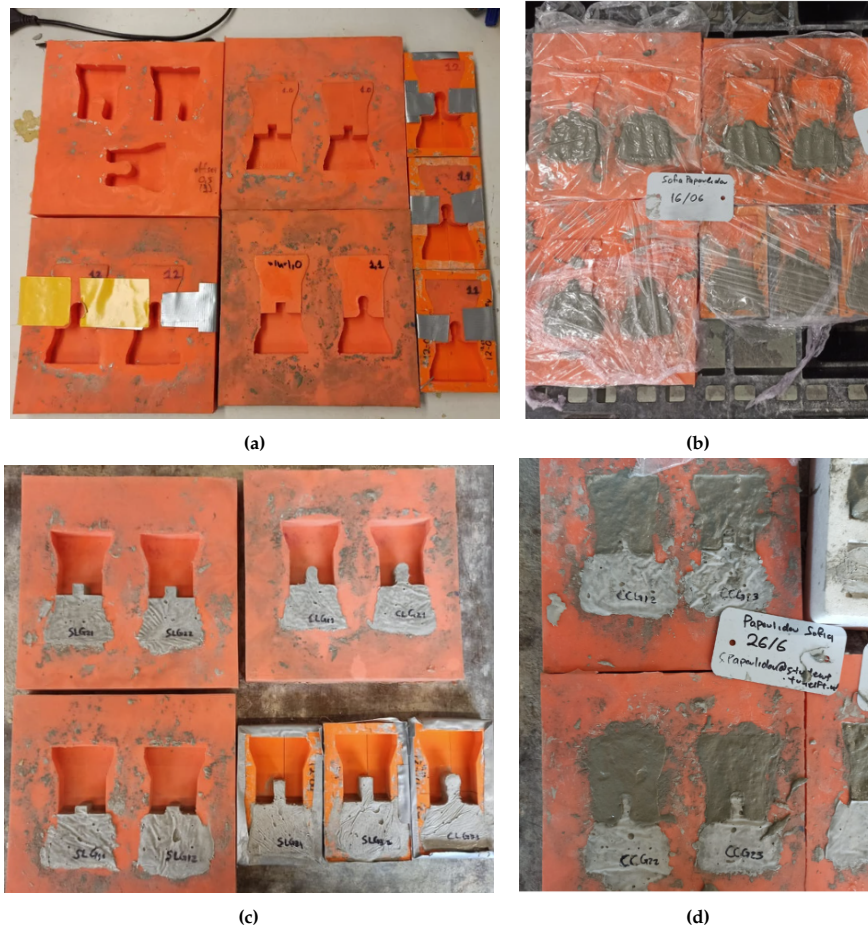
Figure 3.16: SHCC casting: (a) mould preparation, (b) casting of bottom parts, (c) mould preparation—removal of excessive material & (d) casting of the top part

In cases where the interface was treated with lubricant, after the hardening of the bottom part and the removal of the silicon top part, an additional step took place. Lubricant (liquid vaseline) was brushed at the interface (Figure 3.17) before the casting of the top part. After that, the excessive lubricant was wiped out.

Figure 3.17: Interface treatment: (a) lubricant & (b) application at the interface

A look at the final demolded specimens is presented in Figure 3.18, before the grinding of their surfaces.

<div align="center">(a)   (b)</div>

Figure 3.18: Specimen overview: (a) a set of SHCC specimens & (b) set of prefabricated key specimens

To test the mechanical properties of interest, such as compressive & tensile strength and tensile strain capacity of the material, separate specimens had to be cast.

During the manufacturing process of the main specimens, six batches of SHCC and one batch of mortar were cast. The casting of all the specimens in one large batch was not feasible due to the limited number of moulds. To ensure that the properties of the SHCC specimens were in a desirable range, two quality control specimens (prisms) were cast and tested from each batch. For the compressive strength, the fresh SHCC mix was cast in polystyrene prism moulds ($40 \times 40 \times 160\ mm^3$). Then the prisms were cut into cubes of ($40 \times 40 \times 40\ mm^3$) to perform the test (Figure 3.19a).

For the tensile properties, SHCC was cast in dogbone moulds (Figure 3.19b). These dogbone-shaped specimens were recommended by the Japan Society of Civil Engineers (JSCE) [59], and had a cross-section of 13×30 mm at the test zone ($80 \times 30 \times 13\ mm^3$ in gauge length volume).

<div align="center">(a)   (b)</div>
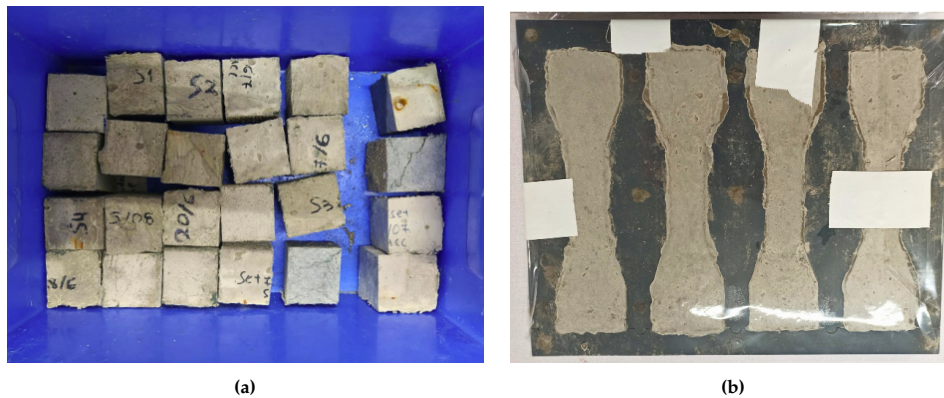
Figure 3.19: Specimens for material properties tests: (a) cubes & (b) dogbones

3.3.3. Digital Image Correlation (DIC) preparation

To perform DIC, the specimens needed to have enough optical contrast. Since the surface of the specimens did not have the required contrast, it had to be artificially created. Consequently, the specimen surfaces were ground and smoothed out. Afterward, the specimens were painted with white paint, and after the paint was completely dry, they were sprayed with black spray to create a speckle pattern for the DIC analysis. More information on the DIC measuring method is provided in subsection 3.4.3.
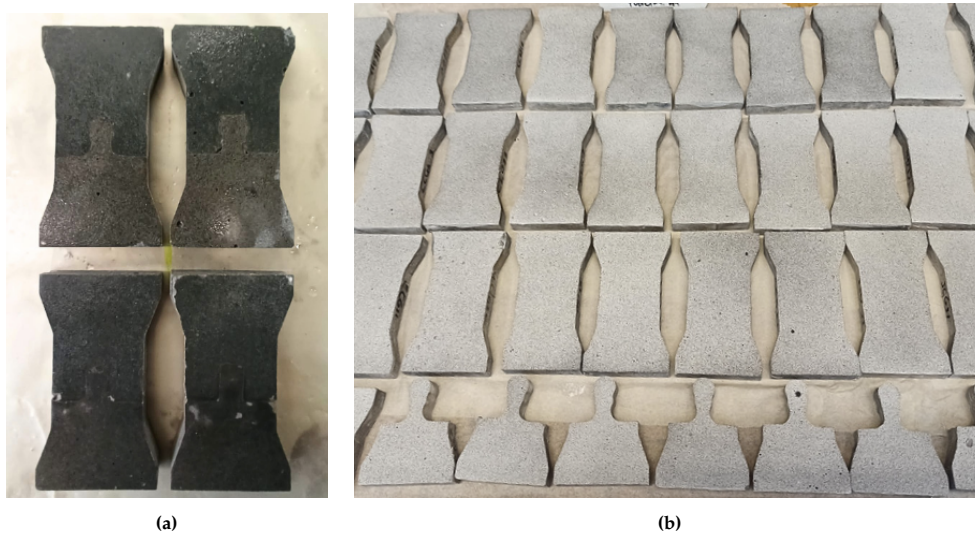
Figure 3.20: Specimen preparation for DIC: (a) ground surfaces & (b) sprayed specimens

3.4. Testing & data measuring
3.4.1. Material properties tests

To investigate the material properties of the specimens, material tests on SHCC and mortar were performed (Figure 3.21). The compressive strength of both mortar and SHCC was determined with uniaxial compression tests on small cubes following NEN-EN 196-1 [64] shown in Figure 3.19a. As mentioned before, for every batch of SHCC & mortar, two SHCC prisms were prepared, cured, cut into cubes, and tested. The loading rate was 0.2 kN/s.

The strain-hardening behavior is an important characteristic of SHCC; thus, it is necessary to confirm that the material used for the specimens can be classified as SHCC. The aforementioned dogbone specimens with a cross-section of (13 × 30) mm were tested under uniaxial tension tests. The testing apparatus was a servo-hydraulic testing machine (Instron®) under displacement control at a rate of 0.005 mm/s (Figure 3.21).
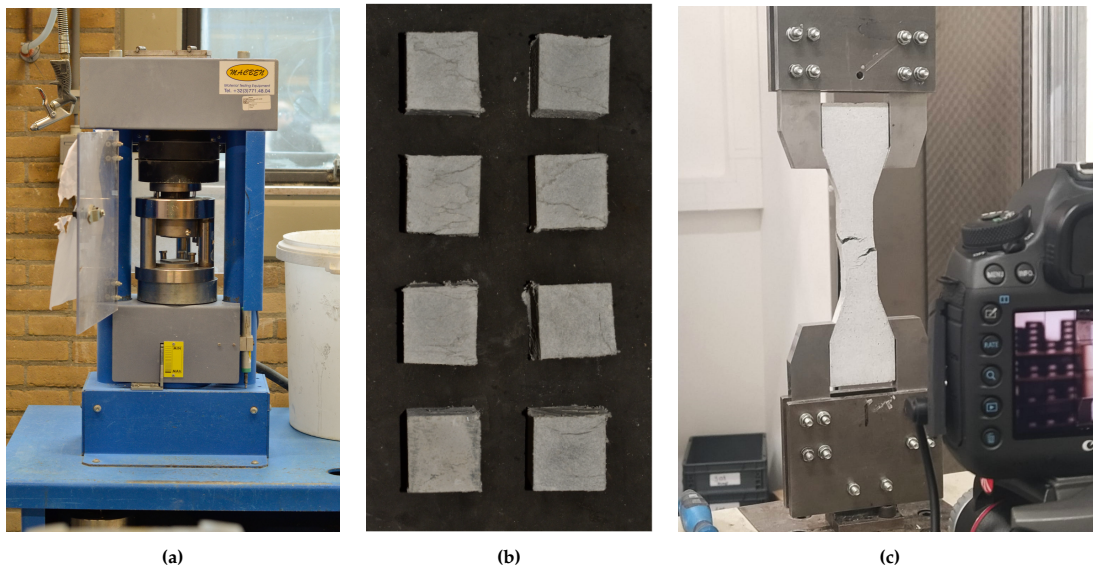
Figure 3.21: (a) Compressive strength test setup (b) cracked specimens & (c) dogbone specimens tensile tests

3.4.2. Tensile testing of main specimens

Uniaxial tension tests were performed by using a servo-hydraulic testing machine (Instron®) (Figure 3.22) under displacement control at a rate of 0.005 mm/s. When it comes to the Instron set up the top clamp was able to rotate while the bottom one was bolted to the testing machine. This helped with the alignment and uniform loading of the specimen, and the elimination of possible bending stresses.

Initially, a pretension of 0.05 kN was applied to the dogbone specimen through the clamps of the setup. During the tests, the deformations were measured with a gauge length of 80 mm and one Linear Variable Differential Transformers (LVDTs) fixed on the back side of the specimens. On the front side, a camera was set to take pictures with a timer set at 10 seconds to perform 2D DIC. This was an effective way to obtain reliable displacement data simultaneously from both methods.

Tests were stopped by releasing the applied tensile load after the tensile load dropped to an approximate value of 0.05kN. The specimens were loaded until failure or full translation of their keys, and were not able to sustain any more load.
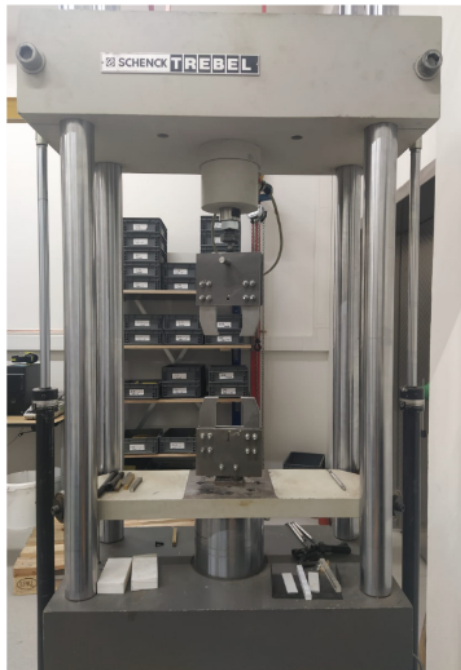
Figure 3.22: Instron setup for tensile testing

3.4.3. Measuring techniques

DIC

Digital image correlation (DIC) is an optical non-contact technique used to measure the displacement of an object or surface as it undergoes progressive strain. The method involves the consecutive capture of images of the object or the surface before and after the application of loading. Then, with the help of specialized software, analysis of the reference images and deformed images can determine the amount and direction of the deformation or displacement [65], [66]. In simple terms, DIC can be compared to having thousands of mini-extensometers on the sample [67].

Figure 3.23: Tensile properties: Dogbone specimen testing

To perform DIC, some simple preparations are needed. At first, a speckle pattern on the surface of the test sample is required, as is a stable light source and image acquisition hardware (camera). The speckle pattern on the surface is the source of deformation information. More specifically, the speckle pattern could be described as a random intensity allocation of a finite number of pixels, which are usually artificially prepared on the surface of the test sample [66]. Airbrushing white and black paint on the surface is the most common method to create an effective speckle pattern. A good speckle pattern on the sample surface should be highly contrasted, stochastic, and isotropic [66]. The accuracy of the data is dependent on the light conditions in the room, on the speckle pattern but also on the stability of the camera setup.
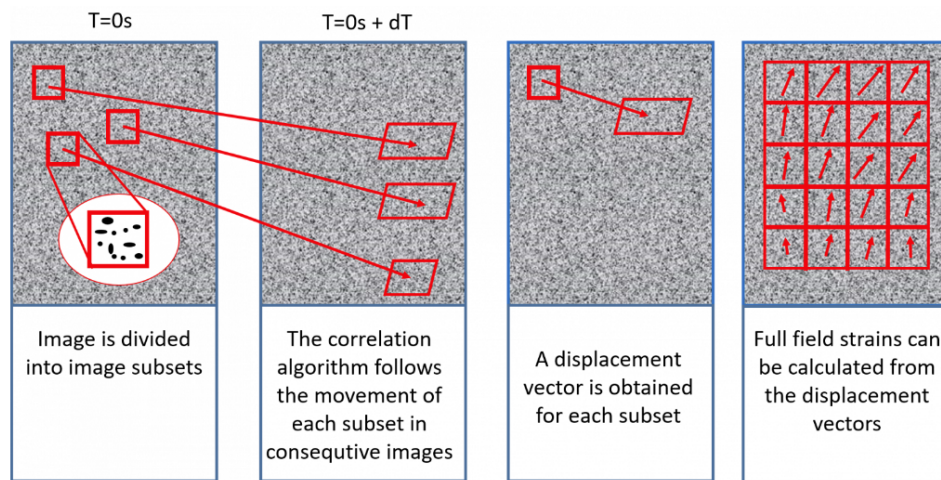
Figure 3.24: Schematic illustration of the 2D DIC method [67]

LVDT

It is common practice to validate the DIC data with strain gauges since DIC is sensitive to setup and pattern quality. Linear Variable Differential Transformers (LVDTs) are electromechanical sensors used to transform mechanical motion into a variable electrical signal (current or voltage) [68]. They are usually employed for the measurement of displacements. The aforementioned mechanical motion involves the compression or relaxation of a spring to evaluate the displacement difference between two specified places (Figure 3.25).

This causes an alteration in the electric circuit's resistance; this change is detected and translated into displacement. The LVDTs are calibrated to determine the conversion factor, which is required to convert the recorded voltage to a displacement [68]. The calibration is performed with the help of a calibration load cell by applying a known displacement and measuring the documented voltage.
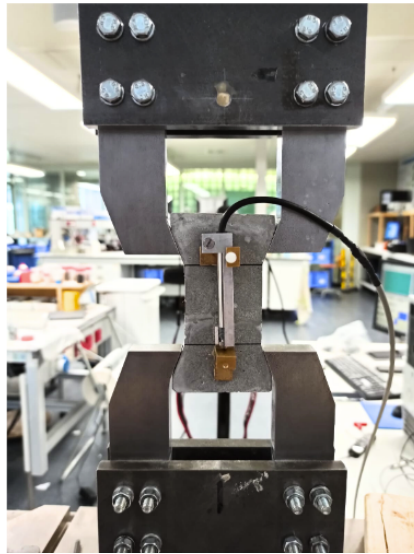
Figure 3.25: LVDT placed on the back side of the specimen

3.5. Summary

In this chapter, the fabrication, testing details, and data acquisition regarding the main specimen tensile tests were presented.

- The design of the specimens is centered around the bistable interlock mechanism. The radii ratio R_1/R_2, is identified as a critical parameter, guided by previous research. Three different geometries (R_1/R_2 = 1.05, 1.10, 1.20) are considered for curved keys. A special case involves the fabrication of separate top and bottom parts for assembly in the out-of-plane direction, to create "prefabricated" keys. The straight key specimens were designed to provide a controlled pull-out mechanism to accommodate comparison with the curved keys. Width/height ratio (w/h) is the governing parameter, with three ratios considered: 1.50, 1.00, and 0.50. This results in three geometric variations of curved and straight keys. With the application of two interface treatments (untreated and lubricated) and three specimens of each case for repeatability,39 SHCC specimens were fabricated. Nine mortar specimens with identical features to the SHCC ones were cast to act as a reference.

- When it comes to the SHCC mix design, the main components were cement CEM III/B 42.5 N, limestone powder, High Modulus Polyethylene (HMPE) fibers, water, and a polycarboxylate-based superplasticizer. The SHCC mix is an adaptation of the original "green" mix design from previous research that took place at TU Delft. The mortar mixture followed the same mix design but excluded fibers.

- When it comes to specimen preparation, many steps were involved. The first one was the 3D printing of initial moulds designed in AutoCAD in parts that interlocked. The first dogbone specimens were cast in those and were used to create more moulds made of silicon rubber. Afterward, the main SHCC specimens were cast in them in two stages to create the two parts of the suture. For the prefabricated keys, the top and bottom parts were cast separately. For specimens with lubricated interfaces, liquid Vaseline was applied at the interface before casting the top part, and for the rest, the interface remained untreated. The specimens were vibrated, wrapped in plastic film, and left to cure for a designated period of at least 28 days. Afterward, surfaces were ground, smoothed, and prepared with a speckle pattern for DIC analysis. Simultaneously, additional specimens to test the material properties (such as compressive and tensile strength) were prepared.

- Compressive strength tests and tensile testing were performed to define the material properties. Uniaxial tension tests with displacement control and a displacement rate of 0.005mm/s were carried out using a servo-hydraulic Instron testing machine. To measure the deformations, Linear Variable Differential Transformers (LVDTs) were employed on one side, and Digital Image Correlation (DIC) was employed on the other side of the specimen.

<div style="text-align: right; font-size: 4em;">4</div>

Results

In this chapter, a detailed analysis of the specimens' tensile response using digital image correlation is performed. Force-displacement graphs are plotted for one "representative" specimen in each category of the SHCC specimens. Different data sources (data from DIC and LVDT) are used to provide a reliable representation of the obtained values. A closer look at the crack formation and patterns is presented. The results of the material tests, presenting the used SHCC mixture properties, are also included.

4.1. Material test results

4.1.1. Compressive Strength

The compressive strength of both concrete and SHCC was determined with uniaxial compression tests. The details about the specimens and testing procedure are mentioned in Chapter 3. The results are presented in Tables 4.1 & 4.2.

The compressive strength for the 6 batches/sets ranged from 72.44 to 92.30 MPa (Table 4.1). The variation was in an acceptable range (below 10%) for all the sets except for set 5 (11.21%).

Control specimens were cast for the mortar set as well. These specimens were tested in the same conditions mentioned above (for the SHCC specimens). Here the coefficient of variation was 12.18% (larger than 10%).

Table 4.1: Results of compression test on SHCC specimens at an age of 90 days

SHCC specimens	Compressive strength (MPa)	Average (MPa)	Standard deviation (MPa)	COV (%)
Set 1 -specimen a	86.89			
Set 1 -specimen b	93.44	87.08	6.27	7.20
Set 1 -specimen c	80.90			
Set 2 -specimen a	88.62			
Set 2 -specimen b	96.66	92.30	4.07	4.41
Set 2 -specimen c	91.61			
Set 3 -specimen a	84.79			
Set 3 -specimen b	91.52	89.58	4.18	4.66
Set 3 -specimen c	92.43			
Set 4 -specimen a	86.02			
Set 4 -specimen b	90.76	87.85	2.55	2.90
Set 4 -specimen c	86.77			
Set 5 -specimen a	79.27			
Set 5 -specimen b	63.46	72.44	8.12	11.21
Set 5-specimen c	74.59			
Set 7 -specimen a	85.97			
Set 7 -specimen b	86.98	89.99	6.11	6.79
Set 7 -specimen c	97.02			

Table 4.2: Results of compression test on mortar specimens at an age of 90 days

Mortar specimens	Compressive strength (MPa)	Average (MPa)	Standard deviation (MPa)	COV (%)
Set 6 -specimen a	64.85			
Set 6 -specimen b	71.37	64.02	7.80	12.18
Set 6 -specimen c	55.84			

4.1.2. Tensile Properties

Dogbone specimens were tested at an approximate age of 90 days. The ultimate tensile strength was found to be 5.25 MPa with a coefficient of variation of 2.20% (Figure 4.3). The low variation showed extremely stable tensile behavior in the specimens. The strain capacity was calculated as 3.08% (strain at peak load) with a coefficient of variation of 10.14% (Table 4.3).
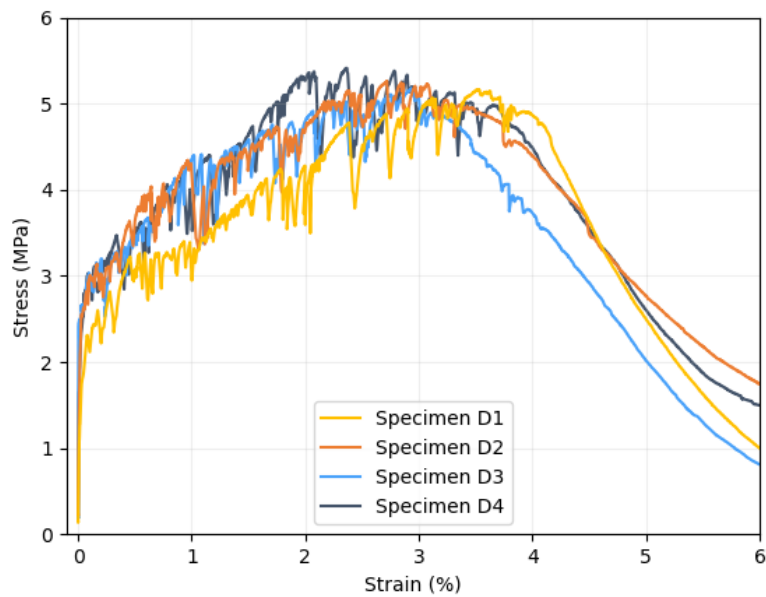
(a)

(b)

Figure 4.1: (a) Results of tensile tests of SHCC dogbones at an age of 90 days & (b) SHCC dogbone specimens after the tensile tests

Table 4.3: (a) Tensile strength and (b) strain capacity of SHCC specimens

SHCC specimens	Tensile strength (MPa)	Average (MPa)	Standard deviation (MPa)	COV (%)
Dogbone 1	5.16			
Dogbone 2	5.26	**5.25**	0.12	2.20
Dogbone 3	5.18			
Dogbone 4	5.41			

(a)

SHCC specimens	Strain capacity (%)	Average (%)	Standard deviation (%)	COV (%)
Dogbone 1	3.51			
Dogbone 2	3.07	**3.08**	0.31	10.14
Dogbone 3	2.93			
Dogbone 4	2.79			

(b)

4.2. Single specimen results

In this section, single-specimen results will be presented. The specimens chosen are 13 in total, each one representing one of the categories shown in Figure 4.2. Results obtained from DIC and LVDT data are plotted on the same graph to compare the displacement in the force-displacement diagram. The strain contours at eight critical points along the force-displacement curve are going to be presented, to document the progressive opening, shape, and location of the cracks.
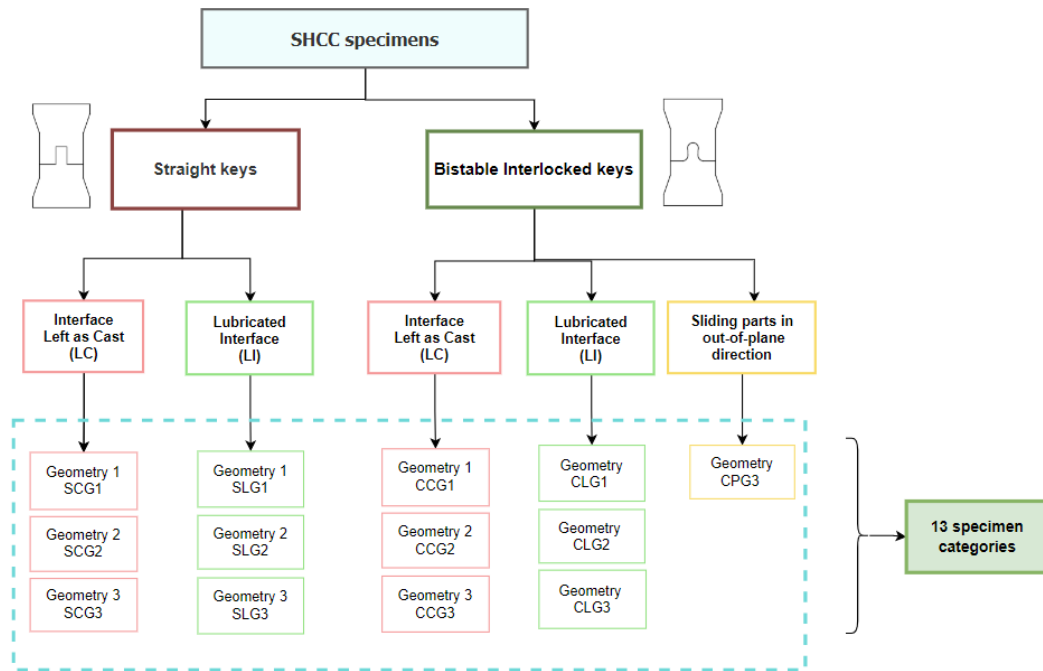
Figure 4.2: Categorization of SHCC specimens
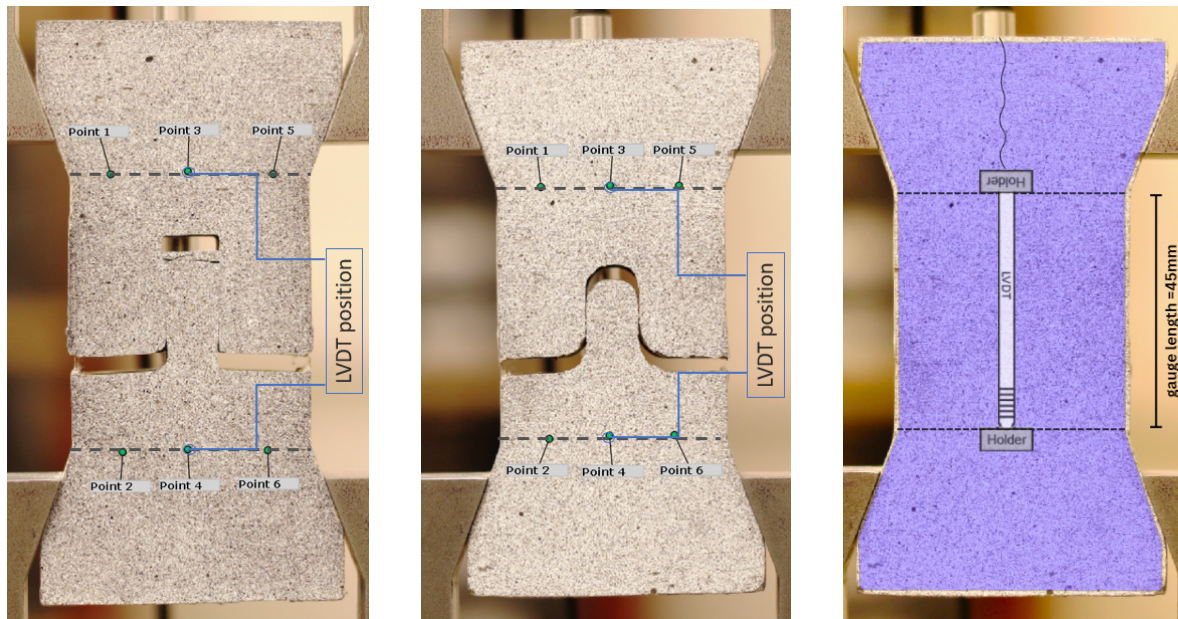
Figure 4.3: (a) Points chosen for DIC analysis in straight keys, (b) in curved keys, & (C) schematic representation of the LVDT position at the back of the specimen

4.2.1. Straight key specimens
Specimen SCG11- Untreated Interface, geometry 1 (w/h=1.5)

Figure 4.4: Force - displacement diagram illustrating the tensile response of the specimen SCG11
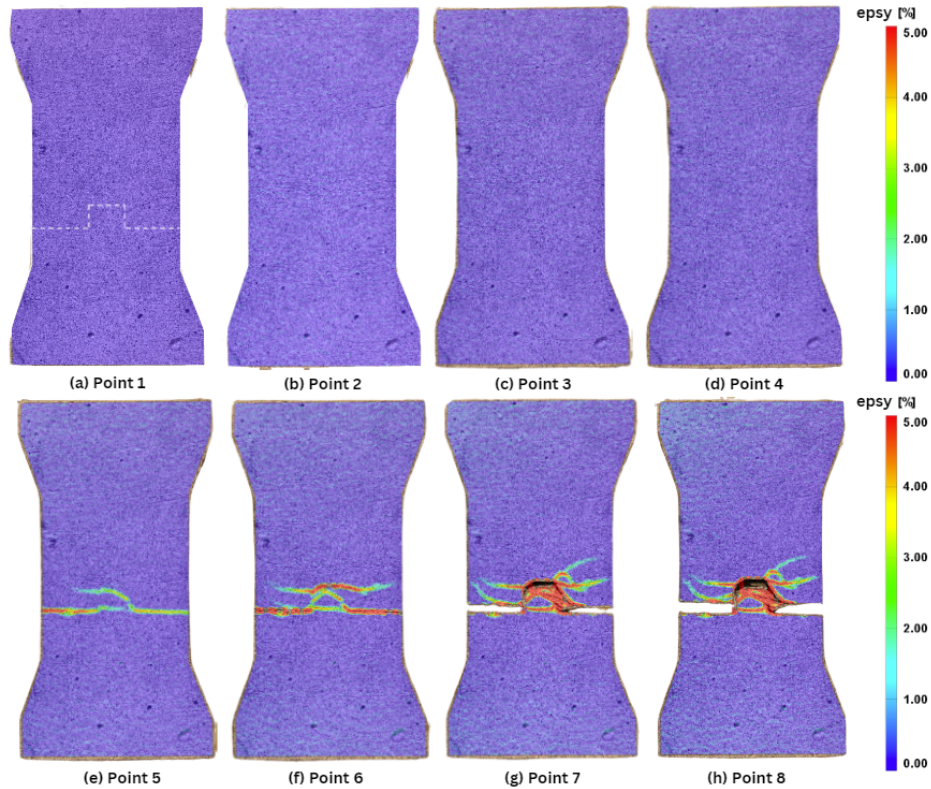
Figure 4.5: Strain contours (ϵ_y) of points 1-8

In Figure 4.4 the tensile response of a straight specimen with an untreated interface and geometry 1 (w/h = 1.5) is examined. This geometry has the smallest length among the straight key specimens. Looking at the Figure 4.4, four force-displacement curves are plotted with different colors. As the legend suggests, these refer to displacements measured from the LVDT (yellow line) and from the DIC, at three different sets of points (see Figure 4.3). It should be noted that points 3–4 of the DIC data (Figure 4.3 b, c) were chosen to coincide with the LVDT location (Figure 4.3a) for a more reliable comparison. The force values (y-axis) are always measured from the Instron output. The sudden drops in force in the LVDT curve can be attributed to the formation of cracks. The force-displacement graphs are plotted in the same way for the rest of the specimens.

Comparing the various displacement values (Figure 4.4), discrepancies occur for SCG11. The differences in values in DIC and LVDT data could be attributed to numerous reasons:

- The LVDT is placed on the back side of the specimen, while the DIC data is taken from the front side. During the pullout, the specimens often experienced out-of-plane bending to smaller or larger degrees. This can result in uneven displacements on the front and back sides of the specimen.
- Another limitation is the specimen imperfections caused by the flexible molds used during the casting process and from the grinding of their surfaces, which can result in slant slopes.
- DIC requires a homogeneous, stochastic speckle pattern on the surface for tracking displacements. The accuracy is affected by the paint application on the specimen, the source of light, and more. LVDT measurements are not affected by surface patterns.
- The set of points 3-4 are located in the same position where the LVDT is placed (Figure 4.3). The other sets of points are located left and right, and the opening is not fully symmetrical on these sides. Displacements can differ from the middle, where the key is located.

As the tensile force increases, three distinct stages are noted in the force-displacement curve (Figure 4.4).

- **Stage 1**: Initially, there is a steep elastic regime until point 4, where the proportionality limit is located since there is a small deviation from linearity at that stage. All the deformations happening in the elastic stage are reversible, and there is no visible damage to the specimen.
- **Stage 2**: The strains are still small up until point 5 (first cracking strength), where crack initiation is documented (Figure 4.5). There, the notched interface of the specimen opens with the propagation of a crack at the "neck" of the key. At the same time, there is partial debonding on the right side of the key. After this point, a small strain-hardening regime (points 5–6) takes place. The strain hardening regime (points 5–6) involves further cracking at the corners of the key & debonding.
- **Stage 3**: Finally, post-peak strain-softening follows (points 6–8) until the full pull-out (point 8), where the force is reduced to almost zero. The key is now open, and after this point, crack propagation and further opening (points 7, 8) occur. Regardless of the cracks and loss of stiffness, the key opened further without rupturing. The cracking was concentrated at the corners of the top part and along the key length at the bottom part.

Since the specimens in this category (straight keys, untreated surface, geometry 1), showed differences in their failure modes, all the specimens of the same group (SCG11, SCG12, and SCG13) are presented in Figure 4.6 at the end of the analysis. The key in SCG11 was fully translated; the key failed at the interface in SCG12, and failure occurred at the edge of the key in SCG13.

Figure 4.6: Failure modes of (a) SCG11 (analysed above), (b) SCG12, & (c) SCG13

Specimen SCG22- Untreated Interface, geometry 2 (w/h=1.0)

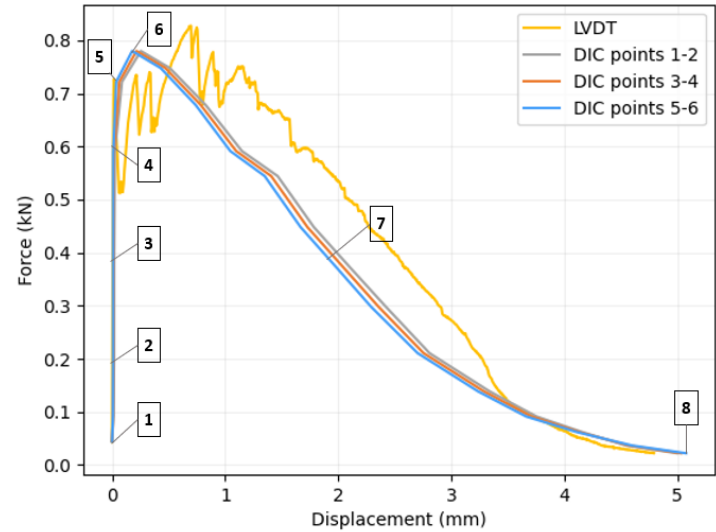**Figure 4.7:** Force - displacement diagram illustrating the tensile response of the specimen SCG22
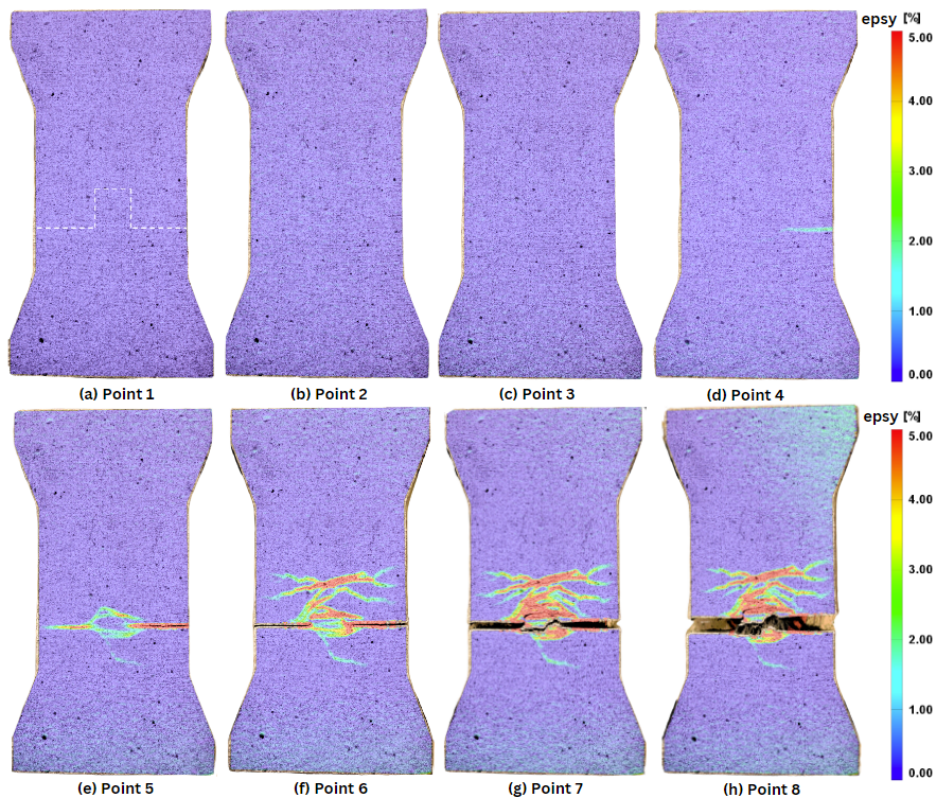
Figure 4.8: Strain contours (ϵ_y) of points 1-8

In Figure 4.7, the tensile response of a straight specimen with geometry 2 (w/h = 1.0) and an untreated interface can be examined. This is the medium-length straight key among the three geometries.

The force-displacement graph can be divided into three stages, similar to before.

- **Stage 1:** As the tensile force increases, initially there is a steep elastic regime up until point 4.
- **Stage 2:** Afterward, from points 4 to 6, a strain-hardening regime occurs, with peak force at point 6 (1.09 kN). Crack initiation is documented in point 4, where the interface of the specimen opens from the right side, suggesting the occurrence of bending (Figure 4.8). The crack pattern became more tortuous, and up until point 6, the bearing capacity increased due to the key resisting the opening, with more cracks forming in different locations (crack bridging property of SHCC).
- **Stage 3:** Post-peak, strain-softening occurs (points 6–8) until the full pull-out (point 8), where the force is reduced to almost zero. At this stage, the cracks open further, resulting in the rupture of the key at the interface. Twisting of the testing clamps was noted in the DIC pictures, which confirms that bending occurred.

In comparison to the previous specimen that had a smaller key size, a larger strain hardening regime occurs with a larger key. The failure mode, which in one case was the opening of the key and in this case was the shearing of the key, does not explain that. However, in the case of a key of a larger length, the key formed numerous cracks before rupturing.

Another thing to address is that for this specimen, the DIC results and LVDT results had a larger discrepancy. As stated before, this is linked to out-of-plane bending. Here, the crack opening from one side, the rupture of the key, and the rotation of the clamps, all suggest that.

For this specimen category (straight keys, untreated surface geometry 2), the failure modes of the identical specimens SCG11, SCG12, and SCG13 are presented in Figure 4.9. The failure modes were similar; key failure occurred at the interface in all three specimens.
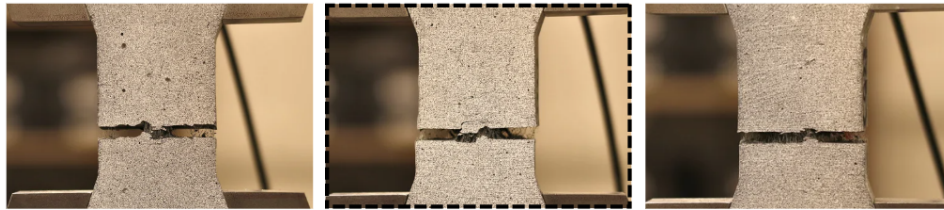
Figure 4.9: Failure modes of (a) SCG21, (b) SCG22 (analysed above), & (c) SCG23

Specimen SCG31- Untreated Interface, geometry 3 (w/h=0.5)

Figure 4.10: Force - displacement diagram illustrating the tensile response of the specimen SCG31
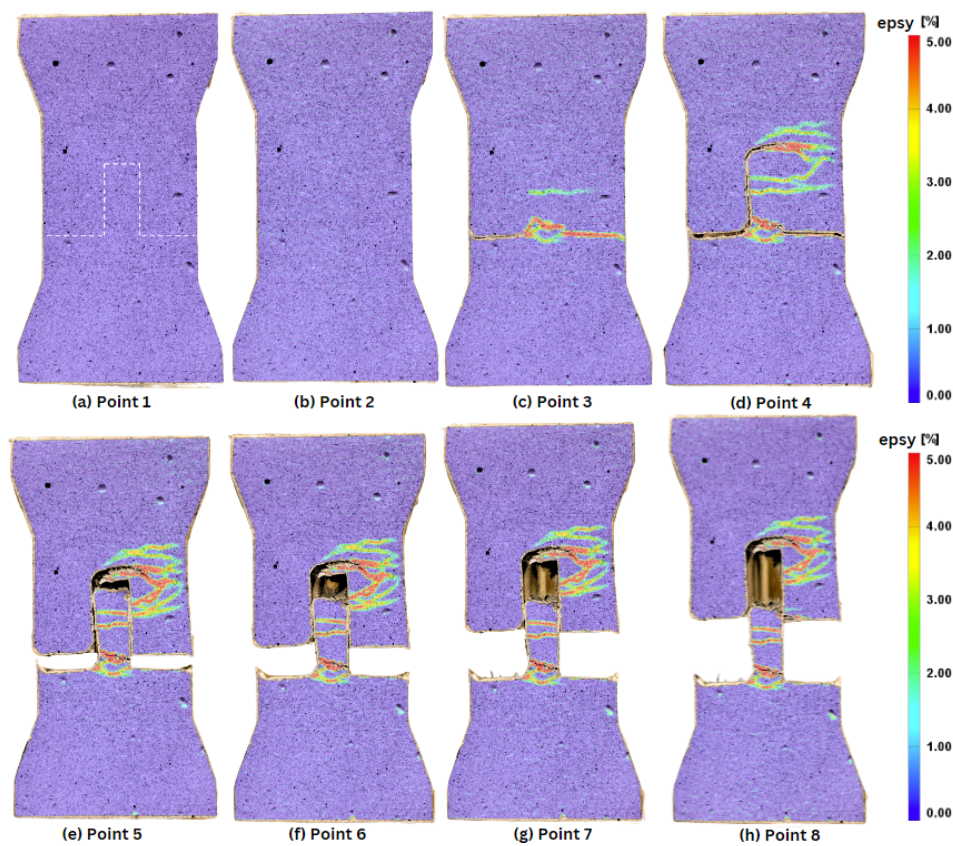
Figure 4.11: Strain contours (ϵ_y) of points 1-8

In Figure 4.10 the tensile response of a straight specimen with geometry 3 (w/h = 0.5) and an untreated interface is analyzed. This is the larger straight key in length.

Looking at the force-displacement graph, there are four characteristic stages.

- **Stage 1:** The elastic stage takes place from points 1-2. The deformations at this stage are reversible if the loading is removed. There are no visible cracks or irreversible damage at the specimen (Figure 4.11).

- **Stage 2:** After point 2, there is a slight deviation of the linear part of the curve suggesting that plastic deformations are taking place. There is an increase in force until point 4. In this stage, the response shows strain-hardening behavior. The specimen was cracking in multiple locations from points 3 to 4, but there was no upward movement of the key since the interface was "glued" at the right side, explaining this increasing-capacity stage. Bond and friction resisted the movement.

- **Stage 3:** After point 4 and until point 5, a sudden drop in force takes place, explained by the opening of the interface and the movement of the key. Now the boundary conditions have changed to sliding friction. No more cracks are forming at the top part of the key itself, and the resistance to the tensile forces is governed by frictional contact.

- **Stage 4:** From point 6 onward, the force has stabilized on a plateau while the key is slowly sliding out of the top part. Friction mechanisms take place; no more major cracks are forming. This continued until the full pull-out of the key (point 8), where the specimen could not resist any more tensile force.

It is worth mentioning that here the specimen showed a uniform response in DIC and LVDT data. Bending was limited in this test, and uniaxial tension was governing.

For this specimen category (straight keys, untreated interface geometry 3), the failure modes of the identical specimens SCG11, SCG12, and SCG13 are presented in Figure 4.12. The failure modes were similar, with full translation/opening of the key in SCG31 and SCG32, and key failure approximately in the middle of the key in SCG33.
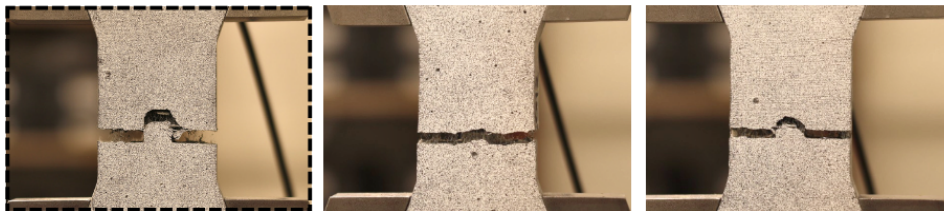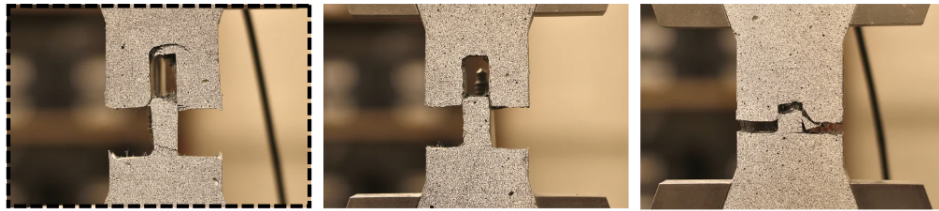

Figure 4.12: Failure modes of (a) SCG31 (analysed above), (b) SCG32, & (c) SCG33

Specimen SLG12- Lubricated Interface, geometry 1 (w/h=1.5)
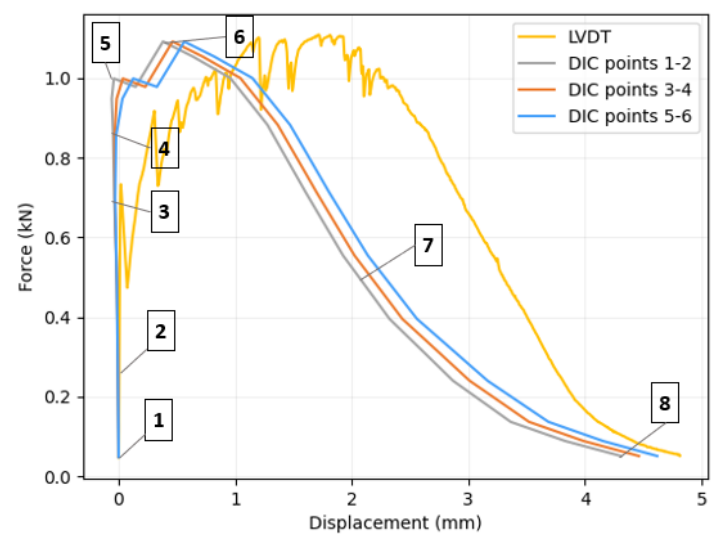

**Figure 4.13:** Force - displacement diagram illustrating the tensile response of the specimen SLG12
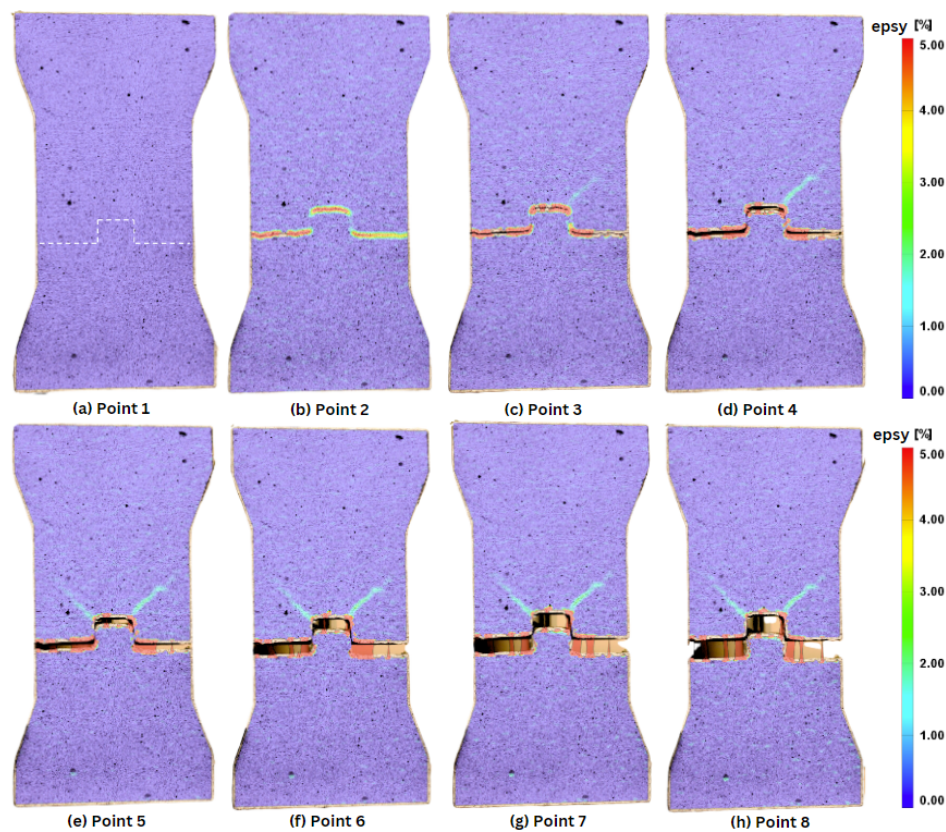
Figure 4.14: Strain contours (ϵ_y) of points 1-8

In Figure 4.13 the tensile response of a straight specimen with a lubricated interface and geometry 1 (w/h=1.5) is presented. This geometry has the smallest length among the straight key specimens.

- **Stage 1:** From points 1 to the onset of point 2, an elastic regime takes place. The peak force has already been reached (at 0.23 kN) at point 2. The elastic regime is limited since the specimen interface opened almost immediately due to the lubrication (Figure 4.14).

- **Stage 2:** After point 2, sliding friction governs the response. There is still geometrical interference while the key slides out of the top part from the imperfections and some remaining bonded areas at the interface that result in a stick-slip-like motion (Figure 4.15). This motion is characterized by periodic oscillations during frictional contact, caused by sudden brittle fracture of locked regions on surfaces in contact [22], and it can be the case for lubricated surfaces with a relatively low coefficient of friction. Diagonal cracks at the high-stress corner areas took place from point 3 onward, combined with the lateral opening of the top part (x-axis).

- **Stage 3:** After point 7, there is minimal contact area to resist the tensile forces, resulting in a major drop in force. A full pull-out happens at point 8.
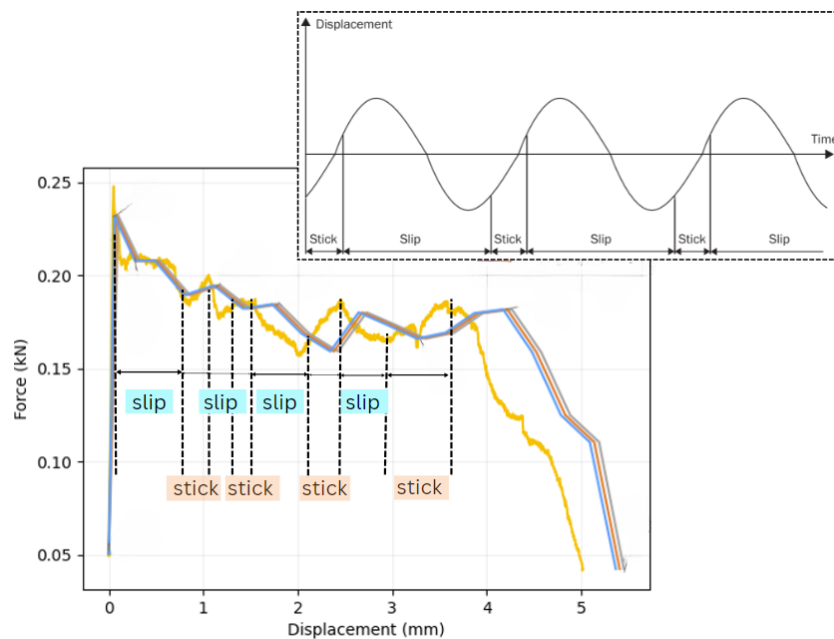
Figure 4.15: Stick slip behavior during the pull-out of SLG12 [22]

For this specimen category (straight keys, lubricated interface geometry 1), the failure modes of the identical specimens SLG11, SLG12, and SLG13 are presented in Figure 4.16. The failure modes were almost identical, with full translation/opening of all the keys. In the SLG11 specimen, failure of the edge of the key occurred.
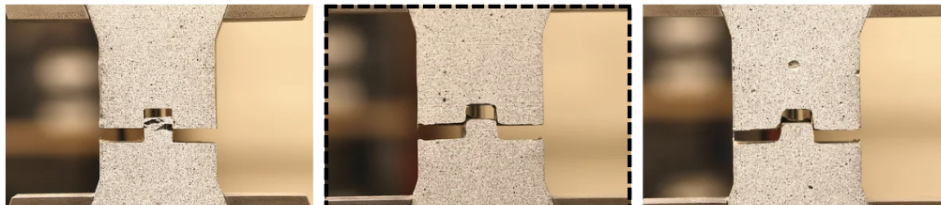
Figure 4.16: Failure modes of (a) SLG11, (b) SLG12 (analysed above), & (c) SLG13

Specimen SLG22- Lubricated Interface, geometry 2 (w/h=1.0)
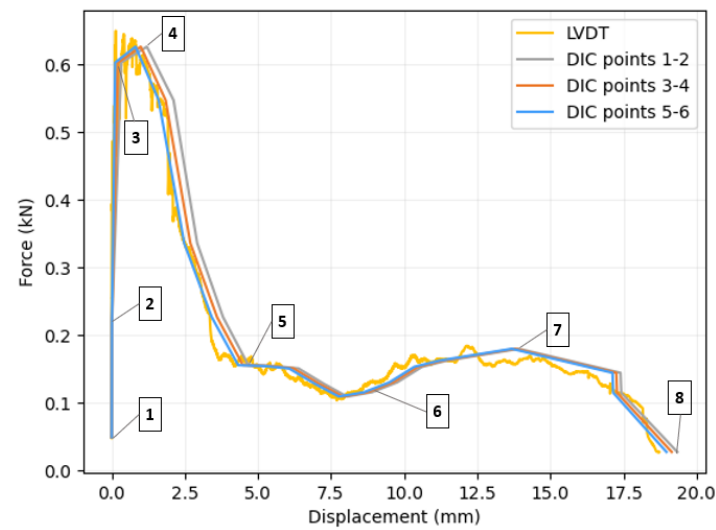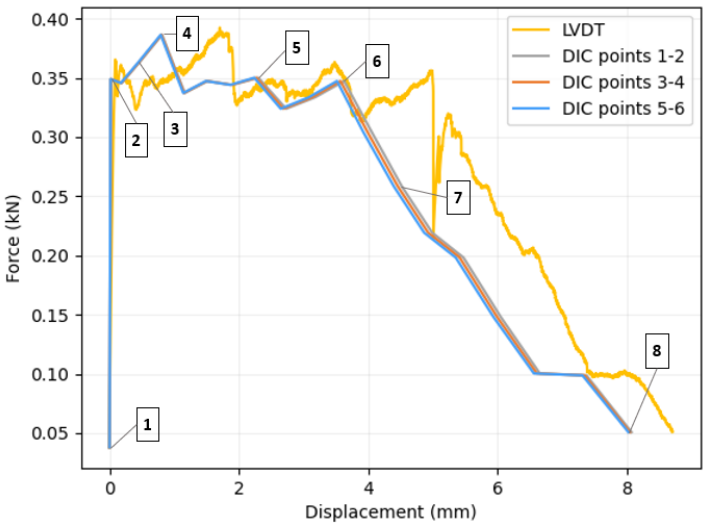

**Figure 4.17:** Force - displacement diagram illustrating the tensile response of the specimen SLG22
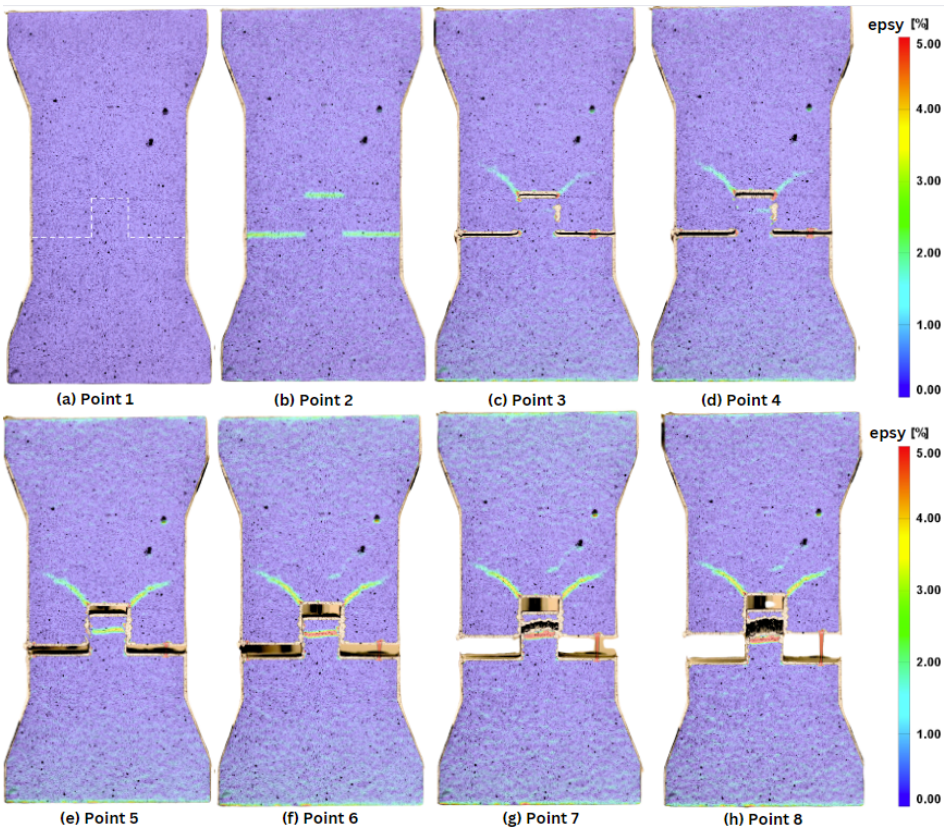
Figure 4.18: Strain contours (ϵ_y) of points 1-8

In Figure 4.17 the tensile response of a straight specimen with a lubricated interface and geometry 2 (w/h=1.5) is presented. This is the medium-length straight key. In the force-displacement graph similar stages as before are noted:

- **Stage 1:** From stages 1 to 2, the specimen interface opened almost immediately due to the lubrication, so the elastic regime is again limited.
- **Stage 2:** From point 2 onward, sliding friction governs the response. Unlike the smaller key, the maximum force is observed at that stage. During the sliding of the key, a crack forms at the key itself, close to the top edge (Figure 4.18). This was associated with dynamic friction phenomena (ploughing, stick-slip) and resulted in a peak force (0.38kN) at point 4. Cracks at the corners form at point 4 and propagate slowly until the end.
- **Stage 3:** From point 6 until the end, there is a strain-softening regime. The drop in force was drastic compared to the previous specimen. This can be explained by the further opening of the previous crack at the key, which decreased the area resisting the tensile forces. The top part of the key was separated, and it was not active anymore, leaving only the fibers to resist the pull-out.

For this specimen category (straight keys, lubricated interface geometry 2), the failure modes of the identical specimens SLG21, SLG22, and SLG23 are presented in Figure 4.19. The failure modes were rather similar, with full translation/opening of all the keys. For all of the specimens, failure of the edge of the key occurred.
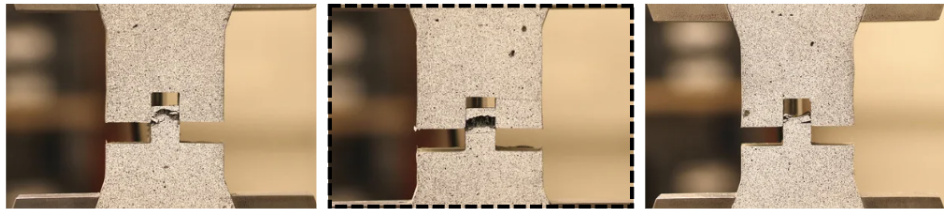
Figure 4.19: Failure modes of (a) SLG21, (b) SLG22 (analysed above), & (c) SLG23

Specimen SLG31- Lubricated Interface, geometry 3 (w/h=0.5
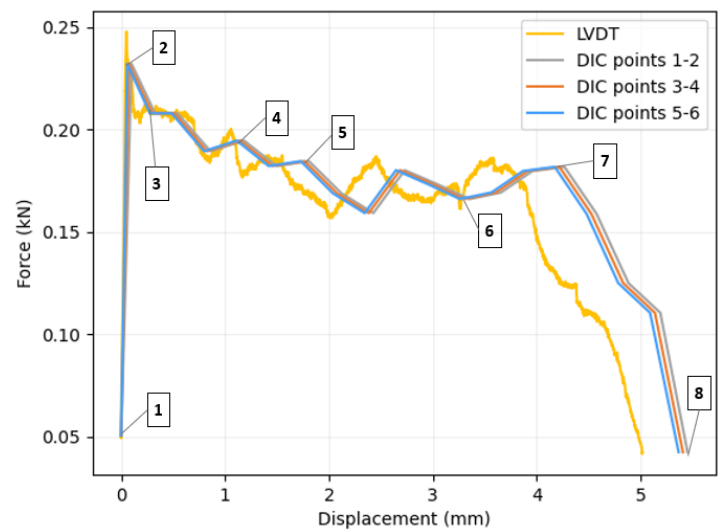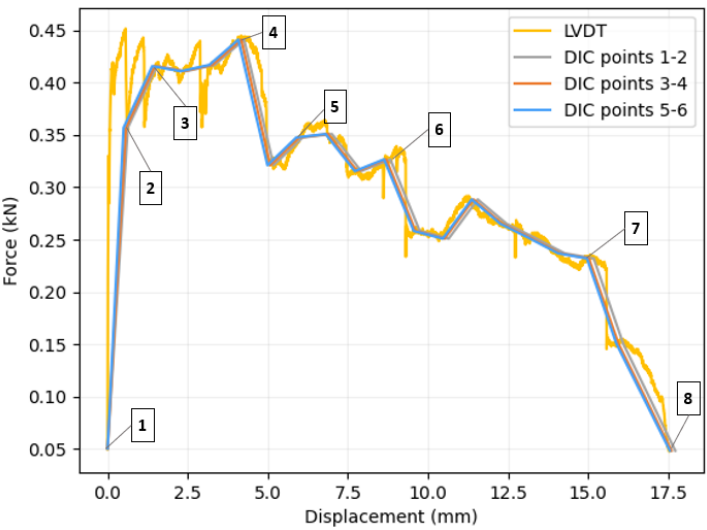

**Figure 4.20:** Force - displacement diagram illustrating the tensile response of the specimen SLG31
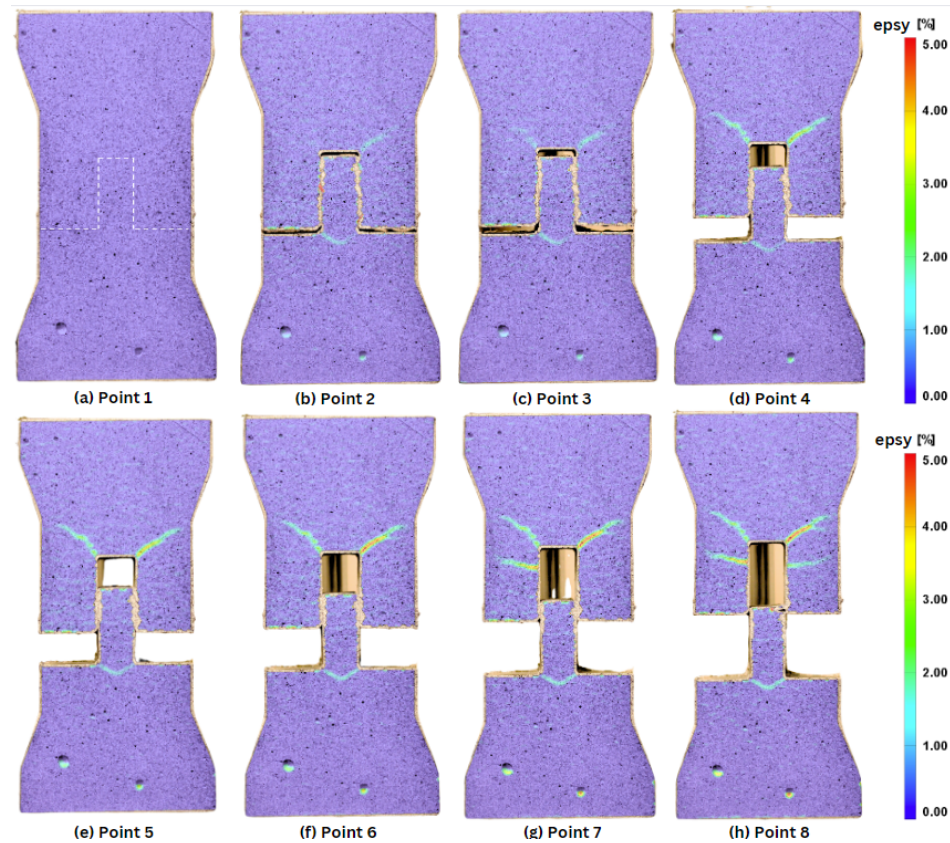
Figure 4.21: Strain contours (ϵ_y) of points 1-8

In Figure 4.20, the tensile response of a straight specimen with geometry 3 (w/h = 0.5) and a lubricated interface is analyzed. This is the larger straight key in length. Looking at the force-displacement graph, there are three characteristic stages.

- **Stage 1:** From points 1 to the onset of point 2, a limited elastic regime takes place. At point 2, the adhesion fails and the two parts open (Figure 4.21).
- **Stage 2:** Until point 4, there is an increase in capacity (peak force of 0.44 kN). The key, almost to its full length, resisted the tensile forces, resulting in a peak at point 4. Sliding friction still governs the response with stick-slip oscillations.
- **Stage 3:** From point 4 onward, there is a gradual loss in capacity related to the decreasing interface resisting the movement and the gradual pull-out. Apart from the characteristic cracks at the corners, where the stresses are high, additional cracks form at the sides of the top part as a result of the local stress concentrations and ploughing phenomena.

The overall cracking pattern of the specimen is symmetric, suggesting that the governing mechanism was uniaxial tension without noticeable bending interfering with the pullout. The deformations achieved were also high, comparable to the initial length of the key.

For this specimen category (straight keys, lubricated interface geometry 3), the failure modes of the identical specimens SLG31, SLG32, and SLG33 are presented in Figure 4.22. The failure modes were rather similar, with full translation/opening of all the keys. For specimens SLG31 and SLG32, failure of the very edge of the key occurred at the end of the analysis.
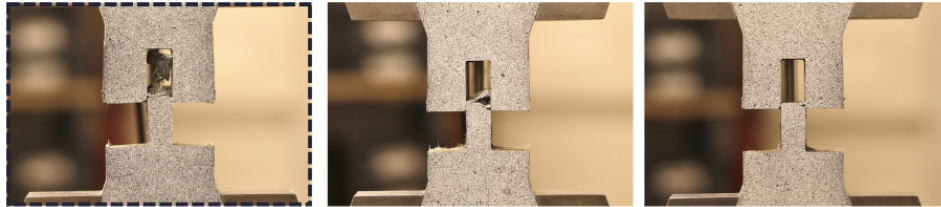
Figure 4.22: Failure modes of (a) SLG31 (analysed above) (b) SLG32, & (c) SLG33

4.2.2. Bistable Interlocked (curved) key specimens
Specimen CCG11- Untreated Interface, geometry 1 (R1/R2=1.05)
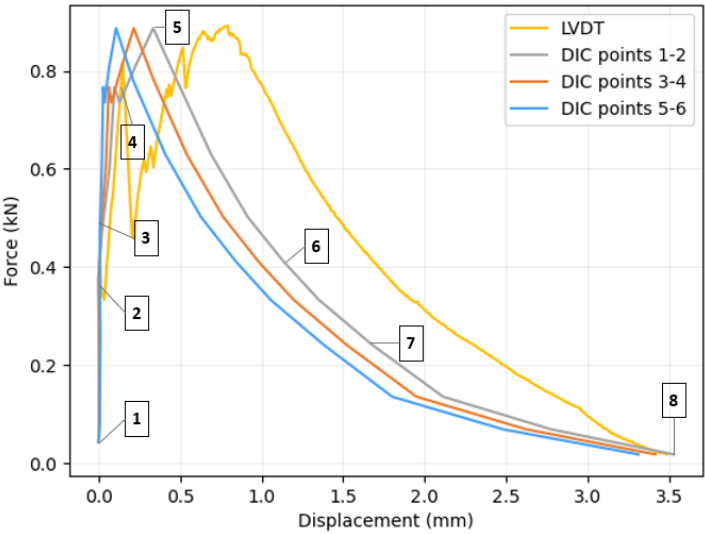
Figure 4.23: Force - displacement diagram illustrating the tensile response of the specimen CCG11
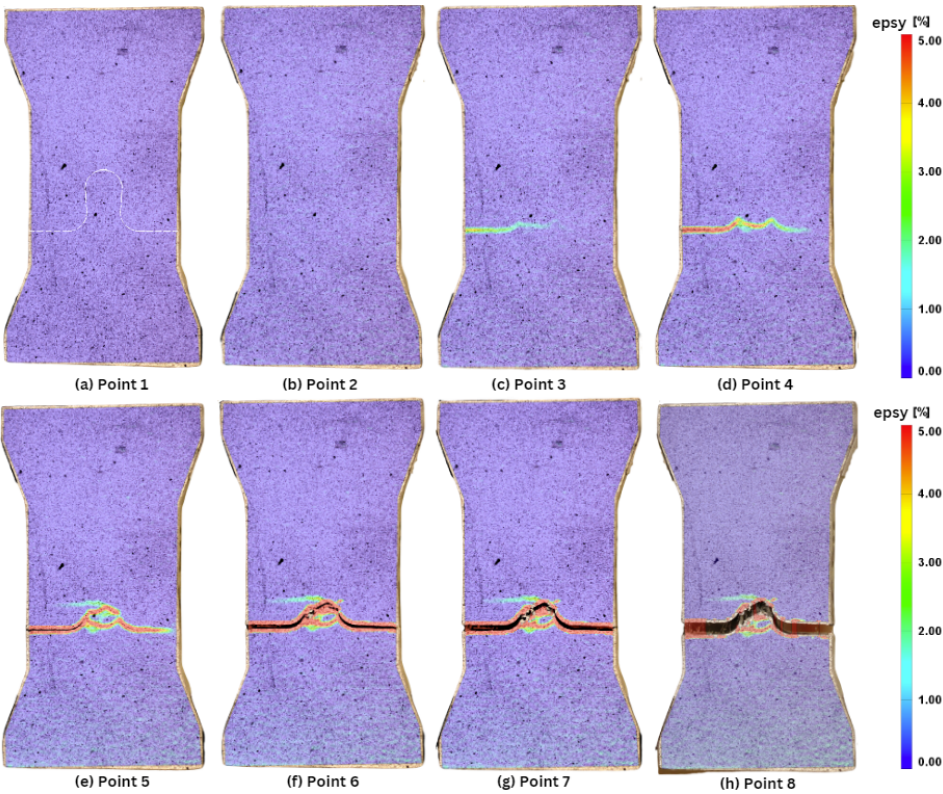
Figure 4.24: Strain contours (ϵ_y) of points 1-8

In Figure 4.23 the tensile response of a bistable interlocked (curved) specimen and untreated surface can be examined. The R_1/R_2 is 1.05; the key has the smallest length and radii ratio among the curved key specimens.

- **Stage 1:** From points 1-3, an elastic regime takes place. In comparison to the lubricated specimens mentioned earlier, the specimen behaves in a monolithic way due to its stronger bond at the interface; more time passes until permanent deformations take place. At point 3, the adhesion partially fails, and the two parts begin to open (Figure 4.24). The opening is happening from one side, suggesting the occurrence of bending. This is also visible from the rotation of the clamps in the pictures taken during DIC.
- **Stage 2:** After point 3, and as the tensile force increases, the force peaks at point 5 (0.887 kN). The interface has debonded, and cracking occurs at the neck of the key.
- **Stage 3:** The strain softening phase takes place after point 5 onward. The cracks at the neck of the key open further, and eventually key rupture occurs.

To give an idea of the remaining specimens in this category (curved keys, untreated surface geometry 1), the failure modes of the identical specimens CCG11, CCG12, and CCG13 are presented in Figure 4.25. The failure modes were almost identical, with key failure at the interface for all specimens.


Figure 4.25: Failure modes of (a) CCG11 (analysed above), (b) CCG12, & (c) CCG13

Specimen CCG22- Untreated Interface, geometry 2 (R1/R2=1.10)

Figure 4.26: Force - displacement diagram illustrating the tensile response of the specimen CCG22
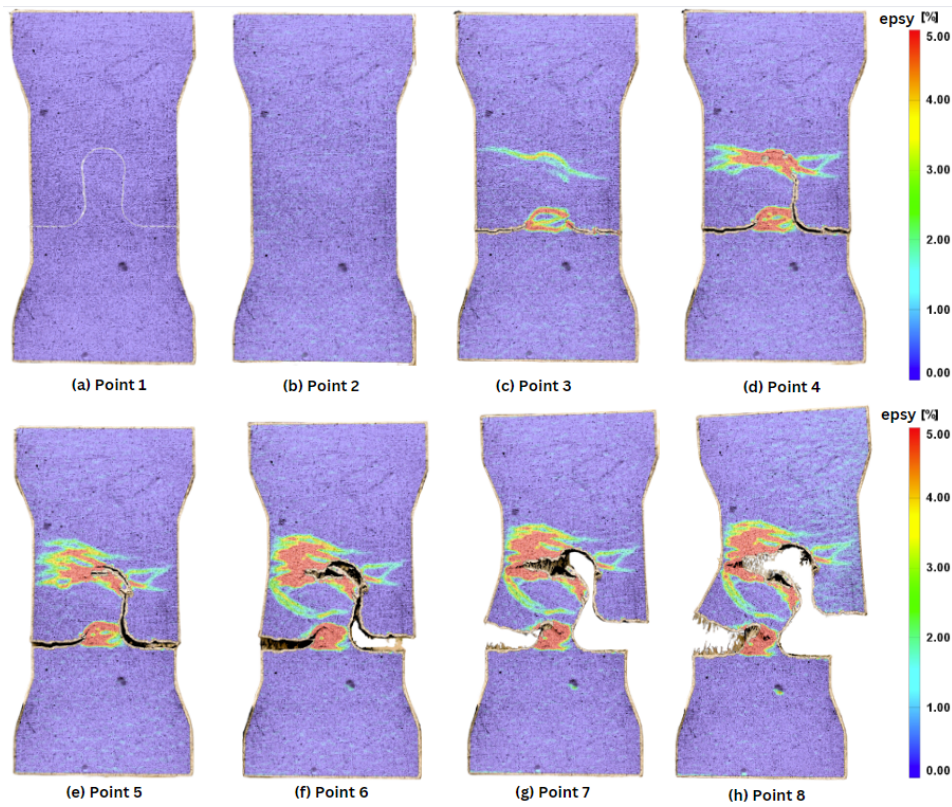
Figure 4.27: Strain contours (ϵ_y) of points 1-8

In Figure 4.26, the tensile response of a bistable interlocked (curved) specimen with an untreated interface can be examined. The R_1/R_2 is 1.10; the key has medium length among the curved key specimens.

- **Stage 1:** From points 1-2, an elastic regime occurs.
- **Stage 2:** After point 2, there is a small strain-hardening regime until point 4, where the force reaches a peak (0.99 kN). The interface has debonded already from point 3, and progressive cracking occurs at the neck of the key and the top (Figure 4.27). In point 3, there are two locations where the debonding is happening: one at the interface itself with cracking at the neck of the key, and one at the top of the key with cracks almost parallel to the interface. Until point 4, these cracks propagate, and more cracks are formed, hence the peak in resistance of the specimen.
- **Stage 3:** The strain softening phase takes place after point 4 onward. The right side of the key is debonded at the interface, but the left side is still bonded, resulting in the rotation of the top part around the bonded region. Due to in-plane bending, the cracks at the neck and left part are opening more, leading to failure (point 8).

In this category (curved keys, untreated surface geometry 2), the failure modes of the identical specimens CCG21, CCG22, and CCG23 are presented in Figure 4.28. The failure modes were fairly different. The specimen CCG21 showed initial debonding at the interface, but it failed at the interface. The specimen CCG22 opened only from one side, and the specimen CCG23 failed at the interface (key rupture).

**Figure 4.28:** Failure modes of (a) CCG21, (b) CCG22 (analysed above), & (c) CCG23

Specimen CCG31- Untreated Interface, geometry 3 (R1/R2=1.20)

**Figure 4.29:** Force - displacement diagram illustrating the tensile response of the specimen CCG31
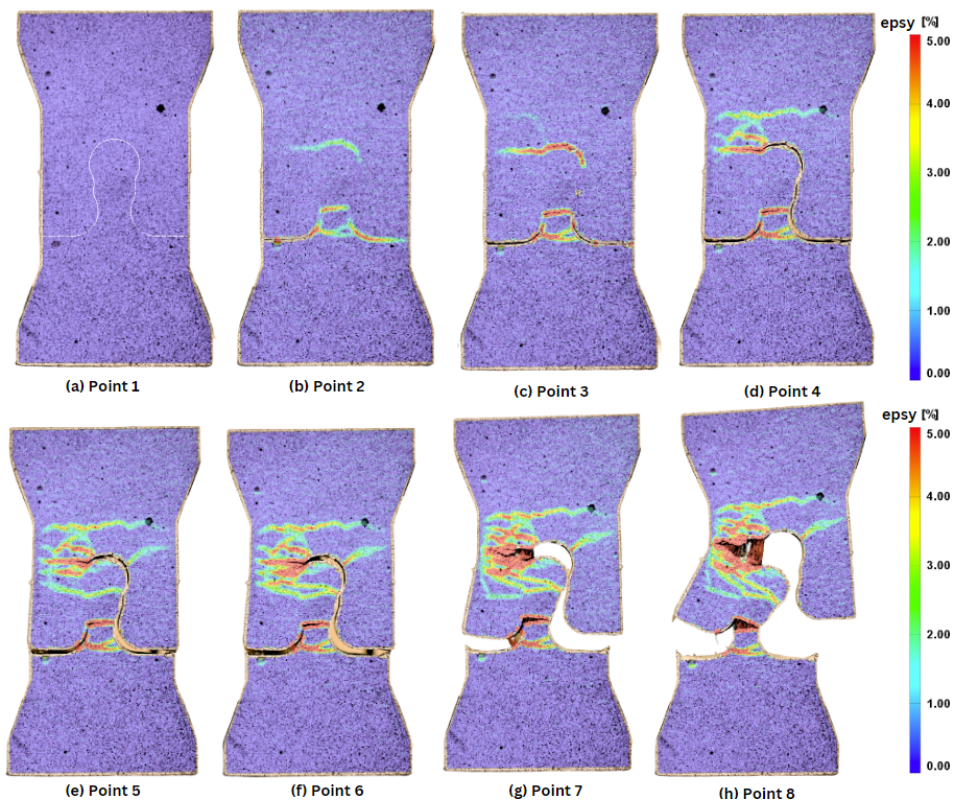
Figure 4.30: Strain contours (ϵ_y) of points 1-8

In Figure 4.29, the tensile response of a bistable interlocked (curved) specimen with an untreated interface can be examined. The R_1/R_2 is **1.20**; the key has the largest length among the curved key specimens.

- **Stage 1:** From points 1 to the onset of point 2, an elastic regime occurs. At point 2, the plastic deformation had already started with debonding and cracking at the interface.
- **Stage 2:** After point 2, there is a small strain-hardening regime until point 4, where the force reaches a peak (0.87 kN). Cracking occurs at the neck of the key and the left side of the top part in the meantime (Figure 4.30). Multiple cracks are forming at this stage.
- **Stage 3:** From points 4–6, a small plateau occurs. This stems from the formation of more cracks and the fiber bridging of SHCC resisting the pull-out.
- **Stage 4:** The strain softening phase takes place after point 6 onward. The right side of the key is debonded, and there is strain localization at the left part at the interface, but the left side is still bonded, resulting in the rotation of the top part around the bonded region. Due to in-plane bending, the cracks at the neck and left part open further, leading to failure (point 8).

In this category (curved keys, untreated surface geometry 2), the failure modes of the identical specimens CCG31, CCG32, and CCG33 are presented in Figure 4.31. The specimen CCG31 opened only from one side, the CCG32 key broke at the neck, and CCG33 experienced key failure at the interface.
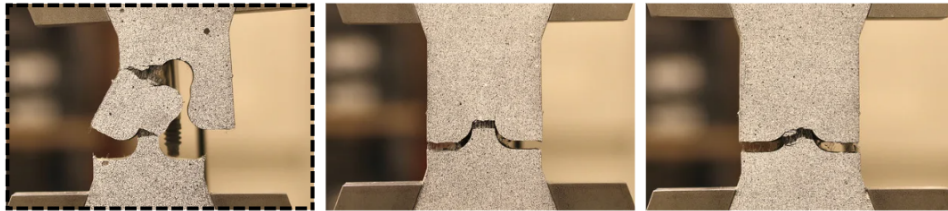
Figure 4.31: Failure modes of (a) CCG31 (analysed above), (b) CCG32, & (c) CCG33

Specimen CLG12- Lubricated Interface, geometry 1 (R1/R2=1.05)

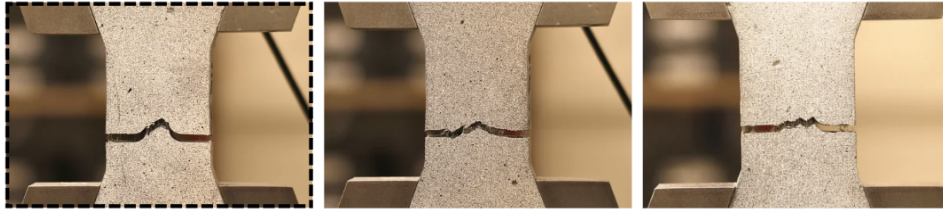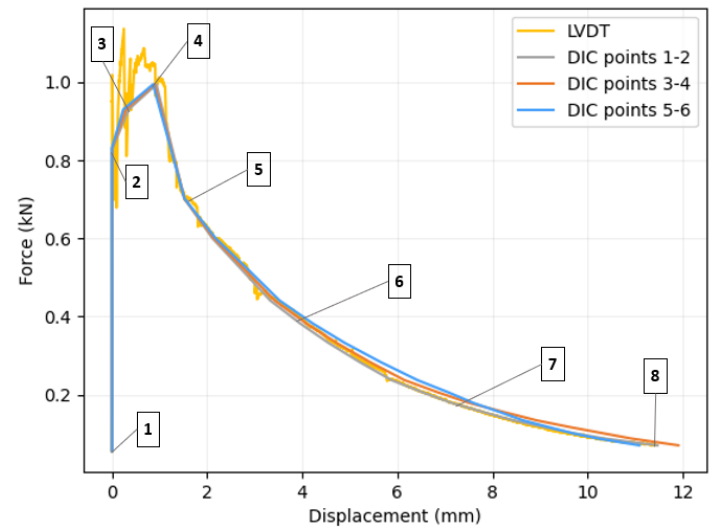**Figure 4.32:** Force - displacement diagram illustrating the tensile response of the specimen CLG12

Figure 4.33: Strain contours (ϵ_y) of points 1-8

In Figure 4.32, the tensile response of a bistable interlocked (curved) specimen with a lubricated interface is examined. The R_1/R_2 is 1.05; the key has the smallest length among the curved key specimens. In this type of specimen as seen in the literature [7], [58], the typical bistable curve takes place.

- **Stage 1:** As the tensile force increases, the pulling out of the tab is resisted by normal and frictional stresses at two pairs of contact points noted with black dots in Figure 4.33, point 3. Initially, a small elastic part can be identified until the onset of point 2. From points 2–5, a strain-hardening regime takes place, with the first peak at point 5. Immediately upon opening, cracks form at the high-stress locations of the neck, and diagonal cracks form radially at the top part. Until the pullout of the first radius R_2 more radial cracks occurred due to the lateral opening of the top part while the first radius was being pulled out. Additionally, parallel curved cracks to the top of the key formed at point 3 onward.
- **Stage 2:** Due to the bistable interlocked key's nature, the force drops after point 5 when the key approaches its second stable position, characterized by a local minimum on the curve. This is the second equilibrium position (point 6).
- **Stage 3:** After this, the force increases again with the same frictional contact mechanisms, while now only one pair of contact points resists the pull-out (noted with black dots in Figure 4.33 point 7). The second peak occurs at point 7.
- **Stage 4:** The strain softening phase takes place after point 7 onward, where the key just slides out with minimal friction at the contacting surfaces. At point 7, when the second radius R_1 was pulled out, the crack pattern was quite symmetrical, leading to a full pull-out without rupture of the key.

In this category (curved keys, lubricated interface geometry 1), the failure modes of the identical specimens CLG11, CLG12, and CLG13 are presented in Figure 4.34. The failure modes were almost identical, with full-key translation for all specimens.
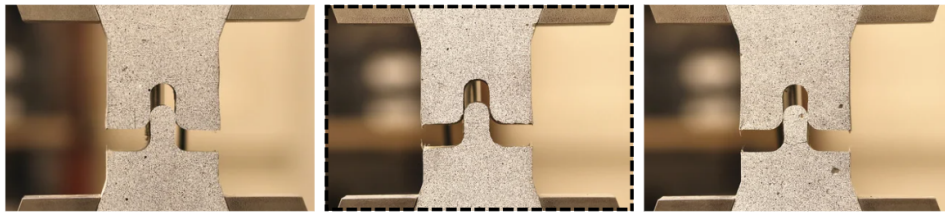
Figure 4.34: Failure modes of (a) CLG11, (b) CLG12 (analysed above), & (c) CLG13

Specimen CLG22- Lubricated Interface, geometry 2 (R1/R2=1.10)
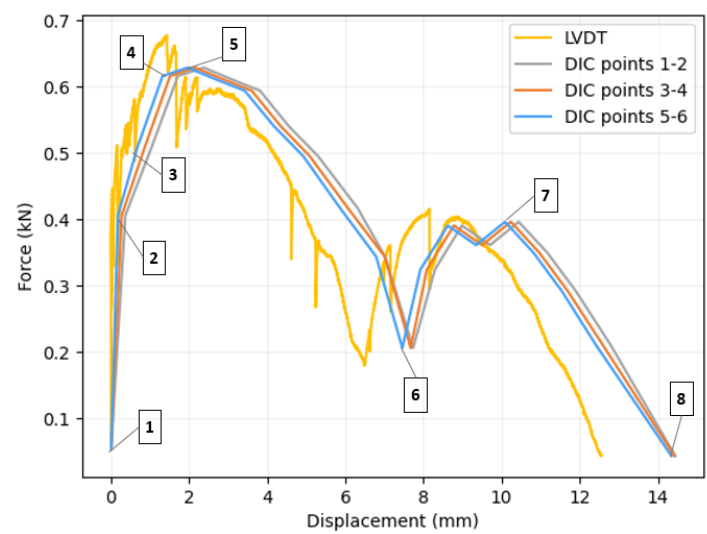
Figure 4.35: Force - displacement diagram illustrating the tensile response of the specimen CLG22
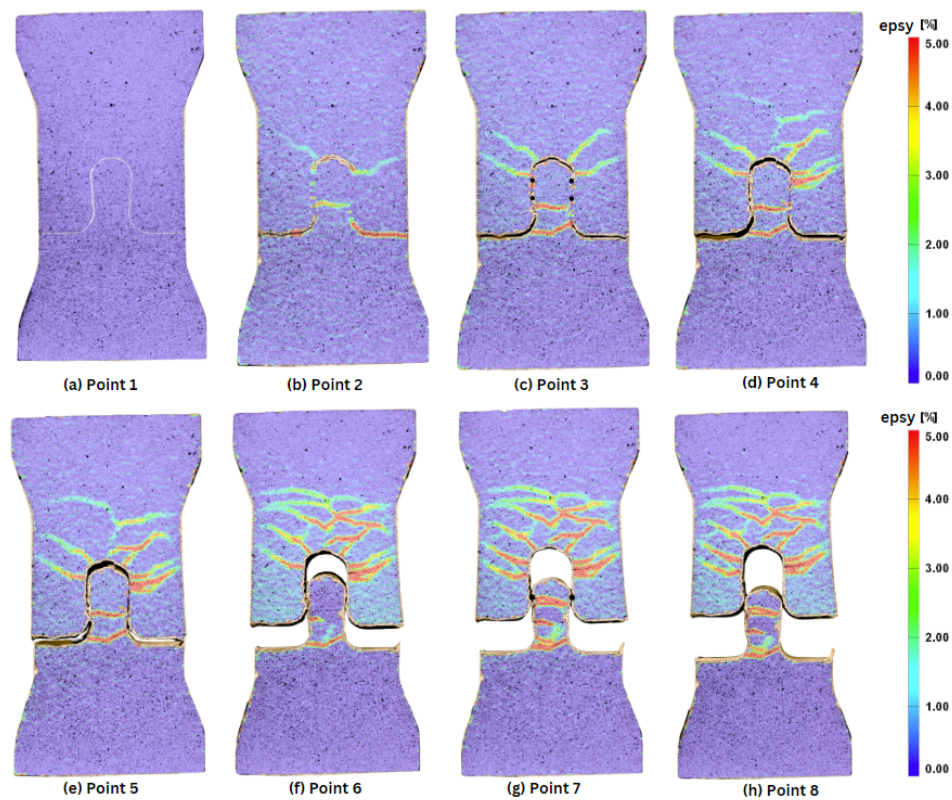
Figure 4.36: Strain contours (ϵ_y) of points 1-8

In Figure 4.35, the tensile response of a bistable interlocked (curved) specimen with a lubricated interface is examined. The R_1/R_2 is 1.10; the key has a medium length among the curved key specimens. In this type of specimen, as seen in the literature [7], [58], the typical bistable curve takes place.

- **Stage 1:** As the tensile force increases, the pulling out of the tab is resisted by normal and frictional stresses at two pairs of contact points noted with black dots in Figure 4.36, point 3. Initially, a small elastic part can be identified until the onset of point 2. At point 2, plastic deformation has already occurred. From points 2–5, a strain-hardening regime takes place, with the first peak at point 5. Immediately upon opening, cracks form diagonally at the high-stress locations of the neck and radially at the top part. Until the pullout of the first radius, more radial cracks occurred due to the lateral opening of the top part. Curved cracks parallel to the top of the key also occurred from point 4 onward.
- **Stage 2:** Due to the bistable interlocked key's geometry, the force drops after point 4 when the key approaches its second stable position, characterized by a local minimum on the curve. This is the second equilibrium position (point 6).
- **Stage 3:** After this, the force increases again with the same frictional contact mechanism, but now only one pair of contact points resists the pull-out (noted with black dots in Figure 4.36 point 7). The second peak occurs at point 7.
- **Stage 4:** The strain softening phase takes place after point 7 onward, where the key slides out with minimal friction at the contacting surfaces. At point 7, when the second radius was being pulled out, the crack pattern was quite symmetrical, leading to a full pull-out without rupture of the key.

The mechanism is the same as the aforementioned CLG12 key, but now the second curve peak is much smaller than the first. What is interesting is that until the end, new cracks were forming in a tortuous pattern without strain accumulation or damage to a specific part of the specimen. No major rotations or bending phenomena took place.

In this category (curved keys, lubricated interface geometry 2), the failure modes of the identical specimens CLG21, CLG22, and CLG23 are presented in Figure 4.37. The failure modes were almost identical, with full-key translation for all specimens.
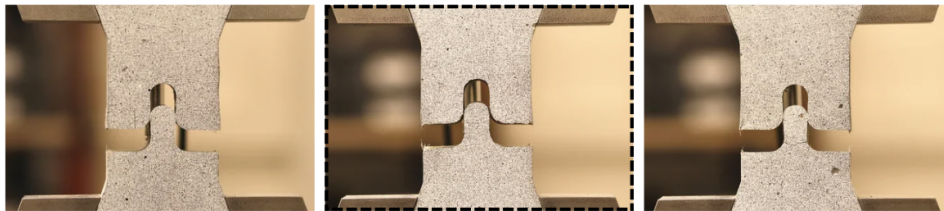
Figure 4.37: Failure modes of (a) CLG21, (b) CLG22 (analysed above), & (c) CLG23

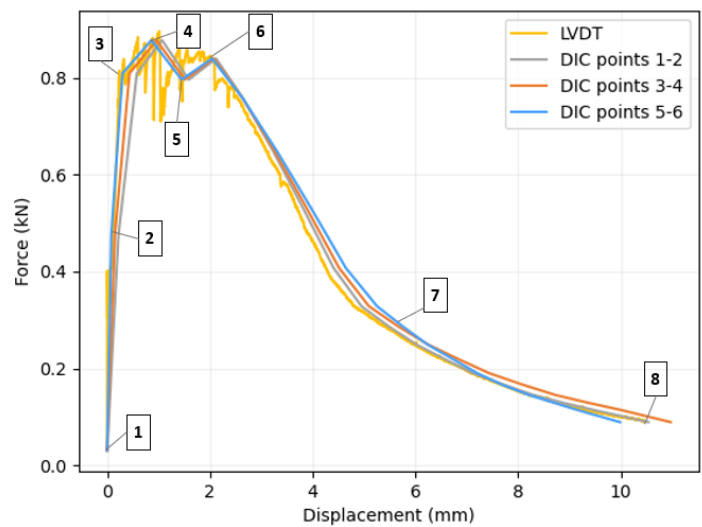**Specimen CLG31- Lubricated Interface, geometry 3 (R1/R2=1.20)**
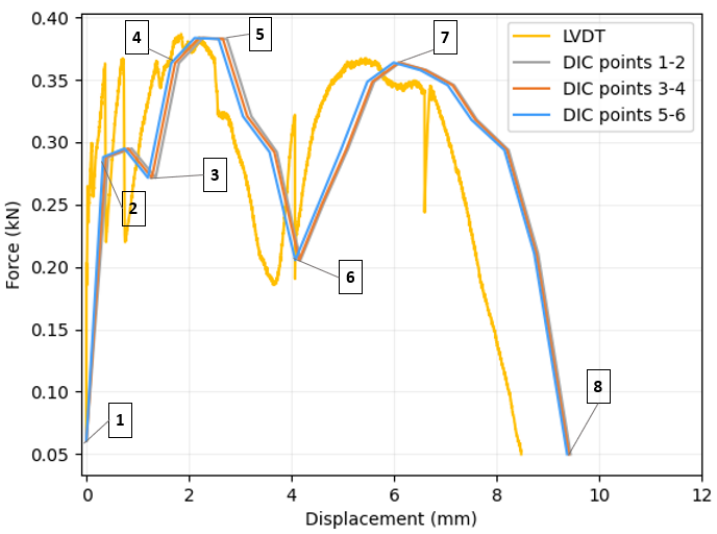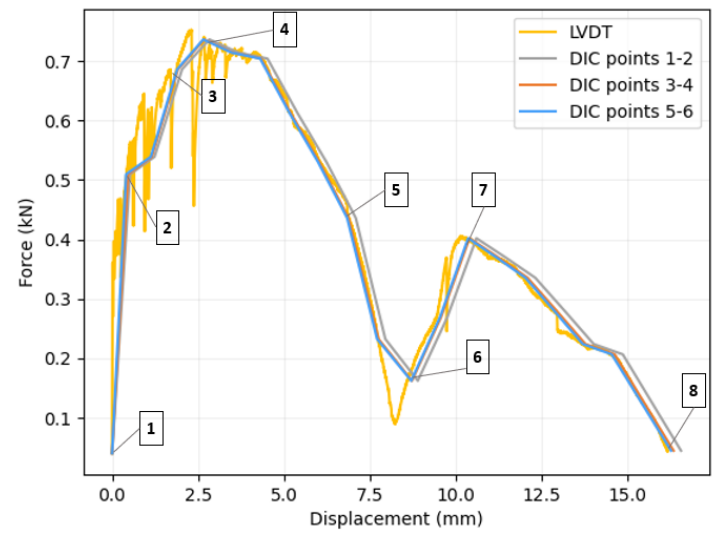

Figure 4.38: Force - displacement diagram illustrating the tensile response of the specimen CLG31
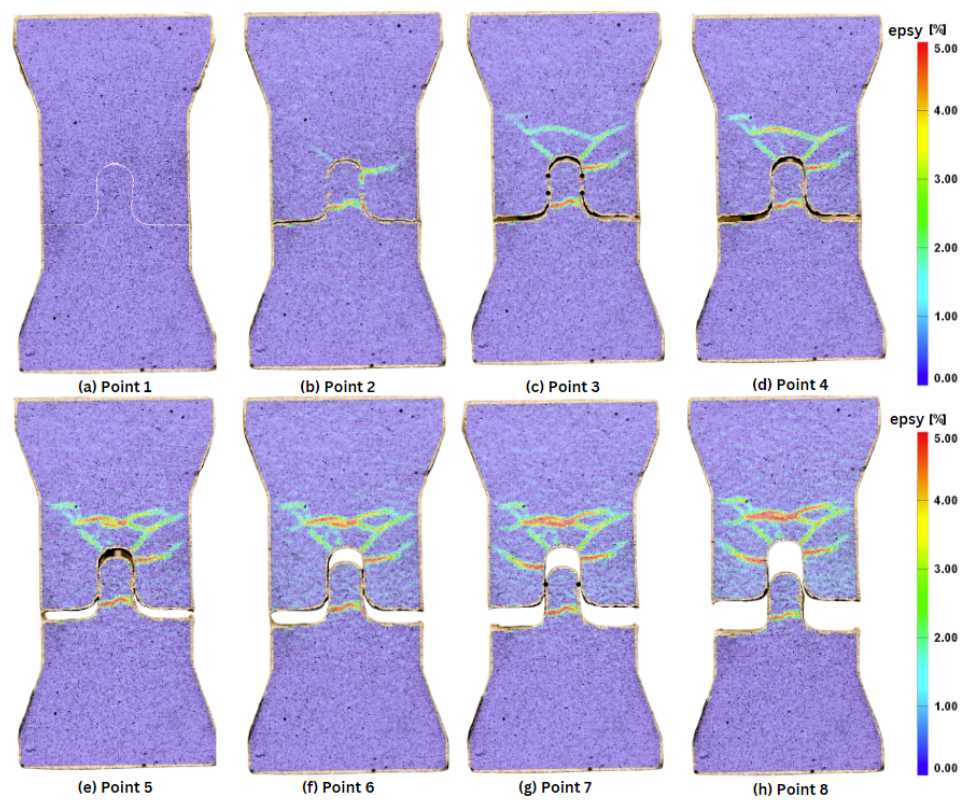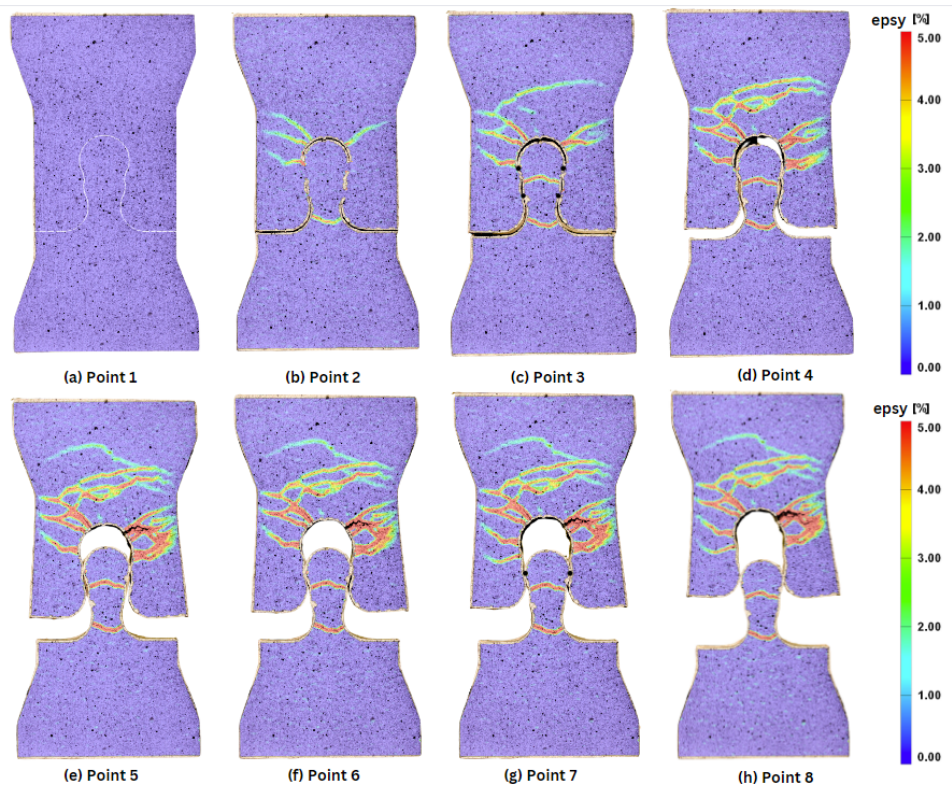

Figure 4.39: Strain contours (ϵ_y) of points 1-8

In Figure 4.38, the tensile response of a bistable interlocked (curved) specimen with a lubricated interface is examined. The R_1/R_2 is 1.20, and the key has the largest length among the curved key specimens. Again, as seen in the literature [7], [58], the typical bistable curve takes place.

- **Stage 1:** As the tensile force increases, the pulling out of the tab is resisted by normal and frictional stresses at two pairs of contact points (see Figure 4.39 point 3). A small elastic regime until the onset of point 2 takes place, followed by a strain-hardening regime, with the first peak at point 4. Immediately upon opening, cracks form diagonally at the high-stress locations of the neck and radially at the top part. Until the pullout of the first radius (point 6) additional radial cracks at the sides of the top part occurred due to the lateral opening of the top part. Parallel, curved cracks to the top of the key also formed from point 3 onward.
- **Stage 2:** Due to the bistable interlocked key's nature, the force drops after point 4 when the key approaches its second stable position, characterized by a local minimum on the curve. This is the second equilibrium position (point 6).
- **Stage 3:** After this, the force increases again with the same contact and friction mechanisms, but now only one pair of contact points resists the pull-out (noted with black dots in Figure 4.39 point 7). The second peak occurs at point 7.
- **Stage 4:** The strain softening phase takes place after point 7 onward, where the key slides out with minimal friction at the contacting surfaces.

A characteristic difference now in comparison to the previous keys is that, due to the high radii ratio and geometrical interference, there is strain localization at the right side of the top part (in red) from point 5 onward. The lateral opening of the top part and the reduced pressure at the interface weaken the frictional contact mechanism. This leads to a much smaller second peak (point 7). Regardless, the key still fully translates (point 8) without rupturing.

In this category (curved keys, lubricated interface geometry 3), the failure modes of the identical specimens CLG31, CLG32, and CLG33 are presented in Figure 4.40. The failure modes were almost identical, with full-key translation for all specimens. As stated before, large cracks laterally at the top part were noticed.

Figure 4.40: Failure modes of (a) CLG31 (analysed above), (b) CLG32, & (c) CLG33

Specimen CPG32- "Assembled" Interface, geometry 3 (R1/R2=1.20)
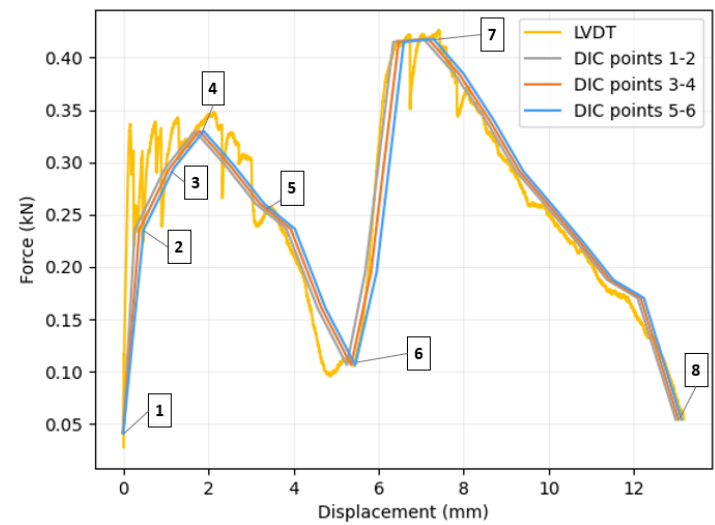
Figure 4.41: Force - displacement diagram illustrating the tensile response of the specimen CPG32

(a) Point 1   (b) Point 2   (c) Point 3   (d) Point 4

(e) Point 5   (f) Point 6   (g) Point 7   (h) Point 8
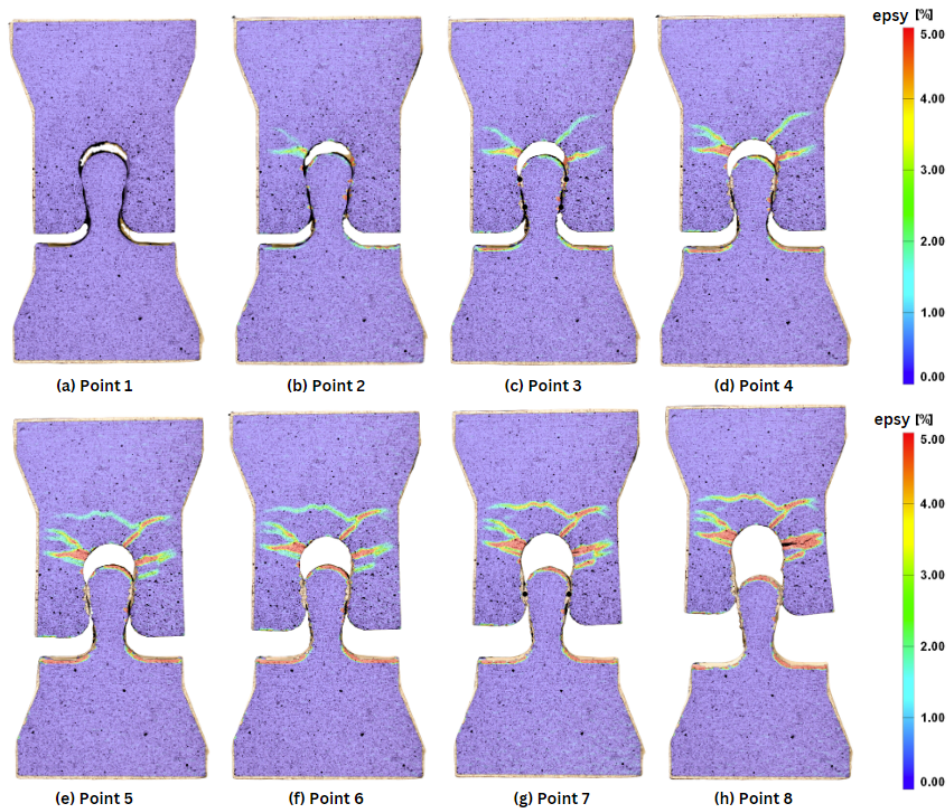
Figure 4.42: Strain contours (ϵ_y) of points 1-8

In Figure 4.41, the tensile response of a bistable interlocked (curved) specimen with an out-of-plane assembled interface is examined. For this special case, the R_1/R_2 was chosen as 1.20, the largest length among the curved key specimens.

- **Stage 1:** As the tensile force increases, the pulling out of the tab is resisted by normal and frictional stresses at **two pairs** of contact points (noted with black dots in Figure 4.42 - point 3). A strain-hardening regime takes place initially, with the first peak at point 4. Immediately upon opening, cracks form at the high-stress locations radially at the top part. This time there are no cracks at the neck of the specimen due to the large manufacturing tolerances, providing relief of stresses for the pulling of the first radius.

- **Stage 2:** Due to the bistable interlocked key's nature, the force drops after point 4 when the key approaches its second stable position, characterized by a local minimum on the curve. This is the second equilibrium position (point 6). Until the pullout of the first radius R_2 (point 6) more radial cracks at the sides of the top part occur due to the lateral opening of the top part. Parallel, curved cracks to the top of the key also occurred from point 5 onward.

- **Stage 3:** After this, the force increases again with the same contact and friction mechanisms, but now only **one pair** of contact points resists the pull-out (see Figure 4.42 point 7). The second peak occurs at point 7. The two parts were assembled in the out-of-plane direction, and due to the clearance at the initial stages, most of the cracking propagation occurred after point 6. This led to a higher second peak.

- **Stage 4:** The strain softening phase occurs after point 7 onward, where the key gradually slides out. The crack pattern was quite symmetrical until point 8, where the lateral crack on the right side opened further due to the tensile forces, leading to a full pull-out without rupture of the key.

For the rest of the specimens in this category (curved keys, assembled interface int the OP direction geometry 1), the failure modes of the identical specimens CPG31, CPG32, and CPG33 are presented in Figure 4.43. The failure modes were almost identical, with full-key translation for all specimens. Additionally, large cracks formed laterally at the top part were noticed.
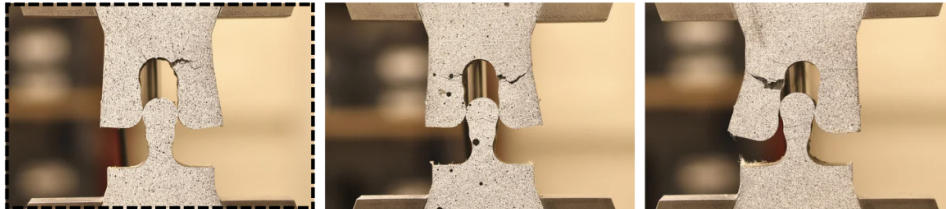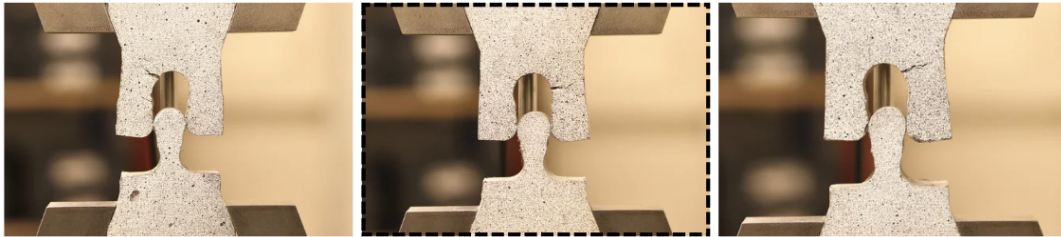

Figure 4.43: Failure modes of (a) CPG31, (b) CPG32 (analysed above), & (c) CPG33

<div style="text-align: right; font-size: 4em;">5</div>

Discussion

In this chapter, a *parametric analysis* is going to be performed to explore the behavior of interlocking keys in SHCC and answer the relevant research questions. The investigated parameters are the **geometry/length** of the key, the **interface treatment** related to the interfacial bond, the **shape** (straight or bistable interlocked), and the **material** the key is made of (SHCC or mortar).

To further comprehend the influence of each of the aforementioned parameters, one parameter is going to change at a time, and the response is going to be evaluated based on that. The evaluation will be performed with the help of key performance indicators. These are the **peak force** and the area under the force-displacement graph, representing the **energy absorbed** by the specimen before failure. Some other parameters to evaluate the response are the pattern, shape, and location of the formed cracks.

5.1. Influence of the key geometry at the tensile response

5.1.1. Straight key specimens- Influence of w/h

To comprehend the impact of key geometry on the tensile response, straight keys with varying width-to-height ratios were examined. As stated before, a consistent interface treatment was maintained to isolate the influence of the geometry. The straight key specimens, featuring distinct color-coded geometries, are presented in Figure 5.1. More information about the three geometries is described in Figure 3.5. The initial length of each geometry is prescribed with vertical lines of the same color to highlight the specimen deformation before failure or translation in comparison to its original form. An overview is given in Figure 5.2, where the force is divided by the cross-sectional area of the specimen and the displacement is divided by the key length. Normalizing the force with the cross-sectional area and the displacement with the length of the key provides a dimensionless measure that allows for better comparison between specimens of different key sizes.

Untreated Keys

The first observation regarding the **untreated keys** (Figure 5.1a) is that specimens of geometry 1 (smaller keys) and geometry 2 (medium keys) show similar trends. As seen in Chapter 4, Figure 4.9 geometry 2 specimens resulted in key failure at the interface. Hence, their length did not significantly affect the response and they behaved similarly to G1. Geometry 3 (larger keys) showed a counter-intuitive result: Although the longer length would increase the possibility of key failure at the interface, most of the keys fully opened. This resulted in the plateau in Figure 5.1a ranging at displacements of 5 to 18 mm. If the G2 keys underwent full translation similarly to the G3 keys without experiencing failure at the interface, they were expected to exhibit a comparable yet reduced plateau. The resistance force is similar (≈ 1.0 kN) for most of the keys except for some extreme cases that reached around 1.5–1.6 kN. These cases are unrelated to geometry but are associated with hardening due to bending or torsion. The combined action of numerous fibers activated during bending or torsion contributes to an increase in the material's effective tensile strength. In terms of displacement magnitude, G1 and G2 behave similarly, with a displacement of approximately 5mm. Geometry 3, due to the aforementioned plateau, reached displacements of approximately 18 mm, comparable to its initial length.

Lubricated Keys

For the case of **lubricated keys** (Figure 5.1b), the trend of the curves is similar for geometry 1, 2, and 3, showing a rather uniform response proportional to their geometry. The peak force extracted is ≈ 0.35 kN for all of the keys, regardless of their length. The displacement reached is proportional to each key's length; this is obvious from the vertical reference-length lines.
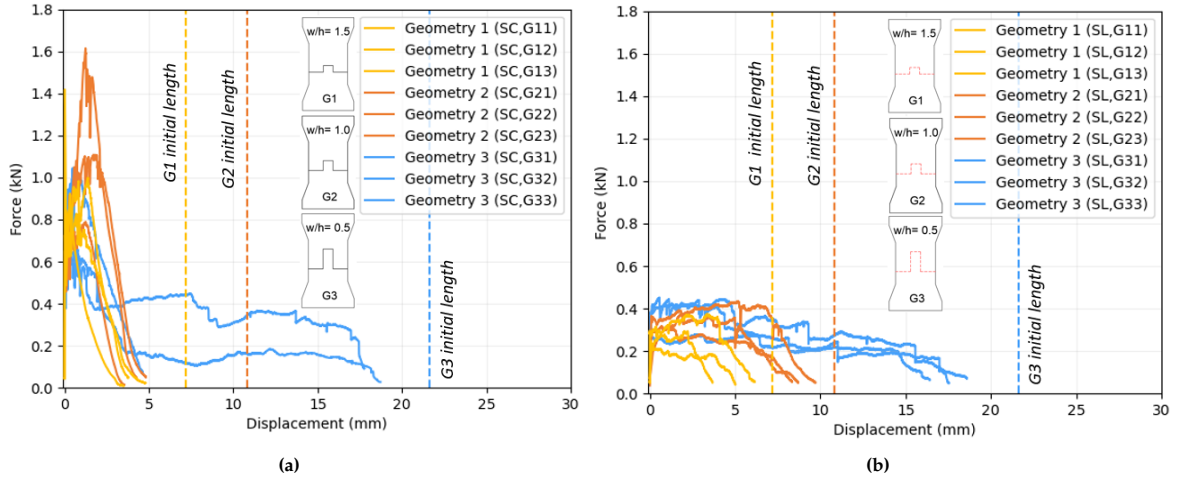
Figure 5.1: Force-displacement diagrams for *straight* key specimens with (a) untreated and (b) lubricated interface

In the traction-normalized displacement graph (Figure 5.2), the x-axis shows the fraction of displacement compared to the original key length. In Figure 5.2a, it is shown that the performance of the untreated keys is case-specific and variable. Since many specimens showed interface failure, they could not reach their full potential. In Figure 5.2b, it is obvious that most of the lubricated straight specimens reached almost **80-90**% of their initial length in displacement. Their performance is more uniform in terms of strength and ductility than that of the untreated specimens.
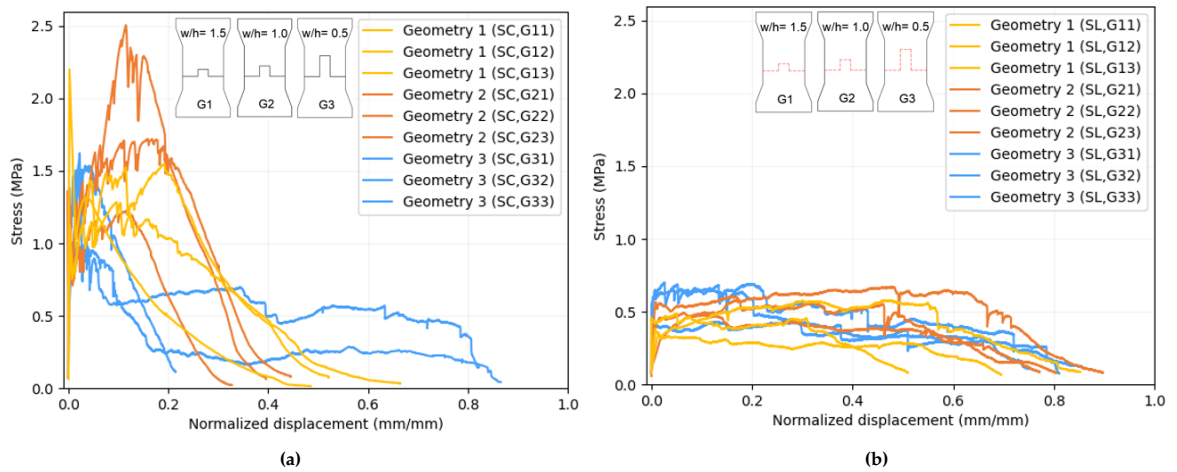
Figure 5.2: Stress - normalized displacement (u/L) diagrams for *straight* key specimens with (a) untreated and (b) lubricated interface

The averaged results of the key performance indicators (peak force and absorbed energy) are displayed in Table 5.1 for *untreated keys* and Table 5.2 for *lubricated keys*. The energy absorbed by the specimens was calculated as the area under the force-displacement graph.

For the untreated keys (Table 5.1), there is a small increase in force along the increase in geometry from G1 → G2 and a small decrease for G2 → G3 keys. The area under the graph is increasing along the increase in length from G1 → G2 → G3. As mentioned above, G2 showed the highest peak force values, and G3 showed the highest energy absorption (due to the plateau in the force-displacement graph).

Table 5.1: Averaged values of peak force and energy (as the area under the f-d graph), for straight untreated specimens (SC)

SC specimens	Peak force (kN)	St.Dev.	Energy (kN*mm)	St.Dev.
SCG1	1.08	0.30	1.57	0.39
				+51.9 %
SCG2	1.20	0.37	2.67	1.08
				+41.3 %
SCG3	0.90	0.21	4.06	2.11

For the lubricated keys (Table 5.2) there is a small increase from G1 → G2 in peak force, and the force remains the same as the geometry further increases to G3. The area under the force-displacement graph is increasing along the increase in length from G1 → G2 → G3 (as seen in Figure 5.1b). Geometry 3 has the best performance in peak force and energy absorbed.

Table 5.2: Averaged values of peak force and energy (as the area under the f-d graph), for straight lubricated specimens (SL)

SL specimens	Peak force (kN)	St.Dev.	Energy (kN*mm)	St.Dev.
SLG1	0.31	0.06	1.11	0.48
				+75.3 %
SLG2	0.38	0.06	2.45	0.64
				+59.4 %
SLG3	0.38	0.09	4.52	0.72

5.1.2. Bistable interlock (curved) key specimens- Influence of R1/R2

To examine the impact of key geometry on the tensile response of the curved keys, varying radii ratios were examined. A consistent interface treatment was maintained to isolate the influence of key geometry. The specimens, featuring distinct color-coded geometries, are presented in Figure 5.3. More information about the three geometries of curved keys is shown in Figure 3.2. The initial length of each geometry is prescribed with vertical lines of the same color in Figure 5.3. This can show how much the specimen has deformed before failure or translation compared to its initial state. A clearer visualization of the relative deformation is seen in Figure 5.6. In Figure 5.6, the force was divided by the cross-sectional area of the specimen responsible for transferring forces and the displacement by the key length to provide a dimensionless measure between different specimens.

Untreated Keys

In the case of the **untreated keys** (Figure 5.3a) the trends of the curves of different geometries are similar. The curves are characterized by a peak force at approximately 1.0 kN, and a rather steep strain softening regime post-peak. Regarding displacement magnitude, the untreated keys have a similar response without any obvious size-displacement connection. This was associated with the fact that most keys failed at the interface (chapter 4 Figure 4.25, Figure 4.28, Figure 4.31) hence not utilized their full potential to obtain large deformations. Most of the specimens reached displacements in the 3–5 mm range. Some keys showed partial debonding (from one side), thus utilizing their ductility more efficiently, resulting in a gradual strain-softening regime.

Lubricated Keys

The **lubricated keys** are shown in Figure 5.3b. There, the trend of the curve followed the bistable interlock mechanism. Two peaks and two equilibrium positions were noted, as seen in the literature [7], [58]. The first peak was always higher than the second for all of the specimens. While the first radius was being pulled out, the top part underwent cracking (drops in force in Figure 5.3b) and plastic deformation (lateral opening at the x-axis). These phenomena led to a reduction of pressure at the interface and contributed to a smaller second peak (Figure 5.4). The second equilibrium position is located at the kink on the curve where the interlocking occurs. This location is dependent on the geometric characteristics of the system. After the kink, the second, smaller peak takes place, and the full pull-out follows. This whole process is presented in Figure 5.5.
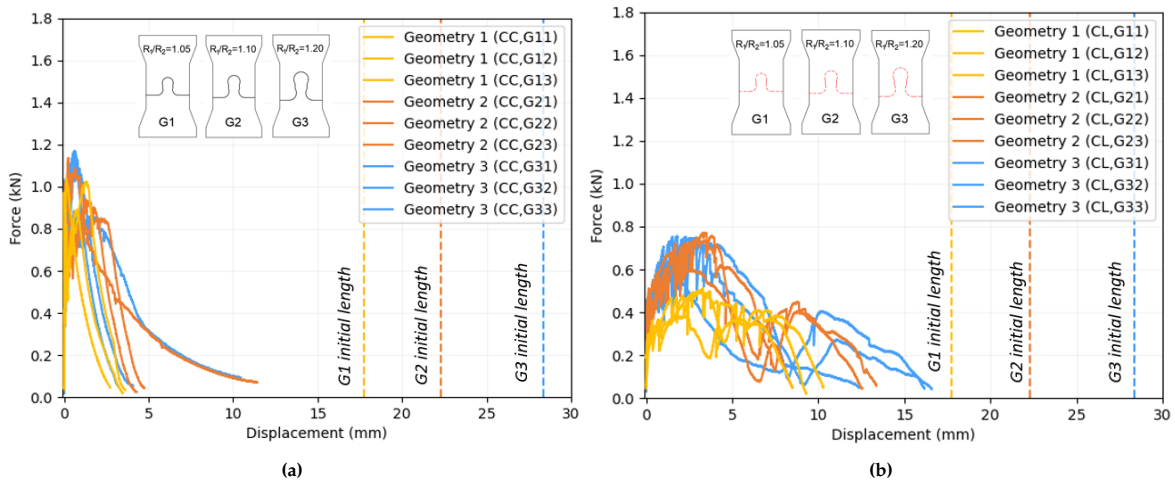
Figure 5.3: Force-displacement diagrams for *curved* key specimens with (a) untreated and (b) lubricated interface
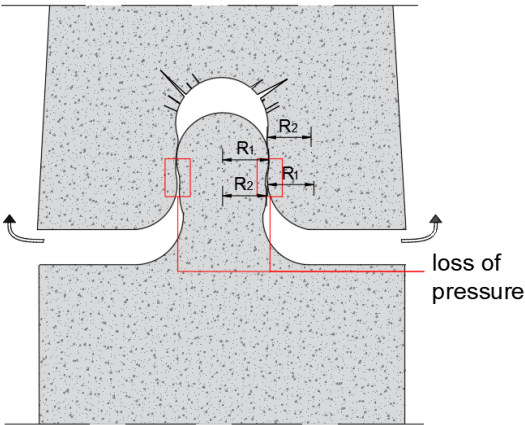
Figure 5.4: Schematic representation of the loss of pressure phenomenon taking place after the second equilibrium position in a bistable interlocked SHCC specimen
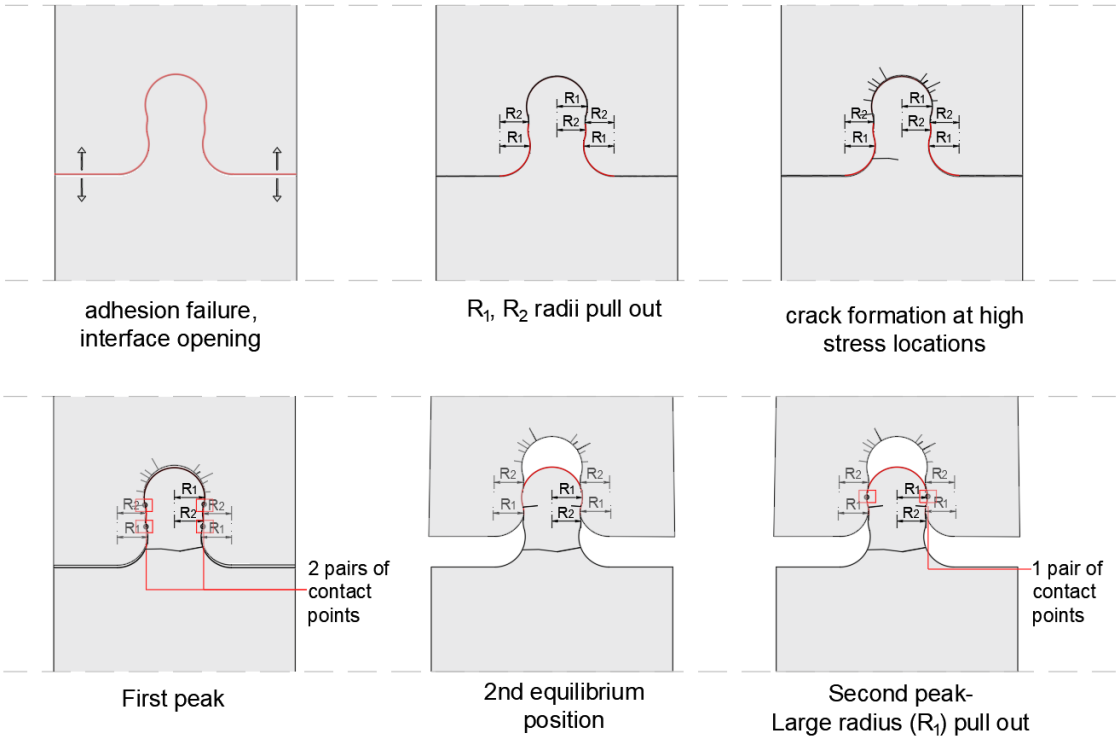
Figure 5.5: Schematic representation of the stages taking place during the pullout of the curved specimens

In Figure 5.6, the curved keys (untreated and lubricated) do not reach more than 60% of displacement compared to their original length. Many of the untreated keys specifically showed interface failure; hence, their displacements were limited (20-50%). This is expected considering the complexity of the double-curved interface combined with the strong bond at the interface. For the lubricated keys, while the top part was being pulled out, plastic deformation and cracking reduced the pressure at the interface, as mentioned before. Additionally, the top part of R_1 slides out immediately after the second peak in force (see Figure 5.7). These phenomena led to displacements of only 40-60% of their original key length.

These results can be compared with the ones found in the literature. As seen in [7], bistable geometries were made out of ABS. Under monotonic pullout, a perfectly elastic behavior was achieved. Even in that case, the keys (R_1/R_2=1.05) reached approximately 45% of their initial length (Figure 5.8). The SHCC specimens of the same geometry reached a 50-60% normalized displacement. The difference between ABS and SHCC displacement values is attributed to the elongation of the SHCC keys.

Additionally, for the SHCC specimens, the second peak is lower than the first due to the extensive cracking and loss of stiffness that occurred at the first peak. This is not the case in [7], where the material used was ABS and the specimens stayed in the elastic regime until the full pullout (Figure 5.9). In such a case, the second peak was higher.
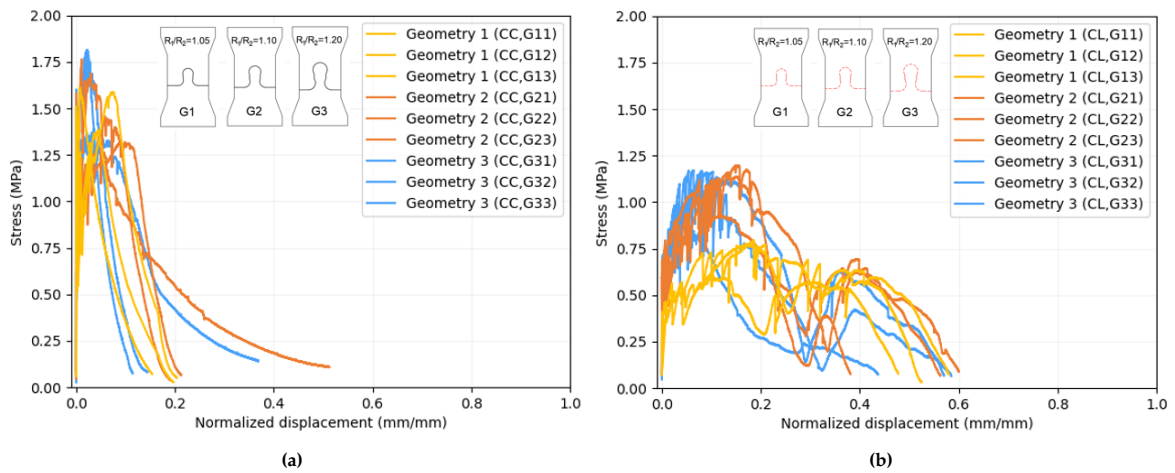
Figure 5.6: Stress - normalized displacement (u/L) diagrams for *curved* key specimens with (a) untreated and (b) lubricated interface
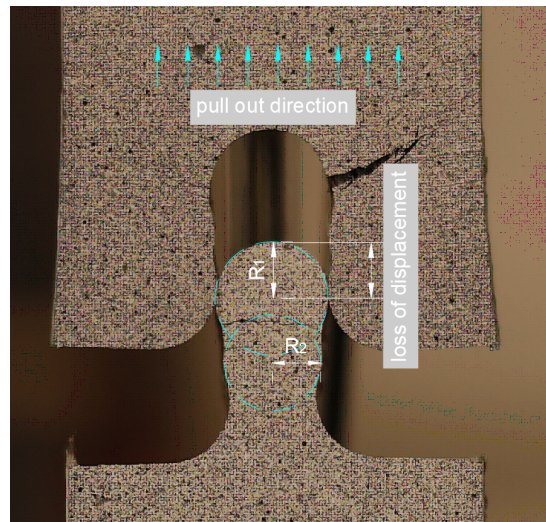
Figure 5.7: Loss of displacement of approximately R1 magnitude in curved key at the end of analysis
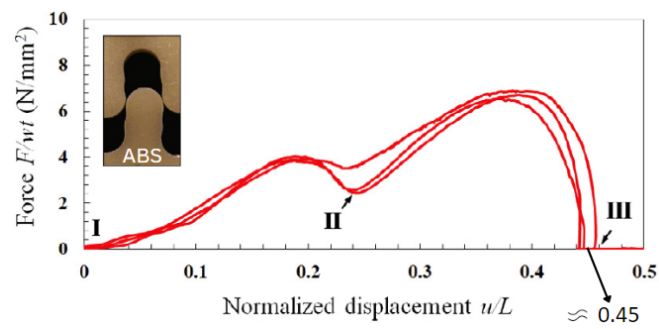
Figure 5.8: Normalized displacement of ABS specimens with $R_1/R_2 = 1.05$ [7]
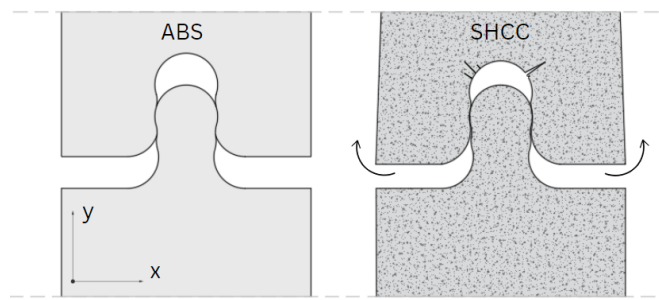
Figure 5.9: Elastic versus plastic deformation of bistable interlocks at the second equilibrium position in ABS and SHCC

In Table 5.3, the averaged values of peak force and absorbed energy are presented for the untreated keys. While increasing the R_1/R_2 ratio (G1 → G2 → G3), the force does not significantly alter. The area under the graph increases along the increase in length from G1 → G2 (64.9%) and then slightly decreases for G3. No geometry combines the best energy and peak force values, a fact attributed to the varying failure modes that the untreated specimens developed due to the strong interfacial bond. In terms of peak force, G3 performs the best, while in terms of absorbed energy, G2 has the highest absorption.

Table 5.3: Averaged values of peak force and energy (as the area under the f-d graph), for curved untreated specimens (CC)

CC specimens	Peak force (kN)	St.Dev.	Energy (kN*mm)	St.Dev.
CCG1	0.98	0.08	1.51	0.47
			+ 64.9 %	
CCG2	0.98	0.15	2.96	0.85
CCG3	1.07	0.15	2.61	1.24

In Table 5.4, the averaged values of peak force and absorbed energy are presented for the lubricated keys. The increase in R_1/R_2 ratio from G1 → G2 resulted in a force increase of 43.33 %. For G2 → G3, there is no significant change. The area under the graph shows a similar trend, with a significant increase in area (35.7%) from G1 → G2 and a small increase for G2 → G3. As it appears, a *threshold* for the increase of R_1/R_2 exists. An increase in geometry G1 → G2 is beneficial regarding force and energy absorption, while a further increase in G2 → G3 does not add more to the tensile response. G2 performs the best among the lubricated keys when it comes to force and G3 when it comes to energy.

Table 5.4: Averaged values of peak force and energy (as the area under the f-d graph), for curved lubricated specimens (CL)

CL specimens	Peak force (kN)	St.Dev.	Energy (kN*mm)	St.Dev.
CLG1	0.47	0.07	3.15	0.60
	+ 43.3 %		+ 35.7%	
CLG2	0.73	0.05	4.52	1.45
CLG3	0.72	0.07	4.96	1.77
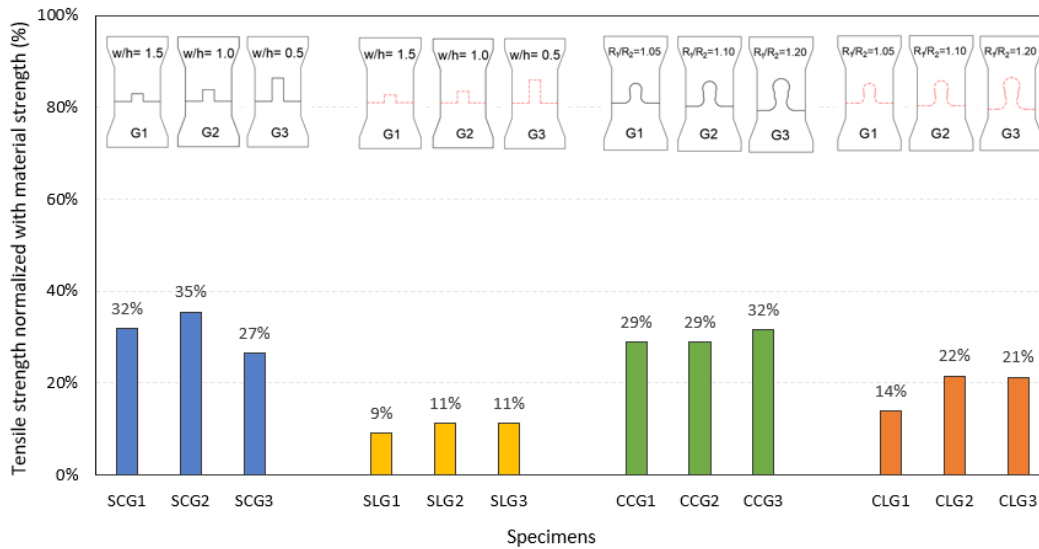
Figure 5.10: Tensile strength of SHCC specimens compared to the obtained material strength of SHCC
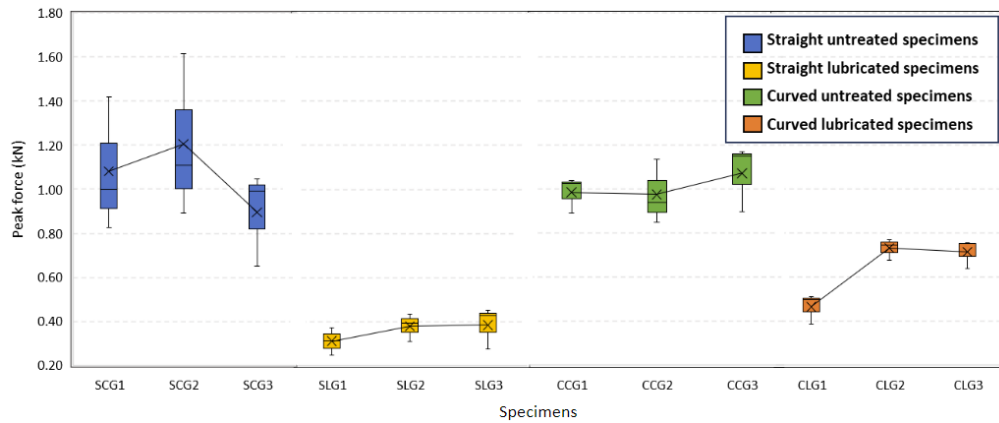
Figure 5.11: Peak force values dispersion

In Figure 5.10, an absolute comparison of the obtained strength of all the specimens compared with the material strength (as presented in Figure 4.3a) is highlighted. In general, the notched interface containing straight or curved keys has 60% lower strength compared to monolithic SHCC. The keys with the highest strength are the straight and curved specimens with an untreated interface (SC, CC). They reach 27–35 % of the material's tensile strength. The geometry of SCG2 showed the best performance (35% of material strength). All of the aforementioned keys failed at the interface, extracting large reaction forces, mostly due to hardening caused by the bending and/or twisting of the key. The same is noted for SCG1 (32%) and CCG3 (32%). Most of those keys failed at the interface due to the same reason. As for the lubricated specimens' strength performance, it was significantly lower, reaching only 9–22% of the materials' strength. All of the keys opened at the interface and showed full or partial pull-out. The adhesive bond at the initial stage added roughly 20% of strength in the case of straight keys and roughly 10% in the case of curve keys.

In Figure 5.11 it is visible that the dispersion of peak force values is greater in the case of **untreated interface** (straight or curved). As mentioned before, this is due to the varying failure modes. Lubrication lowers the peak force but makes the tensile response more uniform.
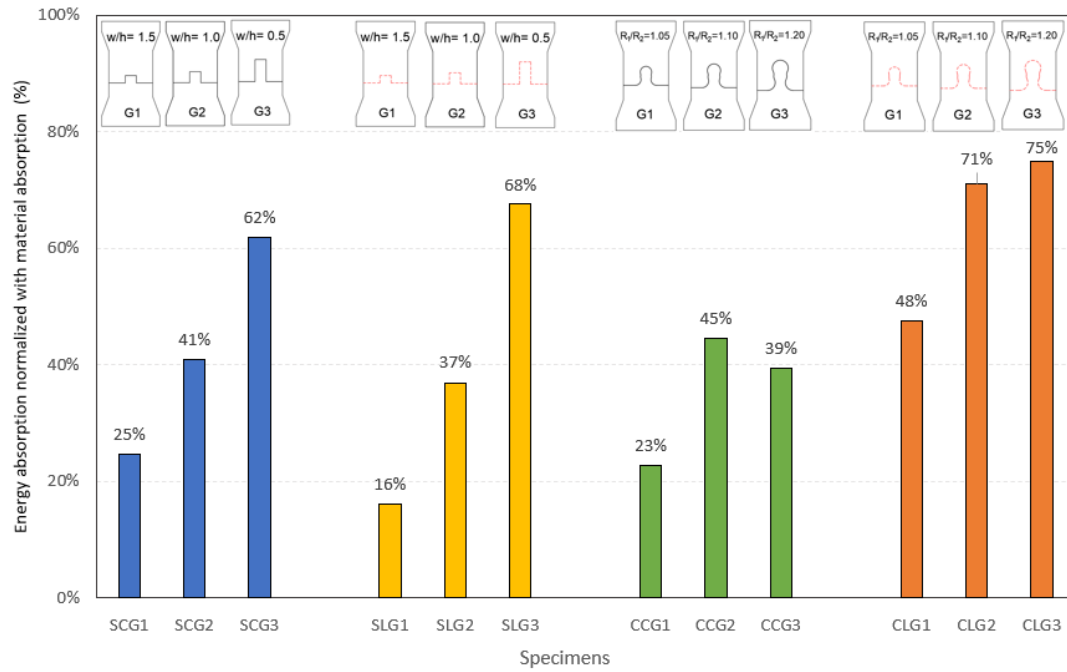
Figure 5.12: Energy absorbed of SHCC specimens compared to the monolithic material's energy absorption. The energy is the area under the stress-normalized displacement (with the gauge length) graph.
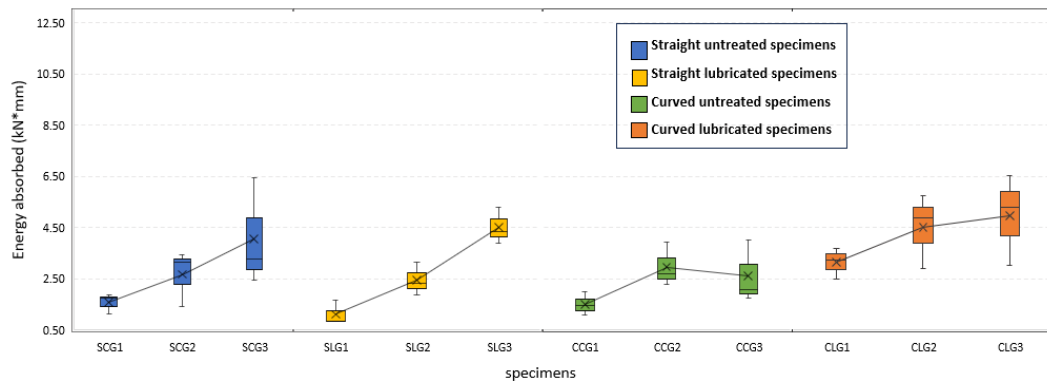
Figure 5.13: Energy absorbed values dispersion

In Figure 5.12, an absolute comparison of the energy absorbed by all the specimens compared to the material's energy absorption is shown. The energy absorption was calculated as the area under the force-displacement graph. Due to the difference in cross-section and heights between specimens, normalization of the energy values was necessary to provide a fair comparison between different specimens. The energy was normalized with the gauge height and cross-sectional area of each specimen (as seen in Figure 5.14).
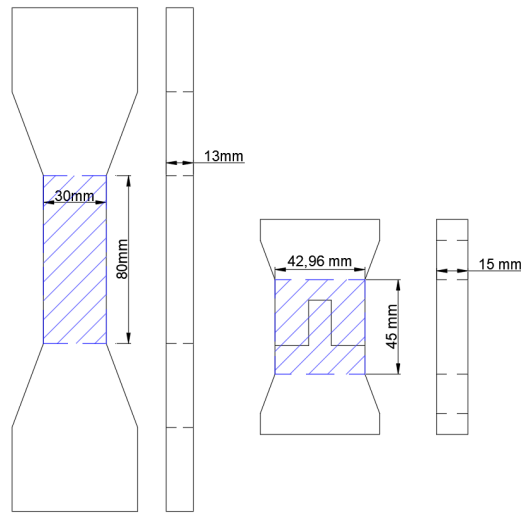
Figure 5.14: Gauge length and height of different specimens used for normalization of energy values

As a result, the energy values were calculated as energy per cubic millimeter (Joules/mm^3). The SHCC specimens are notched and transfer force through the keys; however, they can absorb a great amount of energy. In some specimen categories, when large deformations take place, the specimens can reach 62-75% of the monolithic materials' energy. The geometrical hardening effect, along with the multiple microcracking behavior of SHCC (strain hardening), allowed the small area of the key (approximately 25% of specimen width and 50 % of specimen gauge length) to absorb energy comparable to the bulk material and develop large deformations.

In Figure 5.13 it is visible that the standard deviation of energy absorbed values is greater in the case of untreated straight keys and curved lubricated keys (especially for the specimens of geometry SCG3, CCG2 & CCG3). In the case of the untreated keys as mentioned before this was due to the variation in failure mode. In the case of lubricated keys, it was due to the different cracking patterns that caused variability in the force-displacement curve and eventually at the absorbed energy.

5.2. Influence of the interface treatment at the tensile response

5.2.1. Straight key specimens

In Figure 5.15, the specimens are divided by their geometry (G1, G2, G3) in 5.15a, 5.15b & 5.15c to highlight the differences in response of the same specimen with *different interface treatments*.
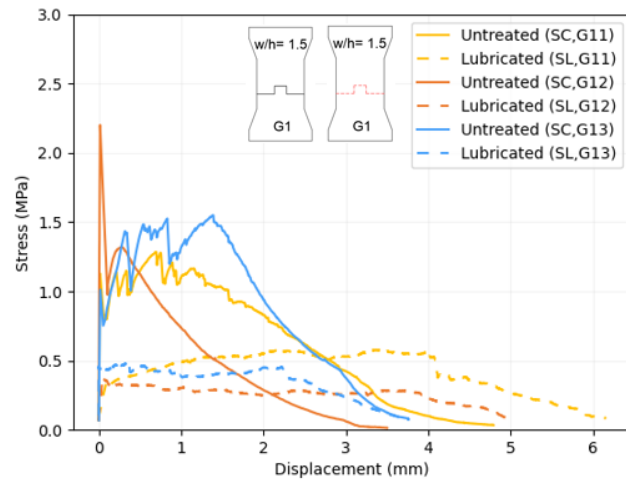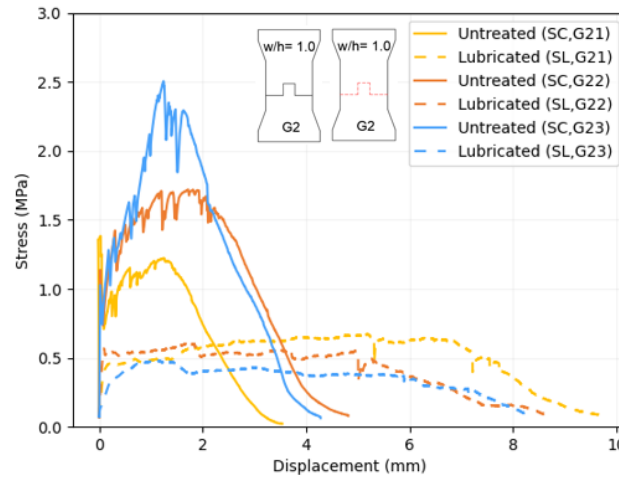
(a) Geometry 1
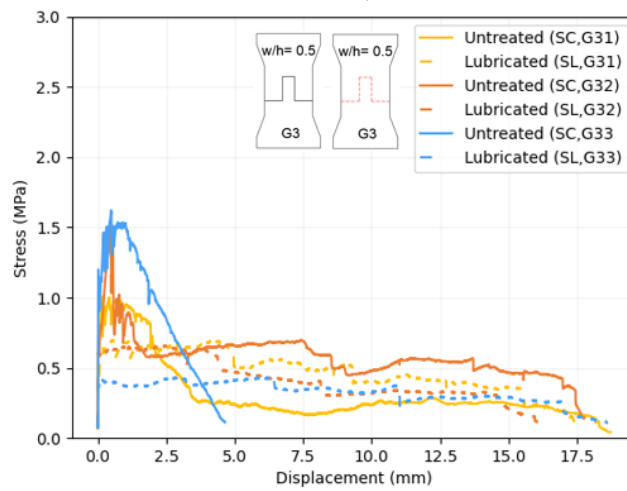
(b) Geometry 2

(c) Geometry 3

Figure 5.15: Tensile response of *straight keys (geometries 1, 2, 3)* with untreated & lubricated interface

A common feature in all straight geometries (5.15a, 5.15b & 5.15c) is that the stress is much higher in every case of the untreated interface (continuous lines). Conversely, for most of the lubricated keys (dashed lines), the displacement reached is higher than that of the untreated. The displacement can indicate the ductility and absorbed energy, but not directly; thus, the area under the graph needs to be computed.

Regarding the trend of the curves in Figure 5.15, for geometry 1 and 2, most of the untreated keys (continuous lines) failed at the interface. This resulted in a gradual and in some cases steep softening regime. On the contrary, the lubricated specimens reached lower stress but were able to sustain that stress level almost until the full pull-out. The case of geometry 3 (Figure 5.15c) shows an interesting effect. After the adhesion failure at the interface, a stress plateau takes place corresponding to sliding friction boundary conditions until displacements of approximately 18mm. The plateau also exists in the case of lubricated keys. This indicates that the bond at the interface increased the stress by approximately 1 MPa, without compromising the energy absorption with a "sudden" key failure as in G1, and G2. By tuning the bond strength in such cases, it would be possible to combine strength and toughness, properties that are usually working in a mutually exclusive way.

In Table 5.5, the values of the peak force and absorbed energy are presented. These are the averaged results of the three specimens in the same group. Each comparison takes place between specimens of the same shape and geometry but with different interface treatments. For G1, the interface lubrication results in a drop in peak force of 110.8% and energy of 34.3%. For G2, the interface lubrication results in a drop in peak force of 103.8% and a small energy drop. For G3 again, there is a drop in force (81.3%) but a small increase in energy. In general, interface lubrication did not show beneficial results in terms of peak force or energy absorbed for straight keys.

Table 5.5: Averaged values of peak force and energy (as the area under the f-d graph), for untreated and lubricated straight specimens (SC & SL)

SC - SL specimens	Peak force (kN)	St.Dev.	Energy (kN*mm)	St.Dev.
SCG1	1.08	0.30	1.57	0.39
SLG1	0.31 -110.8%	0.06	1.11 -34.3%	0.48
SCG2	1.2	0.37	2.67	1.08
SLG2	0.38 -103.8%	0.06	2.45	0.64
SCG3	0.9	0.21	4.06	2.11
SLG3	0.38 -81.3%	0.09	4.52	0.72

5.2.2. Bistable interlock (curved) key specimens

In Figure 5.16, the specimens are divided by their geometry (G1, G2, G3) in 5.16a, 5.16b & 5.16c to highlight the differences in response of the same specimens with different interface treatments.

(a) Geometry 1

(b) Geometry 2

(c) Geometry 3
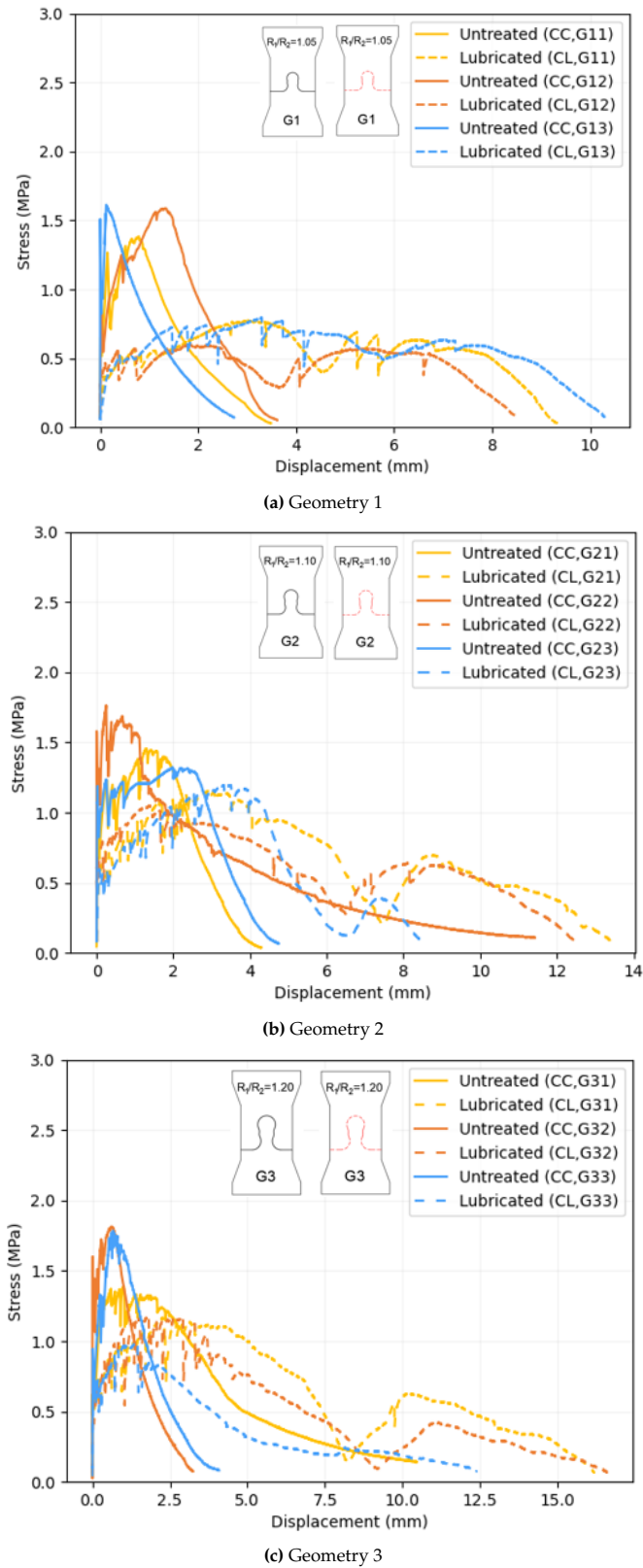
Figure 5.16: Tensile response of *curved keys* (geometries 1, 2, 3) with untreated & lubricated interface

A common feature of all curved geometries is that the peak stress is higher in every case of untreated interface (continuous lines). For most of the lubricated keys (dashed lines), the displacement reached is higher than that of the untreated. The displacement can indicate the ductility and absorbed energy, but not directly; thus, the area under the graph needs to be computed.

The overall behavior of untreated and treated specimens is quite similar to that of an inherently brittle monolithic material versus a tougher-architectured version made of the same material. Such behavior was seen in the Literature chapter in Figure 2.3, Figure 2.5, Figure 2.7. The untreated specimens created a stronger bond at the interface, making the two parts of the specimen behave like a monolithic material. These materials gain their strength by utilizing the strong interfacial bond. On the other hand, lubricated specimens with an artificially weak interface can utilize friction and interlock to delay strain localization and absorb a significant amount of energy before failure (Figure 5.17).
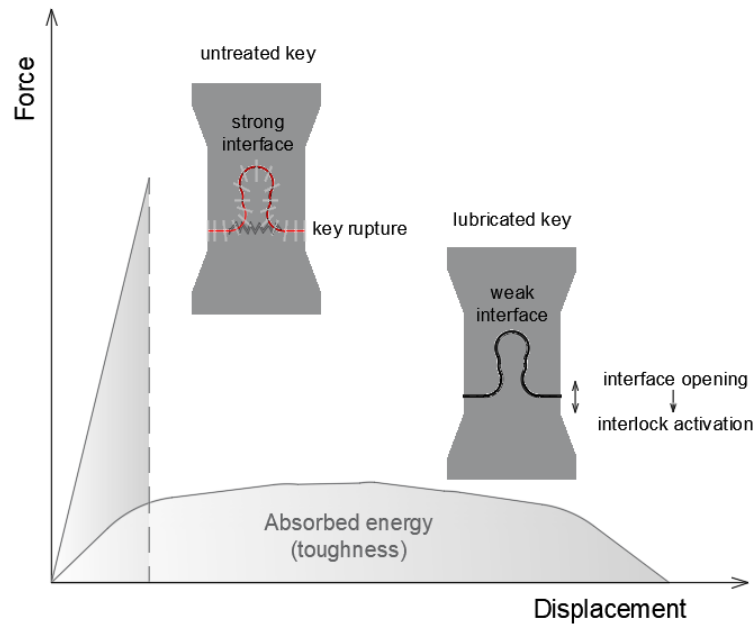
Figure 5.17: Schematic representation of a strong (untreated) and weak (lubricated) interface in terms of toughness

An interesting phenomenon takes place when increasing the radii ratio from 1.05 (geometry 1) to 1.20 (geometry 2) for the lubricated keys. For Geometry 1, the first and second peaks were almost of the same magnitude. This can be attributed to the fact that the smaller radii ratio of G1 caused less geometrical interference and fewer and smaller cracks at the first peak and before the interlock position (Figure 5.18). In this way, the G1 key had a higher remaining stiffness and was able to resist more force when the second radius was sliding out. For the G3 ($R_1/R_2 = 1.20$), during the first peak, the large outer radius R_1 pullout already created larger cracks and lateral openings of the sides of the top part (Figure 5.18).
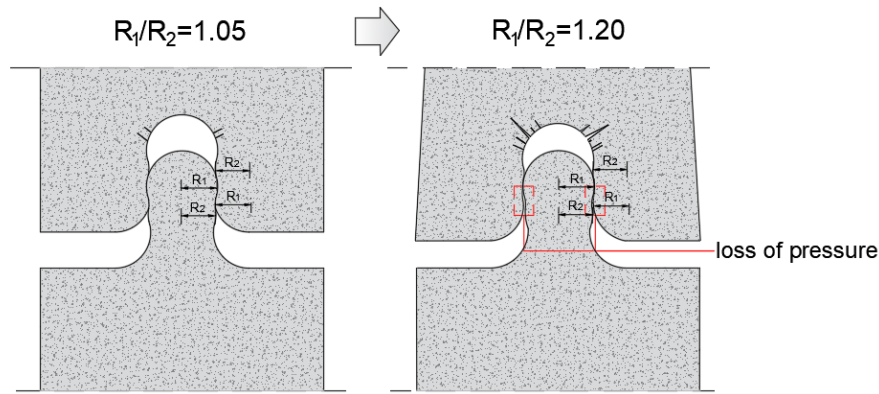
Figure 5.18: Schematic representation of G1 (R_1/R_2=1.05) and G3 (R_1/R_2=1.20) at the second equilibrium position. Cracking and lateral opening lead to loss of pressure for the second radius pullout.

In existing literature [7], a metric to quantify the relative magnitudes of these peak forces was defined as the ξ ratio (peak force ratio F_2/F_1). For lubricated keys across the G1, G2, and G3 cases, the ξ ratio exhibits a decreasing trend, moving from 0.89 to 0.52, and 0.38 (table 5.7). This decrease indicates a progressively higher first peak relative to the second. From a mechanical stability perspective, a higher ξ ratio is generally deemed preferable.

In Table 5.6, the averaged values of the peak force and energy absorbed are quantified. Each comparison happens between specimens of the same shape and geometry but with different interface treatments. For G1, the interface lubrication results in a drop in peak force of 70.3% but an increase in energy of 70.4%. For G2 the interface lubrication results in a drop in peak force of 29.2% and an increase in energy of 41.7%. Lastly, the same trend is followed for G3 where lubrication decreases the peak force by 39.1% and increases the energy absorbed by 62.1%.

As mentioned before, via lubrication, uniformity is introduced to the tensile response of the specimens. Mainly, tensile ductility is increased while the peak force is lowered. Geometry 2 has the lowest "sacrifice" of force and a significant increase in ductility, showing a good balance between strength and ductility.

Table 5.6: Averaged values of peak force and energy (as the area under the f-d graph), for untreated and lubricated curved specimens (CC & CL)

| CC - CL specimens	Peak force (kN)	St.Dev.	Energy (kN*mm)	St.Dev.
CCG1	0.98	0.08	1.51	0.47
CLG1	0.47 − 70.3 %	0.07	3.15 + 70.4 %	0.60
CCG2	0.98	0.15	2.96	0.85
CLG2	0.73 − 29.2 %	0.05	4.52 + 41.7 %	1.45
CCG3	1.07	0.15	2.61	1.24
CLG3	0.72 − 39.1 %	0.07	4.96 + 62.1 %	1.77

In the specific case of geometry 3 ($R_1/R_2 = 1.20$) the prefabricated key can also be compared with the untreated and lubricated ones (Figure 5.19). In terms of peak force, the untreated keys showcase the highest, followed by the lubricated and then prefabricated keys. For the prefabricated keys, an interesting phenomenon takes place. For the first time, the second peak of the bistable interlock curve was higher than the first. As seen in the literature [7], [58], this feature can enhance the overall mechanical stability of the system. The aforementioned ξ ratio (peak force ratio F2/F1) is now increased to 1.14. This comes in contrast to other keys, where the highest ξ ratio achieved was 0.89 (see table 5.7).
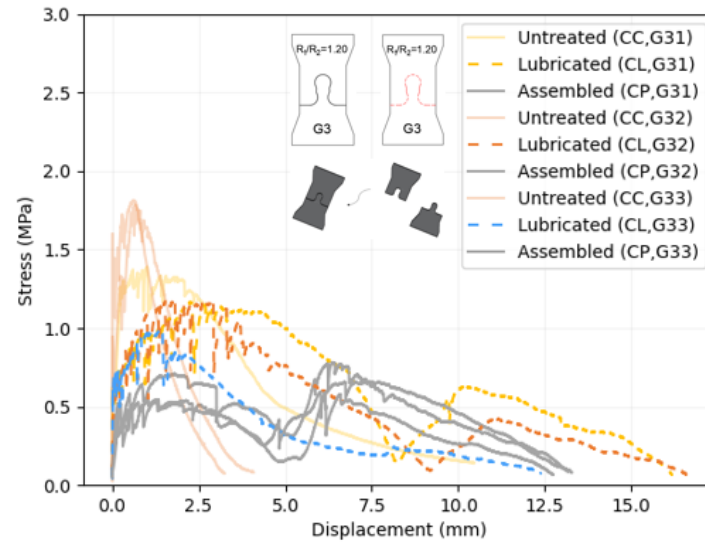
Figure 5.19: Curved keys *(geometry 3)* with untreated & lubricated & out-of-plane assembled interface

Table 5.7: Peak force (F_2/F_1) ξ ratio in lubricated and "prefabricated" keys

Specimen	ξ (F2/F1)	average	st.deviation	COV
CLG11	0.88			
CLG12	0.95	0.89	0.05	6%
CLG13	0.85			
CLG21	0.61			
CLG22	0.63	0.52	0.17	33%
CLG23	0.32			
CLG31	0.55			
CLG32	0.36	0.38	0.16	43%
CLG33	0.22			
CPG31	1.09			
CPG32	1.27	1.14	0.11	10%
CPG33	1.07			

In table 5.8 the three different interface conditions are compared regarding force and absorbed energy. The untreated key showed the highest peak force and the lubricated key showed the highest energy absorbed.

Table 5.8: Averaged values of peak force and energy (as the area under the f-d graph), for untreated, lubricated, and prefabricated specimens (CC, CL & CP)

CC - CL - CP specimens	Peak force (kN)	St.Dev.	Energy (kN*mm)	St.Dev.
CCG3	1.07	0.15	2.61	1.24
	- 39.1 %		+ 62.1 %	
CLG3	0.72	0.05	4.96	1.77
	- 48.3 %		- 32.9 %	
CPG3	0.44	0.06	3.56	0.62

5.3. Influence of the key shape at the tensile response

5.3.1. Untreated interface specimens

In Figure 5.20, the specimens are divided by their geometry (G1, G2, G3) in 5.20a, 5.20b & 5.20c to highlight the difference in response of the **straight** and **bistable interlocked keys** with untreated interface.

(a) Geometry 1

(b) Geometry 2

(c) Geometry 3

Figure 5.20: Tensile response of untreated keys (geometries 1, 2, 3) for straight and curved keys

For the untreated interface, the straight keys (continuous lines) show no significant differences compared to the curved keys (dashed lines) in strength and absorbed energy. The dashed lines follow the continuous ones with no major discrepancies, except for some extreme values out of the normal range, usually stemming from bending/torsion phenomena. As stated before, many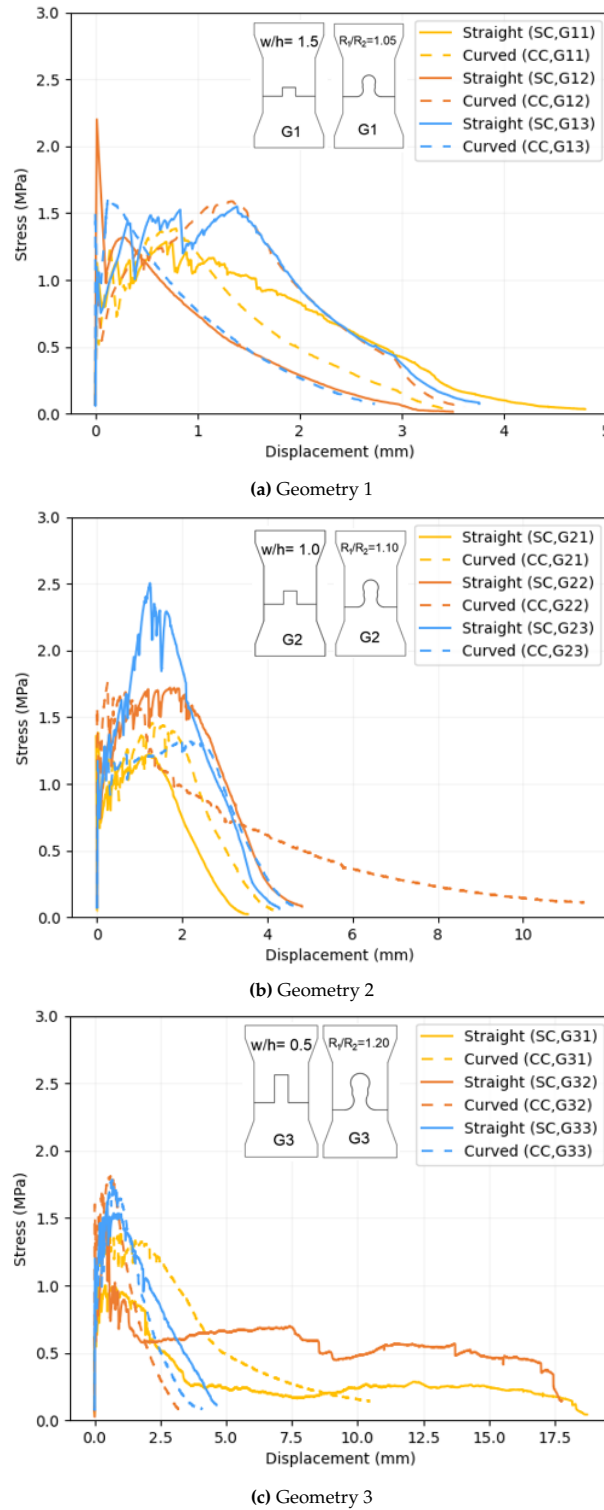 keys (especially in geometries 1 and 2) sheared off at the interface. In such cases, the shape of the key (straight or curved) did not affect the response, hence the similarity in their curves.

This is the case for geometry 1 and 2. Looking at Figure 5.20c (geometry 3) some differences can be identified. In the case of straight keys, the plateau associated with sliding friction results in large displacements of the straight keys. Their curved equivalents do not show this behavior since they show rupture at the interface due to the strong interfacial bond combined with the complex curved geometry.

In Table 5.9, the averaged values of the peak force and energy absorbed are presented. The comparison takes place between untreated specimens of straight and curved shapes of the same geometry. For a straight to curved shape, there are no major changes in peak force or energy, except for G3 specimens. For G3 straight specimens → curved G3, the difference in shape decreased the energy absorbed by 43.5%. This stems from the aforementioned plateau in the force-displacement graph of G3 straight keys in comparison to the premature interface failure of the G3 curved keys.

Table 5.9: Averaged values of peak force and energy (as the area under the f-d graph), for untreated curved and straight specimens (SC & CC)

SC - CC specimens	Peak force (kN)	St.Dev.	Energy (kN*mm)	St.Dev.
SCG1	1.08	0.30	1.57	0.39
CCG1	0.98	0.08	1.51	0.47
SCG2	1.2	0.37	2.67	1.08
CCG2	0.98	0.15	2.96	0.85
SCG3	0.9	0.21	4.06	2.11
CCG3	1.07	0.15	2.61	1.24

- 43.5 %

5.3.2. Lubricated interface specimens

In Figure 5.21, the specimens are divided by their geometry (G1, G2, G3) in 5.21a, 5.21b & 5.21c to highlight the difference in response of **straight** and **bistable interlocked keys** with lubricated interface.

(a) Geometry 1

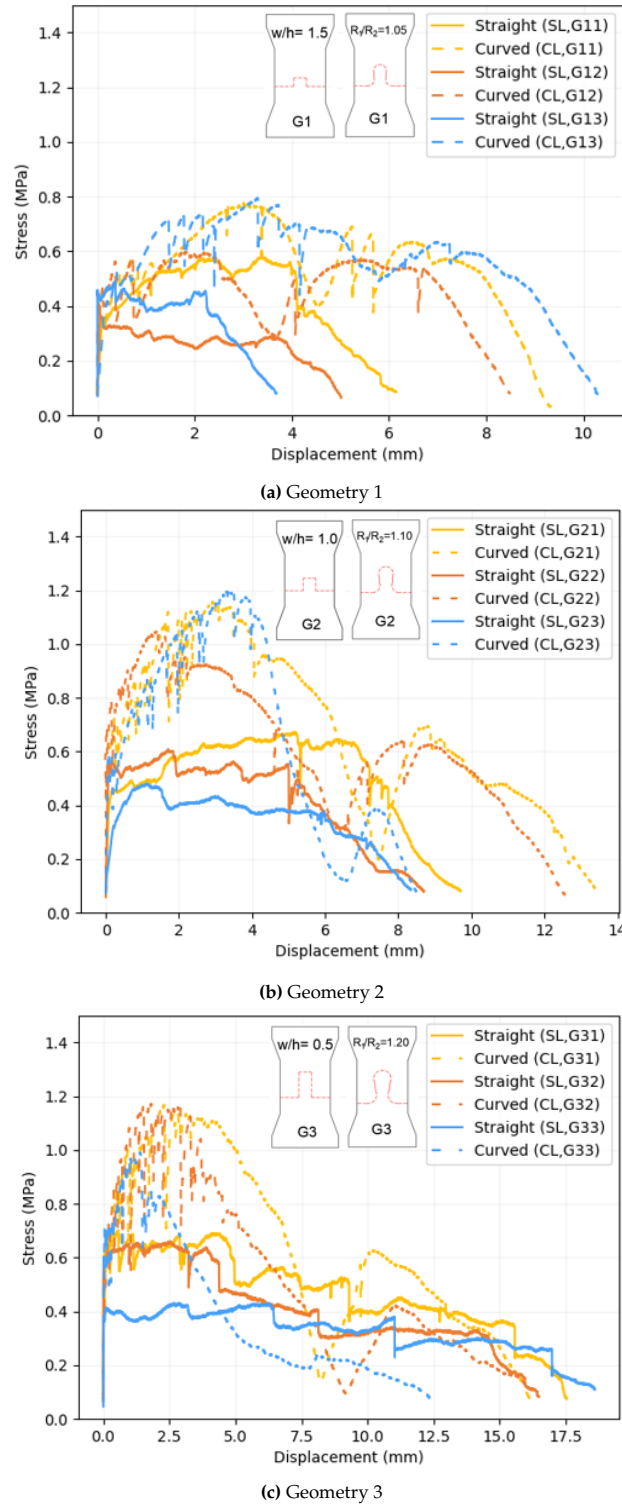**(b)** Geometry 2

(c) Geometry 3

Figure 5.21: Tensile response of lubricated keys (geometries 1, 2, 3) for straight and curved keys

Unlike the previous case of untreated keys, it is obvious that lubrication has a major effect on the response of straight and curved keys. For all of the curved key specimens (dashed lines), the

characteristic double-peak curve of the bistable interlock took place.

Looking at the peak stress in Figure 5.21, there is a uniform behavior for all different geometries. All of the curved keys (dashed lines) showcase higher stress compared to the straight equivalents (continuous lines). Additionally, for all of them, the first peak was always higher than the second. The displacements reached are much larger for curved keys compared to their straight equivalents in the cases of G1 and G2. The area under the graph representing the energy absorbed is visibly larger for all of the curved key cases.

In Table 5.10, the averaged values of the peak force and energy absorbed are presented. The comparison takes place between lubricated specimens of straight and curved shapes of the same geometry. There is a clear increase for every case when moving from straight to curved specimens. The most balanced performance between strength and energy absorbed (63.1% and 59.4%) was for the curved geometry 2.

Table 5.10: Averaged values of peak force and energy (as the area under the f-d graph), for lubricated curved and straight specimens (SL & CL)

SL- CL specimens	Peak force (kN)		St.Dev.	Energy (kN*mm)		St.Dev.
SLG1	0.31	+41 %	0.06	1.11	+95.8 %	0.48
CLG1	0.47		0.07	3.15		0.60
SLG2	0.38	+63.1 %	0.06	2.45	+59.4 %	0.64
CLG2	0.73		0.05	4.52		1.45
SLG3	0.38	+61.8 %	0.09	4.52		0.72
CLG3	0.72		0.07	4.96		1.77

5.4. Influence of the key material at the tensile response

To provide a reference for the SHCC specimens, some specific geometries were chosen to be recreated in mortar (see Figure 3.7). Mortar is a well-understood and standardized material suitable to create a benchmark for material comparison. This allows for a clearer understanding of how SHCC performs in terms of mechanical properties, durability, and other characteristics. It can additionally offer validation of the experimental techniques.

5.4.1. Straight key specimens

For the straight key specimens of geometry 2, the mortar and SHCC comparison is shown in Figure 5.22. In terms of strength, SHCC performs better, but mostly due to hardening related to bending or torsion caused by sample imperfections. When it comes to absorbed energy, SHCC, as expected, performs better compared to the brittle mortar.
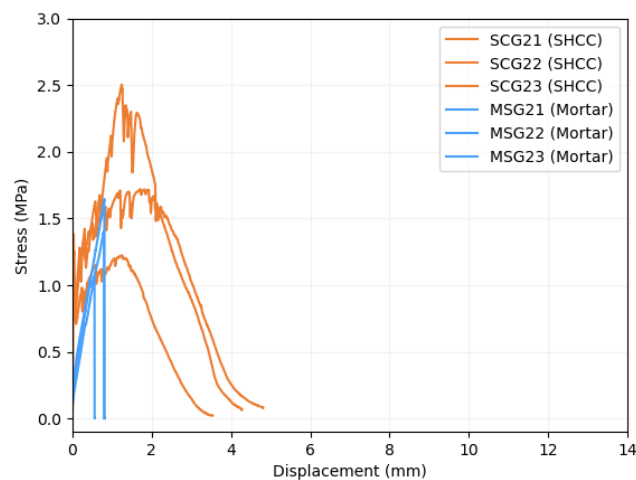
Figure 5.22: Straight keys *(geometry 2)* made out of mortar & SHCC

5.4.2. Bistable interlock (curved) key specimens

For the curved key specimens of geometry 2, the mortar and SHCC comparison is shown in Figure 5.23. In terms of strength, SHCC performs better, showing in most cases higher stress values. When it comes to absorbed energy, SHCC, as expected, absorbs more energy than mortar before failure.
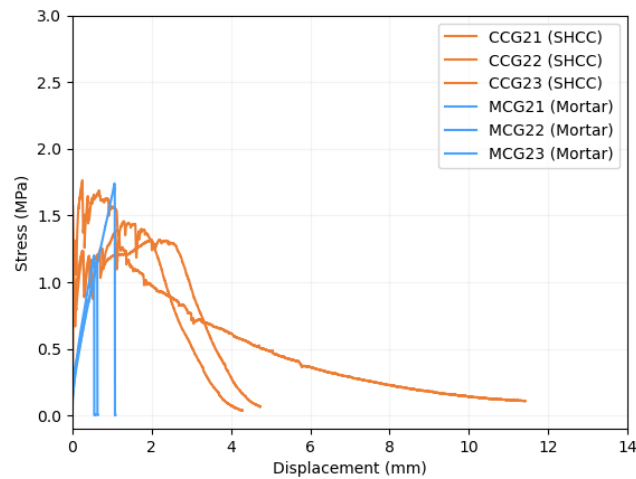
Figure 5.23: Curved keys *(geometry 2)* made out of mortar & SHCC

For the prefabricated key specimens (geometry 3), the mortar and SHCC comparison is shown in Figure 5.24. In terms of strength and energy absorption, SHCC performs better. The SHCC specimens show a bistable interlock curve effect with two peaks, maximizing the area under the graph in comparison to their mortar equivalents.
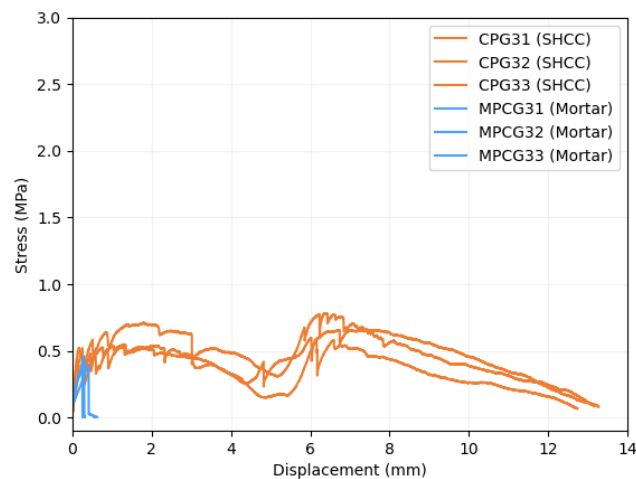
Figure 5.24: Curved "prefabricated" keys *(geometry 3)* made out of mortar & SHCC

In table 5.11 the averaged peak force and energy absorbed values are presented. As expected, the SHCC specimens showed greater ductility (151-195% higher) compared to mortar. The peak force was also greater for all the SHCC specimens, especially in the case of the prefabricated key. The table highlights the superior performance of SHCC in comparison to plain mortar.

Table 5.11: Averaged values of peak force and energy (as the area under the f-d graph), for SHCC & mortar specimens of same geometry

SHCC - Mortar specimens	Peak force (kN)	St.Dev.	Energy (kN*mm)	St.Dev.
SCG2	1.2	0.37	2.67	1.08
MSG2	0.88	0.18	0.37	0.15
	- 30.8 %		- 151.3 %	
CCG2	0.98	0.15	2.96	0.85
MCG2	0.88	0.21	0.40	0.24
			- 152.4 %	
CPG3	0.44	0.06	3.56	0.62
MPCG3	0.27	0.03	0.05	0.01
	- 47.9 %		- 194.5 %	

5.5. Analytical model describing the behavior of the straight keys

As an initial step to understanding the intricate contact mechanisms that take place at the interface of the bistable interlocked keys, the straight keys act as a simplified case. The straight-key specimens' tensile response is further analyzed in terms of the mechanisms that take place (tensile bond, shear bond, friction) in small and large deformations.

Upon examining the tensile response, certain assumptions and simplifications were introduced, seen below:

- The keys that were chosen for the model are those that responded in a pure tension state to the tensile forces; no torsion or bending was noticed. This was the case for the specimens of Geometry 3 (longer keys).
- Areas A, B, C and D, E were defined as areas with different mechanisms resisting tension (normal and parallel to the loading direction) as seen in Figure 5.25.
- Smooth interface was assumed ($R_a \leq 1.5mm$).
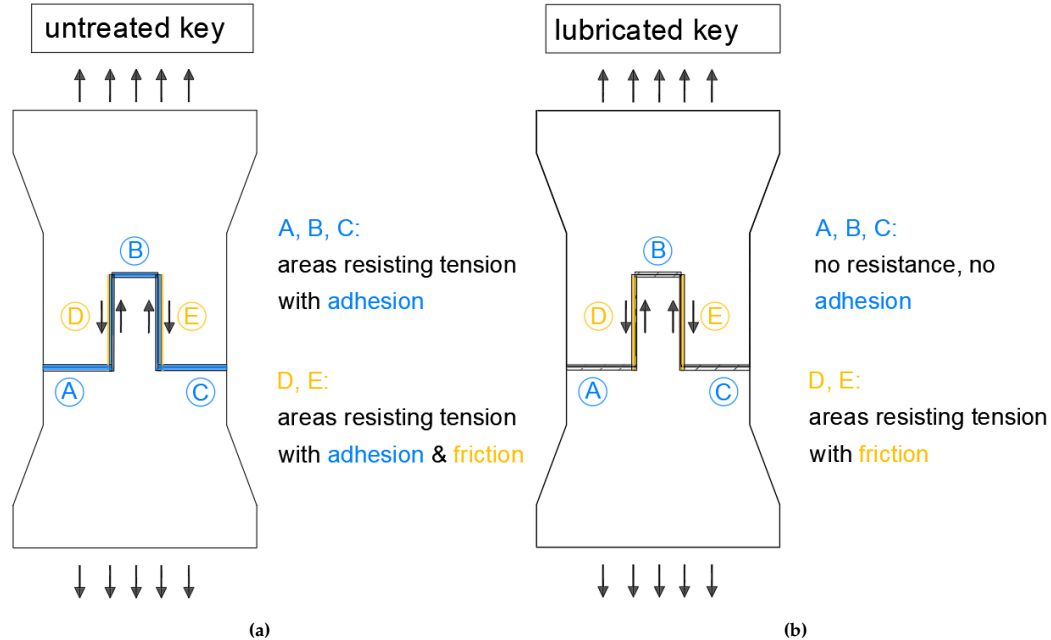
Figure 5.25: Interface of untreated and lubricated keys responding to external tensile forces

The tensile response of untreated and treated keys (Figure 5.26) follows a similar trend. These trends can result in simplified curves (Figure 5.27) for untreated and lubricated specimens.

(a) Untreated key
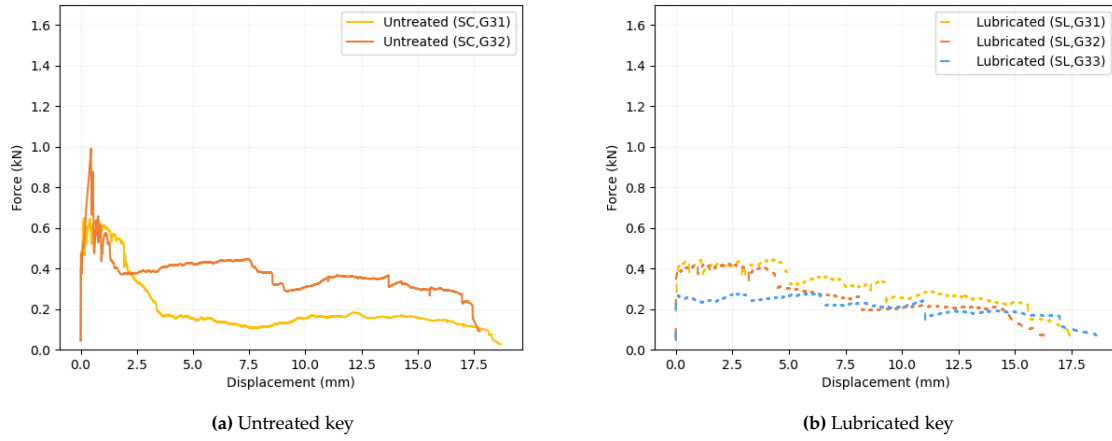
(b) Lubricated key

Figure 5.26: Untreated and lubricated specimens (geometry 3) tensile response

(a) Untreated key
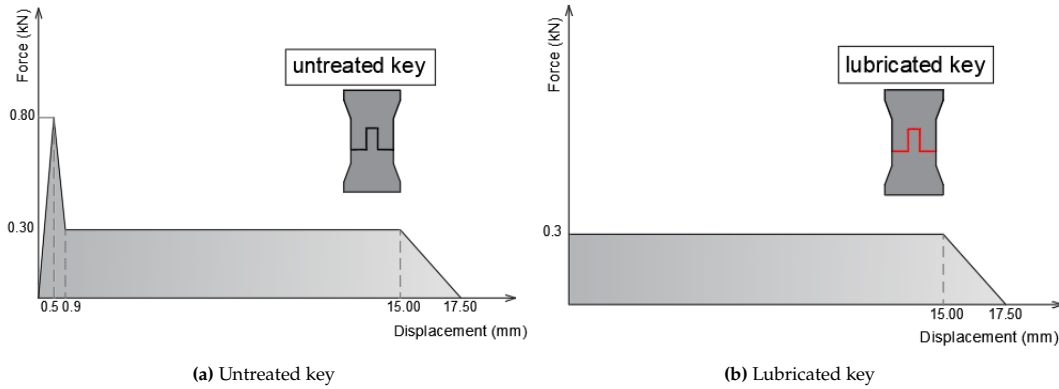
(b) Lubricated key

Figure 5.27: Schematic representation (simplified) of the tensile response of untreated and lubricated keys

Analyzing the Figure 5.27 for the **untreated** key, *four regimes* are observed for the reaction force:

For displacement 0 - 0.5 mm:

$$\Sigma RF = \textbf{Adhesion} \text{ (tensile- surfaces A, B, C \& shear- surfaces D, E)} + \textbf{Sliding friction} \quad (5.1)$$

For displacements 0.5 - 0.9 mm:

$$\Sigma RF = \textbf{Sliding friction} \quad (5.2)$$

For displacements 0.9 - 15 mm:

$$\Sigma RF = \textbf{Sliding friction (stabilized)} = \mu_k * N \quad (5.3)$$

Pressure declines as the interface decreases gradually due to the pullout, but friction is not reduced due to ploughing and dynamic phenomena taking place.

For displacements 14 - 17.5 mm:

$$\Sigma RF = \textbf{Sliding friction (decaying)} \to 0 \quad (5.4)$$

Analyzing the Figure 5.27 for the **lubricated** key, two main regimes are observed for the reaction force:

For displacements 0 - 15 mm:

$$\Sigma RF = \textbf{Sliding friction (stabilized)} = \mu_k * N \tag{5.5}$$

No adhesion resists the pullout at the lubricated key; hence, the response starts with a plateau. Pressure declines as the interface decreases gradually due to the pullout, but friction is not reduced due to ploughing and dynamic phenomena taking place.

For displacements 15 - 17.5 mm:

$$\Sigma RF = \textbf{Sliding friction (decaying)} \to 0 \tag{5.6}$$

Adhesive bond

Adhesion refers to the bonded areas that resist the tensile forces through shear or tensile bond, depending on the direction of the bonded surface to the force application.

An estimation of the bond strength based on the experimental data follows:

Looking at Figure 5.27 a & b the friction force can be estimated at 0.3 kN. In the case of untreated keys, the peak force (0.8 kN) is caused by the combined resistance of the adhesion and friction mechanisms. Assuming sliding friction happens almost immediately as the interface translates, the friction force can be assumed at 0.3 kN from the beginning. That leaves the adhesive bond force at 0.5 kN.

That force is caused by the tensile and shear bond along areas of the interface. By allocating a percentage to shear and tensile bond as an assumption, an estimation of tensile and shear bond strength can be made. As an assumption 40% of the resistance force is allocated to tension and 60% to shear. Then:

$$\textbf{Tensile bond strength} = 0.2kN/(43 * 15)mm = 0.31MPa \tag{5.7}$$

$$\textbf{Shear bond strength} = 0.3kN/(2 * 21.62 * 15)mm = 0.46MPa \tag{5.8}$$

In [69], the surface preparation in the debonding mechanism of concrete-to-concrete interfaces was examined via numerical simulations. For a smooth concrete-to-concrete interface the tensile strength of the bonded interface was calculated at 0.30-0.31 MPa and the shear strength of the bonded interface at 0.54-0.55 MPa. Compared to the tensile and shear strength of the SHCC-to-SHCC bonded areas (Equation 5.7 and Equation 5.8) the results are similar.
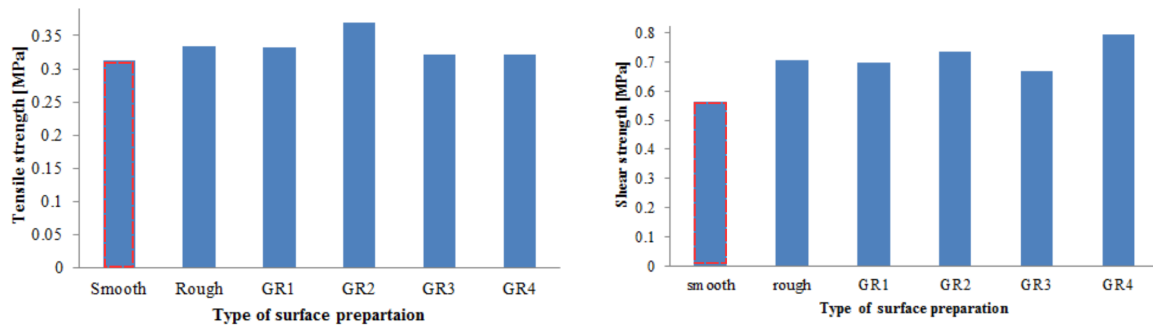

Figure 5.28: Tensile and shear strength at the interface [69]

6

Conclusions & Recommendation

This chapter presents the conclusions drawn from the research conducted in this thesis. Further recommendations for the implementation of bistable interlocks in engineering practice and directions for further research are suggested.

6.1. Conclusions

The goal of this research is to investigate the tensile performance of bistable interlocks in sutured geometries made of Strain-Hardening Cementitious Composites (SHCC). The ultimate goal is to design reliable connections of cementitious materials with higher damage tolerance by exploiting the shape of bistable interlocks and fine-tuning geometrical properties to "customize" the tensile response.

RQ1: To what extent can the implementation of the bistable interlock mechanism enhance the toughness and strength of interlocking keys made of SHCC under tensile loading?

What is the tensile response of straight interlocking SHCC keys, in terms of toughness and strength?

- The specimens incorporating *straight keys* were made of SHCC in three geometry variations: short, medium, and longer keys (based on their width-to-height ratio) and two interface variations (untreated and lubricated).
- 44% (4 out of 9) of the *straight untreated* keys failed at the interface, revealing that the interface treatment governed the failure mode. The bond was strong enough to lead to the rupture of the keys at the interface. In some cases, failure modes that were not representative of the tensile response occurred (e.g. geometry 2). This was attributed to specimen imperfections or slanted surfaces; not pure tension but bending and torsion (twisting) occurred, documented visually from the setup's rotation and DIC images. This led to variations in the failure modes and cracking patterns of different specimen sizes.
- The *straight-lubricated* keys had more uniform failure modes. 89% of the specimens (8 out of 9) showed full translation of the key. In this case, the length of the key governed the response, regarding strength and energy absorption. For all of the specimens, interface debonding happened almost immediately, and cracks were initiated at high-stress locations (corners). In cases where damage accumulation along the key length occurred (due to dynamic friction phenomena), increased resistance of the key led to a strain-hardening behavior in the force-displacement graph. This clearly shows that cracking along the SHCC key leads to better use of the key's ductility in comparison to a smoother key pull-out.
- The straight-untreated key specimens showed a *strength* range of 27–35% of the monolithic material's strength, the highest achieved of all of the SHCC specimens. For the lubricated case, the strength was much smaller (9-11%) since, without adhesive bonding, the resistance was gained only from frictional contact. The standard deviation of peak force is larger in the case of untreated keys due to the difference in failure modes and overall response.

- Straight, untreated keys showed *energy absorption* of 25-62%, compared to the monolithic SHCC. A similar trend is noted for the lubricated keys, ranging from 16-68%. These percentages are size-specific; while moving from smaller to longer keys, more energy is absorbed. For the lubricated keys, the standard deviations of peak force and energy are noticeably lower, due to the uniformity of the tensile response.

What is the difference in the tensile response of curved interlocking SHCC keys compared to straight SHCC keys?

- The specimens incorporating *curved geometries* with bistable interlocked keys were made in three geometry variations: small, medium, and larger keys (based on their radii ratio) and two interface variations (untreated and lubricated).
- 78% (7 out of 9) of the *curved untreated* keys showed key failure at the interface. The strong interfacial bond, combined with the complex curved geometry, governed the response. An influencing factor was the additional bending and torsion (twisting) of the keys caused by specimen imperfections. For the remaining 22% (2 out of 9) no full pull-out happened but a partial debonding from one side, suggesting inhomogeneities at the bond strength along the interface. Different cracking patterns emerged, with a common feature: the fracture zone reached the interface and debonding started propagating, leading to the failure of the base of the key near the interface.
- 89% (8 out of 9) of the lubricated keys showed pull-out. In this case, the geometry governs the response. All of the lubricated specimens resulted in the characteristic double equilibrium, double peak force-displacement graph. Similar cracking patterns with geometry-related differences were noticed. For all the keys, cracking was initiated radially at the top part and the neck of the key. While the radii ratio of specimens increased, the cracking pattern at the top became more tortuous, and more cracks occurred along the length of the key. For larger keys, strain localization at one lateral crack decreased the contact pressure during the pullout of the second radius. The effectiveness of bistable interlock is then decreased.
- The untreated curved keys showed a *strength* range of 29-32% of the material's strength. The standard deviation of peak force values is large due to the difference in failure modes. For the lubricated case, the strength was much smaller (14-22%) since there was no adhesive bonding; all the resistance was offered by frictional contact and mechanical interlock. The standard deviation of peak force is low, meaning results are less dispersed due to the uniform tensile behavior.
- Compared to the monolithic SHCC, the curved, untreated keys showed *energy absorption* of 23-45%. These percentages were not proportional to the radii ratio increase. The lubricated keys, on the other hand, resulted in an increase in energy absorption alongside the radii ratio increase. After geometry 2, the benefits in force and energy decrease, suggesting a threshold on how the radii ratio increase can benefit the response. When the length of lubricated keys is increased, there is a wide variation in energy values. This happens because the difference in radii ratio leads to uneven energy absorption due to various crack patterns.

To provide an answer to the first research question, the main conclusions of the subquestions are summarized. The tensile response (regarding toughness and strength) of the interlocking keys under tensile loading is highly influenced by the shape of the key. The influence is different for untreated and lubricated specimens. In the case of the untreated keys, a large percentage of the specimens failed (44% for straight 78% for curved keys). This was predominantly due to the strong bond at the interface and secondarily due to imperfections causing additional loads. Regarding strength, no added benefits followed the change from straight to curved geometry. The straight specimens showed higher energy absorption since more specimens opened during pull-out and exploited their full length. For the lubricated keys, 89% of specimens showed a full pull-out. In this case, changing the geometry from straight to bistable interlocked added benefits regarding the peak force and energy absorbed.

RQ2: How can the tensile response of different interlocking SHCC keys be optimized in terms of toughness and strength?

What is the influence of an untreated interface & interface lubrication on the tensile response of both straight and curved keys? What is the influence of an out-of-plane assembled interface on the tensile response of curved keys?

- The introduction of lubrication significantly alters the mechanical response of *straight keys*. Untreated specimens show higher reaction forces due to the presence of strong interfacial bond. This leads to an interface key for 44% of specimens. This response hinders the exploitation of sliding friction and leads to less energy absorption. For the remaining 56 %, untreated interface has a positive effect on the tensile response. The interface bond was weak enough to fail first, leading to a distinct peak in force followed by a sliding friction plateau on the force-displacement graph. This peak in force is contributing to higher energy absorption. For the lubricated interface, the response of 89% of all specimens is a full-length pullout, resulting in lower force and energy absorption. A notable characteristic of straight lubricated keys is their ability to sustain approximately 50% of their peak force for roughly 80% of their deformation.

- Lubrication of *bistable interlocked keys* introduces a significant change in their tensile response: the formation of a double peak in the force-displacement curve. The interface treatment governs the failure mode. Without lubrication, 78% of the keys predominantly fail at the interface, rendering the bistable interlock unused. This was expected due to their complexity, which allowed for stronger adhesion than the simpler straight keys. With lubrication, 100% of the specimens showed full or partial pullout. Untreated curved keys exhibit higher force and more 'brittle' behavior, whereas lubricated keys demonstrate greater energy absorption. This trend is consistent with broader literature findings: inherently brittle monolithic materials compared to their architectured counterparts exhibit greater strength but lower toughness. An interesting development is observed in the case of assembled, prefabricated keys. While they do not show substantial improvements in peak force or energy absorption, they exhibit a phenomenon not seen for the previous keys: the second peak in the force-displacement diagram was higher than the first. This characteristic is beneficial for mechanical stability.

How do straight keys with different width-to-height ratios & curved keys with different radii ratios behave under the aforementioned interface treatments regarding strength and toughness? What types of failure are observed as the geometry changes?

- For *straight untreated keys* a counter-intuitive phenomenon took place: shorter keys failed at the interface more often than longer keys. The longer keys, with a higher probability of failure due to the larger bonded area, opened and translated for more than 50% of their key length. This was attributed to bending and torsion stemming from specimen imperfections for shorter keys. An increase in the key length increased proportionally the energy absorption (25% to 41% and 62%). However, the increase in length did not proportionally enhance the strength of the keys.

- For *straight lubricated keys*, the correlation between key length and ductility is more pronounced due to the facilitation of sliding friction at longer key lengths. For lubricated specimens, since 89% opened fully, longer keys absorbed more energy. However, the augmentation in key length does not contribute to a corresponding increase in the force-bearing capacity of the material. The failure modes were similar: full translation of the key with cracks initiating at the corners. While the key length increased, more cracks were observed along the neck and above the key.

- For *curved untreated keys*, the propensity for additional friction connected to surface imperfections and the complex geometry, led to shearing of the key. Even in the absence of these factors and considering only the bond, most specimens were unable to debond fully and to transcend to the frictional sliding phase. The increase in geometry (radii ratio) did not yield noticeable improvements in terms of force or energy absorption since most of the keys failed at the interface soon after the load was applied.

- For *curved lubricated keys* the response is notably influenced by the radii ratio. In the force-displacement graph across all specimens, a bistable interlock curve with two peaks and two equilibrium positions is observed. However, for small keys, the two peaks are of comparable

magnitude. For medium keys, the first peak becomes more pronounced than the second, and for the larger keys, even more. Extensive cracking due to the geometrical interference of larger keys decreased the post-kink force-bearing capacity. From a mechanical stability perspective, a high second peak is preferable. Furthermore, increasing the R_1/R_2 ratio does not consistently yield benefits in the tensile response. Moving from small to medium keys added benefits in terms of force and energy absorption were noticed but not from medium to larger keys. This suggests a threshold at R_1/R_2=1.10 similar to the one seen in the literature.

To provide an answer to the second research question, the main conclusions of the subquestions are summarized. The tensile response (regarding toughness and strength) of the interlocking keys under tensile loading can be optimized by changing the interface and geometry of the key.

Regarding *interface treatment*, it was seen that the adhesive bonding at the interface rarely improved the toughness of the connection. As seen in the literature, by increasing the bond strength, debonding mechanisms are delayed, but the level of restraint at the interface also increases, leading to higher cracking probabilities. An interface with a lower bond strength is beneficial for ductility, as it was in the case of curved keys, where lubrication enabled the exploitation of the geometrical interlock of the curved geometry. Lubrication makes the failure more stable, compared to the untreated specimens with very different failures. Large amounts of untreated specimens failed, while 100% of lubricated specimens were partially (for more than 50% of their length) or fully translated. On the other hand, lubrication leads to lower peak forces for all keys.

When it comes to the *geometry* of the specimens, the influence on the tensile response was not as great as the interface treatment. However, improvements were noticed with an increase in the geometry. For the straight keys, a proportional increase in absorbed energy was noticed for untreated and lubricated specimens, but not in strength. For the untreated curved specimens, the increase in geometry yielded no major differences since the interface treatment governed the response. Conversely, for the lubricated specimens, the response was enhanced in both strength and energy and eventually a design threshold at $R_1/R_2 = 1.10$ was noticed.

6.2. Recommendations

- As a first approach to creating bistable interlocks in SHCC, a high volume of fibers was used (2.6%). This was chosen to accommodate fiber bridging, allow large deformations of the key (y-axis), and simultaneously increase the bending capacity while the sides of the top part opened laterally (x-axis). The volume should be decreased to a more realistic value in a later study. In addition, it is highlighted that the fiber dispersion of SHCC especially when using a higher volume fraction can create a manufacturing bias when it comes to the fiber dispersion inside the small area of the key. Further research is needed to confirm this suggestion.

- From an execution point of view, flexible mould prototypes made of silicone rubber were used in this study. Although extra care was taken in the experimental process, this occasionally led to warping and non-plane surfaces of certain specimens. Additionally, the grinding of the surface should be sufficient while still making sure that the surface of the specimen remains plane.

- The interfacial bond of the specimens was often strong enough to cause failure of the key at the interface without exploiting the complex key shape. The specimens were cured for more than 28 days. The prestudy's untreated specimens (presented in Annex A) with a curing period of 7 days were tested and showed a full pull-out. This highlights the importance of bond strength in bistable, interlocked geometries. Fine-tuning the bonding and/or changing the bonded areas is recommended to be studied further. Decreasing the bond in the high-stress areas with local lubricant application could have a positive effect on the strength and ductility of the connection.

- Geometry 2 of the curved keys was found to have a good balance of strength and ductility. More geometry variations with radii ratios close to geometry 2 ($R_1/R_2 = 1.10$) are recommended to be tested. Adjusting even slightly the dominant parameters as $R_1, R_2, \theta_1, \theta_2$ can have a major influence on the tensile response.

- The prefabricated key, while not showing outstanding peak force or ductility in comparison to the rest of the specimens, had manufacturing benefits and offered extra mechanical stability. Casting of prefabricated components with lines of sutures is suggested. A line of interlocks cast on top of each other could create constraints for the pullout of the keys and lead to their eventual rupture.

However, in the prefabricated case, with manufacturing tolerances between the two parts, the danger of key failure is smaller. Additionally, the manufacturing process is easier.

In table 6.1, a first step in the implementation of bistable interlocks in engineering practice is presented. The table is divided into different key shapes and interface treatments based on the results of the tensile response. It should be noted that this is only based on the results of the present study; further loading conditions and design exploration are necessary.

Table 6.1: Possible applications involving straight and bistable interlocked keys

Straight untreated keys	*Straight lubricated keys*
Shear keys	Shear keys Structures susceptible to imposed deformation (resistance at higher strain levels)
Curved untreated keys	*Curved lubricated*
Not different than the straight untreated case	Protective structures against impact loads (energy dissipation) Earthquake resistance structures (energy dissipation) Connections (reducing tensile reinforcement) Prefab to prefab connections (demountability) Structures susceptible to imposed deformation (resistance at higher strain levels)

References

[1] M. Luković. "Influence of Interface and Strain Hardening Cementitious Composite (SHCC) Properties on the Performance of Concrete Repairs". PhD thesis.

[2] Fédération internationale du béton. *Model code 2010 : first complete draft.* Fédération internationale du béton, 2010. ISBN: 9782883940956.

[3] P. Wang et al. "Research on bonding and shrinkage properties of SHCC-repaired concrete beams". In: *Materials* 13.7 (Apr. 2020). ISSN: 19961944. DOI: 10.3390/ma13071757.

[4] S. Mustafa et al. "Experimental and numerical investigation on the role of interface for crack-width control of hybrid SHCC concrete beams". In: *Engineering Structures* 251 (Jan. 2022). ISSN: 18737323. DOI: 10.1016/j.engstruct.2021.113378.

[5] R. O. Ritchie. "The conflicts between strength and toughness". In: *Nature Materials* 10.11 (2011), pp. 817–822. ISSN: 14764660. DOI: 10.1038/nmat3115.

[6] I. A. Malik, M. Mirkhalaf, and F. Barthelat. "Bio-inspired "jigsaw"-like interlocking sutures: Modeling, optimization, 3D printing and testing". In: *Journal of the Mechanics and Physics of Solids* 102 (May 2017), pp. 224–238. ISSN: 00225096. DOI: 10.1016/j.jmps.2017.03.003.

[7] M. Mirkhalaf and F. Barthelat. "Design, 3D printing and testing of architectured materials with bistable interlocks". In: *Extreme Mechanics Letters* 11 (Feb. 2017), pp. 1–7. ISSN: 23524316. DOI: 10.1016/j.eml.2016.11.005.

[8] V. Li. "Tensile strain hardening behavior of polyvinyl alcohol engineered cementitious composite (PVA-ECC)". In: *ACI Materials Journal* (Nov. 2001).

[9] E. Lin et al. "3D printed, bio-inspired prototypes and analytical models for structured suture interfaces with geometrically-tuned deformation and failure behavior". In: *Journal of the Mechanics and Physics of Solids* 73 (Dec. 2014), pp. 166–182. ISSN: 00225096. DOI: 10.1016/j.jmps.2014.08.011.

[10] M. K. Ahamed, H. Wang, and P. J. Hazell. *From biology to biomimicry: Using nature to build better structures – A review.* Feb. 2022. DOI: 10.1016/j.conbuildmat.2021.126195.

[11] F. Barthelat. *Architectured materials in engineering and biology: Fabrication, structure, mechanics and performance.* Nov. 2015. DOI: 10.1179/1743280415Y.0000000008.

[12] M. Mirkhalaf et al. "Toughness by segmentation: Fabrication, testing and micromechanics of architectured ceramic panels for impact applications". In: *International Journal of Solids and Structures* 158 (Feb. 2019), pp. 52–65. ISSN: 00207683. DOI: 10.1016/j.ijsolstr.2018.08.025.

[13] Y. Zhang et al. "Bio-inspired interfacial strengthening strategy through geometrically interlocking designs". In: *Journal of the Mechanical Behavior of Biomedical Materials* 15 (2012), pp. 70–77. ISSN: 18780180. DOI: 10.1016/j.jmbbm.2012.07.006.

[14] A. V. Dyskin et al. "Fracture resistant structures based on topological interlocking with non-planar contacts". In: *Advanced Engineering Materials* 5.3 (Mar. 2003), pp. 116–119. ISSN: 14381656. DOI: 10.1002/adem.200390016.

[15] A. Molotnikov et al. "Design of responsive materials using topologically interlocked elements". In: *Smart Materials and Structures* 24.2 (Feb. 2015). ISSN: 1361665X. DOI: 10.1088/0964-1726/24/2/025034.

[16] A. V. Dyskin et al. "A new principle in design of composite materials: Reinforcement by interlocked elements". In: *Composites Science and Technology* 63.3-4 (Feb. 2003), pp. 483–491. ISSN: 02663538. DOI: 10.1016/S0266-3538(02)00228-2.

[17] A. Söderberg. "Interface modeling : Friction and Wear". PhD thesis. 2009. ISBN: 9789174152159.

[18] J. S. McFarlane and D. Tabor. "Friction and Adhesion". In: (Jan. 1950).

[19] J. T. Oden and J. A. C. Martins. "Models and Computational Methods for Dynamic Friction Phenomena". In: *COMPUTER METHODS IN APPLIED MECHANICS AND ENGINEERING*. Vol. 52. 1985, pp. 527–634.

[20] John G. L. "Tribology". In: *Primer on Flat Rolling: Second Edition*. Elsevier, Jan. 2014, pp. 193–266. ISBN: 978-0-08-099418-5. DOI: 10.1016/B978-0-08-099418-5.00009-3.

[21] G. Sheng Chen and X. Liu. "Friction Dynamics". In: *Friction Dynamics*. Elsevier, 2016, pp. 91–159. DOI: 10.1016/B978-0-08-100285-8.00003-1. URL: https://linkinghub.elsevier.com/retrieve/pii/B9780081002858000031.

[22] A. E. Jiménez and M. D. Bermúdez. "Friction and Wear". In: *Tribology for Engineers*.

[23] B. Bhushan. "Contact mechanics of rough surfaces in tribology: multiple asperity contact". In: *Tribology Letters* 4 (1998), pp. 1–35.

[24] S. Yazawa, I. Minami, and B. Prakash. "Reducing friction and wear of tribological systems through hybrid tribofilm consisting of coating and lubricants". In: *Lubricants* 2.2 (June 2014), pp. 90–112. ISSN: 20754442. DOI: 10.3390/lubricants2020090.

[25] B. Bissonnette, M. A. Vaysburd, and F. K. von Fay. *Best Practices for Preparing Concrete Surfaces Prior to Repairs and Overlays*. Tech. rep. U.S. Department of the Interior Bureau of Reclamation, 2012.

[26] Clímaco J. C. T. S. and P. E. Regan. "Evaluation of bond strength between old and new concrete in structural repairs". In: (2001).

[27] B. Bissonnette et al. *Bonded Cement-Based Material Overlays for the Repair, the Lining or the Strengthening of Slabs or Pavements*. Tech. rep. URL: www.springer.com/series/8780.

[28] J. Silfwerbrand. "Shear bond strength in repaired concrete structures". In: *Materials and Structures* 36.6 (July 2003), pp. 419–424. ISSN: 1359-5997. DOI: 10.1007/bf02481068.

[29] ASTM International. *Tensile Strength of Concrete Surfaces and the Bond Strength or Tensile Strength of Concrete Repair and Overlay Materials by Direct Tension (Pull-off Method)*. Tech. rep. 2009. URL: www.astm.org,.

[30] D. S. Santos, P. M. D. Santos, and D. Dias Da Costa. "Effect of surface preparation and bonding agent on the concrete-to-concrete interface strength". In: *Construction and Building Materials* 37 (Dec. 2012), pp. 102–110. ISSN: 09500618. DOI: 10.1016/j.conbuildmat.2012.07.028.

[31] E. N. Brito and S. Júlio. "Interface Shear Transfer on Composite Concrete Members". In: *ACI Structural Journal* (2014). URL: https://www.researchgate.net/publication/267211456.

[32] European Committee for Standardisation. *EN 1992-1-1: Eurocode 2: Design of concrete structures - Part 1-1: General rules and rules for buildings*. Tech. rep. 2004.

[33] S. Mustafa, S. Singh, and M. Luković. "Effect Of Interface Treatment On The Cracking Behaviour Of Hybrid SHCC (Strain Hardening Cementitious Composite) Concrete Beams". In: *Citation*. 2020, pp. 456–462.

[34] S. Omairey, N. Jayasree, and M. Kazilas. "Defects and uncertainties of adhesively bonded composite joints". In: *SN Applied Sciences* 3.9 (Sept. 2021). ISSN: 25233971. DOI: 10.1007/s42452-021-04753-8.

[35] A. Hamilton et al. "Enhancing strength and toughness of adhesive joints via micro-structured mechanical interlocking". In: *International Journal of Adhesion and Adhesives* 105 (Mar. 2021). ISSN: 01437496. DOI: 10.1016/j.ijadhadh.2020.102775.

[36] M. Amiri and M. Farahani. "Adhesive composite joint reinforcement using button shape interlocking features". In: *International Journal of Adhesion and Adhesives* 102 (Oct. 2020), p. 102651. ISSN: 0143-7496. DOI: 10.1016/J.IJADHADH.2020.102651.

[37] G. van Zijl et al. "Durability of strain-hardening cement-based composites (SHCC)". In: *RILEM Bookseries* 15 (2018), pp. iii–iv. ISSN: 22110852. DOI: 10.1007/978-94-024-1194-2.

[38] V. C. Li, D. K. Mishra, and H-C. Wu. *Matrix design for pseudo-strain-hardening fibre reinforced cementitious composites*. Tech. rep. 1995, pp. 586–595.

[39] Z. Lin and V. C. Li. *Crack Bridging in Fiber Reinforced Cementitious Composites with Slip-Hardening Interfaces*. Tech. rep. 5. 1997, pp. 63–181.

[40] F. Jiang et al. *Tensile strain-hardening cementitious composites and its practical exploration without reinforcement: A review*. Tech. rep. Dec. 2022. DOI: `10.3389/fmats.2022.1066796`.

[41] G. Van Zijl and F. Wittmann. *Durability of Strain-Hardening Fibre-Reinforced Cement-Based Composites (SHCC)*. Tech. rep. 2011. URL: `www.springer.com/series/8780`.

[42] A. Bentur and S. Mindess. *Fibre reinforced cementitious composites*. Taylor & Francis, 2007, p. 601. ISBN: 9780415250481.

[43] J. Zhou et al. "Development of engineered cementitious composites with limestone powder and blast furnace slag". In: *Materials and Structures/Materiaux et Constructions* 43.6 (July 2010), pp. 803–814. ISSN: 13595997. DOI: `10.1617/s11527-009-9549-0`.

[44] J. Campbell. "Fracture of solids". In: *The Mechanisms of Metallurgical Failure*. Elsevier, 2020, pp. 193–271. DOI: `10.1016/b978-0-12-822411-3.00003-4`.

[45] C.V. Li et al. "Interface Tailoring for Strain-hardening (PVA-ECC)". In: *ACI Materials Journal* (2002).

[46] V. C. Li. "Tailoring ECC for Special Attributes: A Review". In: *International Journal of Concrete Structures and Materials* 6.3 (Sept. 2012), pp. 135–144. ISSN: 22341315. DOI: `10.1007/s40069-012-0018-8`.

[47] D. Kumar and R. Ranade. "Development of strain-hardening cementitious composites utilizing slag and calcium carbonate powder". In: (). DOI: `10.1016/j.conbuildmat.2020.122028`. URL: `https://doi.org/10.1016/j.conbuildmat.2020.122028`.

[48] Y. J. Kim. *Advanced Composites in Bridge Construction and Repair*, p. 640. ISBN: 9780857097675.

[49] M. Luković et al. "Strain hardening cementitious composite (SHCC) for crack width control in reinforced concrete beams". In: *Heron* 64.2 (2019), pp. 189–206. URL: `http://heronjournal.nl/64-12/10.html`.

[50] H. R. Pakravan and T. Ozbakkaloglu. *Synthetic fibers for cementitious composites: A critical and in-depth review of recent advances*. May 2019. DOI: `10.1016/j.conbuildmat.2019.02.078`.

[51] K. Q. Yu et al. "Development of ultra-high performance engineered cementitious composites using polyethylene (PE) fibers". In: *Construction and Building Materials* 158 (Jan. 2018), pp. 217–227. ISSN: 09500618. DOI: `10.1016/j.conbuildmat.2017.10.040`.

[52] A. Zhou et al. "Interfacial technology for enhancement in steel fiber reinforced cementitious composite from nano to macroscale". In: *Nanotechnology Reviews* 10.1 (Jan. 2021), pp. 636–652. ISSN: 21919097. DOI: `10.1515/ntrev-2021-0037`.

[53] S. Zhang. "Micromechanics-guided development of strain-hardening alkali-activated composites Towards a low-carbon built environment". In: (2022). DOI: `10.4233/uuid:cdea2e9d-e069-4683-a8ca-c436b43fa64c`. URL: `https://doi.org/10.4233/uuid:cdea2e9d-e069-4683-a8ca-`.

[54] I. Curoşu. "Influence of Fiber Type and Matrix Composition on the Tensile Behavior of Strain-Hardening Cement-Based Composites (SHCC) under Impact Loading". PhD thesis.

[55] G. Van Zijl and G. Song. "Tailoring ECC For Commercial Application". In: (2017). URL: `https://www.researchgate.net/publication/250285119`.

[56] Y. Wang et al. "Effect of polyethylene fiber content on physical and mechanical properties of engineered cementitious composites". In: *Construction and Building Materials* 251 (Aug. 2020). ISSN: 09500618. DOI: `10.1016/j.conbuildmat.2020.118917`.

[57] W. Chen, X. Ji, and Z. Huang. "Influence of fiber type on mechanical properties of lightweight cement-based composites". In: *Science and Engineering of Composite Materials* 28.1 (Jan. 2021), pp. 249–263. ISSN: 21910359. DOI: `10.1515/secm-2021-0021`.

[58] H. Wang, Y. Mengzhu, and W. Yufan. "Closed-loop optimization and investigation of bistable interlocked structure". In: *International Journal of Mechanical Sciences* 144 (Aug. 2018), pp. 10–23. ISSN: 00207403. DOI: `10.1016/j.ijmecsci.2018.05.037`.

[59] S. He et al. "Effects of bacteria-embedded polylactic acid (PLA) capsules on fracture properties of strain hardening cementitious composite (SHCC)". In: *Engineering Fracture Mechanics* 268 (June 2022). ISSN: 00137944. DOI: `10.1016/j.engfracmech.2022.108480`.

[60]   Y. He et al. "Effects of interface roughness and interface adhesion on new-to-old concrete bonding". In: *Construction and Building Materials* 151 (Oct. 2017), pp. 582–590. ISSN: 09500618. DOI: `10.1016/j.conbuildmat.2017.05.049`.

[61]   European Committee for Standardization. "NEN-EN 197-1". In: ().

[62]   Y. Xu et al. "Cementitious cellular composites with auxetic behavior". In: *Cement and Concrete Composites* 111 (Aug. 2020), p. 103624. ISSN: 0958-9465. DOI: `10.1016/J.CEMCONCOMP.2020.103624`.

[63]   *What is FDM (fused deposition modeling) 3D printing?* URL: `https://www.hubs.com/knowledge-base/what-is-fdm-3d-printing/`.

[64]   European Committee for Standardization. *NEN-EN 196-1*. Tech. rep.

[65]   N. Raluca et al. "Experimental analysis of three tetra-anti-chiral auxetic honeycomb structures". In: *IOP Conference Series: Materials Science and Engineering*. Vol. 997. 1. IOP Publishing Ltd, Dec. 2020. DOI: `10.1088/1757-899X/997/1/012025`.

[66]   J. Zhao, Y. Sang, and F. Duan. "The state of the art of two-dimensional digital image correlation computational method". In: *Engineering Reports* 1.2 (Sept. 2019). ISSN: 25778196. DOI: `10.1002/eng2.12038`.

[67]   Impact research group. *Digital Image Correlation*. URL: `https://research.tuni.fi/impact/equipment/digital-image-correlation/`.

[68]   H. J. Bezemer. *The Effect of Height Scaling on the Flexural Crack Width Controlling Behavior of Hybrid R/SHCC Beams A Numerical and Experimental Study*. Tech. rep. URL: `http://repository.tudelft.nl/..`.

[69]   M. Luković et al. "Impact of Surface Roughness on the Debonding Mechanism in Concrete Repairs". In: *VIII International Conference on Fracture Mechanics of Concrete and Concrete Structures*.

A

Appendix A: Experimental Pre-study of straight and bistable interlocked key specimens

Since no documented experimental research on bistable interlocks in SHCC was found in the literature, it was deemed necessary to perform some small-scale tests before the main tests. These tests would investigate the feasibility and eliminate mistakes in the following experimental tests. Additionally, some initial results would be beneficial to check the initial hypothesis regarding the added ductility of the bistable interlock mechanism.

A.1. Initial specimen design

Four specimens were designed before the main tests. Two of them were straight keys with identical designs (Figure A.1a). The other two were bistable interlocked keys with identical designs (Figure A.1b).

(a) Straight key   (b) Curved keys
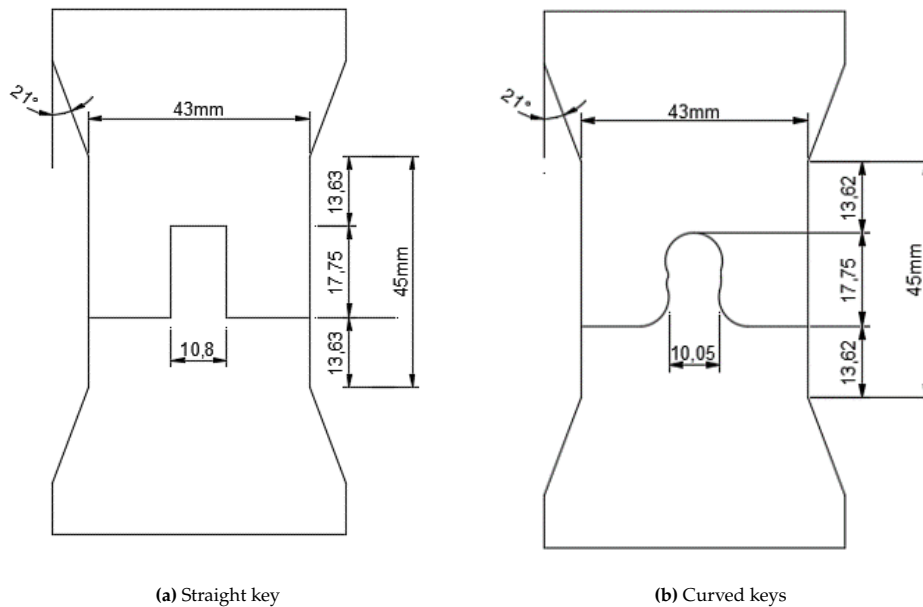
Figure A.1: Initial specimen design

A.2. SHCC casting

After the design and 3D printing of the specific geometries of the keys (with different width/height ratios and radii ratios), silicon molds were prepared to cast the keys in two parts, as shown in Figure A.2. When the first part was cast, it was left one day to harden at room temperature, and the second part was cast on top of the first one with the interface left untreated. The specimens were cured for 7 days in a curing room (20 ° C and ≥ 98% RH).

(a) Casting of the bottom part   **(b)** Casting of the top part
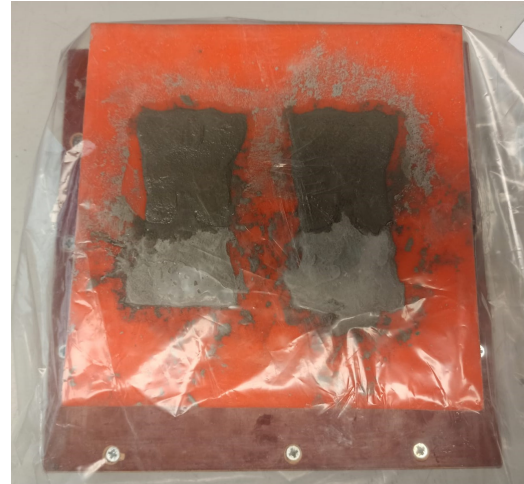
Figure A.2: Casting of top and bottom parts of straight and curved keys

A.3. Tensile tests

The samples were tested under monotonic tension using a servo-hydraulic testing machine (Instron® 8872) under displacement control at a rate of 0.005 mm/s. The displacements were measured with Digital Image Correlation (DIC) and verified with LVDT measurements as seen in Figure A.3.
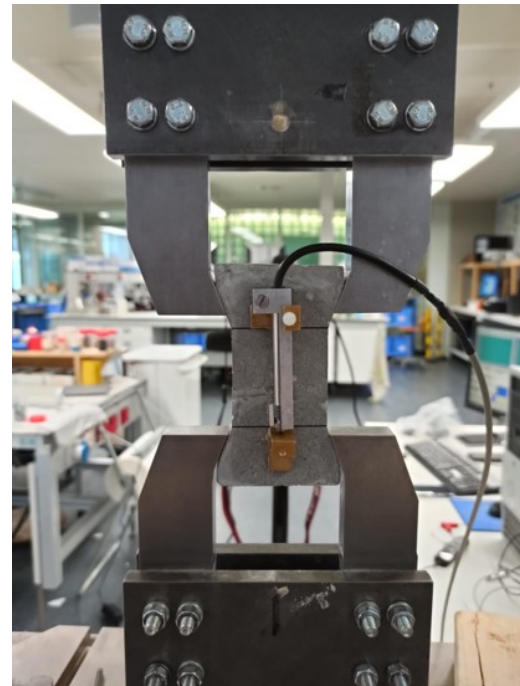
(a) Instron & DIC setup   **(b)** LVDT application

Figure A.3: Test setup

A.4. Results

The force-displacement graph for the curved and straight specimens is shown below. The force was extracted from the Instron output. For the displacement, 3 pairs of points were chosen in similar locations for the straight and curved keys as shown in Figure A.4.
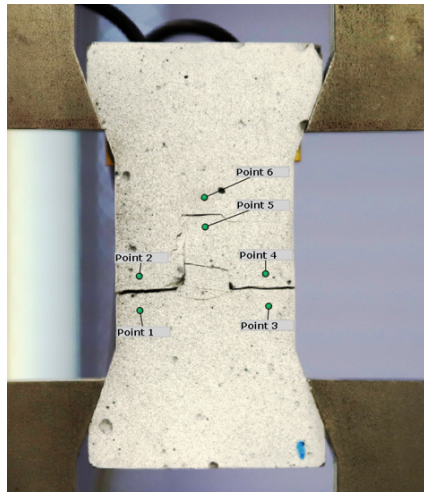
(a) Points chosen for displacement definition -straight key
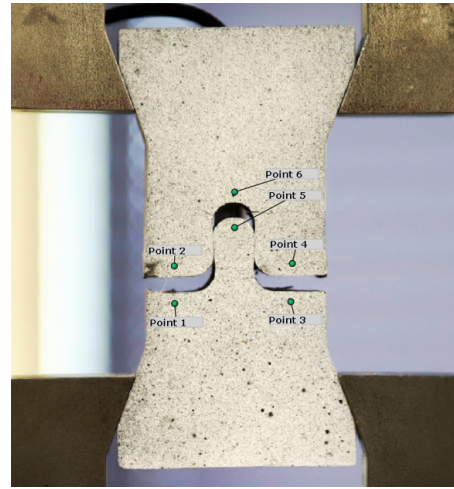
(b) Points chosen for displacement definition - curved key

Figure A.4: Sets of points to define the displacement for straight and curved specimens

The force-displacement graph for the straight key is shown in Figure A.5 and for the curved key in Figure A.7. There are 3 curves in each graph representing the displacements measured at different pairs of points (points 1-2, 3-4, 5-6). For each curve at 3 characteristic points along the curve, the strains and crack patterns are shown (Figure A.6, Figure A.8).
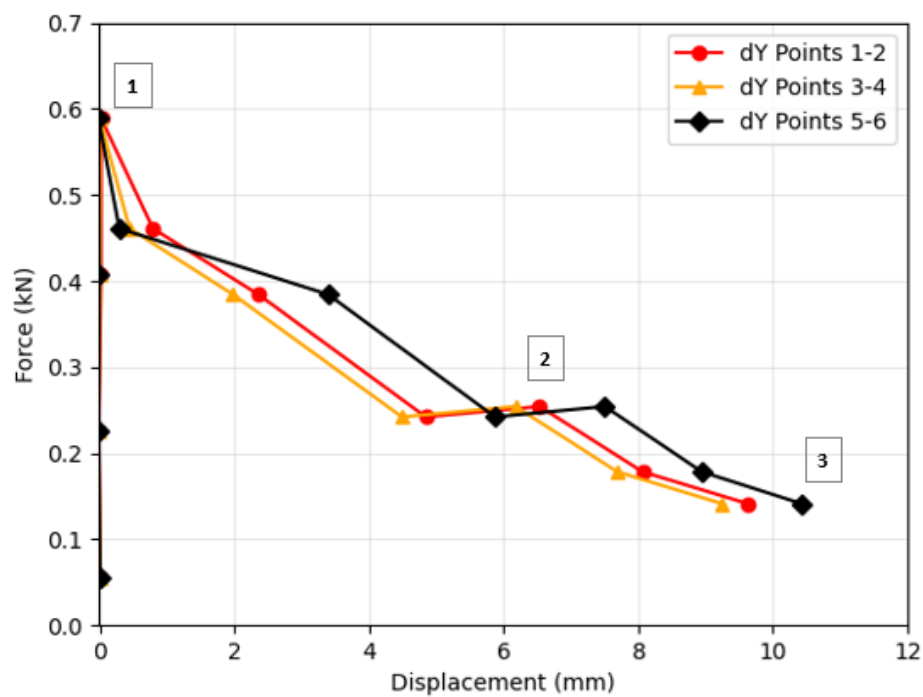
Figure A.5: Force - displacement graph - Straight key

(a) Strain contour at characteristic point 1   **(b)** Strain contour at characteristic point 2   **(c)** Strain contour at characteristic point 3
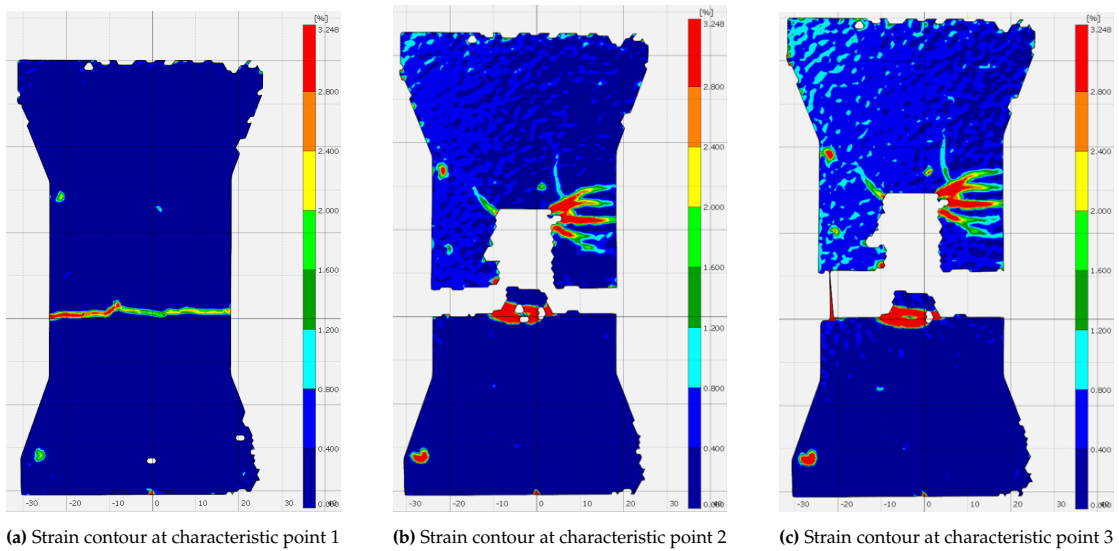
Figure A.6: Strain contour showing the crack propagation at the straight key at characteristic points 1-3
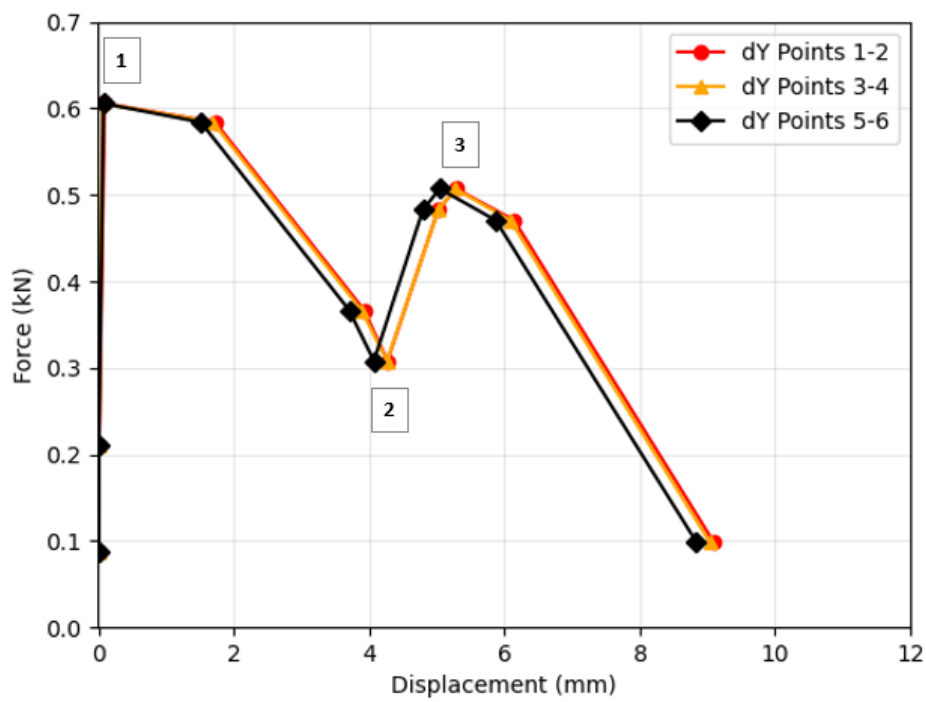
Figure A.7: Force - displacement graph - Curved key

(a) Strain contour at characteristic point 1   (b) Strain contour at characteristic point 2   (c) Strain contour at characteristic point 3
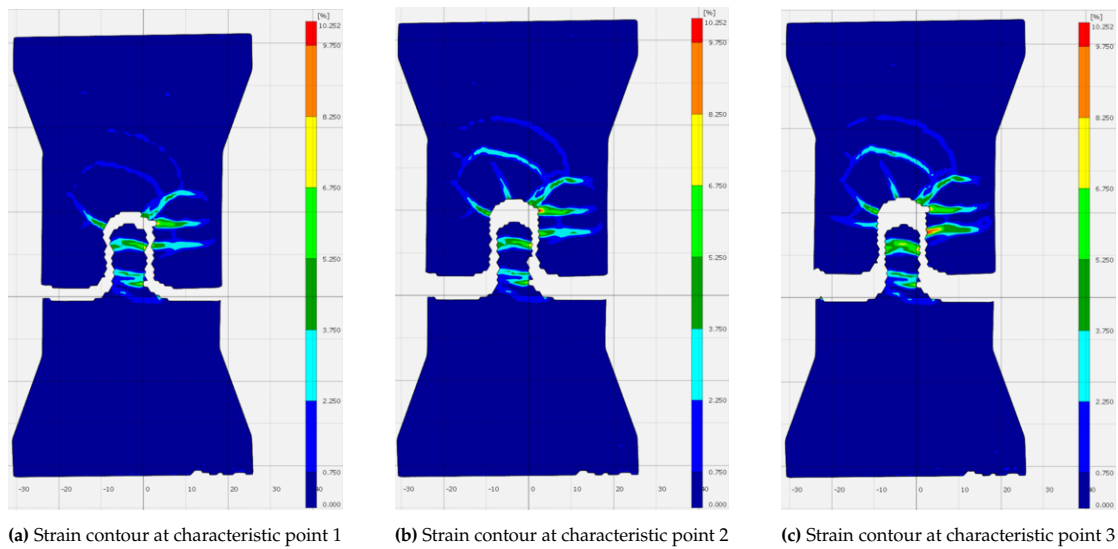
Figure A.8: Strain contours showing the crack propagation at the curved key at characteristic points 1-3

The area under the force-displacement curve, representing the work done by the force, is also a measure of the absorbed energy by the material. The ductility of the connection can be measured by evaluating the area under the graph. For ductile materials, the area tends to be larger since they can absorb more energy before failure.
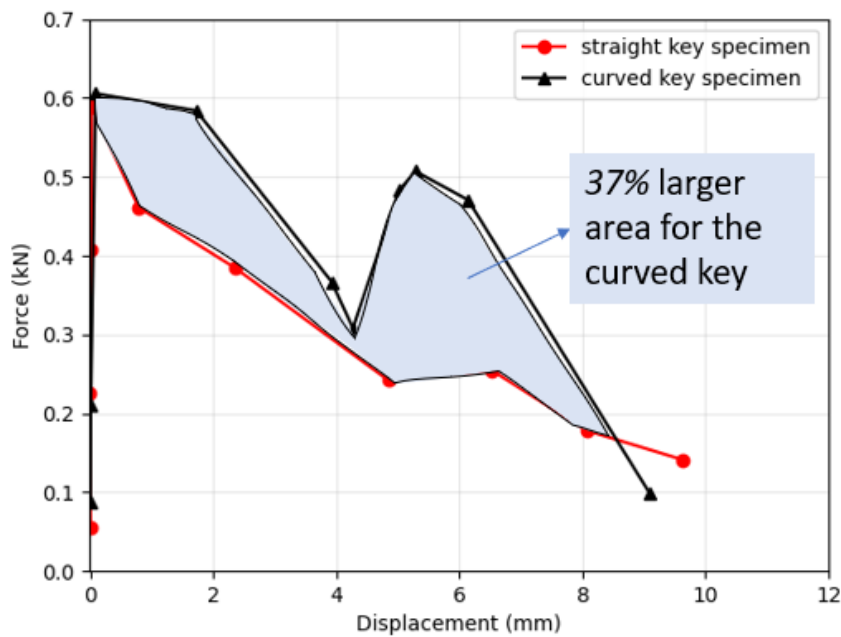
The curve for the straight key presents a **semi-brittle** failure (Figure A.5) while for the curved key, there is the characteristic shape with 2 equilibrium positions and two peaks (Figure A.7) as found in the literature ([7]). This **geometric hardening** behavior of the curved key results in roughly *37%* larger area under the F-δ curve compared to the straight key. Another benefit is that with the bistable interlock mechanism, there is essentially no sacrifice in force but only the addition of energy absorbed. Usually, these two properties are hard to combine and in some cases mutually exclusive.

This initial evaluation of the ductility shows promising results for the bistable interlocked key. The experimental procedure was followed with the rest of the samples with different surface treatments

and geometries to evaluate how these parameters affect the strength & toughness of the connections. Oppositely, the main specimens were cured for at least 28 days.

B

Appendix B: DIC analysis of all specimens

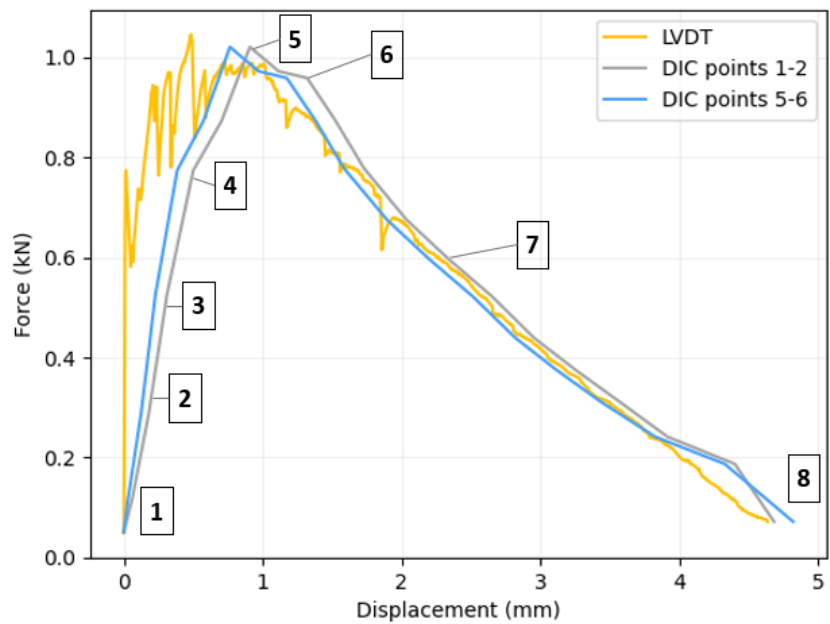### B.1. Specimen SCG12- Untreated interface, Geometry 1
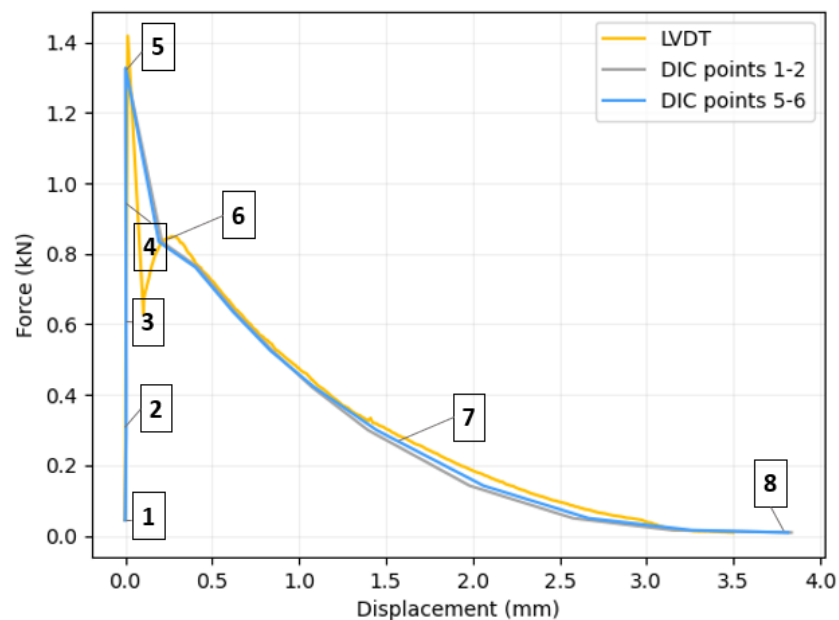
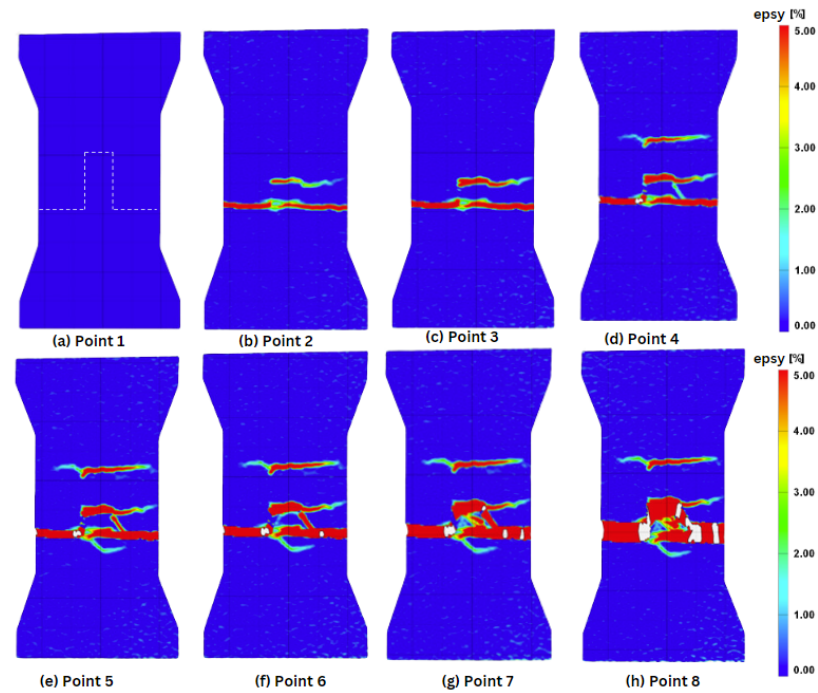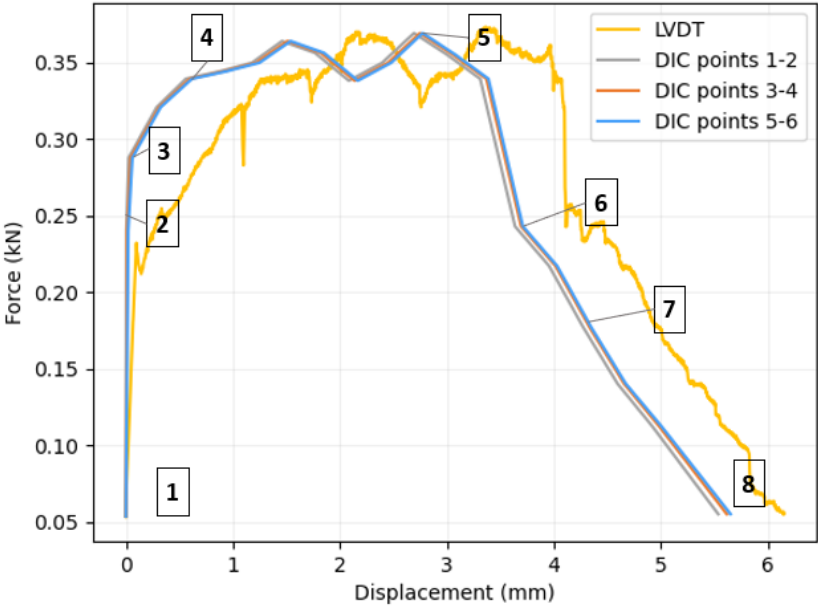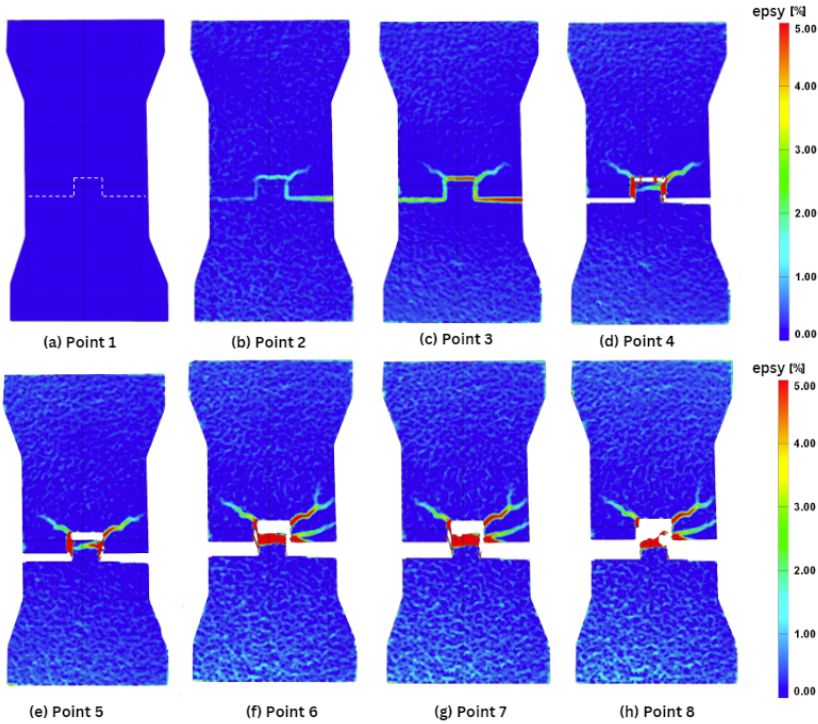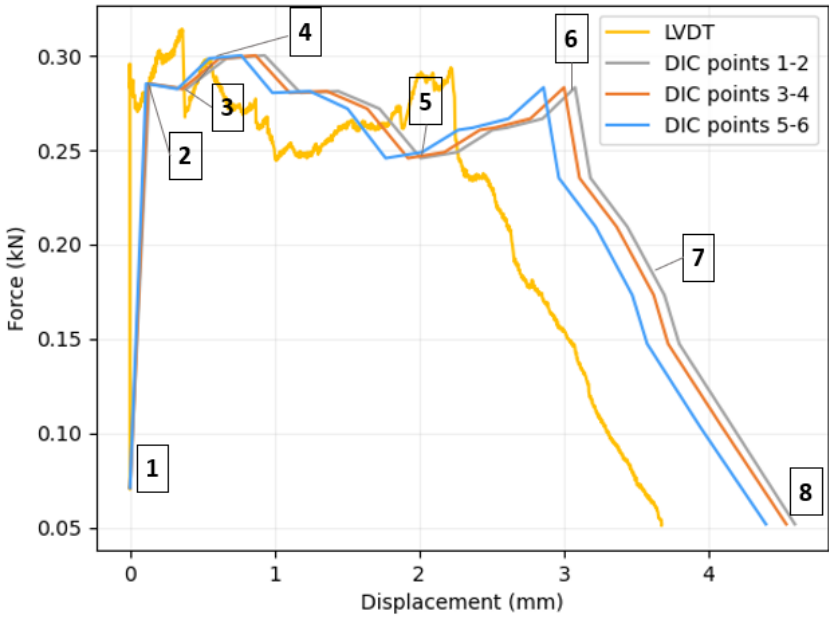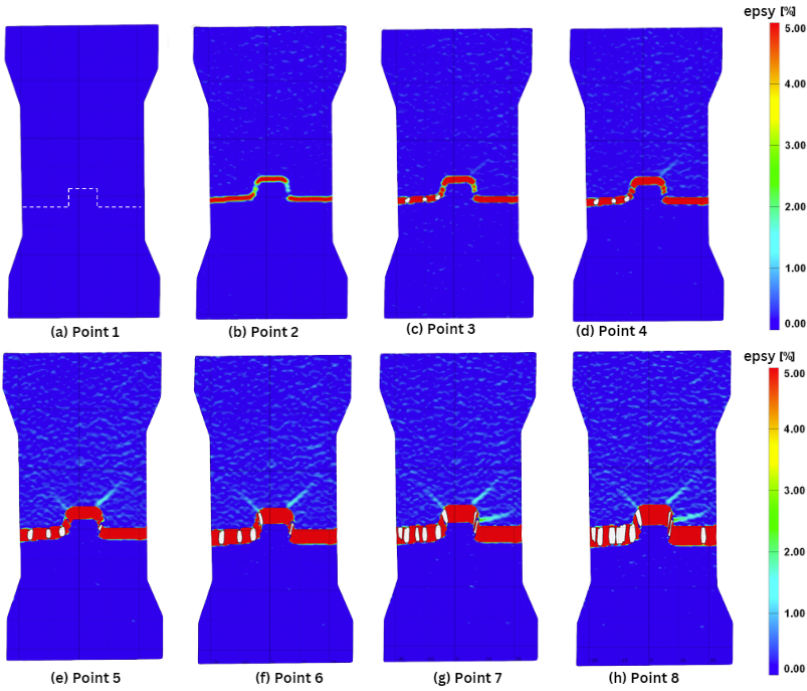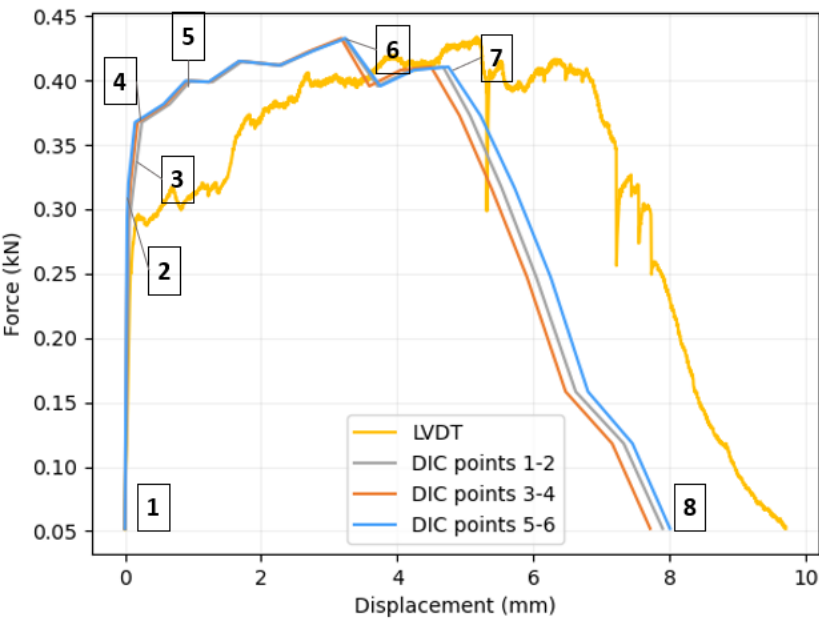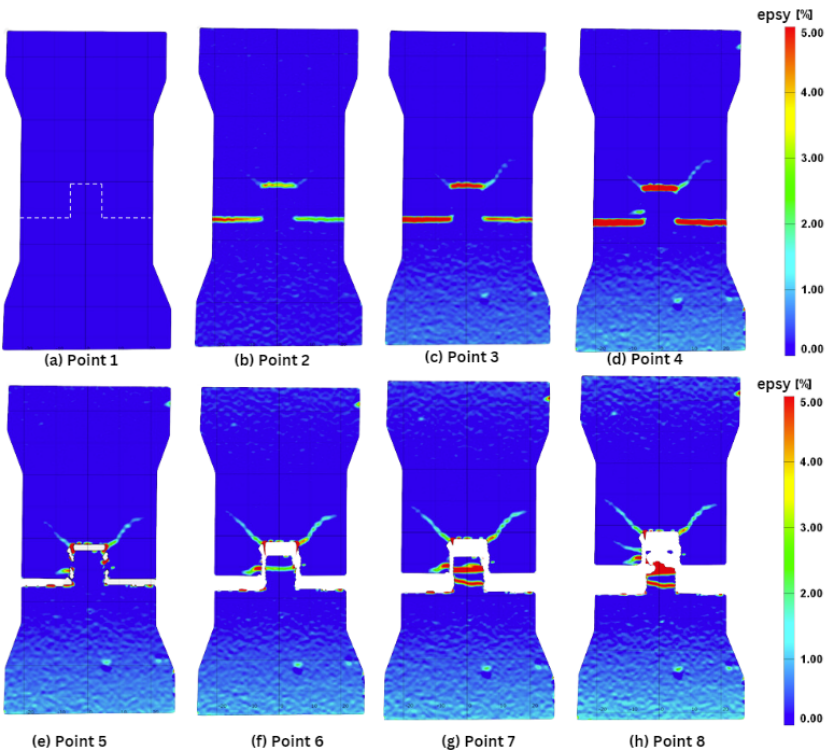**Figure B.1:** Force - displacement diagram illustrating the tensile response of the specimen SCG12
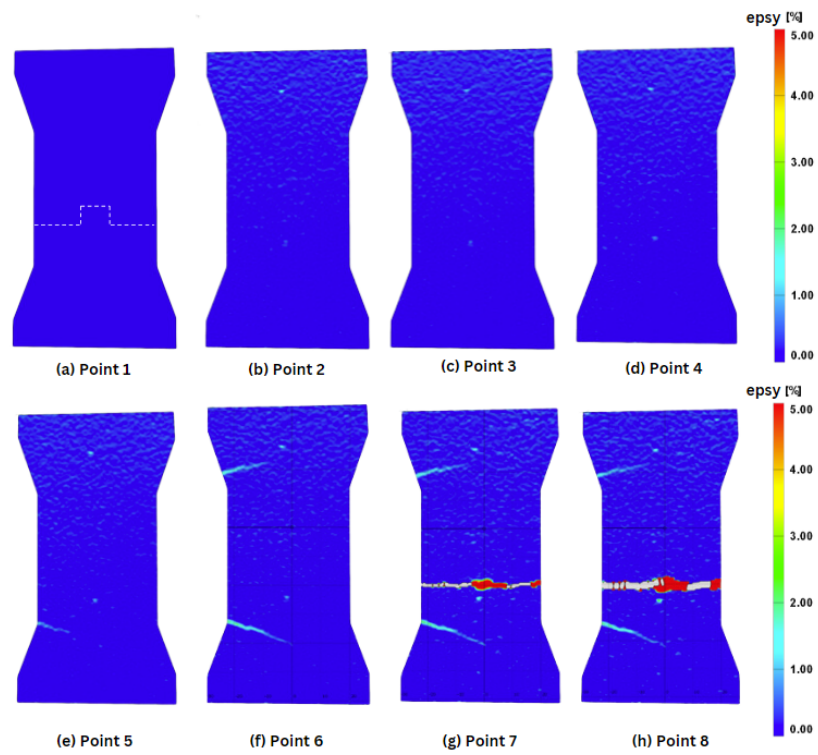
Figure B.2: Strain contours (ϵ_y) of points 1-8

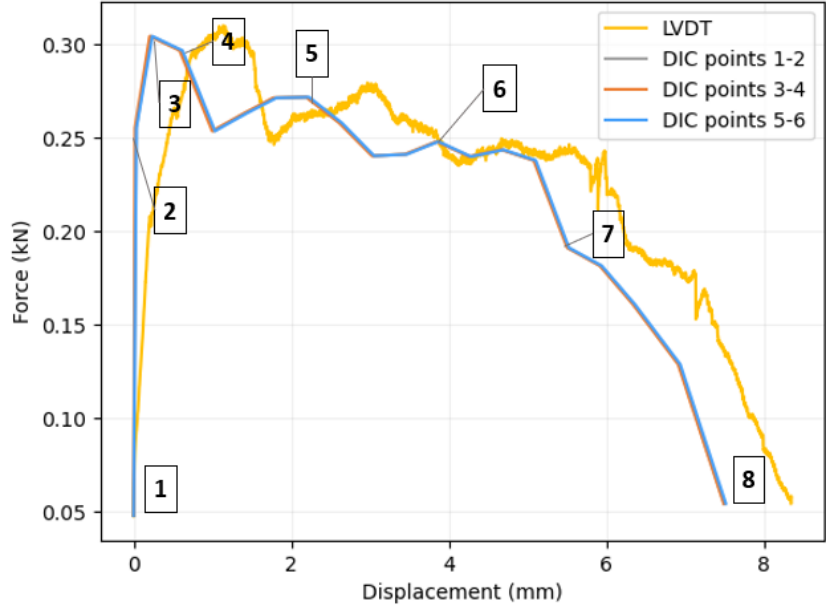## B.2. Specimen SCG13- Untreated interface, Geometry 1
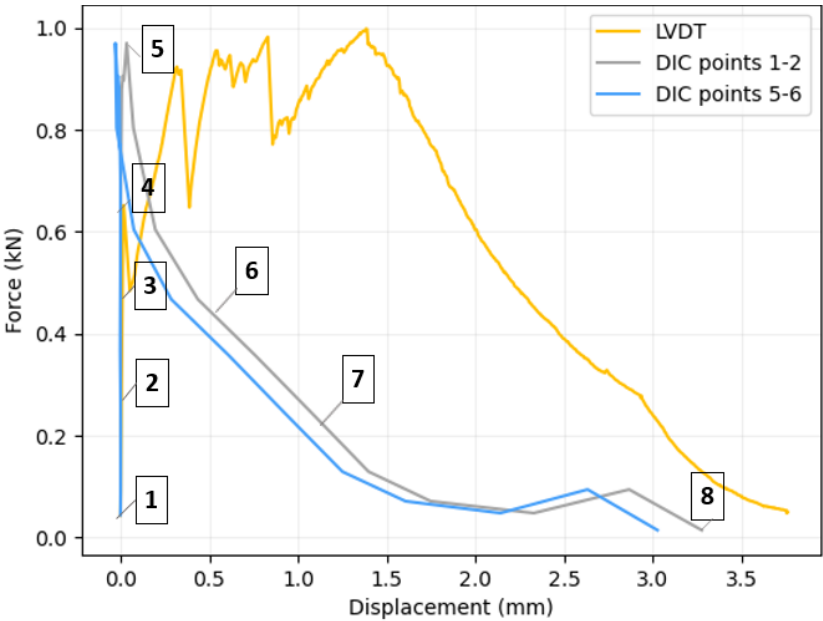
Figure B.3: Force - displacement diagram illustrating the tensile response of the specimen SCG13
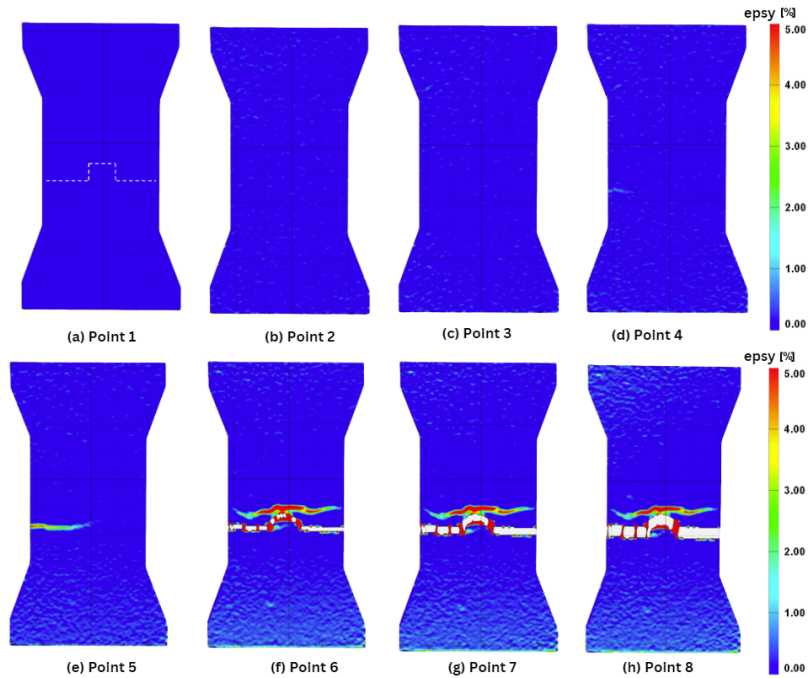
Figure B.4: Strain contours (ϵ_y) of points 1-8

B.3. Specimen SCG21- Untreated interface, Geometry 2
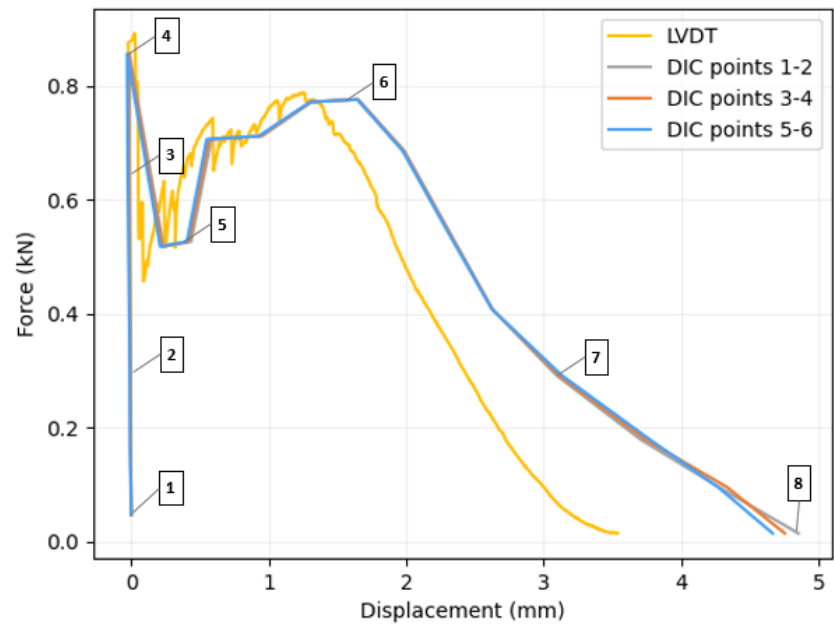
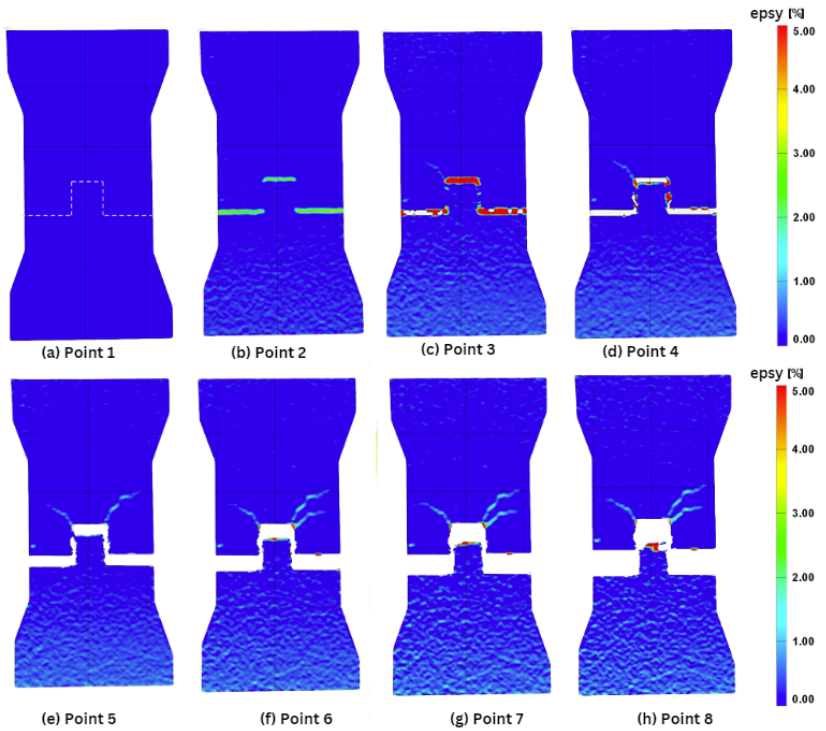**Figure B.5:** Force - displacement diagram illustrating the tensile response of the specimen SCG21
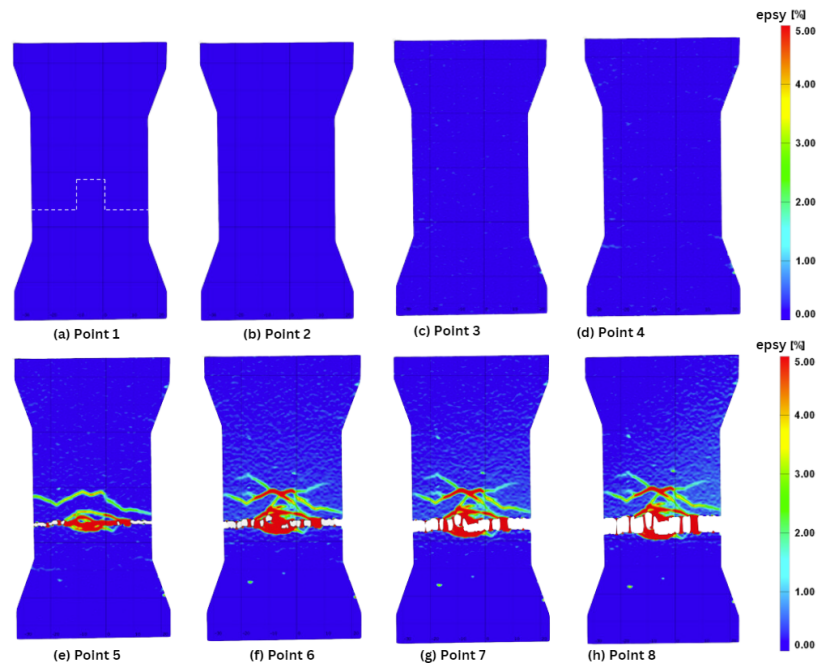
Figure B.6: Strain contours (ϵ_y) of points 1-8

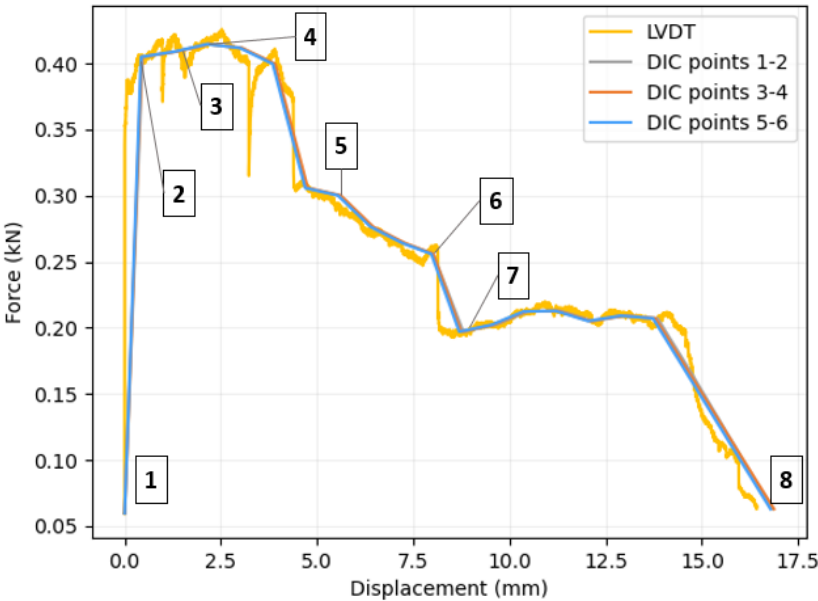## B.4. Specimen SCG23- Untreated interface, Geometry 2
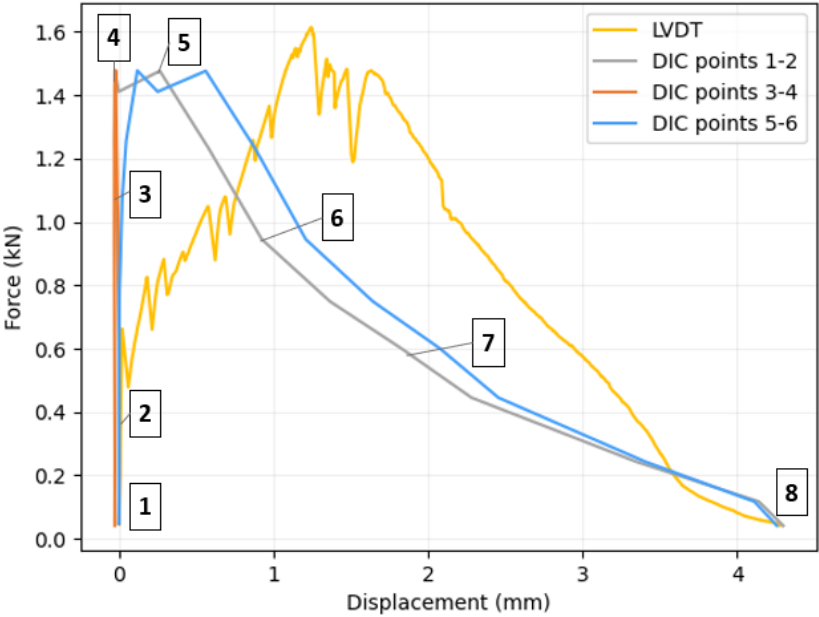
Figure B.7: Force - displacement diagram illustrating the tensile response of the specimen SCG23
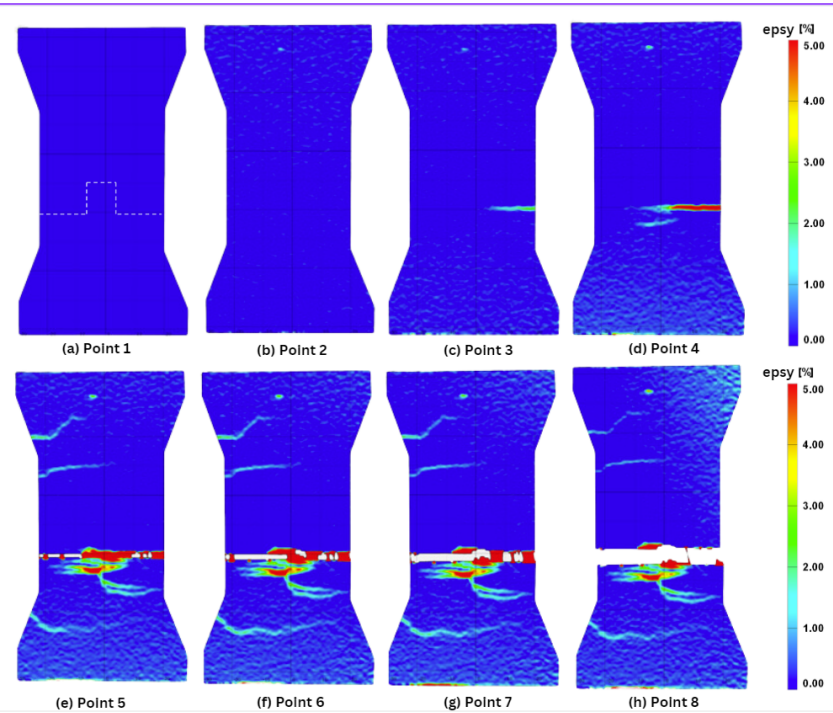
Figure B.8: Strain contours (ϵ_y) of points 1-8

B.5. Specimen SCG23- Untreated interface, Geometry 3
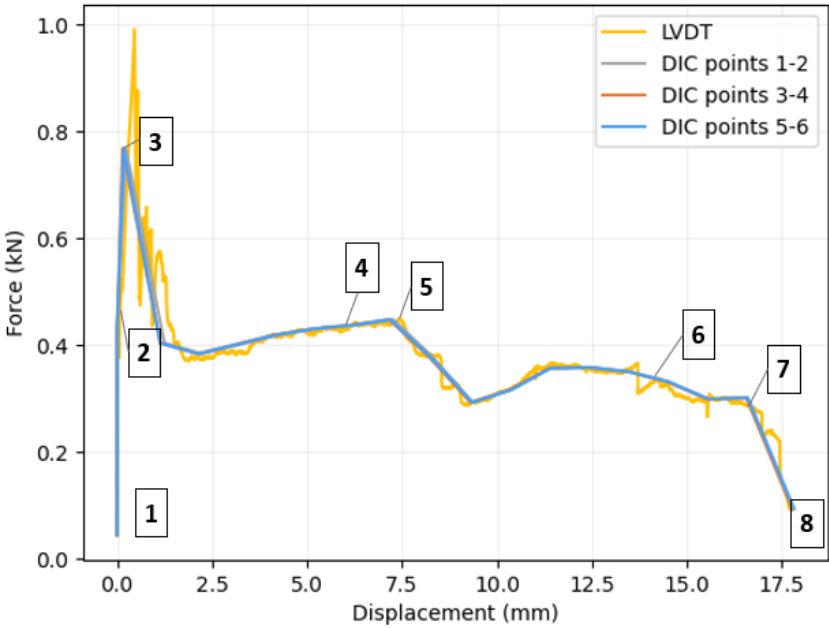
Figure B.9: Force - displacement diagram illustrating the tensile response of the specimen SCG32
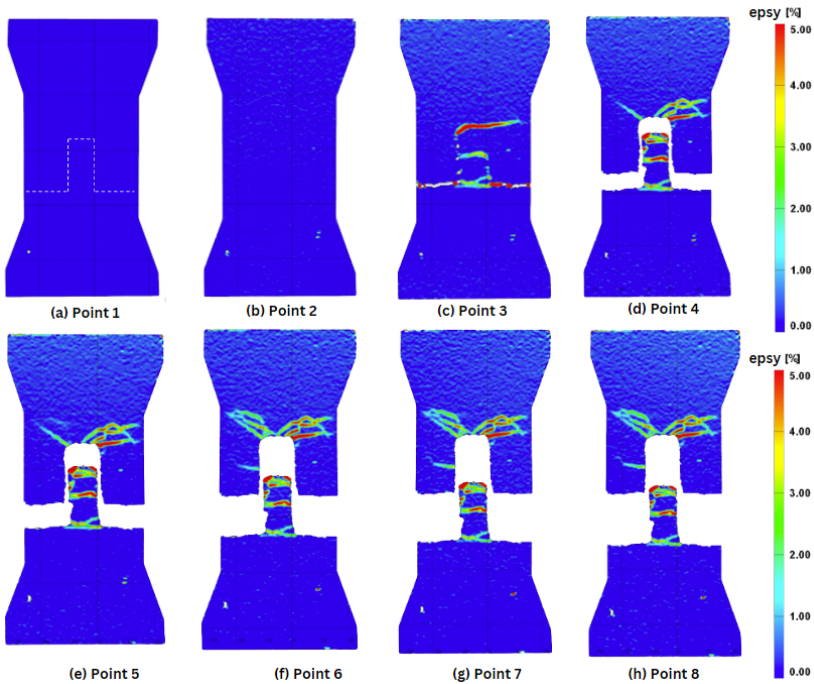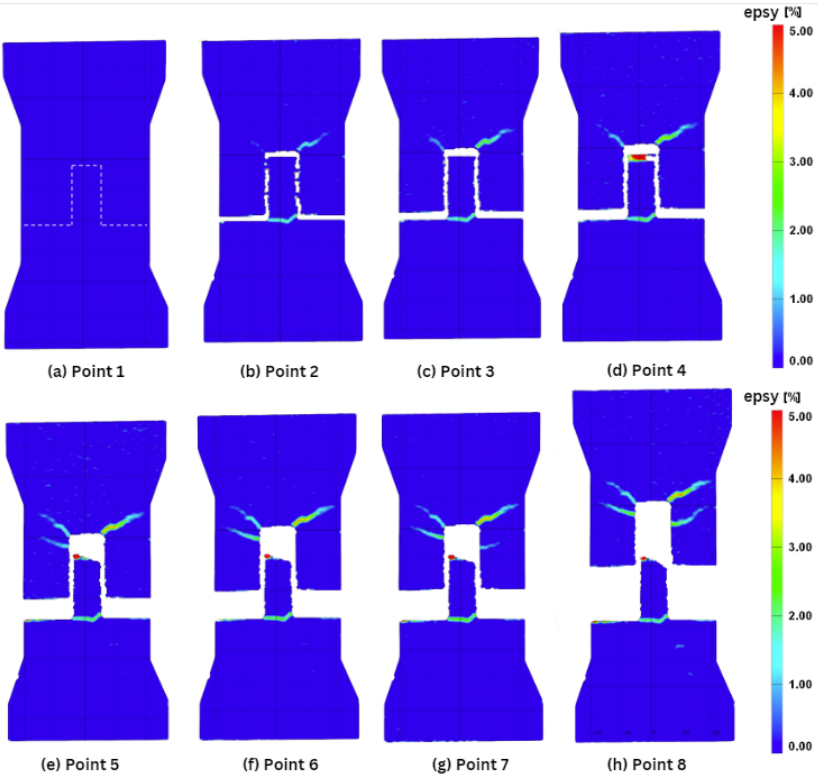

Figure B.10: Strain contours (ϵ_y) of points 1-8

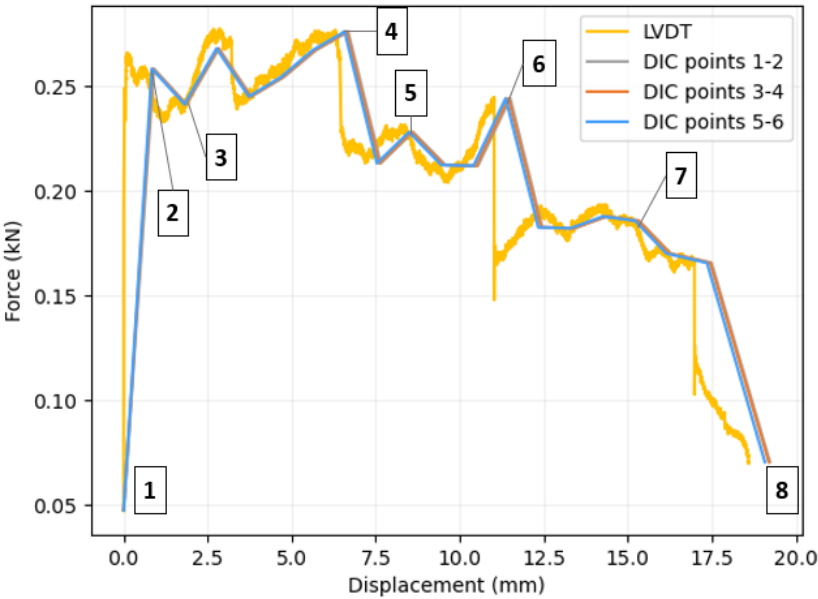## B.6. Specimen SCG33- Untreated interface, Geometry 3

Figure B.11: Force - displacement diagram illustrating the tensile response of the specimen SCG33

Figure B.12: Strain contours (ϵ_y) of points 1-8

B.7. Specimen SLG11- Lubricated interface, Geometry 1

Figure B.13: Force - displacement diagram illustrating the tensile response of the specimen SLG11
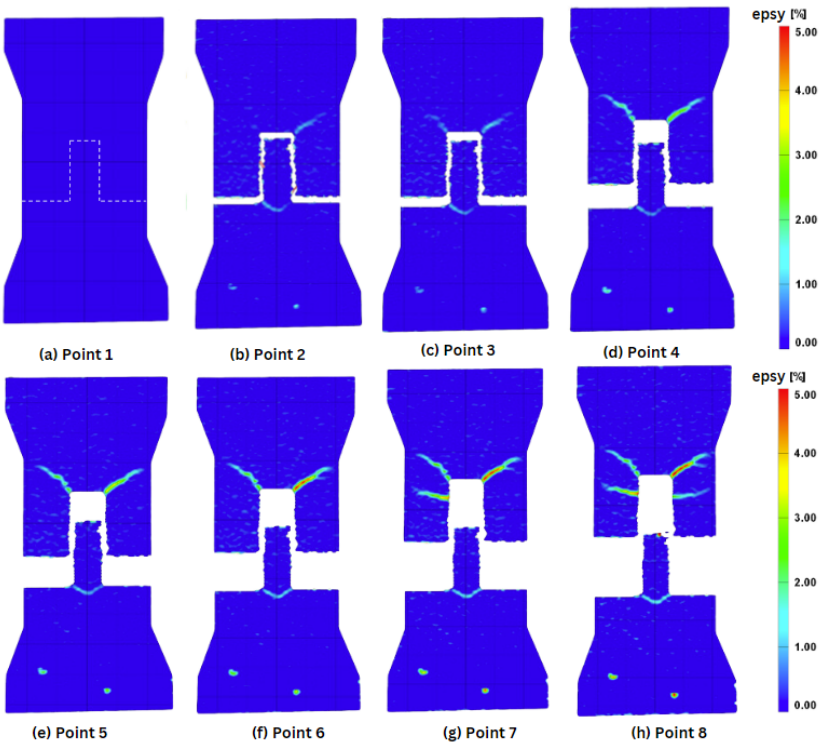

Figure B.14: Strain contours (ϵ_y) of points 1-8

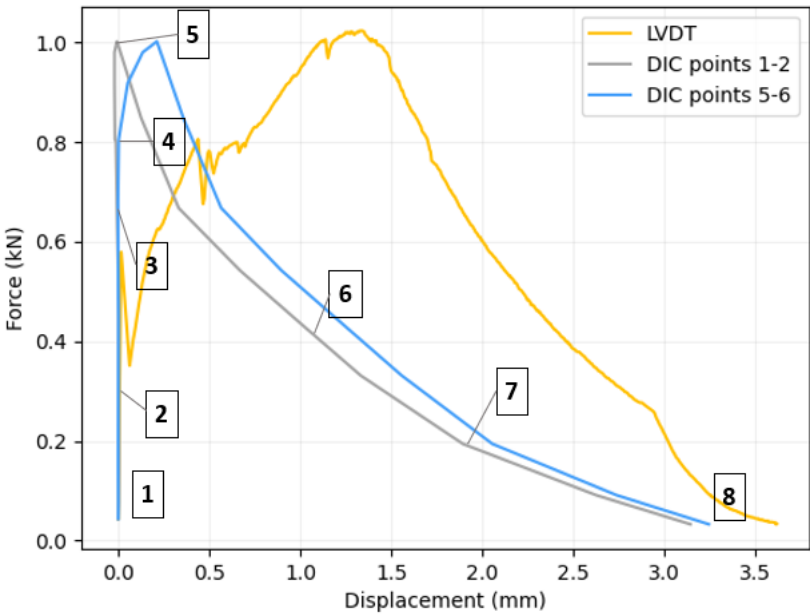## B.8. Specimen SLG13- Lubricated interface, Geometry 1

Figure B.15: Force - displacement diagram illustrating the tensile response of the specimen SLG13

Figure B.16: Strain contours (ϵ_y) of points 1-8

B.9. Specimen SLG13- Lubricated interface, Geometry 2

Figure B.17: Force - displacement diagram illustrating the tensile response of the specimen SLG21
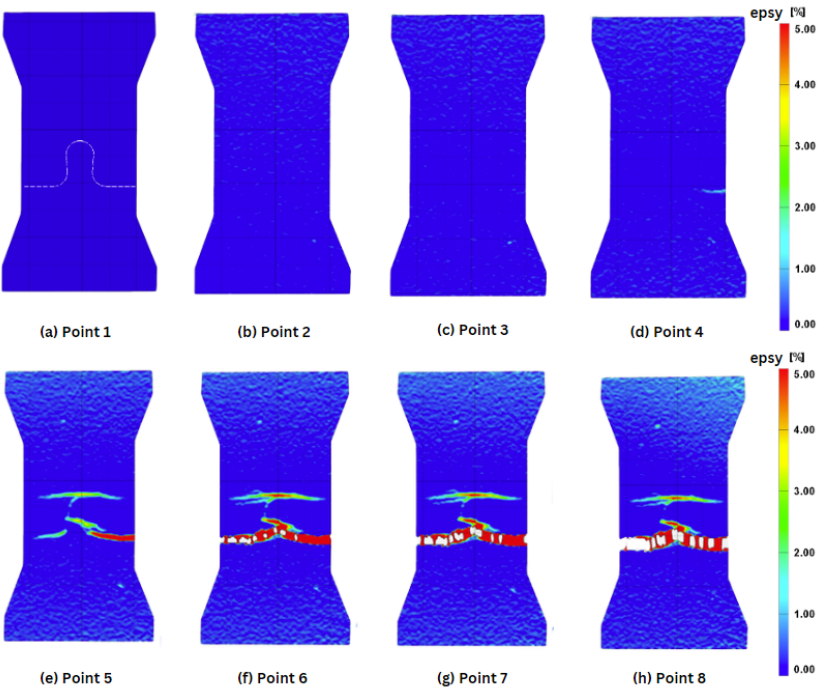

Figure B.18: Strain contours (ϵ_y) of points 1-8

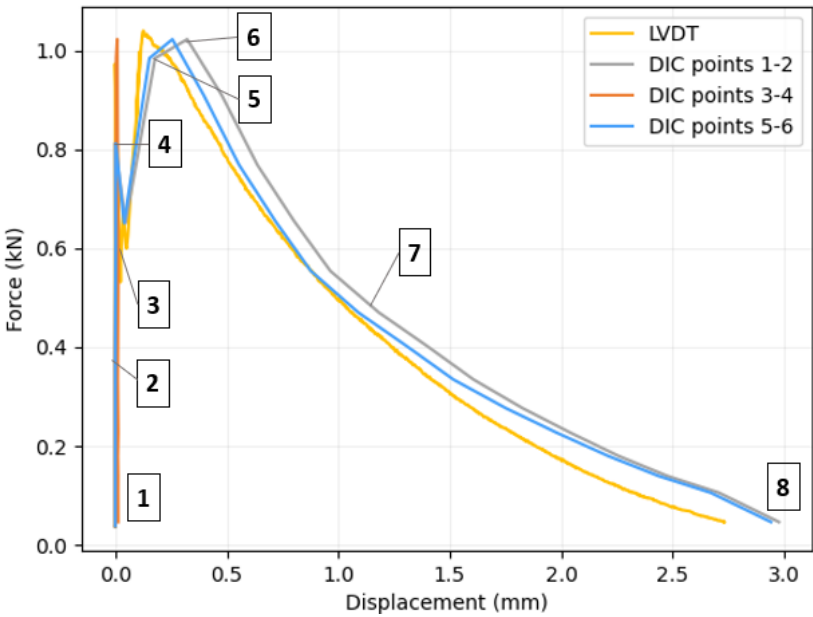## B.10. Specimen SLG23- Lubricated interface, Geometry 2

Figure B.19: Force - displacement diagram illustrating the tensile response of the specimen SLG23

Figure B.20: Strain contours (ϵ_y) of points 1-8

B.11. Specimen SLG23- Lubricated interface, Geometry 3

Figure B.21: Force - displacement diagram illustrating the tensile response of the specimen SLG32
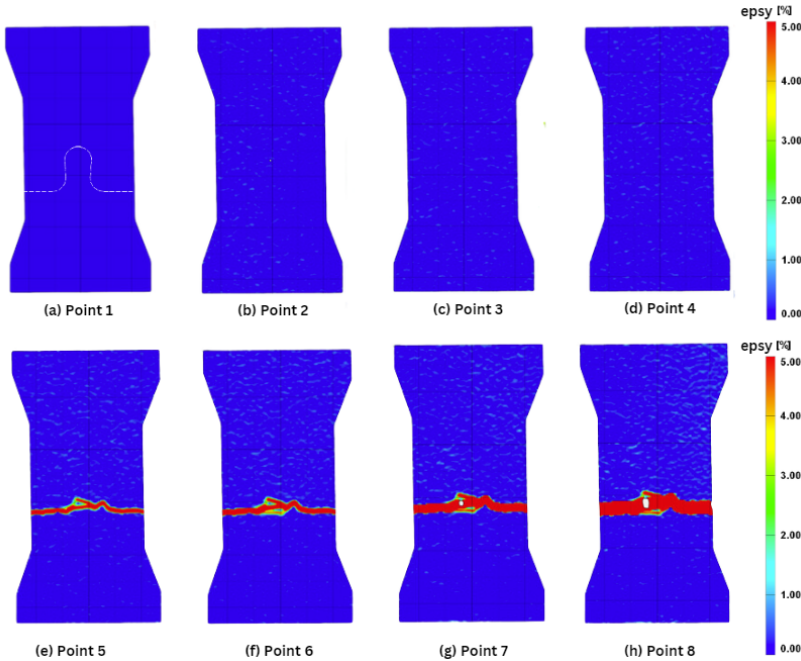

Figure B.22: Strain contours (ϵ_y) of points 1-8

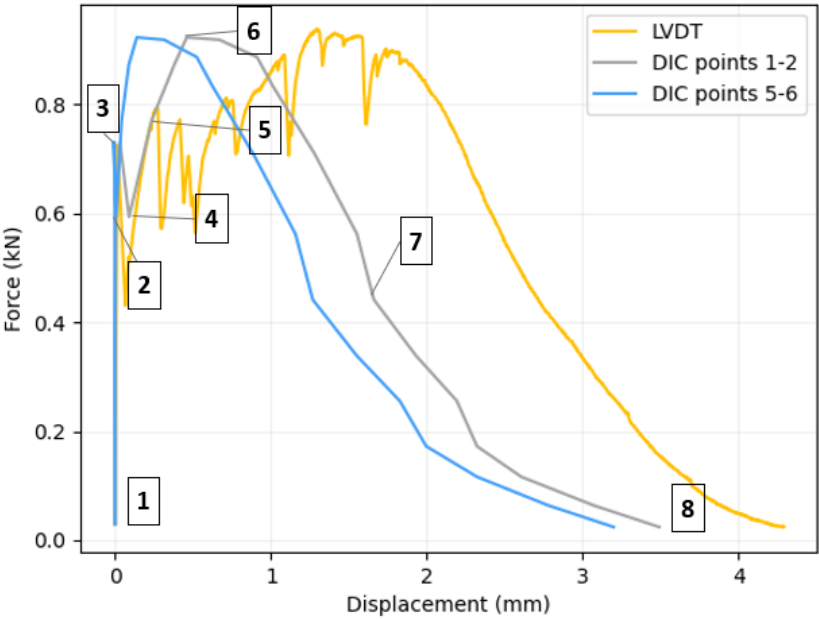## B.12. Specimen SLG33- Lubricated interface, Geometry 3

Figure B.23: Force - displacement diagram illustrating the tensile response of the specimen SLG33

Figure B.24: Strain contours (ϵ_y) of points 1-8

B.13. Specimen CCG12- Untreated interface, Geometry 1

Figure B.25: Force - displacement diagram illustrating the tensile response of the specimen CCG12


(a) Point 1   (b) Point 2   (c) Point 3   (d) Point 4

(e) Point 5   (f) Point 6   (g) Point 7   (h) Point 8

Figure B.26: Strain contours (ϵ_y) of points 1-8

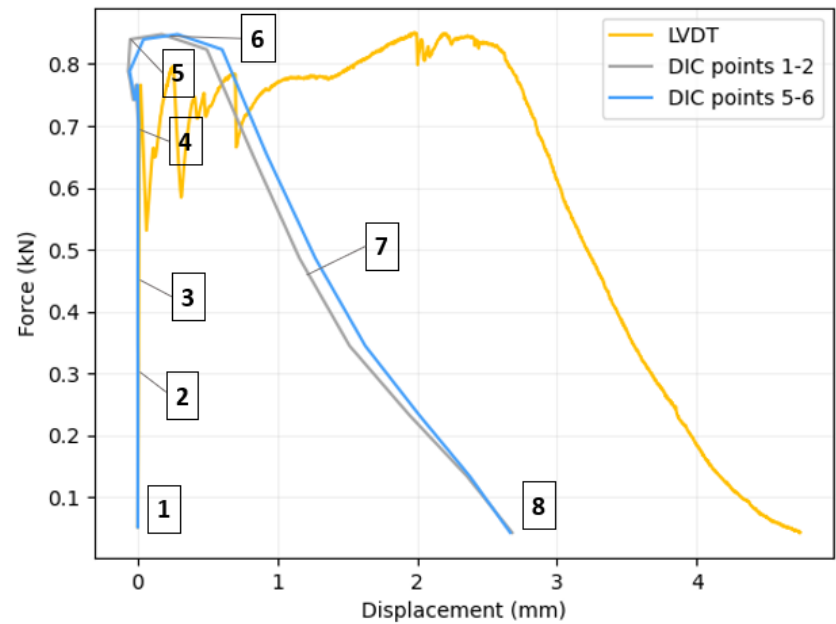## B.14. Specimen CCG13- Untreated interface, Geometry 1

Figure B.27: Force - displacement diagram illustrating the tensile response of the specimen CCG13

Figure B.28: Strain contours (ϵ_y) of points 1-8

B.15. Specimen CCG21- Untreated interface, Geometry 2

Figure B.29: Force - displacement diagram illustrating the tensile response of the specimen CCG21
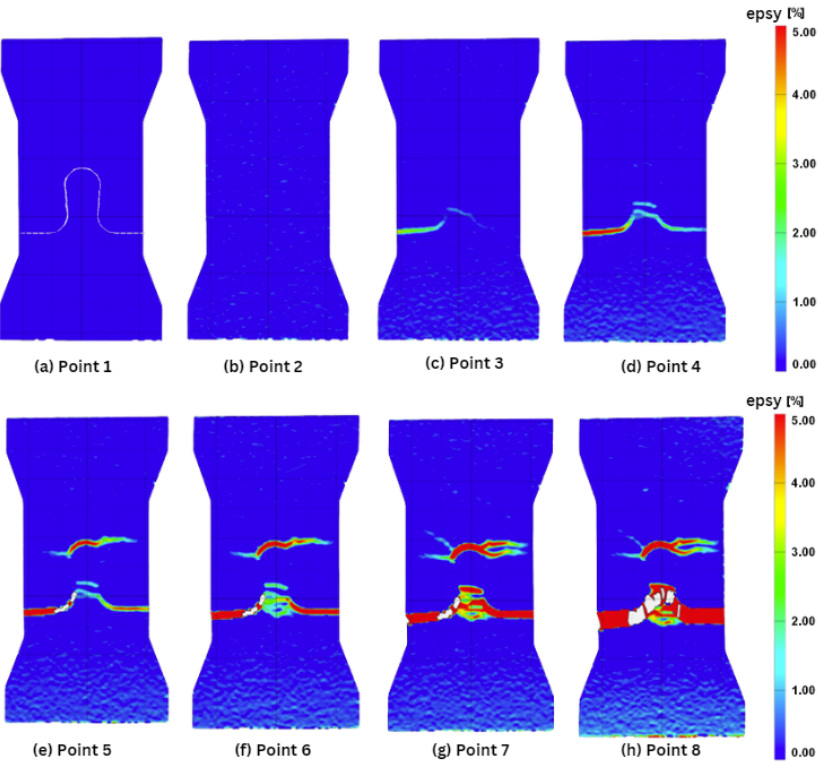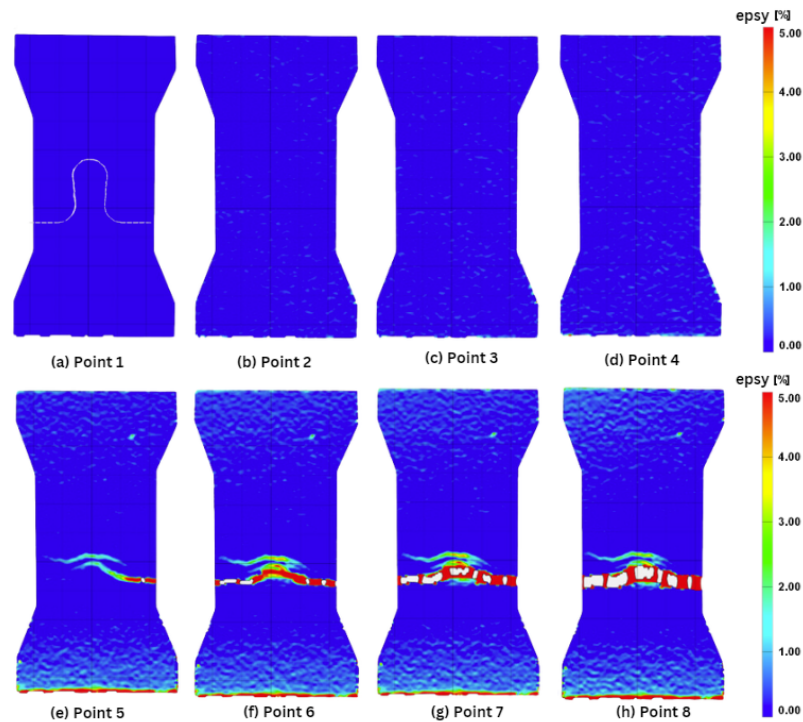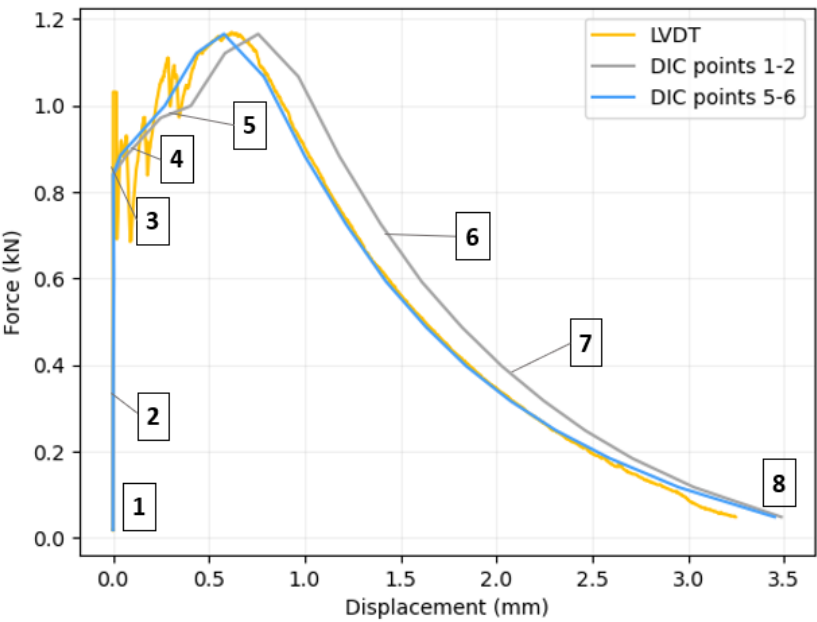

Figure B.30: Strain contours (ϵ_y) of points 1-8

B.16. Specimen CCG23- Untreated interface, Geometry 2

Figure B.31: Force - displacement diagram illustrating the tensile response of the specimen CCG23
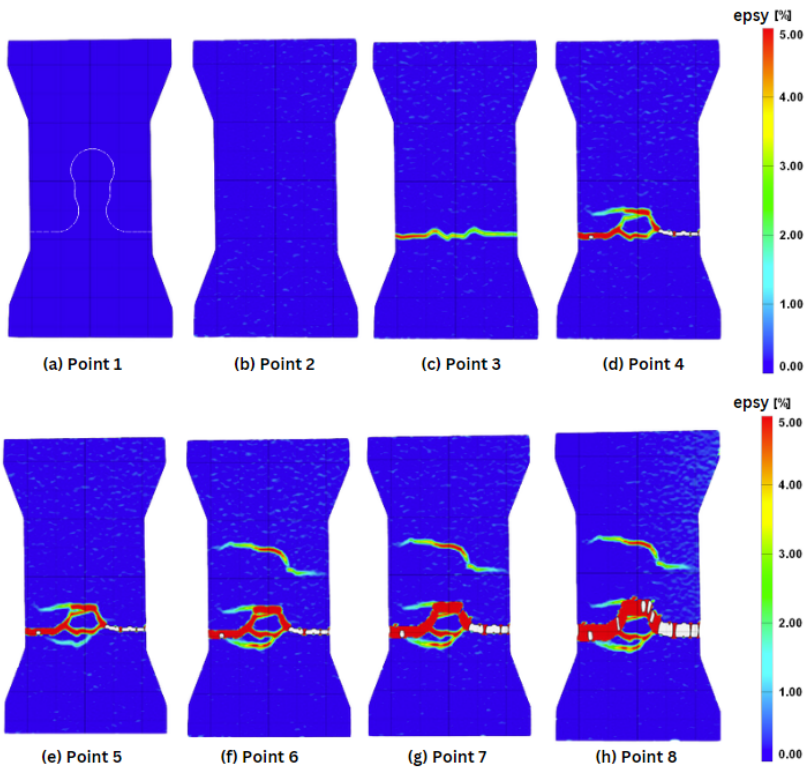

Figure B.32: Strain contours (ϵ_y) of points 1-8

B.17. Specimen CCG32- Untreated interface, Geometry 3

Figure B.33: Force - displacement diagram illustrating the tensile response of the specimen CCG32

Figure B.34: Strain contours (ϵ_y) of points 1-8

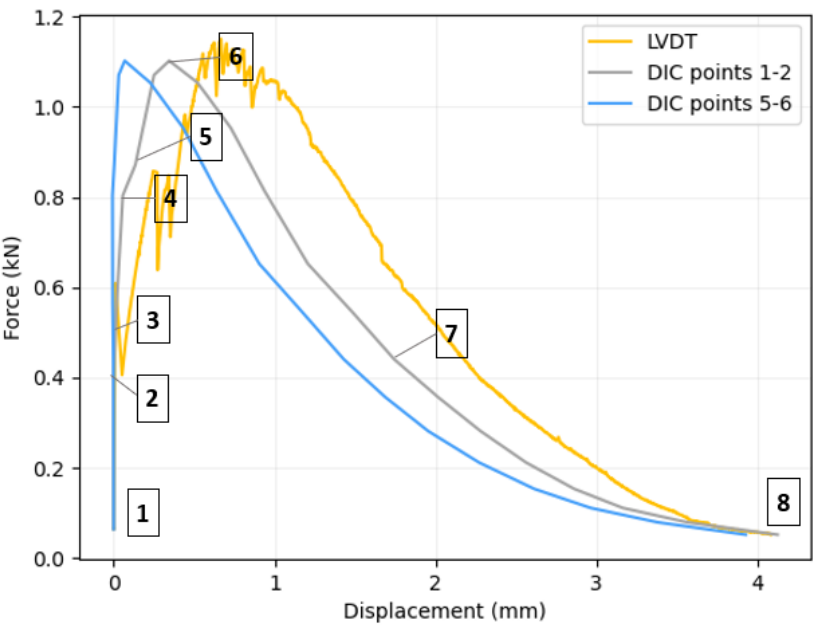## B.18. Specimen CCG33- Untreated interface, Geometry 3

Figure B.35: Force - displacement diagram illustrating the tensile response of the specimen CCG33
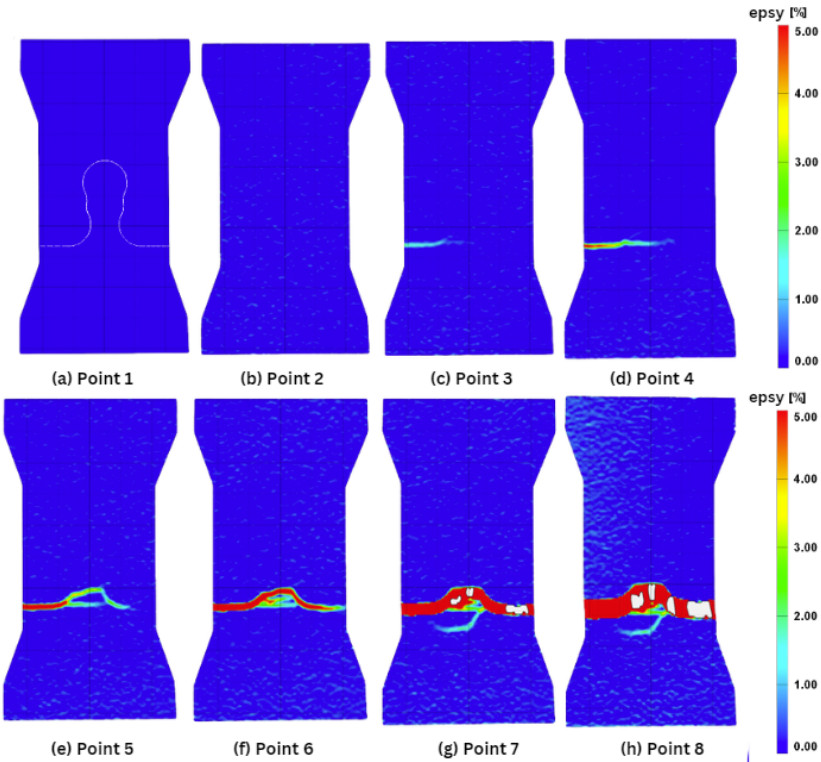

Figure B.36: Strain contours (ϵ_y) of points 1-8
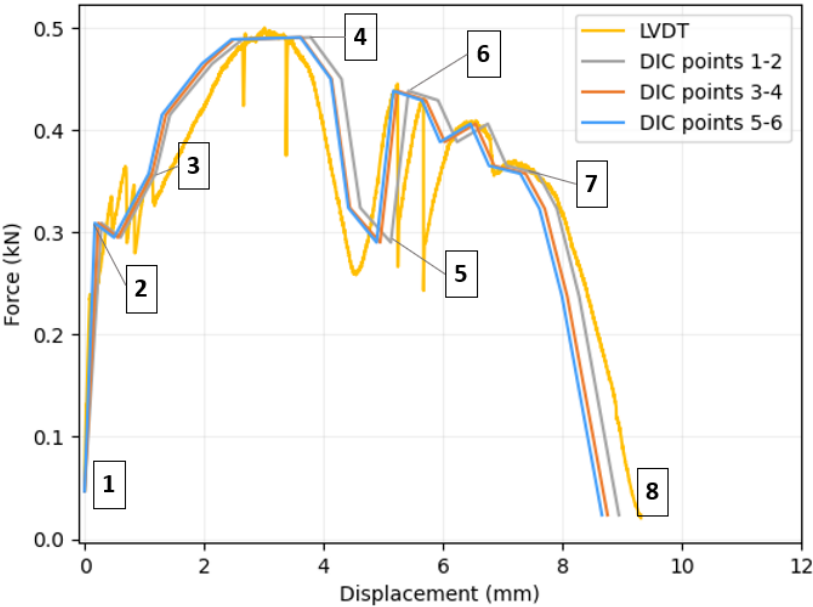
B.19. Specimen CLG11- Lubricated interface, Geometry 1

Figure B.37: Force - displacement diagram illustrating the tensile response of the specimen CLG11

Figure B.38: Strain contours (ϵ_y) of points 1-8

B.20. Specimen CLG13- Lubricated interface, Geometry 1

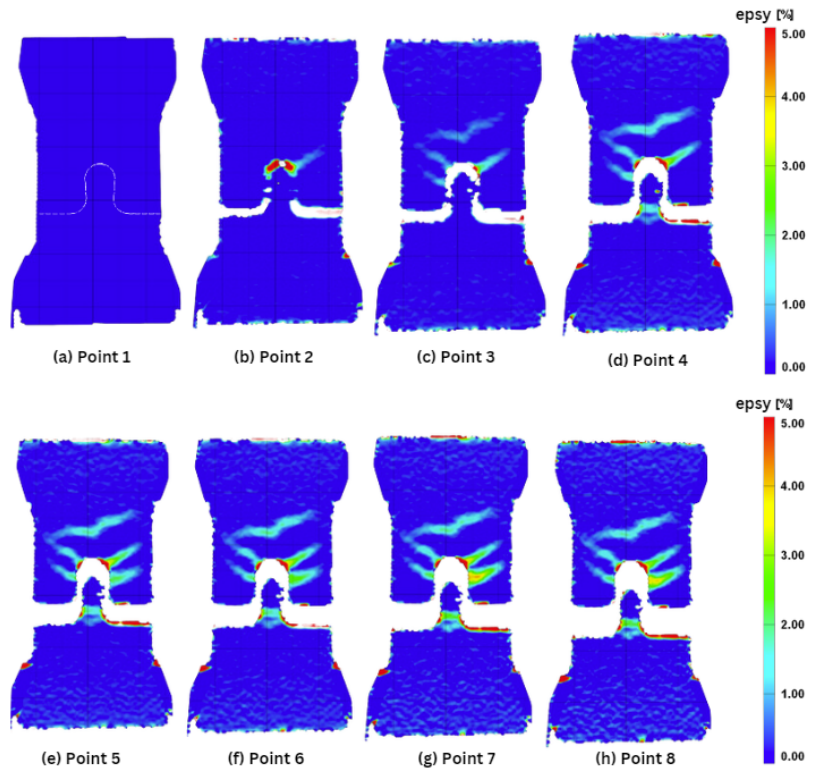**Figure B.39:** Force - displacement diagram illustrating the tensile response of the specimen CLG13

Figure B.40: Strain contours (ϵ_y) of points 1-8

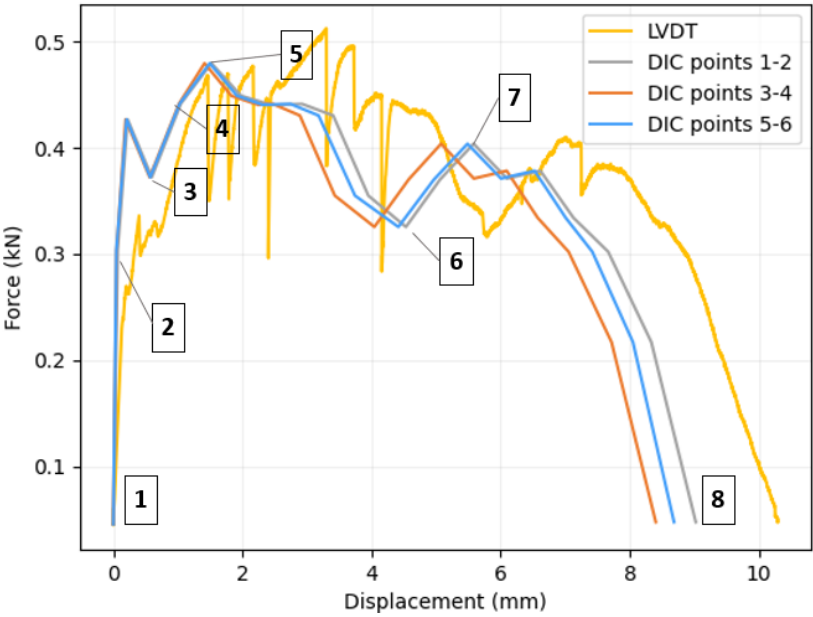## B.21. Specimen CLG21- Lubricated interface, Geometry 2

Figure B.41: Force - displacement diagram illustrating the tensile response of the specimen CLG21

Figure B.42: Strain contours (ϵ_y) of points 1-8

B.22. Specimen CLG23- Lubricated interface, Geometry 2

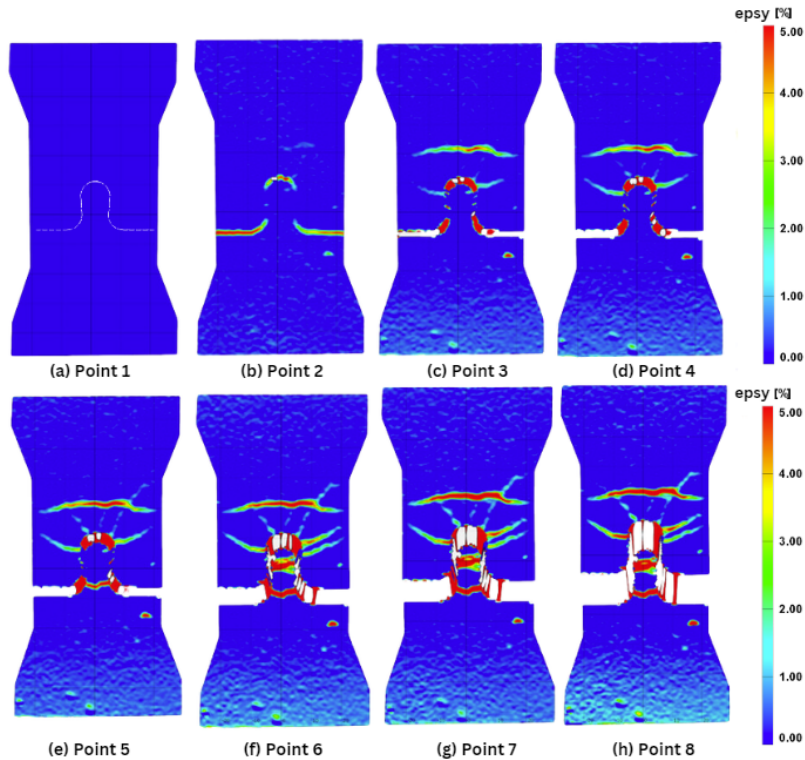**Figure B.43:** Force - displacement diagram illustrating the tensile response of the specimen CLG23

Figure B.44: Strain contours (ϵ_y) of points 1-8

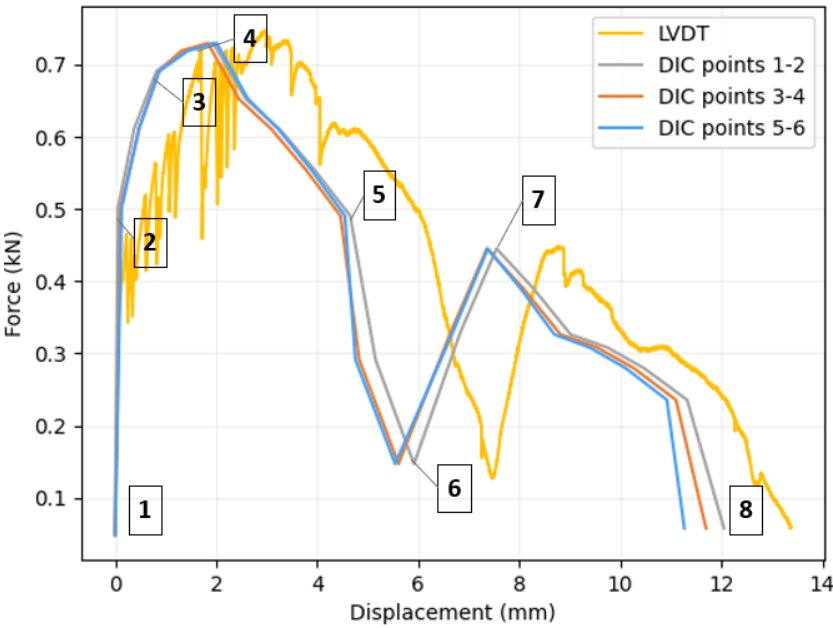## B.23. Specimen CLG32- Lubricated interface, Geometry 3

Figure B.45: Force - displacement diagram illustrating the tensile response of the specimen CLG32

Figure B.46: Strain contours (ϵ_y) of points 1-8

B.24. Specimen CLG33- Lubricated interface, Geometry 2
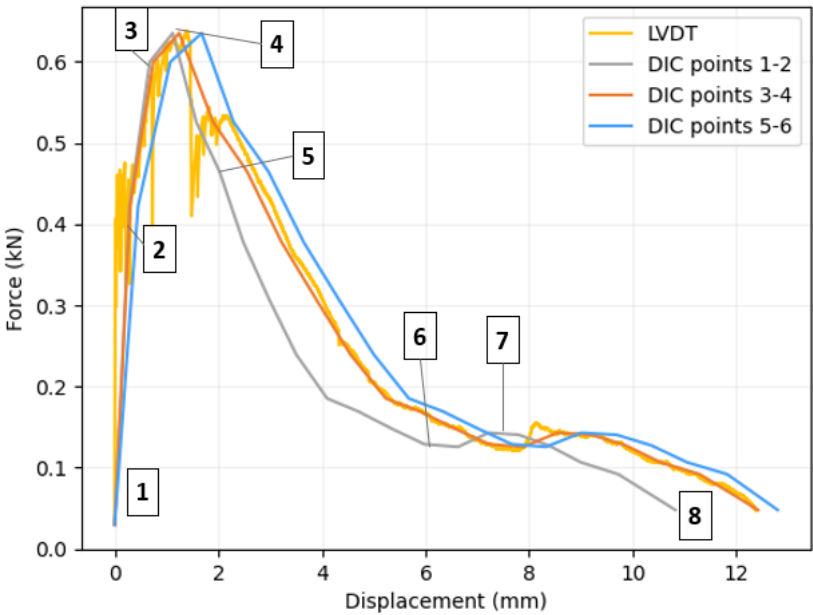
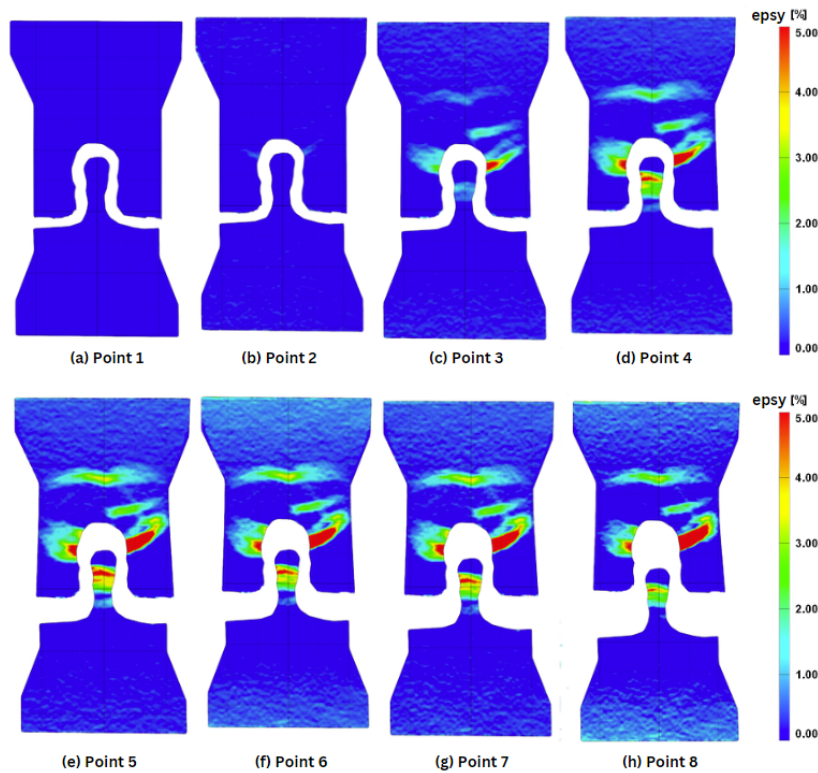**Figure B.47:** Force - displacement diagram illustrating the tensile response of the specimen CLG33
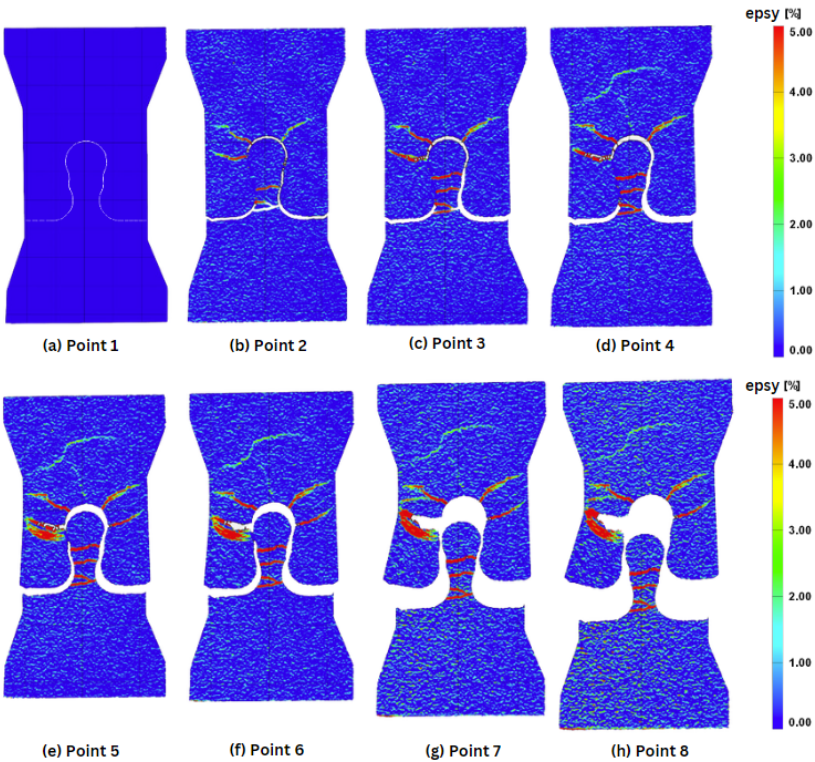
Figure B.48: Strain contours (ϵ_y) of points 1-8

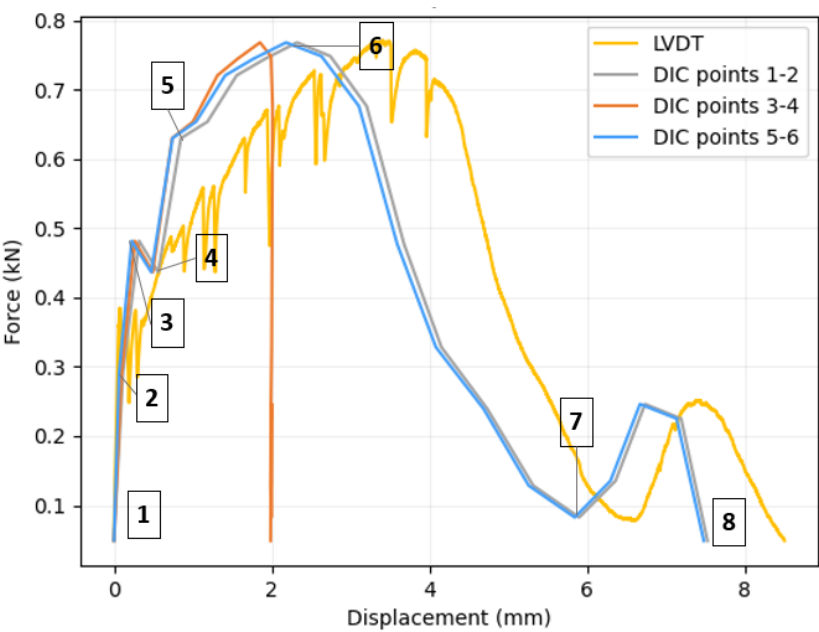## B.25. Specimen CPG31- "Assembled" interface, Geometry 3
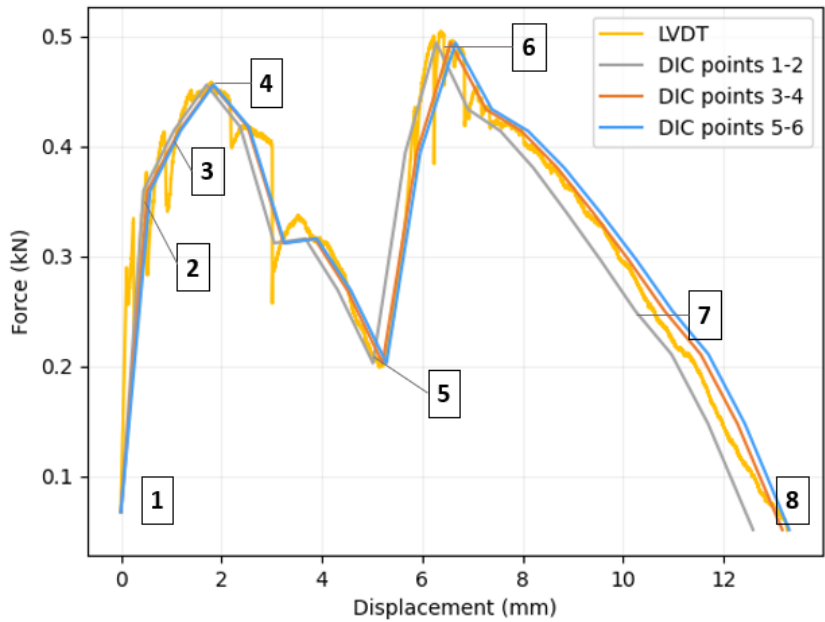
Figure B.49: Force - displacement diagram illustrating the tensile response of the specimen CPG31
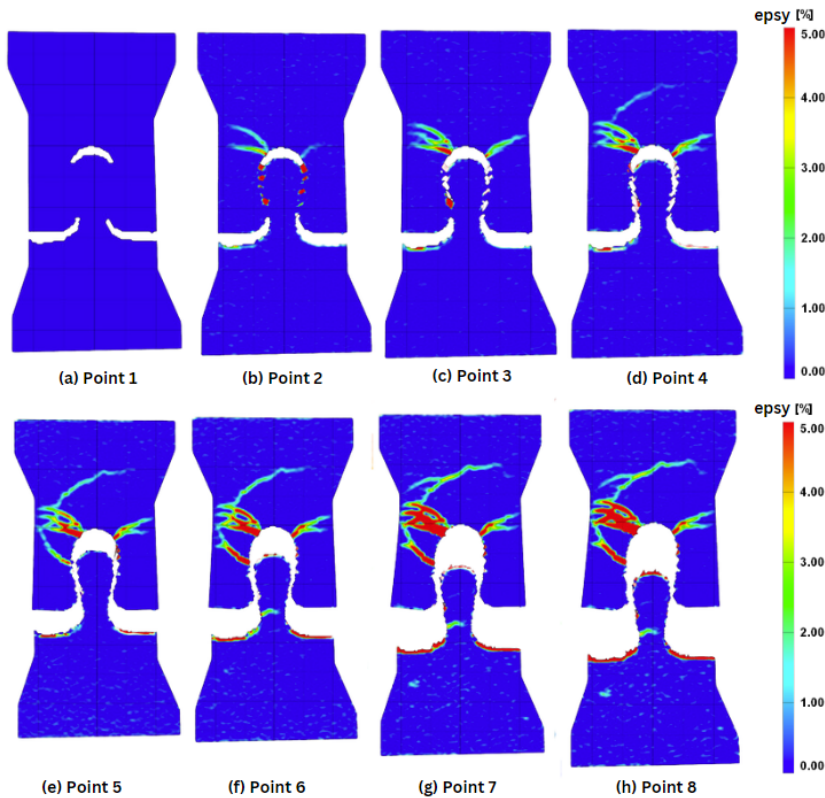
Figure B.50: Strain contours (ϵ_y) of points 1-8

B.26. Specimen CPG33- "Assembled" interface, Geometry 3

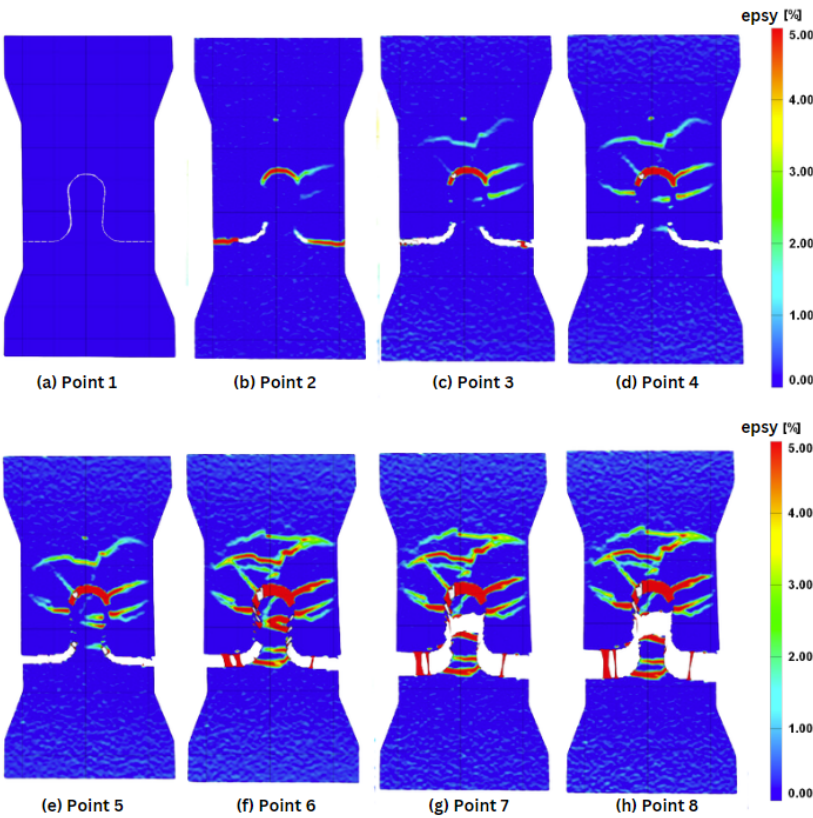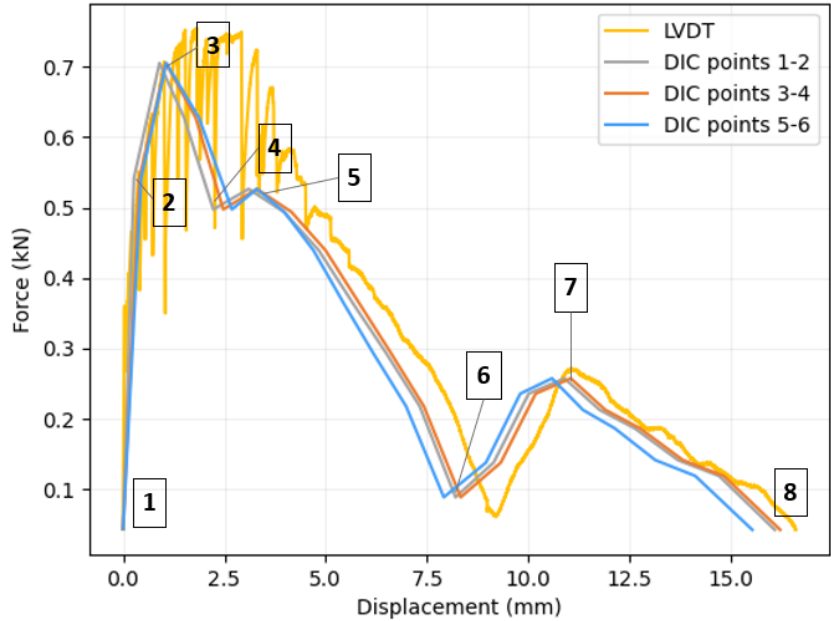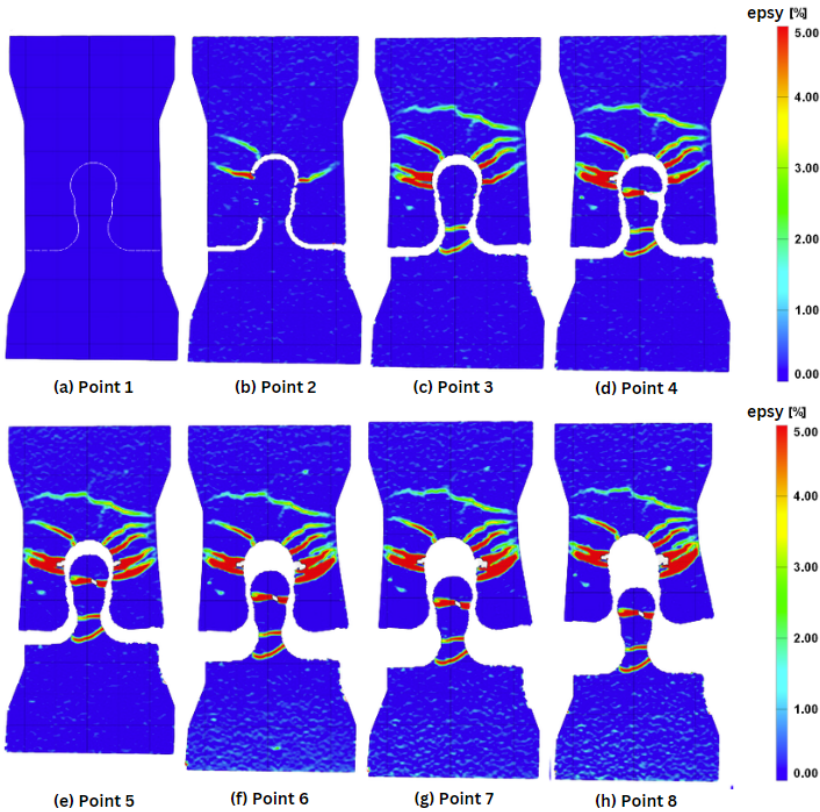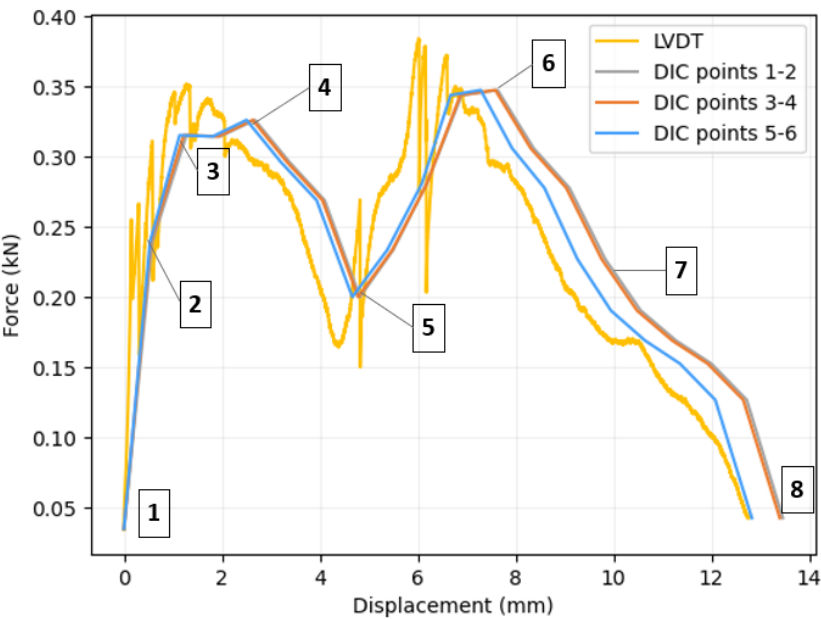**Figure B.51:** Force - displacement diagram illustrating the tensile response of the specimen CPG33
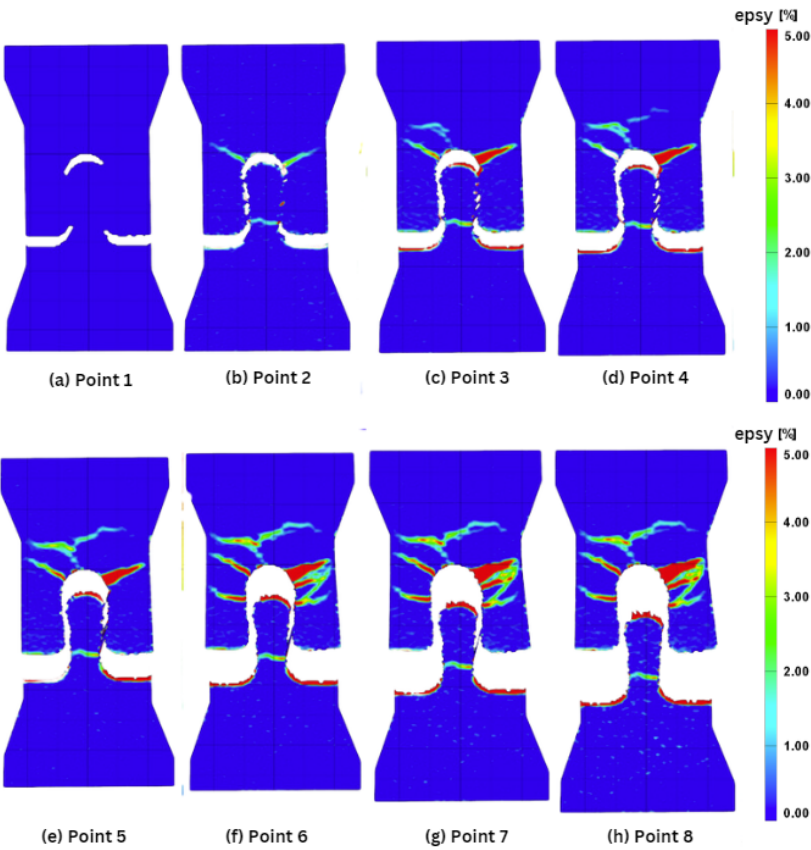
Figure B.52: Strain contours (ϵ_y) of points 1-8

B.27. Filtering the noise of DIC values

(a) Specimen SCG11

(b) Specimen SCG22

(c) Specimen SCG31

(d) Specimen CCG11

(e) Specimen CCG21

(f) Specimen CCG31
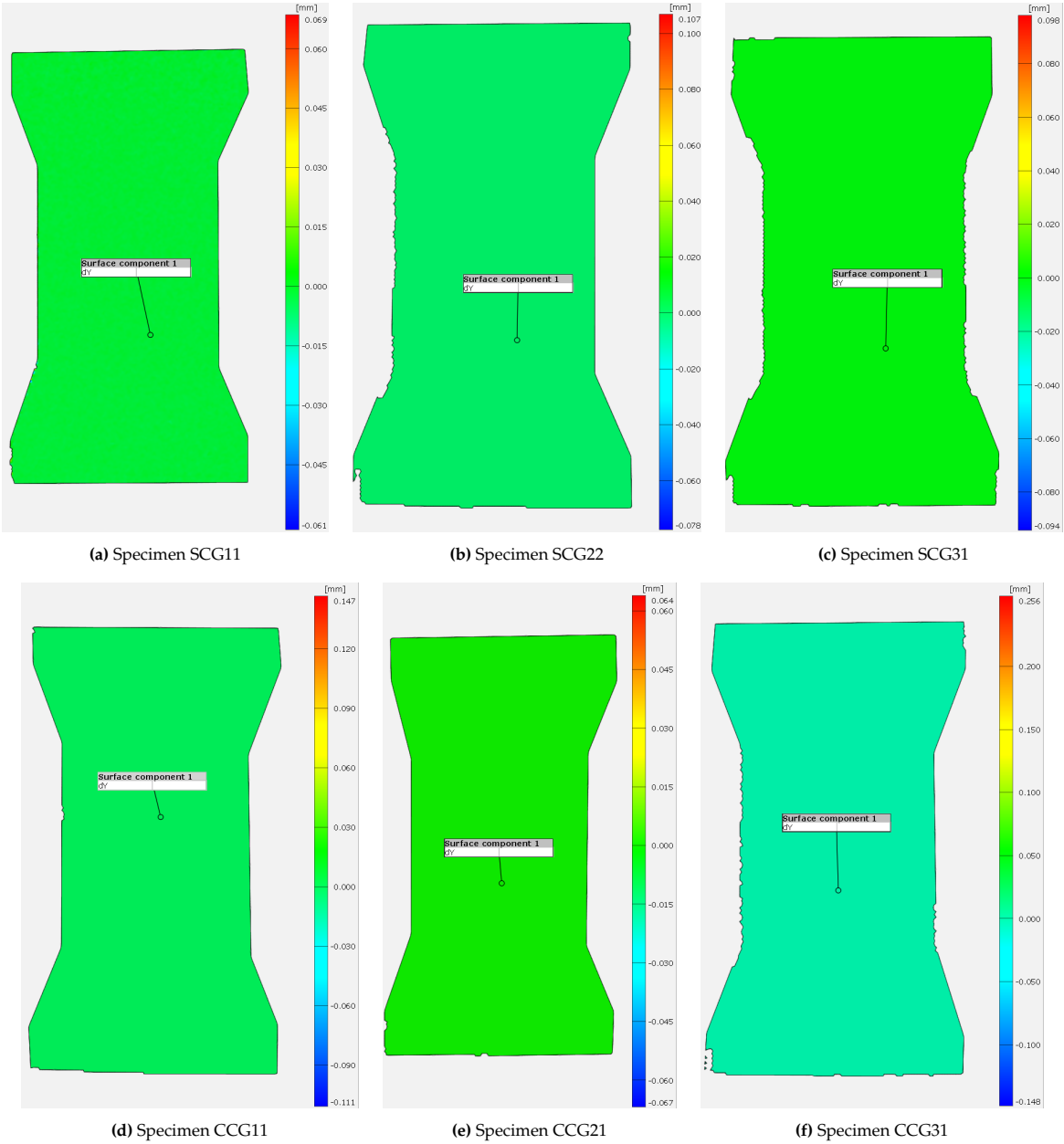
Figure B.53: Dy contours of straight and curved specimens, representing the "noise" before load application of various specimens

C

Appendix C: Maple scripts used for area under the force-displacement graph calculation

SCG11
$y := 0.4099\,x^2 - 1.1095\,x + 0.7611$

$$y := 0.4099\,x^2 - 1.1095\,x + 0.7611 \tag{1}$$

$\int_0^{1.845} y\,dx;$

$$0.3739621875 \tag{2}$$

SCG12

$$SCG12 \tag{3}$$

$y := 14.756\,x^2 - 8.5662\,x + 0.9377$

$$y := 14.756\,x^2 - 8.5662\,x + 0.9377 \tag{4}$$

$\int_0^{0.524} y\,dx;$

$$0.02300539138 \tag{5}$$

SCG13

$$SCG13 \tag{6}$$

$y := 1.3481\,x^2 - 2.1393\,x + 0.9029$

$$y := 1.3481\,x^2 - 2.1393\,x + 0.9029 \tag{7}$$

$\int_0^{0.8247} y\,dx;$

$$0.2691717188 \tag{8}$$

SCG21

<div align="center">

SCG21 **(9)**

</div>

$$y := -530.79\,x^2 + 28.766\,x + 0.6483$$

<div align="center">

$$y := -530.79\,x^2 + 28.766\,x + 0.6483$$ **(10)**

</div>

$$\int_0^{0.0786} y\ dx;$$

<div align="center">

$$0.05389895470$$ **(11)**

</div>

SCG22

<div align="center">

SCG22 **(12)**

</div>

$$y := 0.2162\,x^2 - 1.014\,x + 1.1692$$

<div align="center">

$$y := 0.2162\,x^2 - 1.014\,x + 1.1692$$ **(13)**

</div>

$$\int_0^{1.86} y\ dx;$$

<div align="center">

$$0.8844334224$$ **(14)**

</div>

SCG23

<div align="center">

SCG23 **(15)**

</div>

$$y := 0.3766\,x^2 - 1.5281\,x + 1.3314$$

<div align="center">

$$y := 0.3766\,x^2 - 1.5281\,x + 1.3314$$ **(16)**

</div>

$$\int_0^{1.3558} y\ dx;$$

<div align="center">

$$0.7134973221$$ **(17)**

</div>

SCG31

(18)

$y := 0.0045\,x^2 - 0.0879\,x + 0.5528$

$$y := 0.0045\,x^2 - 0.0879\,x + 0.5528 \qquad \textbf{(19)}$$

$$\int_0^{15.7527} y\ \mathrm{d}x;$$

$$3.665498456 \qquad \textbf{(20)}$$

SCG32

(21)

$y := -0.0009\,x^2 - 0.0082\,x + 0.6728$

$$y := -0.0009\,x^2 - 0.0082\,x + 0.6728 \qquad \textbf{(22)}$$

$$\int_0^{14.804} y\ \mathrm{d}x;$$

$$8.088255337 \qquad \textbf{(23)}$$

SCG33

(24)

$y := 0.3076\,x^2 - 1.0183\,x + 1.0071$

$$y := 0.3076\,x^2 - 1.0183\,x + 1.0071 \qquad \textbf{(25)}$$

$$\int_0^{1.716} y\ \mathrm{d}x;$$

$$0.7470159758 \qquad \textbf{(26)}$$

SLG11
$y := -0.0537\, x^2 + 0.0198\, x + 0.4981$

$$y := -0.0537\, x^2 + 0.0198\, x + 0.4981 \tag{27}$$

$$\int_0^{3.187} y\, \mathrm{d}x;$$

$$1.108571035 \tag{28}$$

SLG12

$$SLG12 \tag{29}$$

$y := -0.0524\, x^2 + 0.0127\, x + 0.2827$

$$y := -0.0524\, x^2 + 0.0127\, x + 0.2827 \tag{30}$$

$$\int_0^{2.0896} y\, \mathrm{d}x;$$

$$0.4590893301 \tag{31}$$

SLG13

$$SLG13 \tag{32}$$

$y := 0.2474\, x^2 - 0.7535\, x + 0.4142$

$$y := 0.2474\, x^2 - 0.7535\, x + 0.4142 \tag{33}$$

$$\int_0^{0.6927} y\, \mathrm{d}x;$$

$$0.1335494615 \tag{34}$$

SLG21

$$y := -0.0343\, x^2 + 0.1542\, x + 0.4858$$

$$y := -0.0343\, x^2 + 0.1542\, x + 0.4858 \tag{36}$$

$$\int_0^{6.73} y \, dx;$$

$$3.276394009 \tag{37}$$

SLG22

$$SLG22 \tag{38}$$

$$y := -0.0142\, x^2 - 0.006\, x + 0.5306$$

$$y := -0.0142\, x^2 - 0.006\, x + 0.5306 \tag{39}$$

$$\int_0^{5.75461} y \, dx;$$

$$2.052032343 \tag{40}$$

SLG23

$$SLG23 \tag{41}$$

$$y := -0.0138\, x^2 + 0.0203\, x + 0.3996$$

$$y := -0.0138\, x^2 + 0.0203\, x + 0.3996 \tag{42}$$

$$\int_0^{5.403} y \, dx;$$

$$1.729799457 \tag{43}$$

SLG31

$$SLG31 \tag{44}$$

$$y := -0.0009\,x^2 - 0.0162\,x + 0.6178$$

$$y := -0.0009\,x^2 - 0.0162\,x + 0.6178 \tag{45}$$

$$\int_0^{14.565} y\,\mathrm{d}x;$$

$$6.352986934 \tag{46}$$

SLG32

$$SLG32 \tag{47}$$

$$y := 0.0016\,x^2 - 0.0505\,x + 0.6074$$

$$y := 0.0016\,x^2 - 0.0505\,x + 0.6074 \tag{48}$$

$$\int_0^{13.492756} y\,\mathrm{d}x;$$

$$4.908713549 \tag{49}$$

SLG33

$$SLG33 \tag{50}$$

$$y := -0.0009\,x^2 - 0.0009\,x + 0.38931$$

$$y := -0.0009\,x^2 - 0.0009\,x + 0.38931 \tag{51}$$

$$\int_0^{15.655} y\,\mathrm{d}x;$$

$$4.833348848 \tag{52}$$

CCG11

<div align="center">CCG11</div> (1)

$y := -475.06\, x^2 + 25.118\, x + 0.6172$

<div align="center">$y := -475.06\, x^2 + 25.118\, x + 0.6172$</div> (2)

$$\int_0^{0.077467244} y \, dx;$$

<div align="center">0.04956394767</div> (3)

CCG12

<div align="center">CCG12</div> (4)

$y := -734.72\, x^2 + 47.426\, x + 0.5366$

<div align="center">$y := -734.72\, x^2 + 47.426\, x + 0.5366$</div> (5)

$$\int_0^{0.0801018} y \, dx;$$

<div align="center">0.06926080148</div> (6)

CCG13

<div align="center">CCG13</div> (7)

$y := -139.23\, x^2 - 12.473\, x + 1.1597$

<div align="center">$y := -139.23\, x^2 - 12.473\, x + 1.1597$</div> (8)

$$\int_0^{0.060557756} y \, dx;$$

<div align="center">0.03705134630</div> (9)

CCG21

$$CC\ G21 \tag{10}$$

$$y := -402.6\,x^2 + 25.765\,x + 0.8163$$

$$y := -402.6\,x^2 + 25.765\,x + 0.8163 \tag{11}$$

$$\int_0^{0.095244889} y\,dx;$$

$$0.07866133037 \tag{12}$$

CCG22

$$CCG22 \tag{13}$$

$$y := 19.508\,x^2 - 9.8961\,x + 1.3666$$

$$y := 19.508\,x^2 - 9.8961\,x + 1.3666 \tag{14}$$

$$\int_0^{0.253685933} y\,dx;$$

$$0.1344125815 \tag{15}$$

CCG23

$$C\ CG23 \tag{16}$$

$$y := -335.57\,x^2 + 25.542\,x + 0.7763$$

$$y := -335.57\,x^2 + 25.542\,x + 0.7763 \tag{17}$$

$$\int_0^{0.105259111} y\,dx;$$

$$0.09275962896 \tag{18}$$

CCG31

$$CCG31 \tag{19}$$

$$y := -3.7328\, x^2 - 4.2367\, x + 1.158$$

$$y := -3.7328\, x^2 - 4.2367\, x + 1.158 \tag{20}$$

$$\int_0^{0.231950511} y \; \mathrm{d}x;$$

$$0.1391018336 \tag{21}$$

CCG32

$$CCG32 \tag{22}$$

$$y := -436.74\, x^2 + 10.266\, x + 1.2192$$

$$y := -436.74\, x^2 + 10.266\, x + 1.2192 \tag{23}$$

$$\int_0^{0.072119022} y \; \mathrm{d}x;$$

$$0.06001766917 \tag{24}$$

CCG33

$$C^2\, G33 \tag{25}$$

$$y := -297.88\, x^2 + 10.982\, x + 1.1025$$

$$y := -297.88\, x^2 + 10.982\, x + 1.1025 \tag{26}$$

$$\int_0^{0.090714933} y \; \mathrm{d}x;$$

$$0.07107615611 \tag{27}$$

CLG11

$y := -35.394 x^2 + 6.3032 x + 0.3945$

$$y := -35.394 x^2 + 6.3032 x + 0.3945 \tag{28}$$

$$\int_0^{0.207036222} y \, dx;$$

$$0.1120657915 \tag{29}$$

CLG12

$$CLG12 \tag{30}$$

$y := -20.843 x^2 + 3.0889 x + 0.4129$

$$y := -20.843 x^2 + 3.0889 x + 0.4129 \tag{31}$$

$$\int_0^{0.188478378} y \, dx;$$

$$0.08616964417 \tag{32}$$

CLG13

$$CLG13 \tag{33}$$

$y := -28.915 x^2 + 5.4839 x + 0.4342$

$$y := -28.915 x^2 + 5.4839 x + 0.4342 \tag{34}$$

$$\int_0^{0.228723644} y \, dx;$$

$$0.1274274669 \tag{35}$$

CLG21

$$CLG21 \tag{36}$$

$$y := -11.109\,x^2 + 0.7862\,x + 0.8732$$

$$y := -11.109\,x^2 + 0.7862\,x + 0.8732 \tag{37}$$

$$\int_0^{0.296965489} y\,dx;$$

$$0.1969995146 \tag{38}$$

CLG22

$$C\,LG22 \tag{39}$$

$$y := -8.6102\,x^2 + 0.2693\,x + 0.7849$$

$$y := -8.6102\,x^2 + 0.2693\,x + 0.7849 \tag{40}$$

$$\int_0^{0.278862978} y\,dx;$$

$$0.1671112684 \tag{41}$$

CLG23

$$CLG23 \tag{42}$$

$$y := -69.967\,x^2 + 8.9203\,x + 0.6452$$

$$y := -69.967\,x^2 + 8.9203\,x + 0.6452 \tag{43}$$

$$\int_0^{0.188702133} y\,dx;$$

$$0.1238577829 \tag{44}$$

CLG31

$$C\,LG3\,1 \tag{45}$$

$$y := -4.4023\,x^2 - 0.7014\,x + 0.9423$$

$$y := -4.4023\,x^2 - 0.7014\,x + 0.9423 \tag{46}$$

$$\int_0^{0.359269667} y\,\mathrm{d}x;$$

$$0.2252245806 \tag{47}$$

CLG32

$$C\,LG\,32 \tag{48}$$

$$y := 2.5947\,x^2 - 3.4368\,x + 1.0149$$

$$y := 2.5947\,x^2 - 3.4368\,x + 1.0149 \tag{49}$$

$$\int_0^{0.368065467} y\,\mathrm{d}x;$$

$$0.1838804269 \tag{50}$$

CLG33

$$CLG33 \tag{51}$$

$$y := 8.3808\,x^2 - 5.0622\,x + 0.8638$$

$$y := 8.3808\,x^2 - 5.0622\,x + 0.8638 \tag{52}$$

$$\int_0^{0.274846044} y\,\mathrm{d}x;$$

$$0.1042124658 \tag{53}$$